THE UNIVERSITY *of* EDINBURGH

Giant Exoplanets and Brown Dwarfs: Exploring the Atmospheric Retrieval Method via Direct Imaging Spectroscopy

Niall Patrick Whiteford

Doctor of Philosophy
The University of Edinburgh
Feb 2022

Abstract

The retrieval method, also known as the inverse method, has become a fundamental analysis technique for modelling and understanding exoplanetary atmospheres. In their simplest form, retrieval approaches aim to obtain the best fit solution via fitting to observed spectra using an atmospheric model defined with varying degrees of flexibility and complexity. The critical chemistry and physics driving parameters sample the parameter space, guided by Bayesian statistics, with the aim of attaining a best fit. This analysis returns estimates for an object's mass, radius, surface gravity, temperature-pressure structure and cloud properties, as well as confirming and constraining the presence and abundance of a variety of molecular species.

TauREx3 (Tau Retrieval of Exoplanets) is a Bayesian retrieval suite developed for application to spectroscopic observations of exoplanet atmospheres. In the past, retrieval techniques, including TauREx3, have mainly been applied to transit spectroscopy. Therefore, the application of retrieval analysis to directly imaged exoplanets and brown dwarfs is still greatly unexplored and novel territory. As such, we have adapted TauREx3 for analysis of near-infrared spectrophotometry from a variety of directly imaged gas giant exoplanets and brown dwarfs, including a significant expansion of the forward model's temperature-pressure structures and cloud capabilities. The objects analysed as part of this work span the L and T spectral and temperature regimes.

We first validate TauREx3 using high-quality data of brown dwarf GJ 570 D, robustly comparing our results to those of other retrieval studies. We then explore the atmosphere of the cool, directly-imaged exoplanet 51 Eri b. This work showed evidence for the presence of ammonia in its atmosphere, as well as the ability to fit the spectra without including cloud modelling in the retrieval.

We then conduct a thorough study of L-type, low surface gravity exoplanets, free-floating objects and brown dwarfs. Our sample included VHS 1256 b, PSO 138, HR 8799cde and Beta Pic b. We employ a variety of cloud modelling approaches, condensate species, cloud particle size distributions as well as probing the inclusion of fractional (patchy) cloud coverage. In summary, these retrievals did not display a clear preference for a particular cloud modelling approach, likely due to the data quality inhibiting the ability of the retrieval to differentiate between the cloud characteristics we probed.

Finally, our retrieval framework was then tested using simulated James Webb Space Telescope (JWST) observations of VHS 1256 b and Ross 458 c. These retrievals resulted in extremely precise, but not always accurate, parameter constraints. This work demonstrated the need for causation when using retrieval analysis as we enter the new high-quality data era of JWST.

Lay summary

In 1995, with the discovery of a planet around a sun-like star beyond our solar system, a new area of astronomy was born. Since then, the study of these so called "exoplanets" has become a rapidly growing research area. For many years, the detection of these foreign worlds was the focus of research, with the development of many different approaches. One such approach is known as "direct-imaging", where light emitted from an Exoplanet is directly pictured via large and sophisticated telescopes.

This light, when pictured at different wavelengths (positions along the electromagnetic spectrum), can be used to construct a spectrum, which offers us a window into the characteristics of the atmosphere of the exoplanet. The endeavour to capture spectra of exoplanets has become one of the main goals of observational astronomy, employing telescopes around the world and in space.

Once a spectrum of an exoplanet is produced, comparisons to atmospheric models can be made. These models vary characteristics such as temperatures, chemistry and cloud structures in the pursuit of replicating the observed spectrum. By comparing to many thousands of model variations, Bayesian statistics can be used to determine the atmospheric properties that best explain the observations. This approach is known as a "retrieval" and is employed in this work to explore the atmospheres of direct-imaged giant exoplanets.

The James Webb Space Telescope, with its large mirror and state of the art

instruments aboard, dawns a new era of astronomy. Poised to observe many exoplanets, it will redefine the quality of spectra we can produce. As such, we also test the retrieval method using a suite of mock JWST observations, exploring the novel characterisation capabilities it will permit and preparing for the arrival of real data from JWST

Declaration

I declare that this thesis was composed by myself, that the work contained herein is my own except where explicitly stated otherwise in the text, and that this work has not been submitted for any other degree or professional qualification except as specified.

At the time of writing, outcomes of this work are in preparation for submission to academic journals:

- Whiteford N., Glasse A., Chubb K. L., Kitzmann D., Shrishmoy R., et al., *Retrieval study of cool, directly imaged exoplanet 51 Eri b*, mnras, in prep.
- Whiteford N., Blain D., Biller, B., Glasse A., Rice K., et al., *Retrieval study of low surface gravity L dwarfs*, mnras, in prep.
- Whiteford N., Patapis P., Glasse A., Biller B., Blain D., et al., *Unlocking substellar companion chemical catalogue with JWST*, mnras, in prep.

(*Niall Patrick Whiteford, Feb 2022*)

Acknowledgements

Firstly, to my (huge!) A-team of supervisors, Prof Alistair Glasse, Prof Beth Biller, Prof Ken Rice and Prof Paul Palmer. I will be forever grateful for their support and guidance during my PhD journey, and also for letting me travel so much! I look forward to continuing working together in the years to come and coming home to the Royal Observatory Edinburgh whenever I can.

I cannot understate the immense support from my Mum and Dad. Without their support, patience, and advice, I would neither have been doing a PhD, nor completed this thesis. From the regular visits, the countless dinners at the Salisbury, and the endless phone calls, you were always there for me throughout this whole journey. For this, I will be forever indebted to them and I hope I have made them proud.

I also want to massively thank Pete Higgins. The Jon Snow lookalike first became a flatmate, then a best friend and finally a brother who's support and company during a lockdown laden 2 years cannot be understated. I will always hold dear, the Christmas we spent together, the dad jokes, the infinite meadows wanders, the shared dinners (especially the roasts!) and takeaways, Mario Kart evenings and trash TV marathons. He will always be my brother and I can't wait to work together with him on many projects together in the future and to visit him Toronto.

I would like to thank Clémence Fontanive for being a limitless source of knowledge, wisdom and inspiration, as well as my closest companion, during my PhD journey. I will forever treasure the wonderful years we spent together in Edinburgh, my visits to Switzerland and our amazing globe-trotting adventures.

To the whole team at Cult, I wholeheartedly thank you for giving me a second home, and the best office, in Edinburgh (with the best coffee!). I will fondly remember the endless days they all kept me company, cheerful and caffeinated during the latter years of my PhD. This thesis was quite literally fuelled and sponsored by Cult coffee. It will always be my first stop when I visit Edinburgh.

To my Holland Annex family, Lewis, Lucy and Emily, I couldn't have asked for a better group of people to live with my first year in Edinburgh. From our Highlands trip to our wine and TV evenings curled up on the sofa, football and rugby games to our trips to the pub, and the endless humour we exchanged, these will be memories I forever cherish. I hope we are all reunited soon!

I had the pleasure of having some wonderful flatmates during my time in Edinburgh, particularly Rachael and Kelsey, and of course Casper! I want to thank them for helping me to make Blackwood Crescent home, especially during some tough and stressful times. I would also like to thank all the fantastic people I met, worked with and became friends with at the Royal Observatory Edinburgh.

Lastly, to Edinburgh itself, thank you for being home for so many years and truly the most wonderful, beautiful and best city in the world! Goodbye, for now...

Contents

Abstract i

Declaration v

Acknowledgements vii

Contents ix

List of Figures xix

List of Tables xxv

1 Background 1

1.1 Introduction 2

1.2 Detection Methods 3

1.2.1 Radial Velocity Method 5

1.2.2 Transit Method 6

1.2.3 Gravitational Microlensing 8

1.2.4 Direct Imaging 10

1.3 Atmospheric observation techniques 14

1.3.1 Transit Spectroscopy 14

1.3.1.1 Transmission spectrum 14

1.3.1.2 Transit emission spectrum 17

1.3.1.3 Transit phase curve 17

1.3.2 High-Resolution Doppler Spectroscopy 18

1.3.3 Direct Imaging Spectroscopy 19

1.4 Defining an exoplanet, brown dwarf and free floating object 20

1.4.1 Brown Dwarfs 22

1.4.2 Free-floating objects 23

1.5 Atmospheric chemistry 23

1.5.1 Chemical equilibrium 24

1.5.2 Chemical disequilibrium 24

1.6 Atmospheric classification 25

1.6.1 L dwarf atmospheres 27

1.6.2 T dwarf atmospheres 27

1.6.3 Low surface gravity L/T transition atmospheres 30

1.7 Atmospheric modelling approaches 30

1.7.1 Self-consistent forward modelling 31

1.7.2 Retrieval models 31

1.8 Outline of Chapters 2-6 32

2 Retrieval method: TauREx3 33

2.1 TauREx3 34

2.1.1 Radiative transfer forward model 34

2.1.2 Emission mode for direct imaging 36

2.1.3 Addition of inferred parameters 36

2.1.4 Atomic and Molecular opacity 38

2.1.4.1 Alkali cross sections 39

2.1.5 Retrieved abundances 39

2.1.6 Temperature-pressure profiles 40

2.1.6.1 *npoint* 40

2.1.6.2 Madhusudhan and Seager (2009) 40

2.1.6.3 Lavie et al. (2017) 42

2.1.7 Bayesian Analysis 43

2.1.7.1 Error inflation 43

2.1.8 Nested Sampling via Multinest 44

2.1.8.1 Multinest 46

2.1.9 Priors 46

2.1.10 Clouds 47

2.1.10.1 Simple powerlaw clouds 47

2.1.10.2 Lee et al. 2013 Mie opacity approximation 50

2.1.10.3 Bohren & Huffman Mie opacity for homogeneous spheres 52

2.1.10.4 Particle size distributions 52

2.1.10.5 Patchy/Fractional clouds 53

3 Retrieval study of cool, directly imaged exoplanet 51 Eri b 57

3.1 Introduction 58

3.2 Two benchmark T dwarfs: GJ 570D and 51 Eri b observations 60

3.2.1 GJ 570D 61

3.2.1.1 Observations and calibration 61

3.2.2 51 Eri b 63

3.2.2.1 Observations 64

3.3 Modelling 65

3.3.1 TauREx3 65

3.3.1.1 Retrieval model setup 65

3.3.1.2 Retrieval priors 66

3.3.2 ATMO 2020 66

3.3.2.1 Sampling using Markov Chain Monte Carlo . . . 70

3.4 Results: GJ 570D 70

3.4.1 Na+K systematic model bias 73

3.4.2 Scaling factors and bulk parameters 75

3.4.3 Abundances 77

3.4.4 Temperature-Pressure profile 78

3.5 Results: 51 Eri b 78

3.5.1 Scaling factors and bulk parameters 82

3.5.2 Abundances, tentative ammonia detection 85

3.5.3 Temperature-Pressure profile 88

3.5.4 The question of formation 90

3.6 Discussion 91

3.7 Summary 99

4 Retrieval study of low surface gravity L dwarfs 103

4.1 Introduction 104

4.2 Targets and data 106

4.2.1 PSO 318 106

4.2.2 VHS 1256b 111

4.2.3 HR 8799cde 112

4.2.4 Beta Pic b 113

4.3 TauREx3 setup 114
4.3.0.1 Retrieval setup 114
4.3.0.2 Priors 115
4.3.1 TEA - Thermochemical equilibrium abundances 116
4.4 Exo-REM setup 116
4.5 TauREx3 results 119
4.5.1 PSO318 119
4.5.2 VHS 1256b 121
4.5.3 HR 8799c 122
4.5.4 HR 8799d 123
4.5.5 HR 8799e 125
4.5.6 Beta Pic b 126
4.6 Discussion 132
4.6.1 Surface gravity / Masses 132
4.6.2 Inability to clearly distinguish between cloud species 132
4.6.3 Fractional cloud 140
4.6.4 Uncertainties in flux calibrations 140
4.6.5 The challenge of combining data 141
4.6.6 Enforcing a radius prior 142
4.6.7 Temperature-pressure profile 143

4.6.8 Chemical equilibrium vs disequilibrium: comparing retrieved abundances to TEA 144

4.6.9 Consistency between retrieval codes? 146

4.6.10 C/O ratio as a formation tracer 146

4.6.11 Importance of K band 147

4.6.12 Outlook to future work 148

4.7 Summary 149

5 JWST and retrievals 151

5.1 Introduction 152

5.2 Method 153

5.2.1 Simulated Objects 154

5.2.1.1 A cloudy L dwarf: VHS 1256 b 155

5.2.1.2 A cloudless T dwarf: Ross 458 c 155

5.2.2 Exo-REM Model 155

5.2.3 MIRI simulations 156

5.2.4 NIRSpec simulations 159

5.2.5 TauREx3 setup 160

5.3 Results 163

5.3.1 Ross 458 c 163

5.3.2 VHS 1256 b 164

5.4 Discussion 166

5.4.1 Our results 166

5.4.2 Future work 177

5.4.2.1 Testing different temperature-pressure profiles . . 177

5.4.2.2 Testing alkali cross sections 178

5.4.2.3 Retrieving same cloud model 178

5.4.2.4 Attempting to retrieve multiple cloud layers . . . 178

5.4.2.5 Retrieving variability? 179

5.4.2.6 Testing NIRSpec by itself 179

5.4.2.7 Reducing retrieval run times 180

5.5 Summary 180

6 Summary and outlook 183

6.1 Summary of chapter 2 184

6.2 Summary of chapter 3 184

6.2.1 Future Work 185

6.3 Summary of chapter 4 185

6.3.1 Future work 186

6.4 Summary of chapter 5 187

6.4.1 Future work 187

6.5 A JWST GO program: PLanetary Abundance Tracing to constrain FORmation in the mid-IR - PLATFORM 188

6.6 Final thoughts 190

7 Appendix 191

Bibliography 209

List of Figures

1.1 Exoplanet detection bar chart 4

1.2 Mass vs separation of exoplanets 4

1.3 Radial velocity method illustration 7

1.4 Transit detection method illustration 9

1.5 Direct imaging method illustration 11

1.6 Exoplanet evolutionary tracks 13

1.7 Transmission spectroscopy illustration 15

1.8 Compilation of exoplanet spectra 21

1.9 Illustration of carbon chemistry disequilibrium 26

1.10 L and T dwarf spectral standards and colour-magnitude diagram . 28

1.11 Cloud spectral impact illustration 29

2.1 Retrieval method flowchart 34

2.2 TauREx3 molecular abundance profile illustration 38

2.2 TauREx3 temperature-pressure profiles 41
2.3 Posterior and likelihood cartoon 45
2.4 TauREx3 cluster speedup demo 47
2.5 Power law deck, powerlaw slab and slab infinity deck cloud structures 50
2.6 Cloud extinction efficiency curves 51
2.7 Cloud particle size distributions 54

3.0 GJ 570 D and 51 Eri b spectra 62
3.1 Planetary evolutionary tracks with 51 Eri b age 67
3.2 GJ 570D retrieval spectral fit 73
3.3 Na and K cross section comparison 74
3.4 GJ 570D bulk parameter posterior probability distributions 76
3.5 GJ 570D mixing ratio posteriors 79
3.5 51 Eri b retrieval spectral fits 83
3.6 51 Eri b ATMO spectral fits 85
3.7 51 Eri b posteriors 86
3.8 Retrieved 51 Eri b vs GJ 570 D temperature-pressure profile . . . 89
3.9 Retrieved vs ATMO Temperature-pressure profiles for 51 Eri b . . 90
3.10 Planetary thermal evolution tracks with retrieved surface gravity . 93

4.1 Color magnitude diagram 107
4.2 L dwarf sample spectral data 110
4.3 Flexible vs inflexible temperature-pressure profile comparison . . . 114

4.4 PSO 318 retrieval spectral fit 133

4.5 PSO 318 corner plot of retrieved cloud parameters 133

4.6 VHS 1256 b retrieval spectral fit 134

4.7 VHS 1256 b corner plot of retrieved cloud parameters 134

4.8 HR8799c retrieval spectral fit 135

4.9 HR 8799c corner plot of retrieved cloud parameters. 135

4.10 HR8799d retrieval spectral fit. 136

4.11 HR 8799d corner plot of the best-fit model's retrieved cloud parameters 136

4.12 HR8799e retrieval spectral fit 137

4.13 HR 8799e corner plot of the retrieved cloud parameters 137

4.14 Beta pic b retrieval spectral fit 138

4.15 Beta Pic b corner plot of retrieved cloud parameters 138

4.17 Currently inferred C/O ratios for low surface gravity objects. . . . 147

5.1 Project flowchart 154

5.2 Simulated JWST spectra of VHS 1256 b and Ross 458 c 157

5.3 Simulated images of VHS1256 b and ROSS 458 c 158

5.4 Retrieval spectral fits of MIRI simulated observations of Ross 458 c and VHS 1256 b 167

5.5 Retrieval spectral fits of NIRSpec and MIRI simulated observations of Ross 458 c. 168

5.6 Retrieval spectral fits of NIRSpec and MIRI simulated observations of VHS 1256 b 169

5.7 Molecular abundance profile comparison for Ross 458 c 170

5.8 Molecular abundance profile comparison from simulated Ross 458 c observations 171

5.9 Molecular abundance profile comparison from simulated VHS 1256b observations 172

5.10 Molecular abundance profile comparison for simulated VHS 1256 b observations 173

5.11 VHS 1256 b retrieval posterior comparison 174

5.12 Ross 458 c retrieval posterior comparison 175

5.13 Temperature-pressure profile comparison 176

6.1 PLATFORM sample, sep vs temp. 188

7.0 ATMO posteriors plots for 51 Eri b 192

7.0 ATMO posteriors plots for GJ 570D 192

7.1 51 Eri b posteriors for GPI J, H and K band data. 193

7.2 51 Eri b posteriors for SPEHRE Y, J, H and GPI K band data . 194

7.3 51 Eri b posteriors for SPHERE Y, J and H band data 195

7.4 PSO 318 corner plot 196

7.5 VHS 1256 b corner plot 197

7.6 HR 8799c corner plot 198

7.7 HR 8799d corner plot 199

7.8 HR 8799e corner plot 200

7.9 Beta Pic b corner plot 201

7.10 Ross 458 c corner plot for NIRSpec and MIRI simulations 202

7.11 Ross 458 c corner plot for MIRI simulations 203

7.12 VHS 1256 b corner plot for NIRSpec and MIRI simulations 204

7.13 VHS 1256 b corner plot for MIRI simulation 205

7.14 Demonstration of Ross 458 c retrieval molecular contribution used across of NIRSpec and MIRI wavelength ranges. 206

7.15 HST vs JWST retrieval precision comparison 207

7.16 JWST retrieval precision at different SNRs 208

List of Tables

2.1 Bayes ratio interpretation 45

3.1 GJ 570 D and 51 Eri b Retrieval priors 68

3.2 Retrieval bulk parameters for GJ 570D 71

3.3 GJ 570D retrieved molecular abundances 72

3.4 Retrieved bulk parameters for 51 Eri b 81

3.5 51 Eri b retrieved molecular abundances 82

4.1 L dwarf study priors 117

4.2 Exo-REM atmospheric model grid overview 119

4.3 Summary of L dwarf retrieval bulk parameters 129

4.4 Bayesian evidence comparison of L dwarf retrievals 139

5.1 Priors used for retrieval analysis. 161

5.2 Exo-REM model input and retrived values. 162

CHAPTER 1

Background

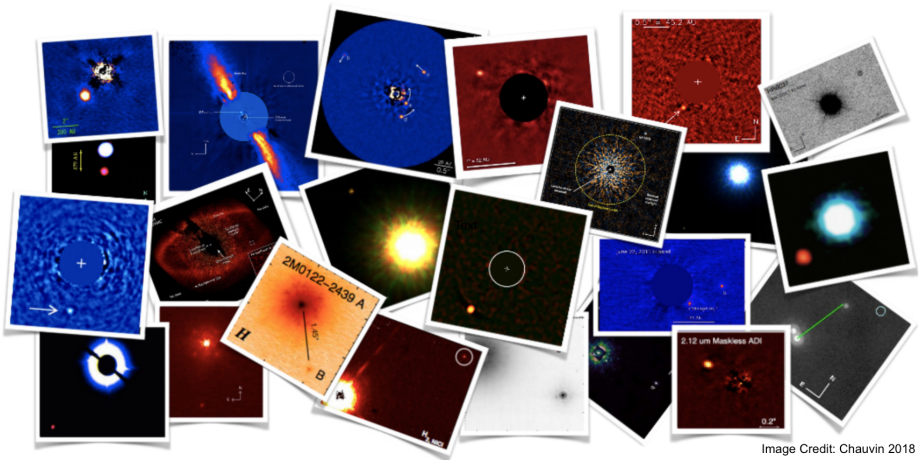

Image Credit: Chauvin 2018

1.1 Introduction

The concept, debate and philosophy relating to the existence of planets beyond Earth dates back thousands of years.

Epicurus (341–270 BCE): *"There are infinite worlds both like and unlike this world of ours. We must believe that in all worlds there are living creatures and plants and other things we see in this world."*

Aristotle (384-322 BCE): *"There cannot be more worlds than one"*

Giordano Bruno (1548-1600 CE): *"There are countless suns and countless Earths all rotating around their suns in exactly the same way as the seven planets of our solar system. We see only the suns because they are the largest bodies and are luminous, but their planets remain invisible to us because they are smaller and non luminous. The countless worlds in the universe are no worse and no less inhabited than our Earth."*

Whilst the debate around the existence of any other planets has long been settled, the debate around the potential existence of planets orbiting sun-like stars beyond our solar system, so called "Extrasolar planets" or "Exoplanets", was finally settled in 1995 with the discovery of a Jupiter-sized planet 51 Pegasi b (or 51 Peg b), orbiting solar-type star Mayor and Queloz (1995).

Since the detection 51 Pegasi b, a further $\sim$ 5000 exoplanets have been discovered using a variety of detection techniques. Along with demonstrable proof that our own solar system architecture is atypical, there have been many distinct types of exoplanets discovered. Examples of these include:

- Terrestrial Planets: Rocky planets with masses and radii approximately equivalent to Earth ($\sim$1$M_\oplus$, $\sim$1$R_\oplus$).
- Super-Earths: Rocky, ocean or lava planets with masses $\sim$2-10 $M_\oplus$ and radii $\sim$1.2-2 $R_\oplus$.
- Neptune-like: Planets resembling Neptune and Uranus, with H and He

dominated atmospheric envelopes surrounding a solid/rocky core.

- Gas-giants: Large gaseous planets with masses and radii equivalent to Jupiter ($\sim$1M_{Jup}, $\sim$1R_{Jup}). This includes so called "hot jupiters" are highly-irradiated exoplanets with very short orbital separations and periods. This class also includes the cooler and wider orbital separation "super-Jupiters" planets which are the focus of this work.

With such a diverse set of exoplanet discoveries, the study of their atmospheres has become a focal point of current research. This has, in turn, also lead to the significant expansion of atmospheric modelling approaches which attempt to explain the atmospheric observations of an exoplanet. The ultimate aim of this work is to characterise exoplanet characteristics, encompassing bulk planetary properties, composition, chemical processes, the presence of clouds and tracing formation pathways. These is all discussed in subsequent subsections.

1.2 Detection Methods

Currently, the four most successful detection methods are: (1) Radial velocity method, (2) Transit method, (3) Gravitational microlensing, and (4) Direct imaging. Initially, the radial velocity method accounted for most of the exoplanet detection but was overtaken by the transit method in 2014. Both the Radial velocity and transit method have so far detected 1 to 2 orders of magnitude more exoplanets than the microlensing and direct imaging techniques.

Most of these techniques, apart from direct imaging, use indirect detection approaches, where the presence of a planet is indicated by the behaviour of star light as a function of time. These techniques probe differing regions of the mass and orbital separation parameter space, as illustrated in Figure 1.2.

The following subsections describe the fundamentals and theory behind these methods, summarising their advantages, limitations and biases. For extensive reviews of these methods, as well as others, see Seager et al. (2010), Wright and Gaudi (2013), Fischer et al. (2014), Perryman (2014) and Perryman (2018).

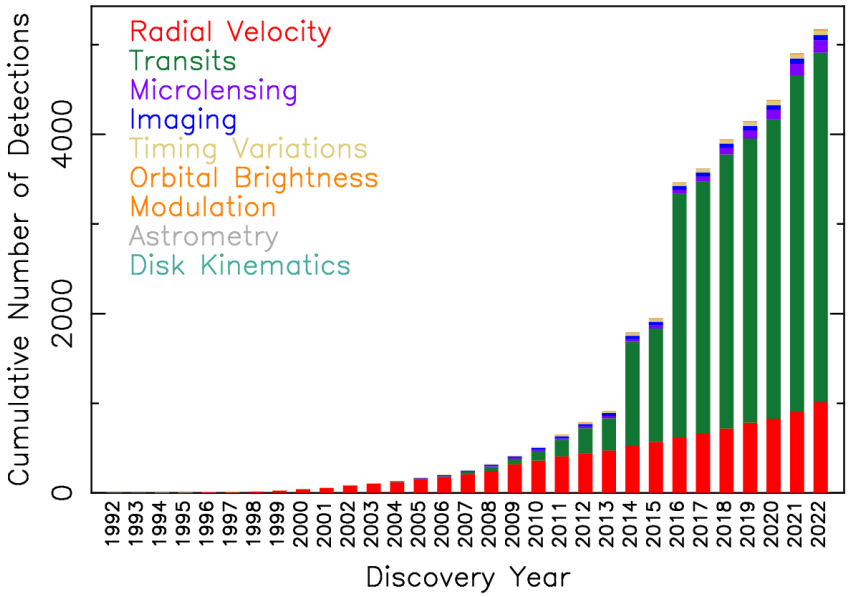

Figure 1.1: Exoplanet detections relative to time with different colours indicating different detection methods. Figure from NASA Exoplanet Archive (2022)

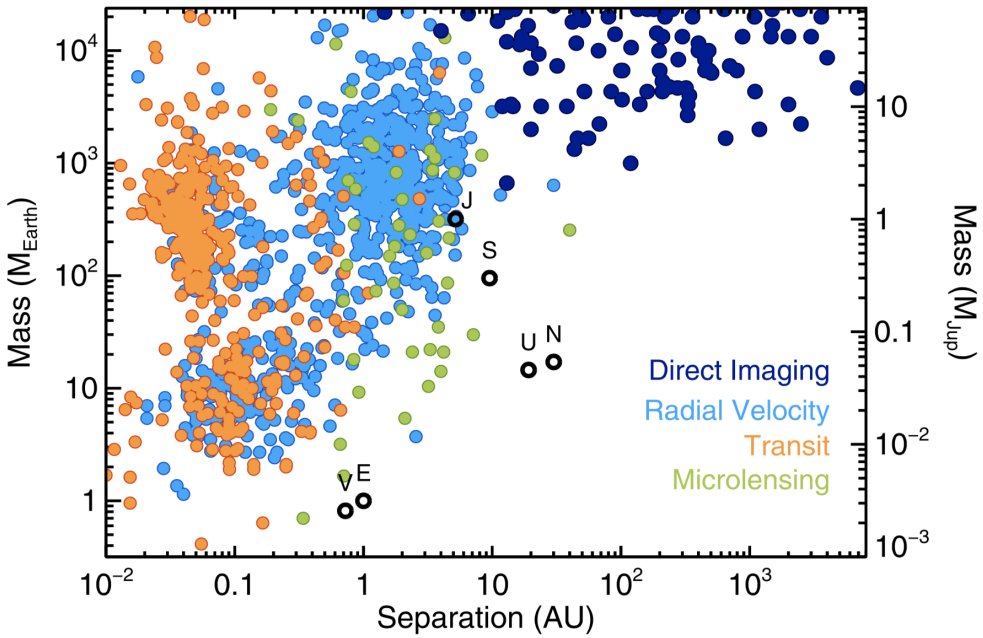

Figure 1.2: The mass vs orbital separation demographics of exoplanets from direct imaging (navy), radial velocity (blue), transit (orange), and microlensing (green) surveys. Figure from Bowler (2016)

1.2.1 | Radial Velocity Method

The radial velocity (RV) method searches for the Doppler wobble of a star caused by an orbiting exoplanet. As shown in Figure 1.3, the presence of a planet causes the star to orbit around around the centre of mass of the system, which causes the starlight to periodically blue shift and red shift relative to Earth. This effect is know as the "Doppler wobble". As the star orbits the system's centre of gravity, observations of the star's varying radial velocity can be made, and thus, the radial velocity semi-amplitude K (maximum radial velocity observed from Earth) can be determined. As outlined by Birkby (2018), the semi-amplitude K can then be used to determine a lower limit on the mass of planet causing the Doppler wobble, M_p, via:

$$K_\star = \left(\frac{2\pi G}{P}\right)^{-1/3} \frac{M_P \sin i}{(M_p + M_\star)^{2/3}} \cdot \frac{1}{1-e^2}^{1/2} \tag{1.1}$$

where $M_\star$ is the stellar mass, P is the orbital period, e is the orbital eccentricity, and i is the planets orbital inclination (see Lovis and Fischer (2010) for full derivation of previous equation). When i=90°, the planet's orbit is viewed edge on. This equation demonstrates that the mass of the planet is degenerate with inclination. This equation also shows that the radial velocity method is best suited to detecting close-in, giant planets which imprint the largest Doppler wobble, as illustrated in Figure 1.2. This detection approach is therefore biased towards detecting hot jupiter planets which cause a semi-amplitude, K, of approximately 100 ms^{-1}.

The radial velocity approach was used to detect 51 Peg b, the first known exoplanet around a sun-like star (Mayor and Queloz, 1995). The radial velocity curve from this detection is shown in Figure 1.3. It was also used to make one of the earliest detection of a multi planet system (Lovis et al., 2005).

The precision of this technique, which employs high resolution spectrographs, has improved greatly during the previous decades. The High Accuracy Radial velocity Planet Searcher (HARPS) (Mayor et al., 2003) and HARPS-N (Cosentino et al., 2012) instruments increased the precision from approximately 10 ms^{-1} to 1

ms^{-1}. Precision has increased even further, to approximately 20 cm^{-1} via Echelle SPectrograph for Rocky Exoplanets and Stable Spectroscopic Observations (ESPRESSO) (Netto et al., 2021, Pepe et al., 2021). This increasing precision has allowed for the detection of smaller planets at smaller orbital separations in Figure 1.2.

A limitation of this technique is that it is best suited for older and quiet stars. Younger stars, with faster rotations and more stellar activity, can mask the signal of orbiting planets. Figure 1.3 also illustrates that this technique has so far been unable to detect planets at wide orbital separations beyond approximately > 15 AU.

1.2.2 | Transit Method

When a planet transits in front of it host star (during a primary eclipse), relative to Earth, it causes a slight dimming of the brightness of the star. This is shown in Figure 1.7, where the flux from the star dips as the planet eclipses the star. This dimming can be observed and used to detect the presence of an exoplanet by monitoring for regular and approximately equivalent dips in brightness of the host star.

However, in order to observe a transit, a high inclination angle is required. Fischer et al. (2014) outlines that the probability of an exoplanet being accessible by transit observations can be determined a function of orbital separation combined with host star and planetary radii:

$$\mathcal{P}_{tr} = 0.0045 \left(\frac{AU}{a}\right) \left(\frac{R_\star + R_P}{R_\odot}\right) \left[\frac{1 + ecos(\pi/2 - \omega)}{1 - e^2}\right] \tag{1.2}$$

where ω is the angle at which orbital periastron occurs, with ω=90° indicating a transit, and e is the orbital eccentricity. Using this, and considering demographic radii and separations, Fischer et al. (2014) highlights that for a typical hot Jupiter $\mathcal{P}_{tr}$=10%, for a typical super-Earth $\mathcal{P}_{tr}$=2.5%, while for a typical Earth-sized terrestrial planet $\mathcal{P}_{tr}$=0.01%. This makes the transit method biased towards primarily detecting giant exoplanets with orbital separations <1 AU as illustrated

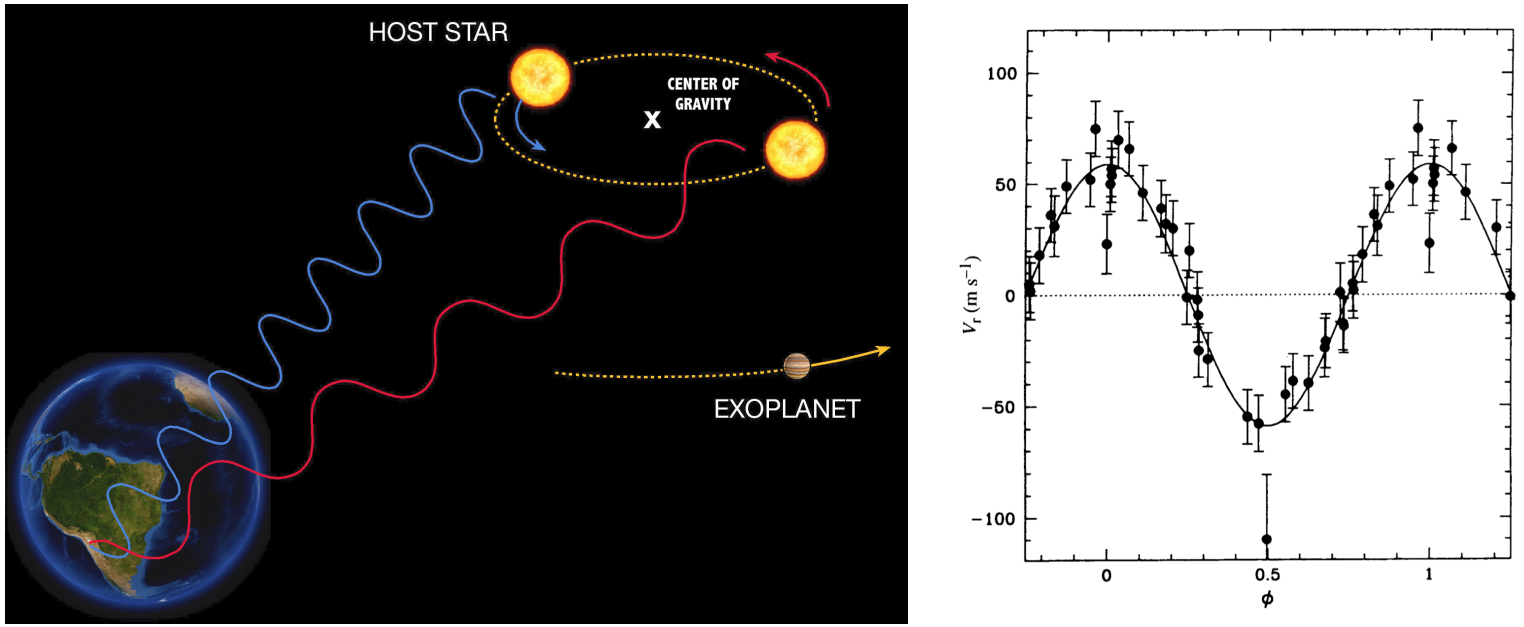

Figure 1.3: Radial velocity detection method illustration. Left: Illustration of the Doppler wobble, where the starlight is blue shifted as it accelerates towards Earth follows by red shifted as it accelerates away due to its orbital motion around the center of gravity. Figure credit: ESO. Right: RV curve of 51 Pegasi from Mayor and Queloz (1995), where the stars exhibits the Doppler wobble due to the presence of the hot jupiter exoplanet 51 Pegasi b.

in Figure 1.2.

Since the first transiting exoplanet detection of OGLE-TR-56b (Konacki et al., 2003), and despite the low probability of a transit, ground-based transit surveys from the Wide Angle Search for Planet (WASP) (Pollacco et al., 2006) and Kilodegree Extremely Little Telescope (KELT) (Pepper et al., 2007), combined with space-based surveys from Kepler (Borucki et al., 2010, 2011), K2 (Howell et al., 2014) and the Transiting Exoplanet Survey Satellit (TESS) (Ricker et al., 2015) have combined to discover many thousands of exoplanets. These transit surveys overcome the low probability of witnessing transiting events by photometrically monitoring thousands of stars across large patches of the sky. For example, TESS will observe 85% of the sky across its primary mission lifetime, approximately 400 times more than the Kepler mission.

The transit method yields the radius and orbital inclination of the exoplanet. Combined with radial velocity observations, the true mass of the exoplanet can be determined by removing the inclination degeneracy.

The transit method has been responsible for 3755 exoplanet discoveries, accounting for almost four out of every five detections in the current total tally of known exoplanets (NASA Exoplanet Archive, 2022). One of the most famous transit discoveries is that of the TRAPPIST-1 system, with 7 terrestrial Earth-sized planets closely orbiting their cool M dwarf host (Gillon et al., 2016, 2017). Figure 1.4 shows the observed transit curves of these seven exoplanets.

The disadvantages of the transit detection method include the high false positive rate (Santerne et al., 2012, Sullivan et al., 2015) with candidates requiring robust observational analysis and verification to confirm their validity.

1.2.3 | Gravitational Microlensing

When a star (lens star) passes in front of another star (source star) relative to Earth it acts to magnify the brightness of the source. If the lens star is host to a planet it acts to further magnify the source star, creating a detectable bump in the observed light curve of the source star.

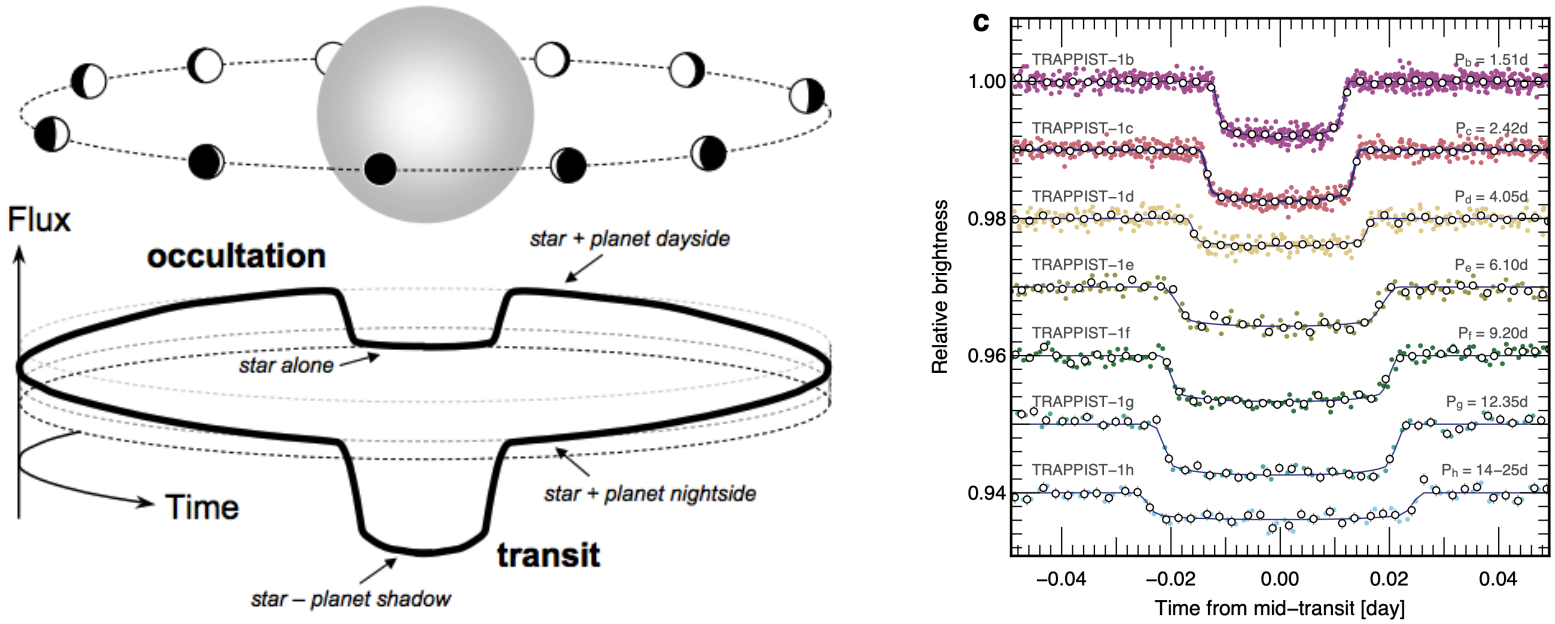

Figure 1.4: Transit detection method illustration. Left: Illustration of a transit (primary eclipse) and secondary eclipse (occultation). The top section illustrates the various phases of day-side vs night-side phases of the tidally locked hot jupiter. The bottom section illustrates the change in brightness of the system as the planet passes in front of, and behind, the host star. Figure from Winn (2010). Right:Transit curves of TRAPPIST-1 planets. Figure from Gillon et al. (2017)

As microlensing detections require stars to pass in front of each other, areas with a high density of stars, such as the galactic bulge, have been the focus of surveys. The Optical Gravitational Lensing Experiment (OGLE) microlensing survey (Udalski, 2003) and the Microlensing Observations in Astrophysics (MOA) survey (Bond et al., 2001) have facilitated in the detection of 121 exoplanets (Akeson et al., 2013). These detections generally have separations within $\sim$10 AU with a variety of masses spanning from $\sim 13 M_{\mathrm{Jup}}$ right down to $\sim 1 M_{\mathrm{Earth}}$ (see Figure 1.2).

A substantial advantage of the gravitational microlensing approach is that it can detect planets at distances of kpc, much further than other detection methods. However, followup observations, especially of their atmospheres, are not possible as these rare lensing events are very unlikely to repeat for a planet, and the significant distance make the detected or candidate microlensing exoplanets inaccessible to other detection methods.

1.2.4 | Direct Imaging

While all the previous detection methods use observations of a star to detect an exoplanet, direct imaging uniquely detects emission directly from an exoplanet. The significant challenge, for this method, is overcoming the extreme contrast in brightness between the host star and an orbiting exoplanet which, for a young giant planet, has a brightness 10^4 to 10^7 times fainter than that of its host (Biller, 2014). This contrast increases to $\sim 10^{10}$ for Earth-like exoplanets. The small angular separation of the exoplanet from its host star, relative to Earth, also requires very high spatial resolution in order to reduce the inner working angle (IWA), which is the smallest angular separation at which a faint exoplanet may be detected. As, $IWA \propto \lambda/D$, where λ is wavelength and D is the diameter of the telescope, observations of closer objects offer a more favourable physical resolution of an imaged system.

Sophisticated adaptive optics systems (AO), combined with coronagraphs, are used to distinguish a planet's light from that of its host, as illustrated in Figure 1.5. This instrument uses a coronagraphs mask and Lyot stop to block much of

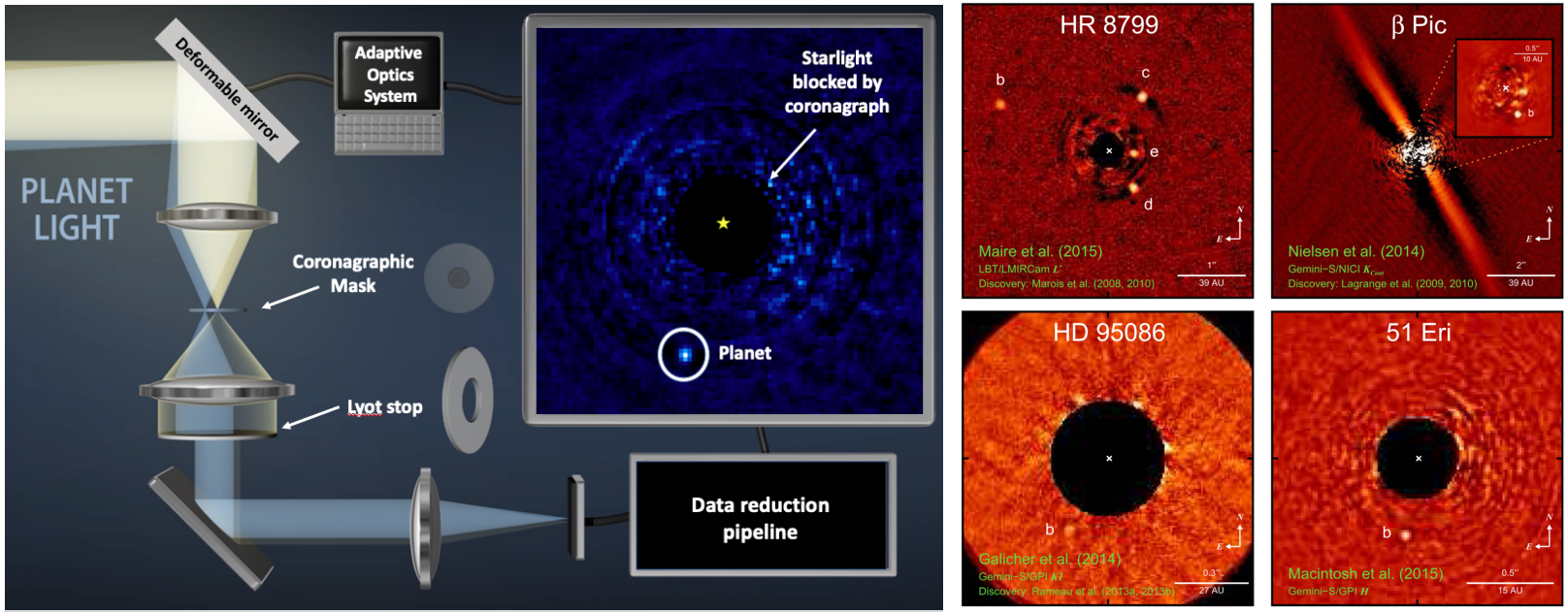

Figure 1.5: Direct imaging method illustration. Left: schematic of adaptive optics system which employs a deformable mirror for phase corrections combined with a coronagraphs mass and Lyot stop to block light from the bright host star while not affecting the planet flux. Figure credit: NASA/JPL-Caltech. Right: Direct images of several exoplanets from Bowler (2016)

the star light. As the planet's light comes in at a slightly different angle, it misses the coronagraphs mask and passes through the central area of the Lyot stop. A deformable mirror is also used to correct for distortions in the incident light. When the instrumental "speckle" noise is suppressed, and a sufficient signal-to-noise level is reached, the faint orbiting exoplanets can be detected. Several examples are illustrated in 1.5. This includes images of the four planets of the HR 8799 system (Marois et al., 2008, 2010), Beta Pic b (Lagrange et al., 2010), HD 95086b (Rameau et al., 2013) and 51 Eri b (Macintosh et al., 2015).

As outlined in Madhusudhan et al. (2014), the bolometric luminosity of a gas-giant planet varies smoothly with respect to time and can be approximated by:

$$\frac{L_{bol}(t)}{L_{\odot}} \propto \left(\frac{1}{t}\right)^{\alpha} M^{\beta}\kappa^{\gamma}, \tag{1.3}$$

where t is time, M is mass, κ is the photospheric Rosseland mean opacity. The terms α, β and γ can be approximated as $5/4$, $5/2$ and $2/5$ respectively (Stevenson, 1991). The evolution, with respect to time, of a gas-giant exoplanet's luminosity is also illustrated in Figure 1.6. As these objects get fainter with age, direct imaging searches are best suited for observations of young stars.

Direct imaging surveys, completed and currently ongoing, have strived to overcome the technical challenges presented by this detection technique. Direct imaging surveys include the Gemini NICI Planet Finding Campaign (Liu et al., 2010, Biller et al., 2013, Nielsen et al., 2013), the VLT NaCo Large Program (Desidera et al., 2015, Chauvin et al., 2015, Reggiani et al., 2016), the International Deep Planet Survey (Vigan et al., 2012, Galicher et al., 2016), Gemini Planet Imager Exoplanet Survey (GPIES; Macintosh et al., 2014, Nielsen et al., 2019), SHINE (SpHere INfrared survey for Exoplanets) via VLT-SPHERE (Chauvin et al., 2017, Desidera et al., 2021, Langlois et al., 2021, Vigan et al., 2021) and the Young Suns Exoplanet Survey (YSES; Bohn et al., 2020). With many null detections, these surveys have also demonstrated the rare and elusive nature of giant exoplanets with wide orbital separations.

A disadvantage of direct imaging, when compared to techniques such as the transit method, is that properties such as mass of the exoplanet can only be

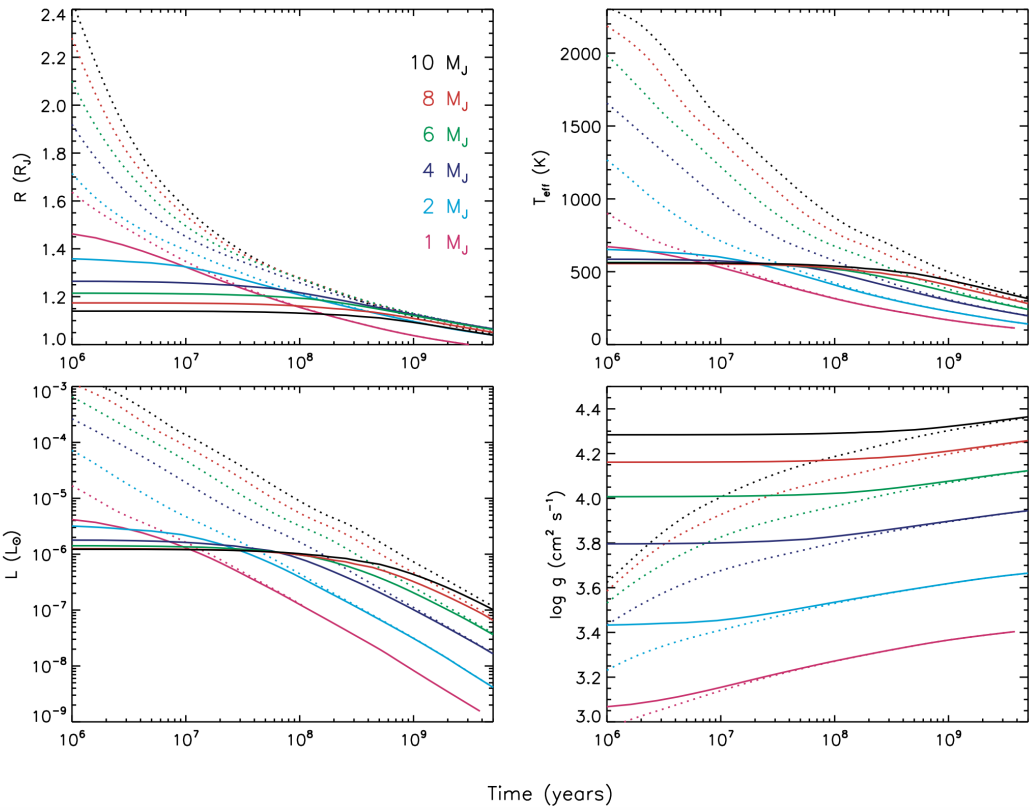

Figure 1.6: Giant exoplanet evolutionary tracks for radius, luminosity, temperatures and surface gravity. The dotted and solid lines indicate different formation pathways. Figure from Fortney et al. (2008).

inferred from evolutionary model which are degenerate with the age of the system (see Figure 1.6). However, when combined with radial velocity and astrometric observations, dynamical masses for directly imaged exoplanets can be yielded (Dupuy and Liu, 2017, Snellen and Brown, 2018a, Brandt et al., 2019, 2021a,b). However, direct imaging has demonstrated advantages such as the ability to capture images of accreting protoplanets within an protoplanetary disk, such as PDS 70 b and c (Keppler et al., 2018, Haffert et al., 2019). Such observations, therefore, offer a unique window into planet formation processes and pathways.

1.3 Atmospheric observation techniques

Following the initial discoveries of exoplanets, techniques were developed to allow for the probing of their atmospheres. Approaches to observe the atmospheres of exoplanets fall into 3 categories: (1) Transit Spectroscopy, (2) High-Resolution Doppler Spectroscopy, and (3) Direct imaging spectroscopy. These techniques are thoroughly outlined in Seager et al. (2010), Fischer et al. (2014), Perryman (2018), Birkby (2018), Madhusudhan et al. (2014), Crossfield (2015), Biller and Bonnefoy (2018), Kreidberg (2018), Parmentier and Crossfield (2018) and Madhusudhan (2019). The following subsections outline these approaches, describing their capabilities and limitations.

1.3.1 | Transit Spectroscopy

Transit spectroscopy has been the most prolific approach for obtaining a spectrum of an exoplanet since its initial employment two decades ago (Charbonneau et al., 2002). It has been used to build a substantial library of transit spectra as shown in Figure 1.8, particular using Hubble Space Telescope (HST). This approach has been greatly facilitated by the significant occurrence rate of planets with the favourable transiting geometry that is required in order to obtain a transmission spectrum. This approach can be broken into the three main categories outlined in the following subsections and are all illustrated in Figure 1.7.

1.3.1.1 | Transmission spectrum

When a transiting exoplanet passes in front of its host star (primary eclipse), light passes thorough the exoplanet atmosphere. Sophisticated post-processing algorithms (eg. iraclis; Tsiaras et al., 2016, 2018) can be used to compare the spectral observation of the star before or after and during the transit (illustrated by positions A and B in Figure 1.7). These spectral differences yield absorption imprints from the planets as the starlight passes through its atmospheric annulus.

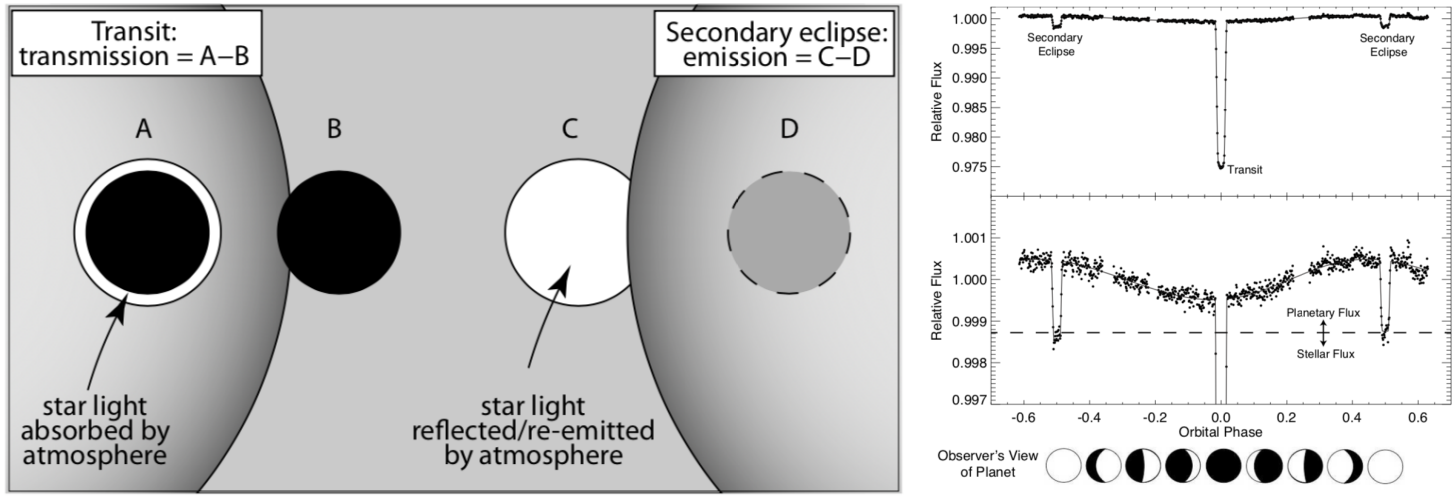

Figure 1.7: Left: Geometry of transmission spectroscopy and secondary eclipse spectroscopy. Transmission spectroscopy is a product of a spectral comparison of before and during a transit (A-B). The exoplanet atmosphere acts to absorb stellar flux as it passes through the atmospheric annulus during a transit. Secondary eclipse spectroscopy is a product of a spectral comparison of before and during a secondary eclipse (C-D), where the star acts to block the thermal emission flux of the planet during the secondary eclipse. Figure from (Perryman, 2018). Right: Phase curve for HD 189733b. This brightness of the system oscillations as the night-side and day-side of the tidally locked exoplanet come in and out of view. This is illustrated by the bottom panel where black indicates night-side and white indicates dayside. Figure from (Madhusudhan et al., 2014)

(Seager and Sasselov, 2000, Brown, 2001). The first successful application of this technique came in 2002 for hot Jupiter HD 209458 b (Charbonneau et al., 2002). This approach is mainly sensitive to the upper section of the planetary atmosphere (10^{-5} to 1 bar) and is, thus, very sensitive to the presence of high-altitude clouds and hazes (Fortney, 2005, Sing et al., 2016).

As outlined in Madhusudhan et al. (2014), the expected depth of the absorption features present, in a haze-free atmosphere, is proportional to the atmospheric scale height:

$$H = \frac{kT}{\mu g} \tag{1.4}$$

where k is the Boltzmann's constant, T is the temperature of the planet's atmosphere, μ is the mean molecular weight of the atmosphere, and g is the surface gravity. Approximating an absorbing atmospheric annulus of to 5-10 scale heights above the planetary radius, the change in the measured transit depth is:

$$\delta_{depth} \simeq \left(\frac{R_P + 10H}{R_*}\right)^2 - \left(\frac{R_P}{R_*}\right)^2 \tag{1.5}$$

where R_P and R_* are the planetary and stellar radii, respectively. If we consider a typical transiting planet with an atmospheric scale height of ∼250 Km, a nominal transit depth of ∼2.5% would increase by 0.1% when observed at wavelengths that possess significant features of atmospheric absorption (Madhusudhan et al., 2014). This change in transit depth can then be used to make inferences about the atmospheric composition of the exoplanet.

Limitations of this approach include the requirement of a transiting geometry, making many exoplanet atmospheres inaccessible to this atmospheric observation technique. Transit spectra only convey signatures from a thin layer of the planetary atmosphere. If this layer has cloud present, observations can often yield a flat spectrum (Berta et al., 2012). The spectrum is also only representative of the day and night-side atmospheric terminator of the a tidally locked hot jupiter.

1.3.1.2 | Transit emission spectrum

A transiting exoplanet passes behind its host star during a secondary eclipse. By comparing spectral observations just before and during this secondary eclipse, indicated by positions C and D in Figure 1.7, and again employing sophisticated post-processing algorithms, the day-side emission spectrum is produced.

As outlined in (Madhusudhan et al., 2014), the observed depth of a secondary eclipse can be predicted via the Rayleigh-Jeans limit:

$$depth = \left(\frac{R_p}{R_*}\right)^2 \left(\frac{T_p}{T_*}\right) \tag{1.6}$$

where R_p and R_* are the planetary and stellar radii, and T_p and T_* are their corresponding temperatures.

Charbonneau et al. (2005) and Deming et al. (2005) detected the first transit emission observations for the hot Jupiters TrES-1 and HD 209458b. With their high temperatures, hot Jupiters emit significant amounts of detectable infrared radiation, making this approach possible. These spectra are generally obtained in the near and mid-infrared as the contrast is more favourable than optical wavelengths.

Limitations of secondary eclipse spectroscopy again include the need for a favourable geometry to permit this approach to be employable. The emission spectrum derived also only conveys information from the day-side face of a tidally locked hot Jupiter.

1.3.1.3 | Transit phase curve

A transit phase curve is the monitoring of the change in brightness throughout an orbit of a transiting exoplanet as a function of time, with an example phase curve illustrated in Figure 1.7. This brightness is a combination of both emission from the exoplanet atmosphere combined with reflected starlight. This brightness oscillates up and down as the hot dayside hemisphere comes in and out of view

during the orbit.

It allows for the probing of longitudinal structure and inhomogeneities present in the atmosphere. Properties related to temperature, chemistry and cloud coverage can be inferred (Knutson et al., 2009, 2012). Phase curves have also be used to make inferences about the weather (wind) present in exoplanet atmospheres (Armstrong et al., 2016) Phase curves are wavelength dependent, with observations in the optical indicating longitudinal variations in albedo and observations in the infrared conveying variations in temperatures and composition.

Whilst a phase curve can offer great insight into the atmospheres of exoplanets, their production requires a large tally of observations, and preferably for an entire orbit. Therefore, this approach is best suited to short period planets (hot-Jupiters) as it is easier to monitor for a whole orbit.

1.3.2 | High-Resolution Doppler Spectroscopy

Doppler spectroscopy probing of exoplanets is a powerful tool in the pursuit of robustly cataloging the chemical species present in their atmosphere. Within phase resolved spectral observations, which include light from both the host star and orbiting exoplanet, this approach searches for the Doppler motion of the exoplanet which has semi-amplitude radial velocity approximately 1000 times higher than that of its host.

For this approach, stellar and telluric lines from the observations are first removed, leaving behind only the high resolution lines of the exoplanet. High resolution spectral templates of molecular species that are predicted to present are then generated. These templates are then employed to perform cross-correlation analysis, where the templates are compared to the observations, aiming to match spectral line positions and depths along with the Doppler shift at different orbital phases. The individual lines have a low SNR, but cross-correlation leverages the presence of many thousands of molecular absorption lines present in the observations where:

$$SNR_p \propto \sqrt{N_{lines}} \tag{1.7}$$

where N_{lines} is the number of lines detected during the cross-correlation process Birkby (2018). The template is compared to to each observation at different phases. The cross-correlation technique will sample different planet semi-amplitude radial velocities, K_p. This requires accounting for the systemic velocity of the system (V_{sys}) and Earth's velocity via the barycentric correction (V_{bary}). Therefore, as outlined in Birkby (2018), the total velocity of the planet can be stated as:

$$V_p = V_{RV} + V_{sys} + V_{bary} \tag{1.8}$$

This allows for the planet to be placed in its rest frame and the summation of all of the cross-correlations at different orbital phases. When the correct K_p is sampled by the cross-correlation, the Doppler shifted line positions within template will match those in the observations. Therefore, there is a spike in signal at the rest frame velocity, indicating a successful detection.

This approach has been used successfully to detect the presence of many molecules and atomic species in hot Jupiter atmospheres (Snellen et al., 2010, Brogi et al., 2012, Birkby et al., 2013, Hoeijmakers et al., 2018). High resolution Doppler spectroscopy has also been used in relation to directly imaged exoplanets and brown dwarfs. Snellen et al. (2014) exploited the fact widely separated planets are not tidally locked and therefore used rotational broadening of CO lines to constrain the rotational velocity to Beta Pic b.

1.3.3 | Direct Imaging Spectroscopy

Spectroscopy of directly-imaged exoplanets, which is the focus of this work, is carried out using the same principles as outlined for detecting direct imaging exoplanets. By combining AO and coronographic systems with spectrographs, spectral observations of direct imaged exoplanets can be made. These spectra

normally possess low resolutions of $R \sim 100$, and have currently been restricted to the near infrared by the need for favourable contrast with the host star.

During the last decade, SPHERE (Beuzit et al., 2008) and GPI (Macintosh et al., 2014) have been the workhorses in the production of direct imaging exoplanet spectroscopy (Macintosh et al., 2015, Zurlo et al., 2016, Bonnefoy et al., 2016, Samland et al., 2017, Chilcote et al., 2017, Rajan et al., 2017). In recent years, direct interferometric imaging has also produced many spectra of direct imaging exoplanets via the VLT's GRAVITY instrument (Gravity Collaboration et al., 2017, 2019, Nowak, M. et al., 2020). High-resolution spectral observations of direct imaged exoplanets has also be conducted via KECK (Konopacky et al., 2013, Wang et al., 2021).

Compared to the atmospheric observation methods previously outlined, direct imaging emission spectroscopy has many advantages. For example, unlike transmission spectroscopy which only probes the upper sections of an exoplanet's atmospheres, direct imaging spectroscopy offers a window into much deeper within the atmosphere. The quality of data also regularly permits for the robust detection of molecules such as H_2O, CH_4 and CO (see Table 1 in Madhusudhan (2019) for extensive list of these detections).

Directly imaged exoplanets are also not tidally locked and thus convey information related to cloud coverage and rotation via variability in their observed spectroscopy (Bowler et al., 2020, Zhou et al., 2020, Biller et al., 2021).

1.4 Defining an exoplanet, brown dwarf and free floating object

Separating exoplanets, brown dwarfs and free floating objects is an ambiguous process due to to intense debate regarding the best properties to use as defining characteristics. The currently adopted classification approach comes from the 2003 Working Group on Extrasolar Planets (WGECP) of the International Astronomical Union (IAU) which outlined (verbatim):

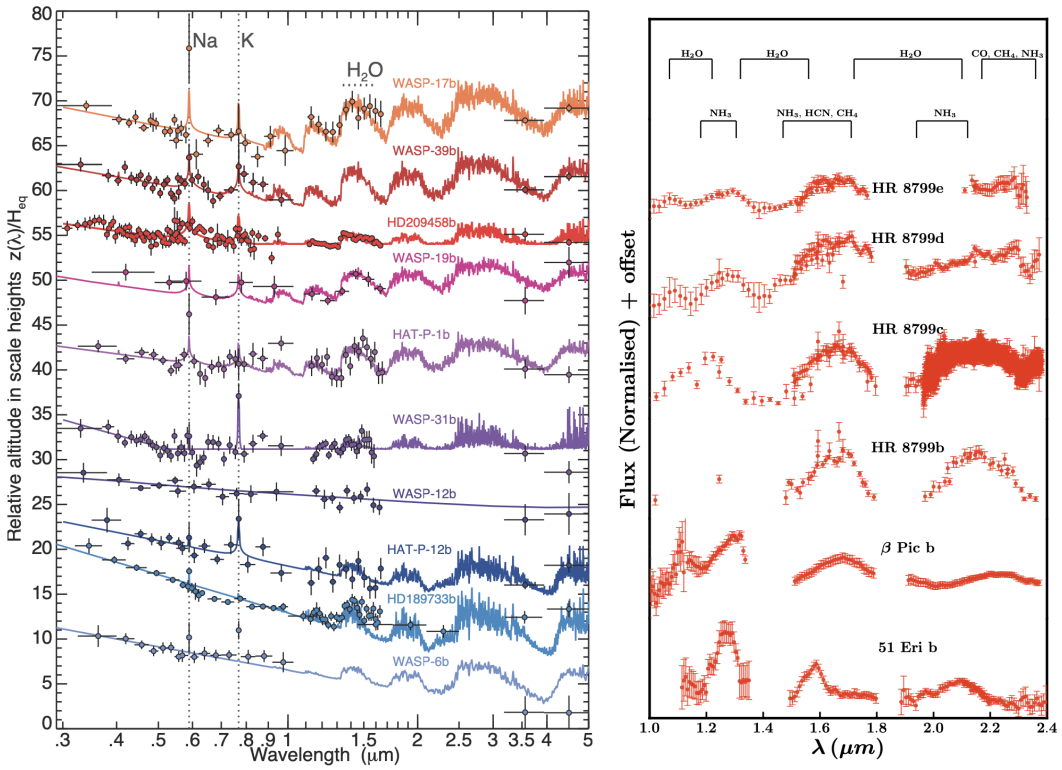

Figure 1.8: Left: Compilation of hot jupiter transmission spectra from Sing et al. (2016). Right: Compilation of direct imaging emission spectra from Madhusudhan (2019).

(1) objects with true masses below the limiting mass for thermonuclear fusion of deuterium (currently calculated to be 13$M_{\rm Jup}$ for objects of solar metallicity) that orbit stars or stellar remnants are planets (no matter how they formed). The minimum mass required for an extrasolar object to be considered a planet should be the same as that used in the solar system;

(2) substellar objects with true masses above the limiting mass for thermonuclear fusion of deuterium are brown dwarfs, no matter how they formed nor where they are located;

(3) free-floating objects in young star clusters with masses below the limiting mass for thermonuclear fusion of deuterium are not planets, but are sub-brown dwarfs (or whatever name is most appropriate).

1.4.1 | Brown Dwarfs

Brown dwarfs, often termed as substellar objects, are objects which posses a lower temperature and luminosity to stars, with masses too low to sustain stable hydrogen fusion, but which are massive enough to sustain a short period of deuterium burning. With defined mass range of ∼13-80$M_{\rm Jup}$, they inhabit the mass space between planets and stars, and are sometimes referred to as "failed stars".

Brown dwarfs, originally called black dwarfs, before being relabeled by Tarter (1976), were first predicted in the 1960s in Kumar (1963) and Hayashi and Nakano (1963). Confirmation of their existence paralleled that of exoplanets in the 1990s, with the discovery of Gliese 229B (GJ 229B) (Nakajima et al., 1995, Oppenheimer et al., 1995). Since this initial discovery, thousands more have been discovered.

As Brown dwarf atmospheric, and thus spectral properties, greatly overlap with those of directly imaging exoplanets, approaches to modelling are identical. Brown dwarf spectra, as they have a higher signal-to-noise ratio and higher resolution than that of directly imaged exoplanet, are ideal for testing and calibrating modelling approaches.

1.4.2 | Free-floating objects

The 'Free floating object', 'free-floating planetary mass object', 'isolated planetary mass object', 'sub brown dwarfs' and 'rogue planet' are terms used to describe a class of object that inhabits the planetary mass regime but does not have a host star. Their origin is difficult to trace, with predictions made that these formed via regular stellar formation processes or that they formed as a planet and were later ejected by processes such as gravitational perturbations. Their properties are almost identical to those of direct-imagined exoplanets. Thus, as in case of brown dwarf spectra, these objects are ideal for developing and testing atmospheric models. This is because, without a host star to suppress during observations, the quality of spectral observations for these objects surpasses that of direct imaging exoplanets.

1.5 Atmospheric chemistry

Atmospheres of giant exoplanets, and brown dwarfs, are constructed predominantly from hydrogen (H) and helium (He). Other key, but much less abundant, elemental species included carbon (C), oxygen (O) and nitrogen (N) (Lodders and Fegley, 2002, 2006). Despite their lower abundances, the chemical behaviour of these elemental species is vital in shaping the observed spectral signatures of these objects. Many factors and processes impact the overall chemistry present in the atmospheres of giant exoplanets and brown dwarfs, but none more so than temperature. These atmospheres can be in a state of chemical equilibrium or disequilibrium, with different sections of the atmospheres existing in one chemical state and other sections in a different chemical state due to dynamical processes present. This is discussed in the following subsections.

1.5.1 | Chemical equilibrium

In a state of chemical equilibrium, the chemical composition of an atmosphere is controlled by temperature, pressure, elemental abundances and the gibbs free energy (Burrows and Sharp, 1999). Chemical equilibrium requires that chemical reactions happen on shorter timescales than other dynamical processes, such as atmospheric mixing and turbulence, and is the dominant chemical state in the hottest and most dense sections of atmosphere. When considerations of chemical equilibrium are made, solar abundances of elemental species are often assumed. In a state of chemical equilibrium, the hot atmospheres of giant exoplanet and brown dwarf atmospheres above temperatures of approximately 1400 to 1300 K are dominated by H_2O, CO and N_2 while cooler atmospheres, below 1300 K but above 500 K, are dominated by H_2O, CH_4 and NH_3. In ultra-hot giant exoplanet and brown dwarf atmospheres, with temperatures above 1800-2000 K, or high pressure atmospheric sections of cooler objects, chemical equilibrium is a good approximation of the atmospheric state. However, at lower temperatures, considerations of the presence of chemical disequilibrium become more important.

1.5.2 | Chemical disequilibrium

Chemical disequilibrium arises when the timescale of dynamical processes within the atmosphere is shorter than that of chemical reactions which maintain a state of equilibrium. A key driver of chemical disequilibrium is the turbulent vertical mixing of atmospheric constituents, otherwise know as eddy diffusion. The level in the atmosphere which departs from a rigid state of equilibrium is known as the quench level or quench pressure. This quench point is crucial, as it is often positioned in or below the observable section of giant exoplanet and brown dwarf atmospheres. Chemical disequilibrium is common in atmospheres of objects with temperatures < 1300 K (Barman et al., 2011a, Zahnle and Marley, 2014). As such, due to the cool nature of the gas-giant planets within our solar system, chemical disequilibrium is also present in their atmospheres. Photochemical reactions are also a key driver of disequilibrium chemistry. However, this is more prevalent in hot Jupiter atmospheres compared to directly imaged exoplanet and

brown dwarf atmospheres due to the high levels of upper-atmospheric irradiation enacted by the proximity to their host star.

Carbon chemistry, at temperatures $\sim$ 1300 K, is the most common tracer of the presence of chemical disequilibrium as it often breaks from the chemical equilibrium predictions. At this temperature, CH_4 should become the dominant carbon bearing species. However, CO is often seen to continue being dominant with CH_4 being observably depleted. This is thought to to be due to CO being transported from deeper and hotter in the atmosphere up to the higher and cooler sections of the atmosphere. An illustration of this is shown in Figure 1.9 where increasing vertical diffusion, K_h, switches CH_4 and CO as the dominant carbon bearing molecules.

1.6 Atmospheric classification

The discovery of Brown dwarfs, defining a new class of objects, brought the need for a novel spectral classifications. The same approach as for stars was adopted, with an extension to the OBAFGKM spectral sequence (Cannon and Pickering, 1901) with the addition of the L, T and Y classifications (Kirkpatrick, 2005, Kirkpatrick et al., 2012, Cushing et al., 2011). Each of these classes have 10 subtypes, numbered 0 to 9, with 0 indicating the earliest of a class and 9 the latest. This same classification approach was then also adopted for directly imaged giant exoplanets and free floating objects as their similarly non-irradiated atmospheres possess characteristics resembling those of brown dwarfs.

These classes are defined primarily by the dominant molecular features present in their spectra and their relative photometric colours (see Figure 1.10). The presence or absence of clouds within the upper atmosphere of these objects also plays an important role in shaping their spectral signatures, as illustrated in Figure 1.11. Within the L, T and Y sequence, H_2O, CO and CH_4 are the dominant molecular features observed. All the aforementioned features are closely linked with temperature such that as these objects' spectral, photometric and color characteristics evolve significantly as a function of spectral type.

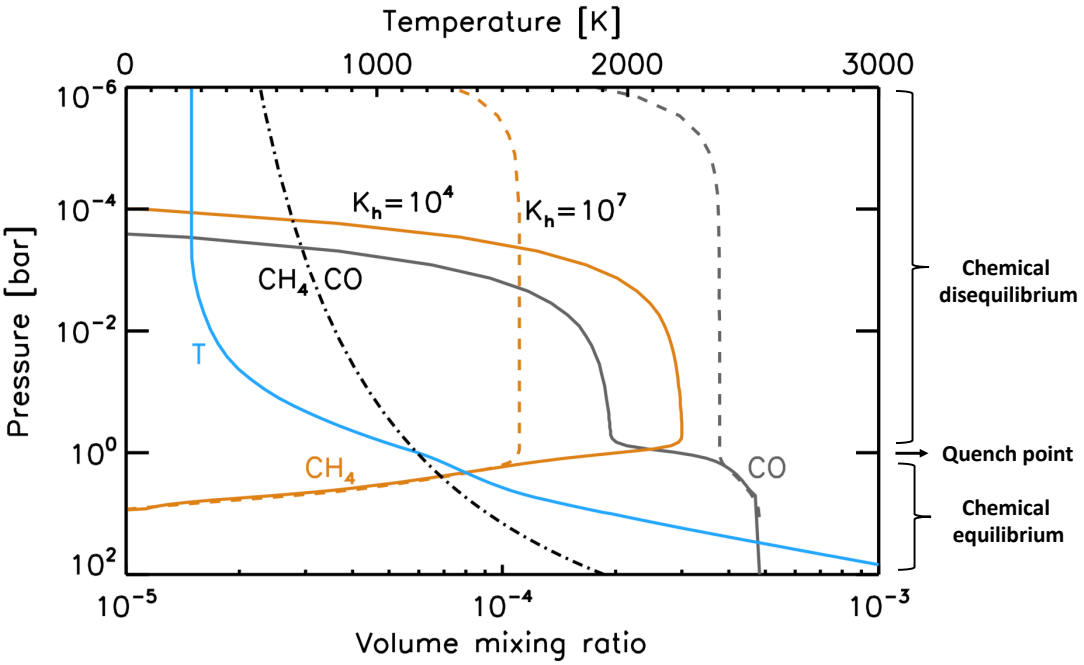

Figure 1.9: Illustration of carbon chemistry disequilibrium for a 600 K giant planet. The temperature-pressure profile, shown in blue, can be compared to the temperature-pressure curve of CH_4 and CO, shown by the black dot-dash line. In a state of chemical equilibrium CH_4 should be dominant when the blue temperature-pressure profile is to the left of the black dot-dash line. The disequilibrium CH_4 (orange) and CO (gray) mixing ratios, above the quench point, are illustrated for different amounts of vertical diffusion K_h, with the solid indicating the lesser and the dashed line indicating the greater. Below the quench point chemical equilibrium is followed. Figure from Marley and Robinson (2015)

1.6.1 | L dwarf atmospheres

L dwarfs have temperatures from approximately 2200 to 1400 K. The spectral standards were defined by Kirkpatrick (2005) and are illustrated in Figure 1.10. The transition from M to L type is set by the weakening of clear TiO and VO absorption features at approximately 0.77 μm and 0.85 μm respectively. These features eventually disappearing at the mid-L stage. H_2O and CO absorption features also begin to appear at this transition, with these features deepening and becoming more pronounced across the L dwarf sub-types. Formation of condensates, linked to the disappearing TiO and VO, also play a key role in the spectral signatures presented by L dwarfs. The formation of silicate, iron, titanium and vanadium clouds, in the upper section of L dwarf atmospheres (Burrows and Sharp, 1999, Lodders and Fegley, 1999, Allard et al., 2001, Lodders, 2002, Marley et al., 2002, Tsuji, 2002, Helling and Casewell, 2014, Gao et al., 2021) acts to reduce the luminosity and make the object appear redder, as illustrated in Figure 1.10. The spread of colours for L dwarfs is also attributed to varying gravity and metallicity (Gao et al., 2021).

1.6.2 | T dwarf atmospheres

T dwarfs have temperatures of approximately 1400 to 600 K. The spectral standard for this class of object were defined in Kirkpatrick (2005) and Burgasser et al. (2006) and is illustrated in Figure 1.10. The transition from L to T type is again marked by changing chemistry and cloud properties. At approximately 1400 K, if chemical equilibrium is present, the CO reservoir in the upper atmosphere of these objects transition to CH_4 (Lodders and Fegley, 2002), with several CH_4 absorption features becoming prominent across the near infrared for T dwarfs as shown in Figure 1.10. Both H_2O and CH_4 features become more pronounced across the T sub-types. This is due to the breakup and sinking of photospheric clouds removing a strong source of opacity from the atmosphere (Allard et al., 2001, Helling and Casewell, 2014, Gao et al., 2021, Ackerman and Marley, 2001, Burgasser et al., 2002, Tsuji and Nakajima, 2003, Marley et al., 2010). The removal of clouds, combined with deepening CH_4 absorption features, acts to

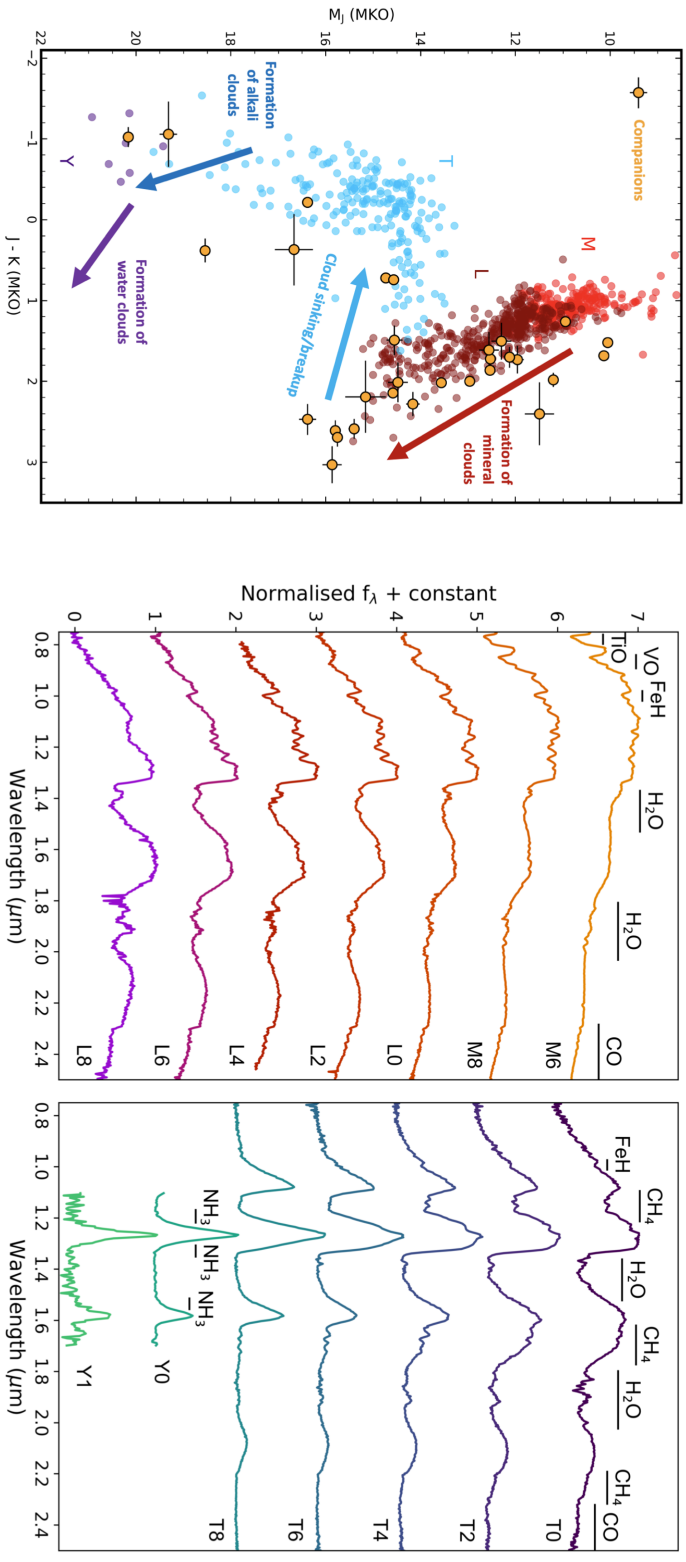

Figure 1.10: Left: Colour-magnitude diagram from (Gao et al., 2021). Right: L dwarf to T dwarf spectral standards. Figure from Fontanive (2019).

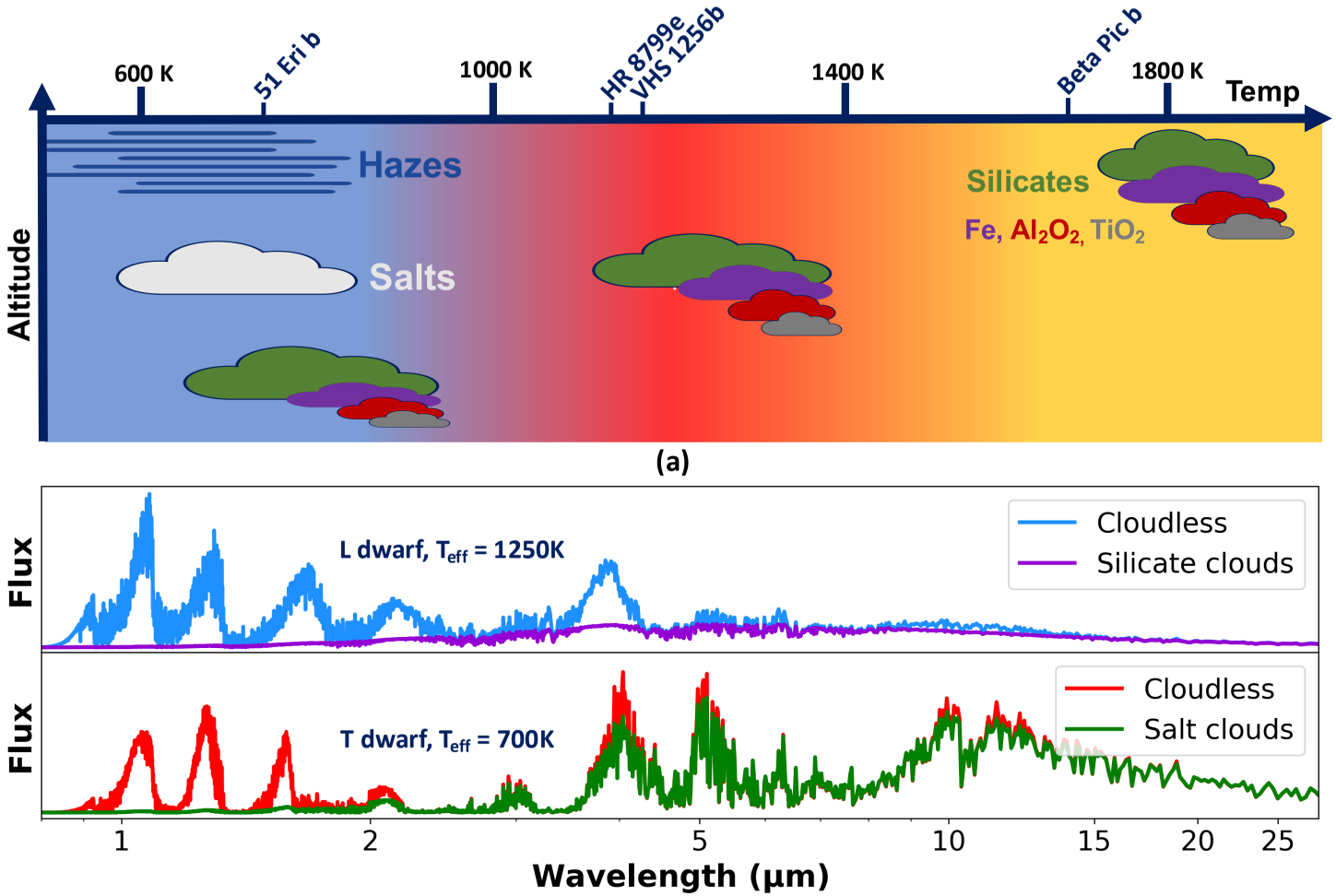

Figure 1.11: Top: Illustration of L and T dwarf cloud species and structure evolution as a function of temperature. Bottom: Forward models of an L and T dwarf comparing spectra with and without clouds.

make the objects bluer across the T dwarf sub types. The eventual dimming in late T dwarfs is suspected to be caused by the appearance of sulfide and chloride clouds (Morley et al., 2012). The end of the T dwarf regime is marked by the emergence of NH_3 absorption between 1.1 and 1.7 μm, as indicated in 1.10.

1.6.3 | Low surface gravity L/T transition atmospheres

Benchmark brown dwarfs and directly imaged exoplanets diverge in colour the end of the L type sequence. The current cohort of direct imaging exoplanets, due to detection biases, are much younger and have much less contracted atmospheres compared to more massive and older benchmark brown dwarfs. As such, for these less massive and puffier objects, the standard brown dwarf L to T transition is now followed. For the lower surface gravity objects the sinking and breakup of clouds in the latter stages of the L dwarf sequence is disrupted. This delayed removal of cloud opacity, combined with the cooling temperatures, means these objects have reduced luminosity and even further reddening. The discovery of many such objects has acted to populate an extension of the initial L dwarf branch on the colour-magnitude diagram shown by the late-L "companions" illustrated in Figure 1.10 where the eventual breakup and sinking of clouds happens at cooler temperatures than those for objects.

1.7 Atmospheric modelling approaches

There has been significant development in the field of modelling exoplanet and brown dwarf atmospheres over the past two decades. Traditionally, the comparison of observed spectra and photometry to modeled spectra was dominated by the use of self-consistent forward models. Now, however, with increases in data quantity and quality, the retrieval method is fast becoming the dominant approach for interpreting observations. These differing approaches are summarised in the following subsections.

1.7.1 | Self-consistent forward modelling

The self-consistent forward modelling approach makes a number of cornerstone equilibrium assumptions. The atmosphere is modelled via assumptions of thermo-chemical equilibrium, radiative-convective equilibrium and local thermodynamic equilibrium (LTE) (Madhusudhan et al., 2014, Madhusudhan, 2019). This approach normally approximates the chemical constituents of the atmosphere using solar elemental ratios. The assumption of radiative-convective equilibrium, along with constraints on chemistry, allows for the self-consistent determination of the temperature-pressure profile. Under this assumptions, paired with considerations of radiative transfer, a spectrum for an atmosphere can be produced.

This approach is then used to produce a suite of so called "grid models" for varying macroscopic properties such as effective temperature and surface gravity. Comparison to these grid models, with iterates across many thousands of spectra, are used to derive the best fit via a chi squared or reduced chi squared fit.

This approach is highly applicable to atmospheres where chemical equilibrium is expected to dominate. However, for cooler or highly dynamical atmospheres, where considerations of the presence of chemical disequilibrium becomes important, such an approach can struggle to correctly account for all features in an observed spectrum. As such, some recent self-consistent models have incorporated considerations of disequilibrium chemistry.

1.7.2 | Retrieval models

In this work we employ the retrieval method. This approach is reviewed in Fortney (2018) and Madhusudhan (2018) and is outlined in Figure 2.1. In its simplest form, the technique obtains a best fit to observed spectra using a parametric forward model constrained by a minimal amount of constraining assumptions. Variations in the forward model are driven by freely adjusting a combination of chemical abundances ("free chemistry") along with a parametric temperature-pressure profile. These critical chemistry and physics driving parameters freely

explore the available parameter space in order to statistically derive the best-fit to an observation. Also known as the "Inverse technique", this approach calculates the probability posterior distributions of these forward model parameters that best fit the observed data.

Retrieval models generally use a Bayesian algorithmic approach to select the best fit model. As outlined in Chapter 2, the use of Bayesian retrievals allows the formal inclusion of prior knowledge and full exploration of the likelihood probability distribution of the data. The statistical sampler allows the parameters to vary freely within the allowed context of the forward model. Bayesian retrievals have now become the norm in atmospheric analyses of transmission and secondary eclipse spectra of transiting exoplanets. However, its use in direct imaging exoplanet and brown dwarf studies is still novel. Bayesian parameter inference has been regularly demonstrated as an effective tool in the pursuit of statistically rigorous exoplanet atmospheric characterisations.

1.8 Outline of Chapters 2-6

In chapter 2 we outline the retrieval code TauREx along with modifications and developments made for this work. In Chapter 3 we apply a retrieval approach to the T dwarf GJ 570 D and the cool exoplanet 51 Eri b. In Chapter 4 we then apply the retrieval approach to 6 L-type objects including PSO 318, VHS 1256 b, HR 8799cde and Beta Pic b. In Chapter 5 we produce a set of James Webb Space Telescope spectral observations simulations and perform retrieval tests on these simulations. In Chapter 6 we summaries this work and outline future work.

CHAPTER 2

Retrieval method: TauREx3

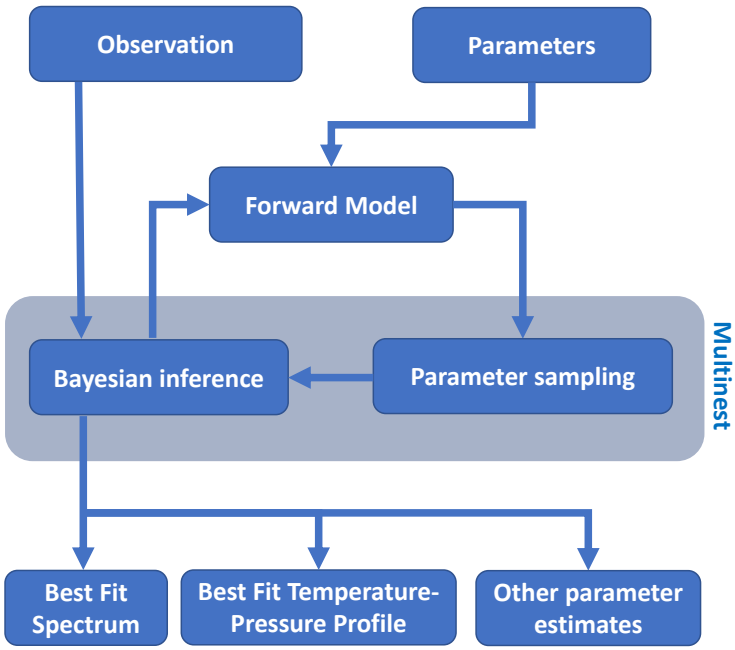

Figure 2.1: Flowchart of the key components used in inverse retrieval techniques.

2.1 TauREx3

TauREx3 (Tau Retrieval of Exoplanets) is a publicly available[1] Bayesian retrieval code designed for application to spectroscopic observations of exoplanet atmospheres (Waldmann et al., 2015a,b, Al-Refaie et al., 2019). It can be employed to analyse emission, transmission and phase-curve spectroscopic data. Figure 2.1 gives an overview of the TauREx code for emission retrieval. The following subsections outline the key components of TauREx.

2.1.1 | Radiative transfer forward model

TauREx3's radiative transfer forward model, as described in Waldmann et al. (2015b), is as follows. The thermal radiation is described by the Schwartzschild equation:

[1] TauREx3: `https://github.com/ucl-exoplanets/TauREx3_public`

$$\mu \frac{dI_\lambda(\tau,\mu)}{d\tau} = I_\lambda(\tau,\mu) - B\lambda(T), \tag{2.1}$$

where I_λ is the intensity per wavelength, λ, $B\lambda$ is the Planck function at temperature T, $\mu = cos\theta$ is the upward inclination, and τ is the total optical depth as a function of altitude (z):

$$\tau_\lambda(z) = \sum_{m=1}^{N_m} \tau_{\lambda,m}(z), \tag{2.2}$$

where $\tau_{\lambda,m}$ is the optical depth per absorbing species, m:

$$\tau_{\lambda,m} = \int_z^{z_\infty} \varsigma_{\lambda,m}(z')\chi_m(z')\rho_N(z')dz', \tag{2.3}$$

$\varsigma_{\lambda,m}(z')$ is the absorption cross section, χ_m is the column density, and ρ_N is the number density. The upwelling radiance is expressed via:

$$I_\lambda(\tau,\mu) = I_\lambda(\tau_s)e^{-(\tau_s-\tau)\mu} + \int_{\tau_s}^{\tau} B_\lambda(T_{\tau'})e{-}(\tau_s-\tau)\mu\frac{d\tau'}{\mu}, \tag{2.4}$$

which sums the radiation at the planetary surface (set as a pressure point for gaseous planets), and the the integrated emission contribution from all the individual plane-parallel layers.

The transmittance of the modelled atmosphere, $\mathcal{T}$, and its derivative is defined as a function of optical depth:

$$\mathcal{T}\tau = e^{-\tau}, \frac{\delta\mathcal{T}\tau}{\delta\tau} = -e^{-\tau}. \tag{2.5}$$

Therefore, the summed top-of-atmosphere radiation (TAO, τ=0, $z = \infty$) is expressed via:

$$I_\lambda(\tau=0) = B_\lambda(T_s)e^{-\tau_s} + \int_0^{\tau_s} B_\lambda(T_\tau)\frac{\delta\mathcal{T}_\lambda(\tau)}{\delta\tau}d\tau, \tag{2.6}$$

where τ_s and T_s are the optical depth and temperature at the planetary surface. We define this quality as F_{emission}:

$$F_{\text{emission}} = I_\lambda(\tau = 0) \tag{2.7}$$

2.1.2 | Emission mode for direct imaging

We modified TauREx3 to allow us to model directly imaged targets. First, we removed stellar emission from the forward model and added an inverse square law scaling for the exoplanet or brown dwarf emission:

$$\text{Absolute Flux} = F_{\text{emission}} \cdot \frac{R^2}{D^2} \cdot S_{\text{cal}}, \tag{2.8}$$

where F_{emission} is the emission flux from the forward model, R is the object radius and D its distance from the Earth. S_{cal} is a scaling calibration factor, to account for imperfect absolute flux calibration assumptions. A calibration factor such as this has been used in Oreshenko et al. (2020), Mollière et al. (2020) and Burningham et al. (2021). Within the retrieval, S_{cal} can also be inversely considered as scaling the observed data to the model derived flux via Obs_{cal}:

$$\text{Obs}_{\text{cal}} = \frac{1}{S_{\text{cal}}}, \tag{2.9}$$

2.1.3 | Addition of inferred parameters

We have added surface gravity $\log(g)$ as an inferred parameter, determined via Newton's Law of Universal Gravity:

$$\log(g) = \log\left[\frac{GM}{R^2}\right], \tag{2.10}$$

where G is the gravitational constant, M is the object's mass and R is the object's

radius.

We have also included the calculation of the carbon to oxygen (hereafter C/O) ratio, which for the brown dwarfs and exoplanets we study in this work, is driven predominantly by the relative abundances of H_2O and CH_4 for T dwarf and H_2O and CO for L dwarfs. The inferred C/O ratio is calculated via:

$$C/O = \sum_{molecules} \frac{\chi_{carbon} \cdot n}{\chi_{oxygen} \cdot n}, \tag{2.11}$$

where χ is the mixing ratio of the relative molecules and n is the number of oxygen or carbon atoms in a given molecule (eg. for CO n_{carbon}=1 and n_{oxygen}=1, for H_2O n_{carbon}=0 and n_{oxygen}=1,).

We also add an inferred metallicity via the retrieved abundances, following the same approach employed in Kitzmann et al. (2020) and Gonzales et al. (2020). This is approximated by summing metal-containing molecules within the retrieval weighted by the number of metal (non-hydrogen) atoms present which is then divided by the abundance of neutral hydrogen. This value is then compared, in log space, to solar metallicity, determined using the relevant elemental abundances using values from Asplund et al. (2009). Metallicity is therefore calculated via:

$$M_{object} = \sum_{molecules} \frac{\chi_m \cdot n}{\chi_{H2} \cdot 2}, \tag{2.12}$$

where χ_m is the mixing ratio of a particular molecule m, n is the number of metal atoms in a given molecule (eg. for CO_2 n=3, H_2O n=1), χ_{H2} is the mixing ratio of neutral hydrogen. Therefore [M/H] is determined via:

$$[M/H] = \log\left(\frac{M_{object}}{M_{solar}}\right), \tag{2.13}$$

where M_{solar} is determined via all relevant solar elemental abundances relative to the solar H abundance. We note this is not how metallicity is determined in self-consistent forward models. The method outlined previously is only possible

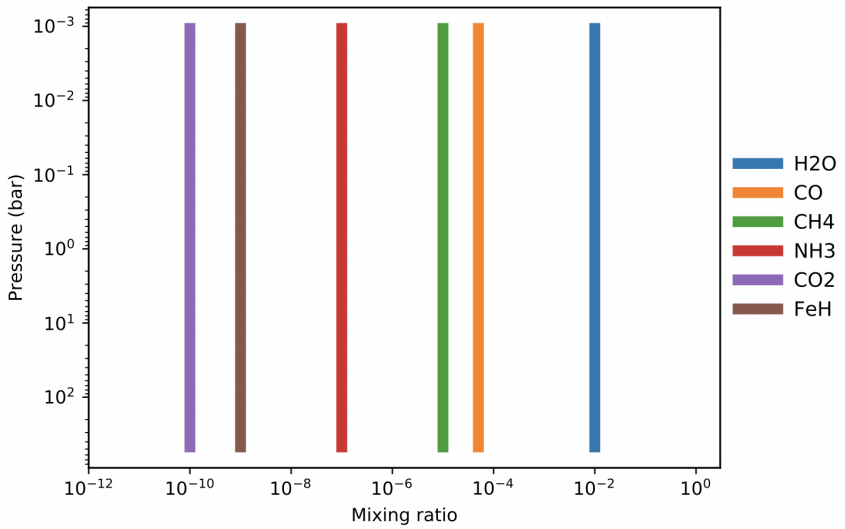

Figure 2.2: Illustrations of TauREx3's constant molecular abundances with pressure/altitude. These are referred to as isoprofiles.

due to employing constant abundances with pressure while this is not the case in self-consistent model.

We have included the effective temperature T_{eff} as a derived parameter which is useful for comparing retrieval results to grid models and evolutionary tracks. For this, we followed the same approach as adopted in Line et al. (2015), integrating the spectrum from 0.1 to 50 μm (at the native resolution of the input cross sections) to calculate the total emission flux. The effective temperature is then derived using the Stefan-Boltzmann law.

2.1.4 | Atomic and Molecular opacity

TauREx has its own purpose built molecular and atomic opacities, which can be accessed from the publicly available ExoMolOP database (Chubb et al., 2020)[2]. The line lists used for this work originate mainly from the ExoMol project (Tennyson and Yurchenko, 2012) but also HITEMP (Rothman et al., 2010), HITRAN (Rothman et al., 1987) and MoLLIST (Bernath, 2020). This includes the latest line lists for H_2O (Polyansky et al., 2018), CO (Li et al., 2015), CO_2

[2]ExoMolOP: `http://exomol.com/data/data-types/opacity/`

(Yurchenko et al., 2020), CH_4 (Yurchenko et al., 2017), VO (McKemmish et al., 2016), TiO (McKemmish et al., 2019), H_2S (Azzam et al., 2016) and NH_3 (Coles et al., 2019). ExoMol provides line lists for extended temperature ranges for a variety of molecules. We note that some of these cross-sections have imperfections, such as in the case of CH_4 (Yurchenko et al., 2017), where a more accurate and complete line list is available via TheoReTS (Rey et al., 2016).

The TauREx3 cross-sections used in this work were sampled at $R = \frac{\lambda}{\Delta\lambda} = 15{,}000$ across the 0.3 - 50μm wavelength region. For a more detailed discussion of TauREx's line list library see Chubb et al. (2020). During the molecular and atomic radiative transfer calculations performed by TauREx, the model is produced at a much higher resolution than that of the observed spectrum. These high resolution spectra are then binned down to the data resolution in order to calculate the log-likelihood during the retrieval.

2.1.4.1 | Alkali cross sections

The pressure and temperature broadened profiles for the resonance doublets of Na and K are computed using methods described in Allard et al. (2016) and Allard et al. (2019). All other line data for these atomic species are taken from either the NIST (Kramida et al., 2013) or Kurucz (Kurucz and Bell, 1995) database. We note here that all the results presented in this work were retrieved using the broadening parameters of Allard et al. and non-resonance lines from the Kurucz database, unless stated otherwise.

2.1.5 | Retrieved abundances

The molecular trace-gas mixing ratio profiles (as a function of pressure), in the forward model are set, and retrieved, as isoprofiles, as shown in Figure 2.2. Therefore, the retrieved abundances convey the mean abundance within the observable atmospheric region. This is the region where there is significant spectral contribution to the observed spectrum. TauREx3 does allow for pressure dependent abundance profiles (Changeat et al., 2019) but this comes at a

significant increase in model complexity and so will be explored in later work.

2.1.6 | Temperature-pressure profiles

To accurately model directly-imaged emission spectroscopy, an appropriate temperature-pressure parameterisation must be adopted. TauREx offers a variety of temperature-pressure profile options, ranging from radiative two-stream modelling such as the Guillot (2010) prescription (for highly-irradiated planets) to more ad-hoc geometric approaches in which temperature-pressure nodes are allowed to vary freely. The Madhusudhan and Seager (2009) and Lavie et al. (2017) prescriptions have also been added to TauREx3. In Figure 2.2, we illustrate the *npoint* and Madhusudhan and Seager (2009) temperature-pressure profiles.

2.1.6.1 | *npoint*

The *npoint* parameterisation (Waldmann et al., 2015a) is a non-physically constrained and very flexible geometric profile. It can be used to model an infinite amount of pressure and temperate points within a model. However, we limit our setup to three points in this work, as illustrated in 2.2 . Therefore our *npoint* profile is determined by parameters including the top of atmosphere temperature, $T_{\rm top}$, and top of atmosphere pressure, $P_{\rm top}$ (set at 10^{-3} bar in this work). The other parameters include the tropopause temperature and pressure, T_1 and P_1, as well as the surface pressure $P_{\rm surf}$ (set at 500 bar for this work) and temperature $T_{\rm surf}$. Temperatures are then linearly interpolated between these temperature-pressure nodes in log space.

2.1.6.2 | Madhusudhan and Seager (2009)

The temperature-pressure profile outlined in Madhusudhan and Seager (2009) is a zonal combination of exponential curves, and hence does not permit local discontinuities (Burningham et al., 2017). The profile is split into three zones

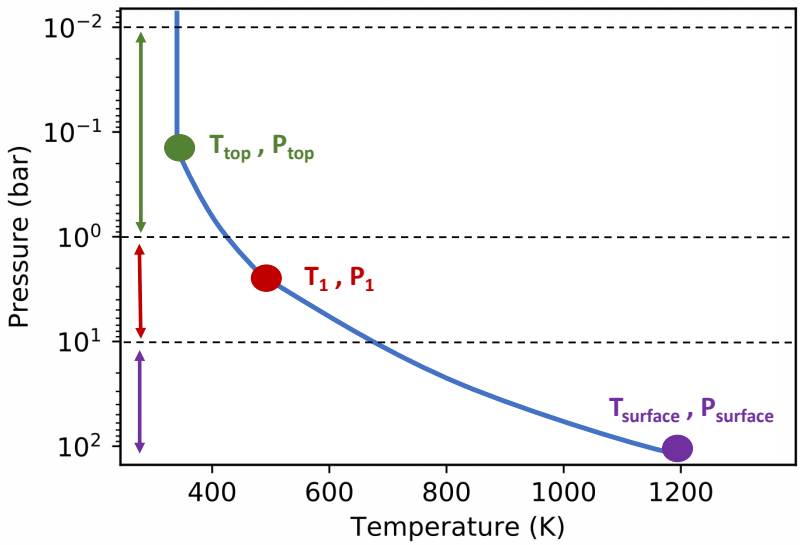

(a) n-point profile

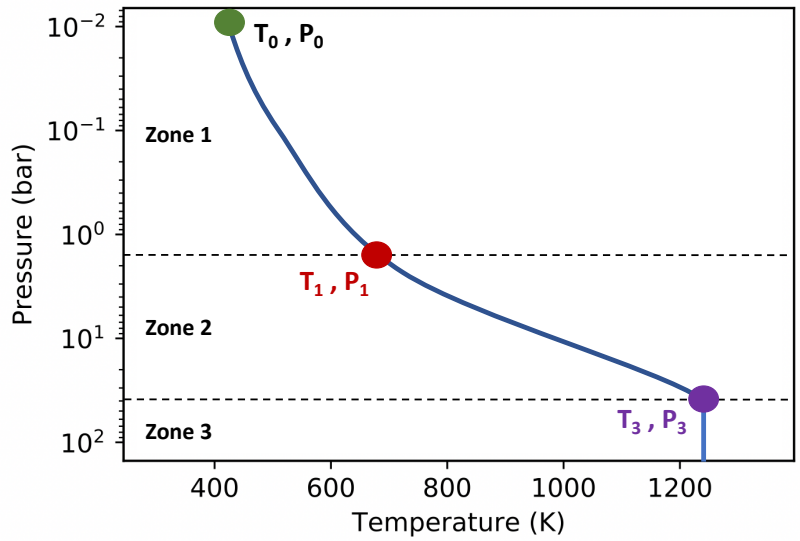

(b) Madhusudhan and Seager (2009) Profile

Figure 2.2: TP profiles used in our analysis. The top panel outlines the structure of the n-point profile, with n = 3 in this example. The bottom panel outlines the structure of the Madhusudhan and Seager (2009) profile, when thermal inversions are ruled out.

with pressure and temperature being related by:

$$\begin{aligned} P_0 < P < P_1 : P &= P_0 e^{\alpha_1 (T-T_0)^{1/2}} \ (Zone\ 1), \\ P_1 < P < P_3 : P &= P_2 e^{\alpha_2 (T-T_2)^{1/2}} \ (Zone\ 2), \\ P > P_3 : T &= T_3 \ (Zone\ 3), \end{aligned} \tag{2.14}$$

where T_0 and P_0 are the top-of-atmosphere temperature and pressure, and T_3 represents the isothermal temperature for atmospheric layers below P_3. Thermal inversions are ruled out by setting $P_2 = P_1$, as inversions are not expected in the objects considered in this work. With this condition in effect, and using principles of continuity at zonal boundaries, we consider five free parameters within our analysis: α_0, α_2, P_1, P_2, and T_3. We note too that P_3, and T_3 act as an anchor point for the temperature-pressure profile and can be set as values beyond the bottom-of-atmosphere (500 bar, hereafter BOA) boundaries of our radiative transfer considerations. This is the same profile parameterisation used in Gonzales et al. (2020), Burningham et al. (2017) and Burningham et al. (2021).

2.1.6.3 | Lavie et al. (2017)

We also added a less flexible profile following a simple parameterisation employed in Lavie et al. (2017) and originating from a reduced version of equation 126 in Heng et al. (2014):

$$T^4 = \frac{T_{int}^4}{4} \left(\frac{8}{3} + \widetilde{m} \kappa_0 \right) \tag{2.15}$$

where T_{int} is the internal temperature and κ_0 the constant component of the infrared opacity. $\widetilde{m}$ is column density determined via $P_0 = \widetilde{m} \cdot g$ with g being the surface gravity at the bottom of our model atmosphere (500 bar). This simpler and radiative equilibrium enforcing profile paramterisation only has two free parameters within our retrievals: κ_0 and T_{int}.

2.1.7 | Bayesian Analysis

TauREx employs Bayesian statistics as the cornerstone for the retrieval analysis, as outlined in Waldmann et al. (2015a). Bayes' theorem states that:

$$P(\theta \mid x, \mathcal{M}) = \frac{P(x \mid \theta, \mathcal{M})\, P(\theta, \mathcal{M})}{P(x \mid \mathcal{M})}, \tag{2.16}$$

where $P(\theta, \mathcal{M})$ is the Bayesian prior, and $\mathcal{M}$ is the forward model. $P(\theta \mid x, \mathcal{M})$ is the posterior probability of the model parameters θ given the data, x, assuming the forward model $\mathcal{M}$. The likelihood, $P(x \mid \theta, \mathcal{M})$ is given by:

$$P(x \mid \theta, \mathcal{M}) = \frac{1}{\mathcal{E}\sqrt{2\pi}} \exp\left[-\frac{1}{2}\sum_{\lambda}^{N}\left(\frac{x_\lambda - \mathcal{M}_\lambda}{\mathcal{E}_\lambda}\right)^2\right], \tag{2.17}$$

where $\mathcal{E}$ is the error on the input spectral data (Waldmann et al., 2015a). An illustration of a 2-dimensional posterior and accompanying likelihood is shown in Figure 2.3.

2.1.7.1 | Error inflation

We added the ability to inflate the $\mathcal{E}$ spectral error, as done in Line et al. (2015) and Burningham et al. (2017), via:

$$\mathcal{E}_\lambda^2 = \sigma_\lambda^2 + 10^b, \tag{2.18}$$

where σ_λ is the measured error for the λth flux and b is a tolerance factor which is included as a free parameter in the retrieval analysis (Tremaine et al., 2002, Hogg et al., 2010, Foreman-Mackey et al., 2013). The 10^b error inflation term can account for imperfections in the forward model's capability to fit the observed emission spectrum (Line et al., 2015) and/or account for underestimated uncertainties.

It also allows for the down-weighting of sections of a spectrum where the spectral resolution is highest as well as possessing the smallest error bars. Such sections of data can lead to the neglect of other important parameters driving regions of a spectrum. Including the error inflation can therefore allow for a more equally weighted consideration of a whole spectrum when performing the Bayesian evidence calculations.

2.1.8 | Nested Sampling via Multinest

TauREx includes the implementation of Bayesian statistics via nested sampling (NS) using Multinest (see section 2.1.8.1) (Feroz and Hobson, 2008, Feroz et al., 2009, 2013) via PyMultinest (Buchner et al., 2014). As outlined by Waldmann et al. (2015a), NS derives the Bayesian Evidence, E, via:

$$E = \int P(\theta \mid \mathcal{M}) P(x \mid \theta, \mathcal{M}) d\theta, \tag{2.19}$$

$$E = P(x \mid \mathcal{M}). \tag{2.20}$$

The Bayesian Evidence allows the retrieval to perform model comparison and selection. The statistical results from MultiNest are then used to derive the parameter estimates which combine to produce the highest Log-Evidence. NS, as performed by Multinest, also allows for efficient parallelisation, permitting the use of high performance cluster computing resources (see Figire 2.4).

Via the nested sampling Log-Evidence, we can compare model results using the Bayes Factor B:

$$log(B) = \Delta log(Ev) = log(Ev2) - log(Ev1). \tag{2.21}$$

This is a ratio of evidence of two competing models (Ev1 and Ev2), allowing for comparison. Table 2.1, from Kass and Raftery (1995) outlines how log(B) can be interpreted.

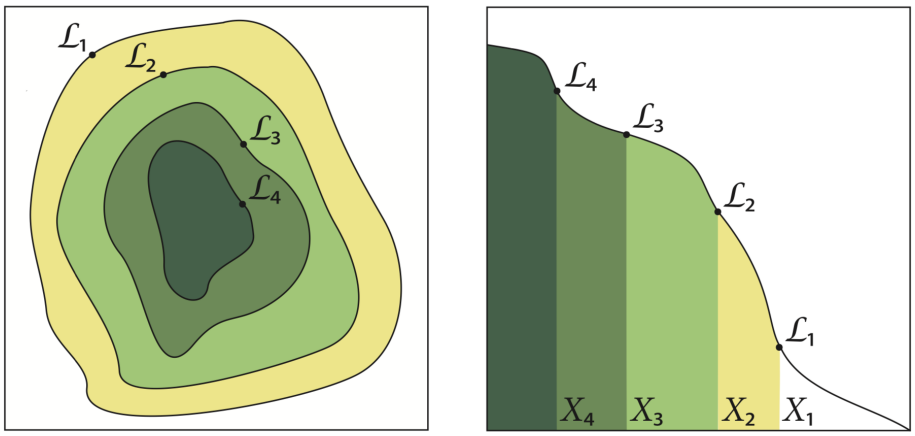

(a) (b)

Figure 2.3: (a) Posterior of two dimensional model fit. (b) Evolving likelihood $\mathcal{L}_i(X)$ for different parameter space points X. Figure from Feroz et al. (2019).

Table 2.1: Interpretation of the Bayes ratio outlined in Kass and Raftery (1995)

$log(B)$	Interpretation
0 - 0.5	*No Evidence*
0.5 - 1	*Some Evidence*
1 - 2	*Strong Evidence*
>2	*Decisive*

2.1.8.1 | Multinest

Multinest is a posterior distribution and global Bayesian evidence estimation tool for tackling and evaluating multi parameter/dimensional problems. Multinest probes the parameter space by firstly initialising samples which are referred to as live points. In the case of our retrievals, these parameter live points combine to create a model spectrum where the likelihood is determined. Multinest then disregards the live points with the lowest likelihood, replacing them with a new value within the permitted parameter space. We note here this parameter space is controlled by the priors set on each individual parameter, which are discussed in section 2.1.9. Multinest repeats the disregarding and re-initializing of live points in an effort to search for the areas of parameter space which maximise the likiehood. A key component of Multinest is that it employs ellipsoidal nested sampling which is outlined in Feroz et al. (2009). Within this work, Multinest allows us to statically probe exoplanet and brown dwarf spectra using models with approximately 15-25 parameters usually employing 1000-5000 live points. By employing high performance computing (clusters), this tool allows us to employ many computer nodes/cores (see Figure 2.4). This is essential as our retrieval, when using multi nest can run for long durations of time depending on model-dimensionality and data quality. Typical retrievals of low to medium-resolution direct imaging data in the mid-IR take only few hours if employing several hundred cores.

2.1.9 | Priors

TauREx has preset default priors set for all the possible free parameters. This includes all that are necessary for the forward model such as mass, radius, temperature-pressure prescription and atmospheric trace gases considered. By default TauREx employs uninformative uniform priors with large prior ranges (e.g. trace-gas abundance priors are log-uniform, $\log(\text{abundances}) = 1.0 - 1.0 \times 10^{-12}$). The default values can be manually over-ridden, allowing the user to limit or open-up the parameter space. Narrowly defined bounds have the benefit of reducing computational expense but run the risk of being overly restrictive.

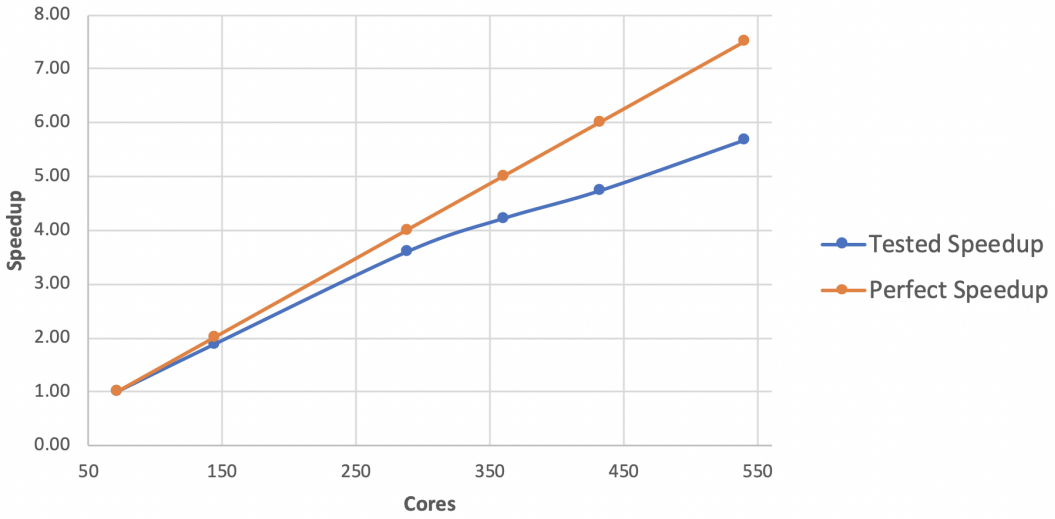

Figure 2.4: TauREx3 speedup demonstration when using Cirrus cluster.

The priors and prior bounds set for the retrieval analysis performed in this work were either uniform, log-uniform or Gaussian priors based on values from previous published studies (when such values were available).

2.1.10 | Clouds

Due to the expectation of the presence of cloud related opacity for many of the objects studied within this work, as highlighted in 2, we tested, expanded and added to the cloud capabilities of TauREx3's forward model. The following subsections outline TauREx3's current and novel cloud paramterisations.

2.1.10.1 | Simple powerlaw clouds

We have added a power law slab and deck cloud capability, following the same prescription outlined in Burningham et al. (2017) and Gonzales et al. (2020). In the case of the slab cloud, the total optical depth is determined via:

$$\tau_{cloud} = \tau_0 \left(\frac{\lambda}{\lambda_0} \right)^{\alpha} = \sum \tau_{Layers} \tag{2.22}$$

where λ_0=1μm. τ_0 and α are the two retrievable components of this cloud prescription as well as the top pressure boundary of P_{top} and the bottom pressure boundary of the cloud P_{bottom}. τ_{cloud} is distributed throughout the layers in the cloud slab pressure boundaries, weighted by $d\tau/dP \propto P$ where dP is relative to P_{bottom}. Therefore, the total optical depth is distributed such that the bottom layer has the maximum optical depth while the top layer has the minimum optical depth present. In total, the power law slab is retrieved via 4 parameters: τ_0, α, P_{top} and P_{bottom}. An illustration of the slab cloud is shown in Figure 2.5(a).

The optical depth of the power law deck cloud again follows $\tau \propto \lambda^{\alpha}$ and is controlled via the P_{top} pressure where the cloud becomes optically thick with τ=1. The cloud opacity scales with pressure via dτ/ dP $\propto \exp(\Delta \mathrm{P}/\Phi)$ where ΔP is the height above and below the P_{top} pressure and ϕ is:

$$\Phi = \frac{P_{top} \cdot (10^{\Delta \log P} - 1)}{10^{\Delta \log P}}. \tag{2.23}$$

The opacity decay is therefore parameterised by $\Delta \log P$. Therefore, in total, the power law slab is retrieved via 3 parameters: P_{top}, $\Delta \log P$ and α. An illustration of the deck cloud is shown in Figure 2.5(b).

We also added a novel cloud setup called Slab Infinity Deck (SID). This parameterisation mirrors that of the aforementioned slab cloud structure but with an infinite opacity below below P_{bottom}. An illustration of the SID cloud is shown in Figure 2.5(c).

We note that these cloud paramerisations can be transformed into grey-clouds, where the cloud opacity is constant with wavelength, by setting α=0. These are flexible and simplistic cloud approach but do lack the rigour of the more physically motivated approaches included in Mollière et al. (2020) and Burningham et al. (2021). As such, the slab and deck approach does not allow us to probe specific cloud species or particle sizes but is still suitable for analysis within this work.

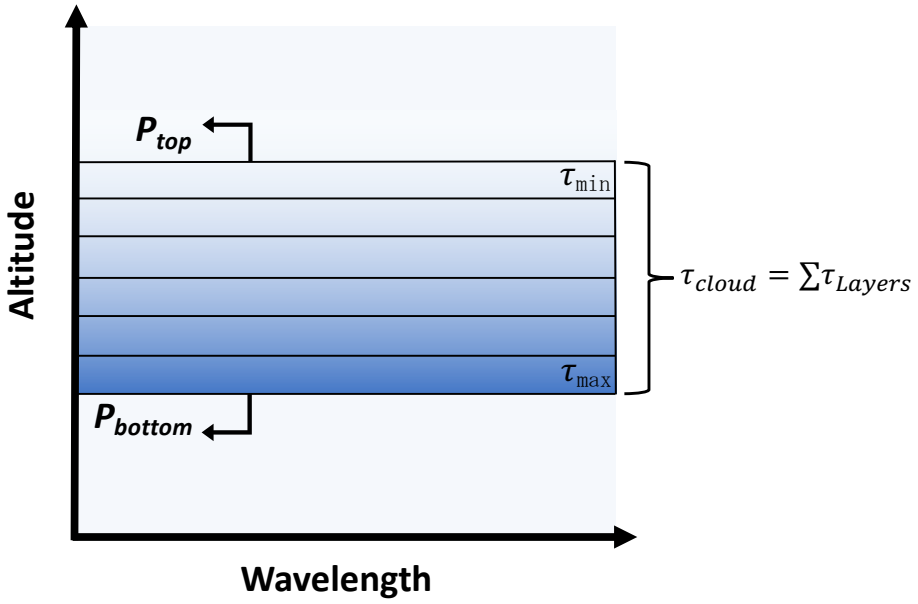

(a) Slab cloud

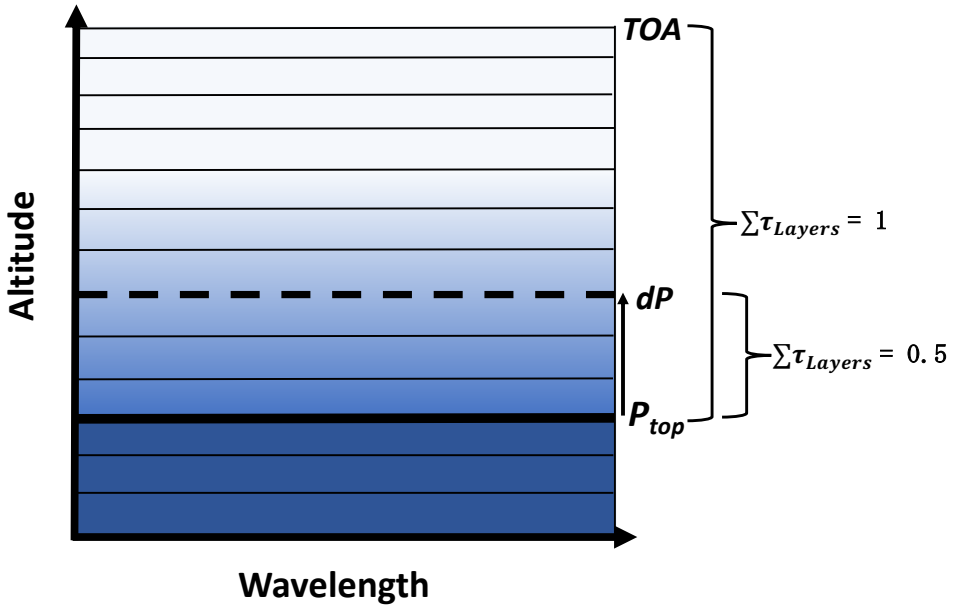

(b) Deck cloud

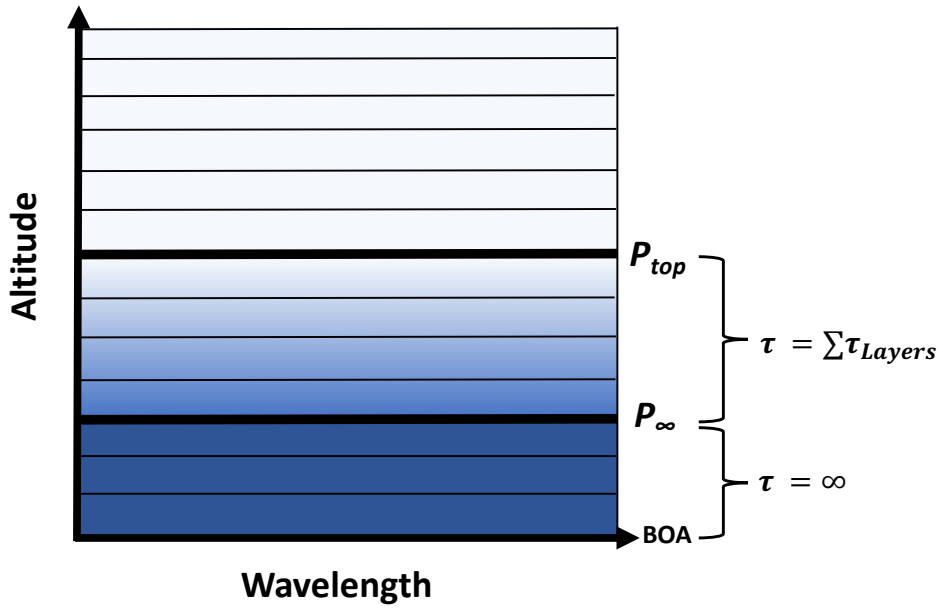

(c) Slab Infinity Deck SID cloud

Figure 2.5: Diagram outlining cloud structures employ in this study. (a) outlines the slab cloud structure. (b) outlined the deck cloud structure. (c) outlined the slab infinity deck (SID) cloud structure.

2.1.10.2 | Lee et al. 2013 Mie opacity approximation

Here we outline a Mie theory cloud opacity prescription offered in TauREx. This cloud prescription is outlined in Lee et al. (2013) and was also employed in Lavie et al. (2017). Using equation 2.3, the cloud's optical depth τ_{cloud} is added via:

$$\tau_{\lambda,m} = \int_{z}^{z_{\infty}} \mathcal{Q}_{ext}(z')\pi r_c^2 \cdot \chi_m(z')\rho_N(z')dz', \tag{2.24}$$

where $\mathcal{Q}_{ext}$ is the extinction efficiency and r_c is the spherical particle radius. The extinction efficiency $\mathcal{Q}_{ext}$ is approximated via the dimensionless, cloud composition quantity $\mathcal{Q}_0$ (see Figure. 2.6):

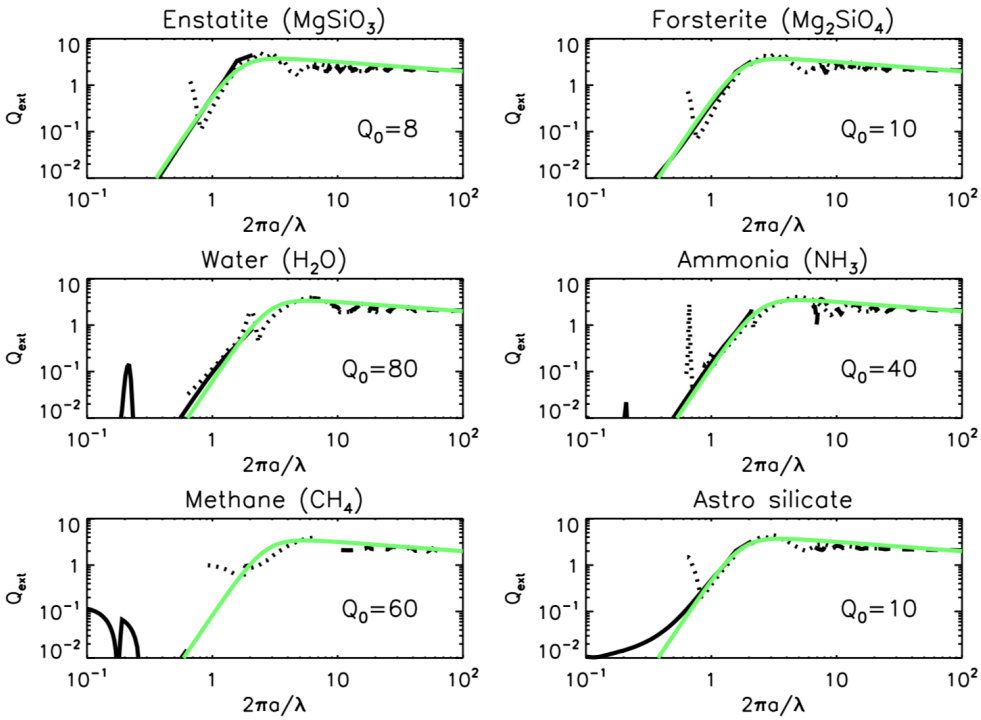

Figure 2.6: Extinction efficiency curves for various condensate species compared to approximations from Lee Mie opacity regime. Figure from Lee et al. (2013).

$$\mathcal{Q}_{ext} = \frac{5}{\mathcal{Q}_0 x^{-4} + x^{0.2}} \tag{2.25}$$

where $x = 2\pi r_c/\lambda$ with λ corresponding to wavelength.

The Lee Mie regime results in five possible parameters for including this Mie opacity cloud prescription in TauREx's retrievals. These are $\mathcal{Q}_0$, r_c, the mixing ratio of the cloud χ, the top pressure of the cloud layer P_{top} and the bottom pressure of the cloud layer P_{bottom} where these last two parameters define the clouds spatial thickness. Given the expectation of silicate clouds being the dominant source of cloud opacity for the objects considered in this work, we set $\mathcal{Q}_0$=10 when employing this cloud parameterisation as this is representative of "astro silcate" Lee et al. (2013).

2.1.10.3 | Bohren & Huffman Mie opacity for homogeneous spheres

We also used the Mie regime for species specific opacity sources from Bohren and Huffman (1983) (hereafter BH Mie) which considered homogeneous spherical particles. This is implemented in a similar way to the aforementioned Lee Mie scattering approximation with some key differences.

In the BH Mie implementation, the cloud's wavelength dependent optical depth τ_{cloud} is computed via the the extinction efficiency which is not approximated and instead determined via:

$$\mathcal{Q}_{ext} = \mathcal{Q}_{abs} + \mathcal{Q}_{scat} \tag{2.26}$$

where $\mathcal{Q}_{scat}$ is the scattering efficiency and $\mathcal{Q}_{abs}$ is the absorption efficiency. The calculation of $\mathcal{Q}_{ext}$ employs the real and imaginary refractory indices for a given cloud condensate species.

Overall, this BH Mie regime results in four possible fitting parameters to include in this cloud opacity in TauREx3's retrievals. These are particle radius r_c, χ, P_{top} and P_{bottom} where the latter three parameters have the same meaning as in the Lee Mie regime. For the BH Mie implementation, we consider a particle size distributions for r_c instead of a constant value (as in the case of the Lee Mie implementation). The different particle size distributions are outlined in following subsection.

2.1.10.4 | Particle size distributions

Several different particle size distributions have been adopted in previous retrieval studies of directly imaged exoplanets and brown dwarfs. Burningham et al. (2021) used the Hansen distribution (Hansen, 1971) as well as a lognormal distribution for analysis of 2M2224-0158. Mollière et al. (2020) also used a lognormal distribution for analysis of HR 8799e. For the BH Mie model TauREx3 offers the "cloud" particle size distribution from Sudarsky et al. (2003):

$$n(r) \propto \left(\frac{r}{r_c}\right)^6 exp\left[-6\left(\frac{r}{r_c}\right)\right] \tag{2.27}$$

The "haze" distribution from Deirmendjian (1964) is also available:

$$n(r) \propto \frac{r}{r_c} exp\left[-2\left(\frac{r}{r_c}\right)\right]^{\frac{1}{2}} \tag{2.28}$$

where r_c is the dominant mean radius. We also added a lognormal particle size distribution akin to that from Ackerman and Marley (2001):

$$n(r) \propto \frac{1}{r\sqrt{2\pi}\ln\sigma_g} exp\left[\frac{-\ln^2\left(\frac{r}{r_c}\right)}{2\ln^2\sigma_g}\right] \tag{2.29}$$

where σ_g is the standard deviation which controls the width of the lognormal distribution. The retrieval calculates Q_{ext} for BH Mie via the radii given by the particle size distribution and determines the average which is weighted by relative concentration of each particle size. A visual comparison of the various particle size distributions is shown in Figure 2.7.

2.1.10.5 | Patchy/Fractional clouds

In an effort to permit investigation into the potential presence and impact of patchy clouds on exoplanet and brown dwarf spectra, the basic patchy cloud consideration from Marley et al. (2010) has been added:

$$F_{Tot} = C_{frac} \cdot F_{Cloudy} + (1 - C_{frac}) \cdot F_{Clear} \tag{2.30}$$

where F_{Tot} is the total flux, F_{Clear} is the flux from regions without clouds, F_{Cloudy} is the flux from regions with clouds and C_{frac} is the fraction of surface area with clouds. The non-cloud properties are identical for the two forward models which are linearly combined. Employing this fractional cloud consideration

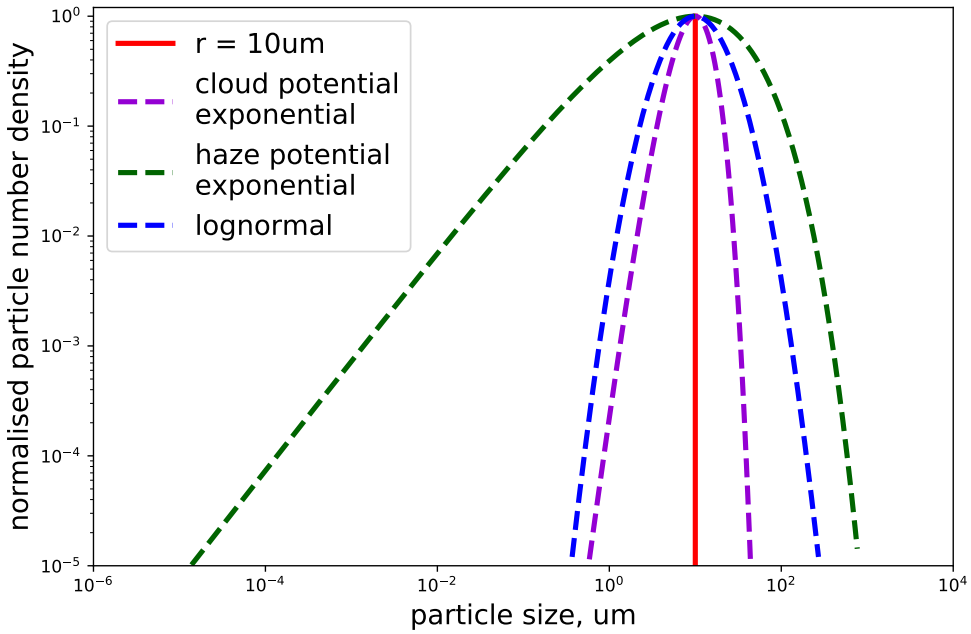

Figure 2.7: Comparison of particle size distributions included in TauREx3. Shown is the lognormal Ackerman and Marley (2001), "cloud" potential exponential from Sudarsky et al. (2003) and "haze" potential exponential from Deirmendjian (1964).

therefore acts to add an additional retrieved parameter, C_{frac}, to the cloud opacity parameterisations.

CHAPTER 3

Retrieval study of cool, directly imaged exoplanet 51 Eri b

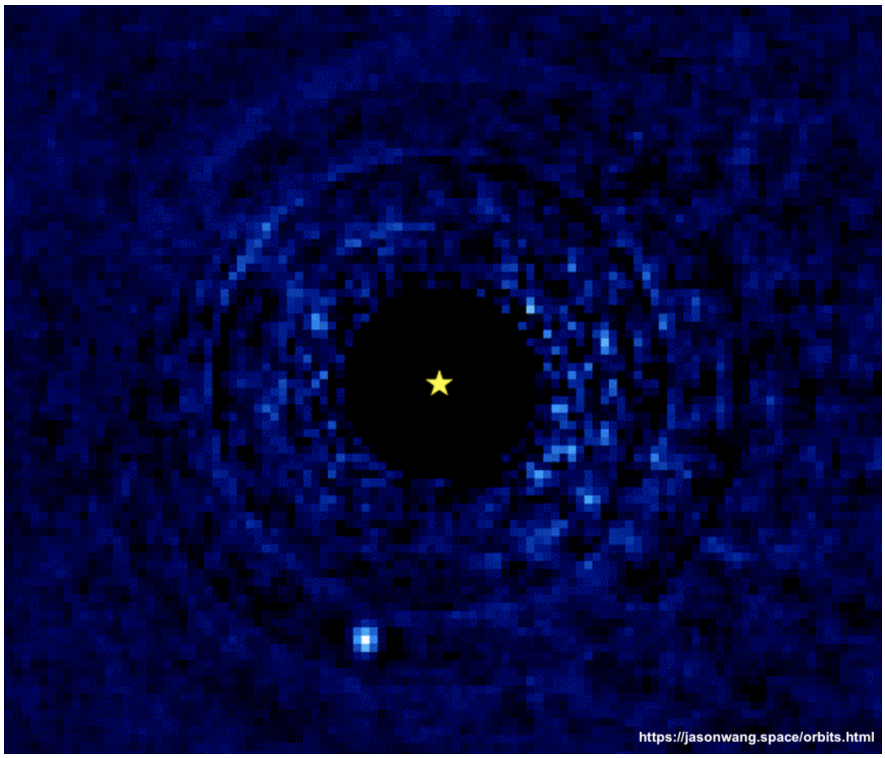

3.1 Introduction

While nearly 5000 exoplanets have been confirmed to date, (NASA Exoplanet Archive, 2022, Akeson et al., 2013), only a very small fraction have been directly imaged due to the significant technical challenge of detecting a signal from an exoplanet many times fainter than its host star. However, extreme coronagraphic spectrometers, including VLT's Spectro-Polarimetric High-contrast Exoplanet REsearch instrument (SPHERE) (Beuzit et al., 2008), the Gemini Planet Imager (GPI) (Macintosh et al., 2014) and VLT's GRAVITY (Gravity Collaboration et al., 2017), have made it possible to start the characterisation and classification effort of directly imaged exoplanet demographics (Nielsen et al., 2019, Vigan et al., 2020). The current state of direct imaging spectroscopy is covered extensively in Biller and Bonnefoy (2018)

The development of extrasolar planetary spectroscopy (see Tinetti et al., 2013) has mainly been driven by studies of transiting hot-Jupiters and has allowed for unprecedented insight into the diversity of their atmospheres. This led to the expansion and application of retrieval (inverse) atmospheric modeling techniques (outlined in Figure 2.1) to exoplanetary spectra (see Line et al. (2013) for a review of early exoplanetary retrieval codes). There are now a variety of retrieval codes developed for exoplanet atmospheric characterisation, examples include Nemesis (Irwin et al., 2008), Chimera (Line et al., 2013), BART (Harrington et al., 2016), SCARLET (Benneke, 2015), POSEIDON (MacDonald and Madhusudhan, 2017), Brewster (Burningham et al., 2017), HyDRA (Gandhi and Madhusudhan, 2018), petitRADTRANS (Nowak, M. et al., 2020, Mollière et al., 2019), Platon II (Zhang et al., 2020), Helios-R2 (Kitzmann et al., 2020) and TauREx3 (Al-Refaie et al., 2019).

In previous studies TauREx has been applied to observations of transiting exoplanets (Tsiaras et al., 2016, 2018, Waldmann et al., 2015a,b, Changeat et al., 2019, Rocchetto et al., 2016, Tsiaras et al., 2019, Edwards et al., 2020, Skaf et al., 2020, Pluriel et al., 2020), with a comparative study of TauREx, CHIMERA and NEMESIS retrieval codes to be found in Barstow et al. (2020) with a review of the

current state-of-the-art in Barstow and Heng (2020) and Madhusudhan (2019).

In comparison to transit spectroscopy, there have only been a handful of attempts to apply a retrieval approach to directly imaged exoplanet and brown dwarf spectroscopy or photometry. These include HR8799b (Lee et al., 2013), GJ 570D (Line et al., 2014), GJ 570D and HD 3651B (Line et al., 2015), 11 T dwarfs (Line et al., 2017), HR8799b-e (Lavie et al., 2017), 2MASS J05002100+0330501 and 2MASS J2224438-015852 (Burningham et al., 2017), GJ 570D and the Epsilon Indi brown dwarf binary system Kitzmann et al. (2020), 6 T and 8 Y dwarfs (Zalesky et al., 2019), β Pic b (Gravity Collaboration et al., 2020), HR 8799e (Mollière et al., 2020), HR 8799c (Wang et al., 2020) and the SDSS J1416+1348AB binary (Gonzales et al., 2020). Here we use the TauREx3 retrieval tool to carry out analysis of directly-imaged exoplanet 51 Eridani b (hereafter 51 Eri b) and brown dwarf benchmark GJ 570D.

Despite the significant development in the field of directly-imaged exoplanet spectroscopy in the last decade, upcoming telescopes will prove essential to further our understanding of these objects. The James Webb Space Telescope (JWST) (Gardner et al., 2006) and the soon to be constructed Extremely Large Telescope (ELT) (Udry et al., 2014, Brandl et al., 2014), will lead to increased observational capacity, requiring refined and robust analysis techniques. Retrieval tools will be a corner stone for the analysis of these next generation of observations.

Facilitated by the aforementioned instruments, direct imaging will be a very important technique for the future with the notable benefits that it offers when compared to the currently dominant technique of transmission spectroscopy. These include the ability to view exoplanet and brown dwarf atmospheres as they rotate (Crossfield et al., 2014) (as they are not tidally locked) and being able to probe further into the atmosphere, unlocking more spectral features and atmospheric characteristics. The currently observed selection of directly imaged exoplanets are limited to young gas-giants which orbit their host stars at large radial distances. They show similar properties to free-floating planetary mass objects and old, field brown dwarfs. As a result, these three subsets of object can have the same spectral types. The youngest start out as a hot M spectral type, evolving via cooling firstly to an L type, then to a T type (Kirkpatrick, 2005)

before finally becoming a very cool Y type (Cushing et al., 2011, Miles et al., 2020), at the limits of current observational capabilities. In this study we will be focusing on T spectral type objects, with their atmospheric signatures dominated by H_2O and CH_4 absorption.

The importance of cloud modelling for directly imaged exoplanets and brown dwarfs has been well explored and debated (Chilcote et al., 2017, Bowler et al., 2020, Zhou et al., 2020, Marley et al., 2010, Morley et al., 2012, Mollière et al., 2020, Burningham et al., 2021, 2017, Lee et al., 2013, Marley et al., 2012, Morley et al., 2014, Charnay et al., 2018, Lew et al., 2020). Previous studies of 51 Eri b, for example, used clouds in their self-consistent grid modelling (Samland et al., 2017, Rajan et al., 2017) to successfully fit the planet's spectral energy distribution (SED). For a recent and extensive review of exoplanet clouds see Helling (2019). Alternative explanations for the observed SEDs have been explored in Tremblin et al. (2016) and Tremblin et al. (2017), who demonstrated that a reduced atmospheric temperature gradient can reproduce the SEDs of late L and T type brown dwarfs, without the need to invoke clouds. The mechanism reducing the temperature gradient in these atmospheres has been proposed to be diabatic convection triggered by the CO/CH_4 chemical conversion in brown dwarf atmospheres (Tremblin et al., 2019).

We now describe the specifics of both our retrieval approach and other tools used in our spectral analysis, as applied to spectra of 51 Eri b and GJ 570D.

3.2 Two benchmark T dwarfs: GJ 570D and 51 Eri b observations

In this section we give a brief overview of our current knowledge and understanding of GJ 570D and 51 Eri b as well as describing the origin of the data used in their model fitting analysis. We chose to focus on T dwarfs in this first application of TauREx3 to directly-imaged targets as in this temperature regime their SED's are thought to be less influenced by clouds, which are expected to exist below

the observable photosphere (Lodders and Fegley, 2006, Burrows and Sharp, 1999, Burrows et al., 1997). The inclusion of GJ 570D allows us to benchmark TauREx3 against previous studies using other retrieval codes (Kitzmann et al., 2020, Line et al., 2015, Burningham et al., 2017). 51 Eri b offers a comparable spectral type object but allows us to investigate a completely different mass regime and it has no existing free-chemistry retrieval analysis. We note that clouds seem to be more prominent in the observable atmosphere for low surface gravity objects such as 51 Eri b (Marley et al., 2012, Charnay et al., 2018).

3.2.1 | GJ 570D

GJ 750D (or 2MASS J14571496-2121477) is a cool T7.5 brown dwarf, with an age of 1-5 Gyr (Liu et al., 2007), and was among the first T dwarf companions to be discovered by Burgasser et al. (2006, 2004). It is a very wide component in a hierarchical quadruple system, comprising the inner spectroscopic binary companions GJ 570B and C and the primary GJ 570A from which GJ 570D orbits at a projected separation of 1525 $\pm$ 25 AU (Burgasser et al., 2000). GJ 570D has been included in order to compare TauREx3 against other retrieval studies as it has become commonly included in novel retrieval approach validations (Kitzmann et al., 2020, Line et al., 2015, Burningham et al., 2017, Line et al., 2014, 2017, Piette and Madhusudhan, 2020). It also offers the opportunity to compare retrieval results against studies using grid model fitting. GJ 570D has a comparable spectral type to the exoplanet 51 Eri b, also included in this study.

3.2.1.1 | Observations and calibration

We used observations of GJ 570D taken by the SpeX spectrograph (Rayner et al., 2003), which is mounted on the 3m NASA InfraRed Telescope Facility. The measured spectrum is part of the SpeX Prism Library (Burgasser, 2014) and was first published in Burgasser et al. (2004). The data were reduced using the pipeline described in Cushing et al. (2004), with the spectrum spanning

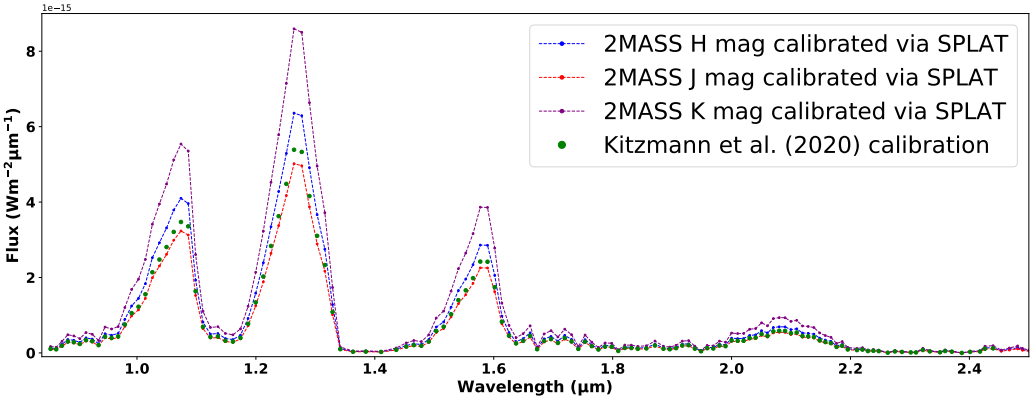

(a) (a) GJ 570D Calibration comparison

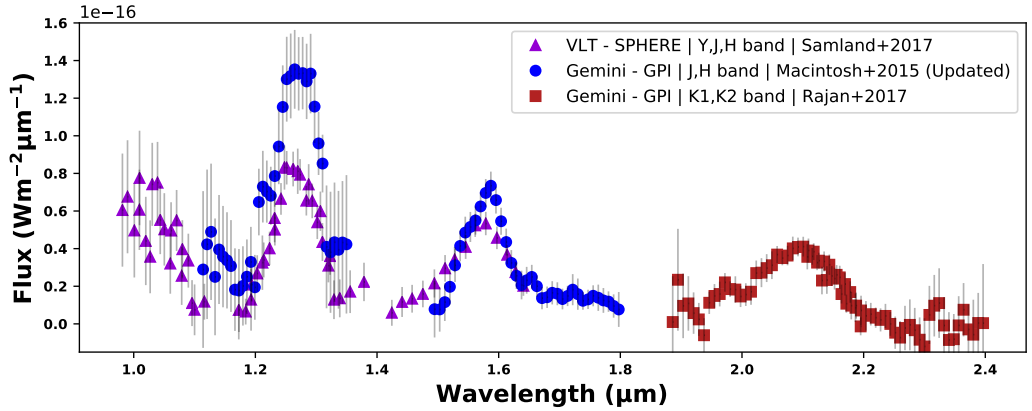

(b) (b) 51 Eri b spectra

Figure 3.0: Top: SpeX prism spectrum of GJ 570D, flux calibrated using SPLAT and the object's 2MASS J, H and K band magnitudes. The spectrum used by Kitzmann et al. (2020), produced using a different absolute flux calibration approach, is included for comparison. Bottom: Published data for 51 Eri b. We include Y, J and H band SPHERE data from Samland et al. (2017), along with the GPI J and H data from Macintosh et al. (2015) (which is updated using a revised stellar flux and presented in Rajan et al. (2017)) along with GPI $K1$ and $K2$ band data from Rajan et al. (2017). There is a clear difference in the J band brightness, and also a difference in the H band brightness, between the GPI and SPHERE observations.

0.65 to 2.56 μm at an average spectral resolving power of 120 (varying with wavelength between 85 to 300). Using the SpeX Prism Library[1] data analysis toolkit (SPLAT[2]) (see Burgasser and Splat Development Team (2017) for details), we flux calibrated the data using photometry from the 2MASS survey[3] (Skrutskie et al., 2006).

The spectra shown in Figure 3.0a have then been calibrated using J (15.324 $\pm$ 0.05 mag), H (15.268 $\pm$ 0.09 mag) and K-band (15.242 $\pm$ 0.16 mag) fluxes. In the following analysis we used the spectrum calibrated using the H-band magnitude. As outlined in Line et al. (2015), neighbouring pixels may not be statistically independent, due to the duplication of flux information. Therefore, when analysing this data set we only include every third data point (pixel) in our model fitting.

3.2.2 | 51 Eri b

51 Eri b was the first exoplanet discovered by GPI (Macintosh et al., 2014), and has one of the smallest angular and physical separations ($\sim$0.5", $\sim$13 AU) of any directly imaged exoplanet. It orbits a young F0-type host, with age estimates of 20 $\pm$ 6Myrs from Macintosh et al. (2014) and 26$\pm$3Myrs from Nielsen et al. (2016). With a spectral type of T6.5$\pm$1.5 (Rajan et al., 2017), 51 Eri b is notably the latest spectral type planet yet imaged.

Exhibiting methane absorption (a first for directly-imaged exoplanets) with its lower effective temperature ($\sim$700K) and low mass (< 10 M_{Jup}), 51 Eri b defined a new category of directly-imaged exoplanets. Further, its SED indicates that the L/T transition occurs at lower temperatures for these lower surface gravity objects compared to the higher surface gravity brown dwarfs (Rajan et al., 2017).

Studies of this exoplanet have included clouds in order to fit the spectroscopic and photometric data. Rajan et al. (2017) used two self-consistent grid models, one with a patchy iron/silicate cloud scattering component, and the other with

[1]SpeX Prism Library: `http://pono.ucsd.edu/~adam/browndwarfs/spexprism/library.html`

[2]SPLAT: `http://pono.ucsd.edu/~adam/browndwarfs/splat/`

[3]2MASS Survey Archive: `https://irsa.ipac.caltech.edu/Missions/2mass.html`

sulfide/salt cloud scattering to explain the spectral profile, while Samland et al. (2017) used grid models produced using petitCODE (Mollière et al., 2015, 2017) which employed a slightly modified version of the Ackerman and Marley (2001) prescription in their cloud modelling. Samland et al. (2017) also tested the Morley et al. (2012) cloud models against their observations. Samland et al. (2017) couldn't differentiate between patchy and uniform clouds while Rajan et al. (2017) found a preference for patchy iron/silicate clouds in the model fitting. Both studies concluded that clouds were needed to fit the spectrum well. We outline previous model fitting results from previous studies in Table 3.4. Neither Samland et al. (2017) or Rajan et al. (2017), however, employed a free chemistry model as we have done in this study.

3.2.2.1 | Observations

In this study we used a combination of observations of 51 Eri b from 2015-2016. These included spectroscopic data taken with GEMINI-GPI's Integral Field Spectrograph (Macintosh et al., 2014) (IFS) in the J, H, $K1$ and $K2$ bands (Rajan et al., 2017) (where J and H band observations are updated from Macintosh et al. (2015)) and VLT-SPHERE's IFS (Beuzit et al., 2008, 2019) using its YJ, YH filters (Samland et al., 2017). The spectra are shown in Figure 3.0b, calibrated as outlined in (Samland et al., 2017) and (Rajan et al., 2017).

We also employed photometric measurements from KECK-NIRC2's (McLean and Sprayberry, 2003) Lp and Ms filters (Rajan et al., 2017), where we used two combinations of data for our analyses: one which combined SPHERE's Y, J and H bands along with GPI's $K1$ and $K2$ band data and the other which combined only the GPI bands. We used this approach as the aforementioned GPI and SPHERE observations differed significantly in brightness in both the J and H bands.

Unlike with the GJ 570D data, we did not exclude any data from the analysis. This was motivated by the data's already low spectral resolution, combined with the relatively large errors, where exclusion of data would severely impact the retrievals ability to constrain parameters. We note that the potential for

correlated noise to impact the retrieval is more prominent when using these full data sets.

3.3 Modelling

3.3.1 | TauREx3

TauREx3 was employed for our retrieval analysis. The following subsections outline our retrieval setup. See Chapter 2 for a full outline of TauREx3.

3.3.1.1 | Retrieval model setup

Using MultiNest, we sampled the parameter space using 3000-5000 live points at a sampling efficiency of 0.8. We employed the the *npoint* temperature-pressure profile for this study which is described in Chapter 2.

We consider a model atmosphere with pressures ranging from 10^{-3} to 500 bar, with 100 layers uniformly sampled in log-space. We assume a hydrogen dominated atmosphere with a H_2 and He mixing ratio $He/H_2 = 0.17567$. In our study we include the cross sections for H_2O (Polyansky et al., 2018), CO (Li et al., 2015), and CH_4 (Yurchenko et al., 2017), NH3 (Coles et al., 2019) and Na+K Allard et al. (2016, 2019). The molecular trace-gas mixing ratio profiles (as a function of pressure), in the forward model are set as constant with pressure (isoprofiles). Collision induced absorption (CIA) of H_2–H_2 and H_2–He (Abel et al., 2011, Fletcher et al., 2018, Abel et al., 2012) is also included.

We use error inflation (as outlined in Section 2.1.7.1) for our analysis of GJ 570D but not for our 51 Eri b analysis. This is because 51 Eri b's observations have much larger error bars and the observation's resolution is more uniform throughout the spectrum, negating the spectral band weighting issue experienced with the GJ 570D data set (again, see Section 2.1.7.1). In our GJ 570D data it is apparent that that K band errors are much smaller than the J band data (see

Figure 3.0a). The impact of adding this error inflation parameter acted to allow the fit to the J band data to improve without affecting the goodness of fit in the K band and also allowed for the overall Log Evidence to increase slightly. This was interpreted as an increase in error size in the K band, while negligible in the J band, allowing for a better overall fit by de-weighting the small error bars found predominately in the K band when performing the Bayesian likelihood calculation.

In the case of the 51 Eri b data analysis we use multiple scaling factors S_{cal} to account for the inclusion of observations from different instruments. This is employed in the case of the SPHERE Y, J and H data ($S_{cal\ SPH}$) being combined with the GPI $K1$ and $K2$ band data ($S_{cal\ GPI}$). When employing data from a single instrument we simply use one scaling S_{cal} factor.

3.3.1.2 | Retrieval priors

The priors and prior bounds set for the retrieval analysis performed in this paper were either uniform, log-uniform or Gaussian priors. See Table 3.1 for a full overview of the priors set.

Given the lower quality of the 51 Eri b data we adopted an informative Gaussian prior for our retrievals. This was based on the system age estimate from Rajan et al. (2017) and the evolutionary tracks from Fortney et al. (2008) as shown in Figure 3.1. We didn't adopt a Gaussian prior on the mass as the reported values in the literature (Macintosh et al., 2015, Nielsen et al., 2019, Samland et al., 2017, Rajan et al., 2017) have a large spread in the planetary mass regime. However, we did enforce a flat planetary mass prior of 1-13M_{Jup} in the case of 51 Eri b.

3.3.2 | ATMO 2020

We compare our cloudless retrievals to self-consistent radiative-convective grid models. For this we use the recently published `ATMO` 2020 set of atmosphere and evolutionary models for cool brown dwarfs and self-luminous giant exoplanets (Phillips et al., 2020).

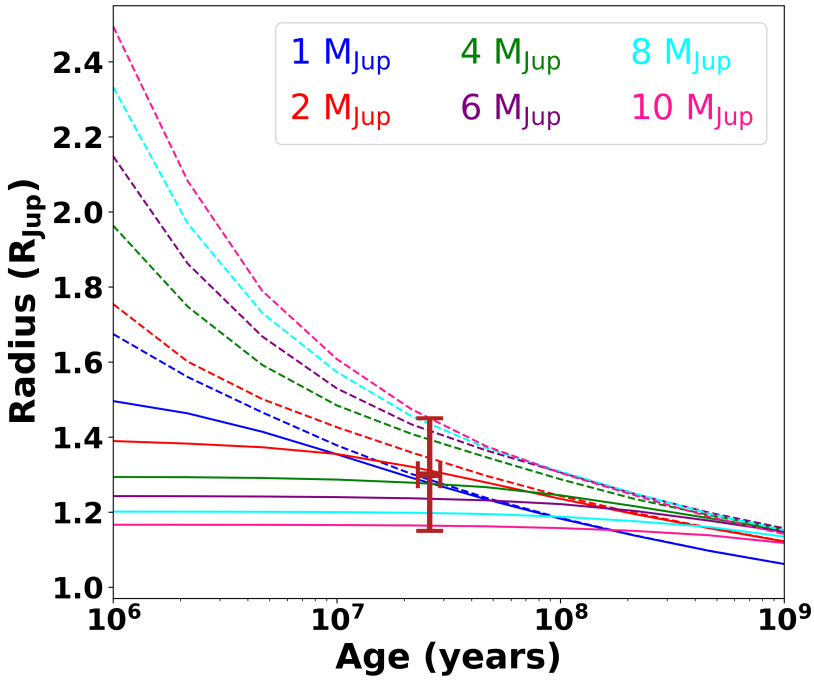

Figure 3.1: Evolutionary tracks from Fortney et al. (2008) with age uncertainty of 51 Eri system from Rajan et al. (2017) indicated. The Gaussian radius prior we adopt for the 51 Eri b analysis is also indicated.

Table 3.1: Table of retrieval priors. The middle sections list the parameters used for the $n-$ *point* and Madhusudhan and Seager (2009) temperature-pressure profiles, while the bottom section outlines the parameters used in the cloud scheme

Retrieved parameter	Distribution Type	GJ 570D Bounds	51 Eri b Bounds
Mixing Ratio	Log-Uniform	1e-12 - 1e-1	1e-12 - 1e-1
Radius	Uniform | Gaussian	0.5 - 2.0 R_{Jup}	1.3 $\pm$ 0.15 R_{Jup} [1,2]
Mass	Uniform	13 - 80 M_{Jup}	1 - 13 M_{Jup}[3]
Distance	Gaussian	5.8819 $\pm$ 0.0029 pc[4]	29.4 $\pm$ 0.3 pc[5]
S_{cal}	Gaussian	1.0, 0.1 STD	1.0, 0.1 STD
10^b	Uniform	0.01 x $\min(\sigma_\lambda^2) \leq 10^b \leq$ 100 x $\min(\sigma_\lambda^2)$	-
T_{surf}	Uniform	1250 - 2500 K	1250 - 2500 K
P_{surf}	Log-Uniform	5e2 - 1e1 bar	5e2 - 1e1 bar
T_1	Uniform	100 - 2000 K	100 - 2000 K
P_1	Log-Uniform	1e1 - 1e-1 bar	1e1 - 1e-1 bar
T_{top}	Uniform	0 - 1000 K	0 - 1000 K
P_{top}	Log-Uniform	1e-1 - 1e-3 bar	1e-1 - 1e-3 bar

[1] Note: Gaussian prior.
[2] Note: We use a Gaussian prior informed using evolutionary models from Fortney et al. (2008) combined with the age presented in Rajan et al. (2017) .
[3] Note: We make the assumption of a planetary mass object.
[4] Note: GJ 570D distance comes from Gaia Archive: https://gea.esac.esa.int/archive/.
[5] Note: The 51 Eri b distance comes from Macintosh et al. (2015).

The ATMO code is a 1D radiative-convective equilibrium model, and has been most recently described in Phillips et al. (2020) and Goyal et al. (2020). Briefly, ATMO defines the TP-profile of an atmosphere on a logarithmic optical depth grid with 100 model levels. The outer boundary condition in the first model level is fixed at a pressure of 10^{-5} bar and is given an optical depth of $\tau \sim 10^{-4} - 10^{-7}$ depending on surface gravity. The inner boundary condition in the last model level is not fixed in pressure and is given an optical depth of $\tau = 1000$. The model then iterates the pressure and temperature in each model level towards radiative-convective and hydrostatic equilibrium using a Newton-Raphson solver. On each iteration chemical equilibrium abundances are calculated for the current TP-profile using a Gibbs energy minimisation scheme based on that of Gordon and McBride (1994). ATMO also has the ability to calculate non-equilibrium chemical abundances self-consistently with the TP-profile, using kinetic networks or relaxation schemes (Phillips et al., 2020, Drummond et al., 2016). Once the chemical abundances have been computed, the opacities used by ATMO can be obtained from pre-computed correlated-k tables for individual gases (Amundsen et al., 2014), and are combined within the code using the random overlap to obtain the total mixture opacity consistently with the pressure, temperature and abundances in each iteration (Amundsen et al., 2017). The radiative flux is computed by solving the integral form of the radiative transfer equation in 1D plane-parallel geometry including isotropic scattering following Bueno and Bendicho (1995). The convective flux is computed using mixing length theory using the same method as Gustafsson et al. (2008), with the adiabatic gradient computed using equation of state tables from Saumon et al. (1995).

This grid includes solar metallicity atmosphere models spanning $T_{\rm eff} = 200 - 3000\,{\rm K}$ and $\log(g) = 2.5 - 5.5$ (g in units of cm/s^2), with steps of 100 K for $T_{\rm eff} > 600\,{\rm K}$, 50 K for $T_{\rm eff} < 600\,{\rm K}$, and 0.5 in $\log(g)$. The ATMO 2020 model set consists of three atmosphere model grids spanning this parameter range. The first is calculated assuming chemical equilibrium, and the second and third are calculated assuming non-equilibrium chemistry with different strengths of vertical mixing. Each model in the grid is generated with the ATMO code and consists of a TP-profile, chemical abundance profiles, and a spectrum of the emergent flux

from the top of the atmosphere, which are publicly available for download[4].

3.3.2.1 | Sampling using Markov Chain Monte Carlo

To calculate the best fits from the ATMO 2020 grid to the spectrophotometry of 51 Eri b (see section 3.2.2), we used a Markov chain Monte Carlo (MCMC) method utilising the *emcee* python package (Foreman-Mackey et al., 2013). We generated each independent model using an interpolation to the ATMO 2020 grid with temperatures ranging from 200 K to 3000 K and $\log(g)$ from 2.5 $\mathrm{cm/s^2}$ to 5.5 $\mathrm{cm/s^2}$ for models assuming chemical equilibrium, and temperature ranging from 350 K to 1800 K and $\log(g)$ from 3.0 $\mathrm{cm/s^2}$ to 5.5 $\mathrm{cm/s^2}$ for models assuming non-equilibrium chemistry due to vertical mixing. The radius was constrained between 0.07 $\mathrm{R_\odot}$ ($\sim 0.7\,\mathrm{R_{Jup}}$) and 0.2 $\mathrm{R_\odot}$ ($\sim 2\,\mathrm{R_{Jup}}$) for both cases, using a rough estimation from the ATMO evolutionary tracks, given the system's age. With this grid, the MCMC was set up with 100 walkers and was executed for 500 steps. The posteriors were constructed after discarding the first 200 steps, to account for the 'burn-in'. This eliminates any bias caused by the initial values supplied to the MCMC as a starting point in the parameter space. All results are reported with an uncertainty of 1σ.

3.4 Results: GJ 570D

In order to evaluate TauREx3's emission model against brown dwarf observations, we perform retrieval analysis on the Spex observations of GJ 570D. We compare our results with previous studies which employed other retrieval codes, with the aim of determining if the results were consistent with these previous studies. The results of the comparison are shown in Table 3.2, with the retrieval priors used

[4]ATMO 2020: http://opendata.erc-atmo.eu

Table 3.2: Summary of retrieval bulk parameters for GJ 570D along with values from previous studies.

	Mass (M_{Jup})	Radius (R_{Jup})	log(g) (cm/s^2)	T_{eff} (K)	C/O	[M/H]
This work (TauREx3)	$48.00^{+13.03}_{-11.87}$	$1.17^{+0.08}_{-0.08}$	$4.93^{+0.11}_{-0.12}$	722^{+23}_{-26}	$0.87^{+0.08}_{-0.07}$	$-0.19^{+0.05}_{-0.03}$
This work (ATMO 2020 - EC FM)	-	$0.71^{+0.04}_{-0.02}$	$4.64^{+0.34}_{-0.30}$	$826.34^{+12.88}_{-17.21}$	-	-
This work (ATMO 2020 - NEC FM)	-	$0.72^{+0.06}_{-0.03}$	$4.63^{+0.16}_{-0.10}$	$813.33^{+14.01}_{-27.19}$	-	-
Kitzmann et al., 2020 (FCR)	53^{+24}_{-20}	$1.13^{+0.05}_{-0.06}$	$5.01^{+0.13}_{-0.19}$	703^{+17}_{-30}	$1.11^{+0.09}_{-0.09}$	$-0.13^{+0.06}_{-0.08}$
Kitzmann et al., 2020 (ECR)	$17^{+3.8}_{-3.0}$	$1.00^{+0.10}_{-0.09}$	$4.61^{+0.08}_{-0.08}$	730^{+18}_{-17}	$0.83^{+0.09}_{-0.08}$	$-0.15^{+0.05}_{-0.04}$
Burningham et al., 2017 (FCR)	$19.80^{+28.60}_{-15.96}$	$0.96^{+0.80}_{-0.11}$	$4.73^{+0.31}_{-1.17}$	$752.25^{+35.51}_{-82.10}$	-	-
Line et al., 2015 (FCR)	$30.90^{+26.64}_{-15.76}$	$1.14^{+0.10}_{-0.09}$	$4.76^{+0.27}_{-0.28}$	$714.11^{+20.19}_{-23.15}$	$1.09^{+0.16}_{-0.14}$	$-0.25^{+0.13}_{-0.12}$
Oreshenko et al., 2020: Sonora (SML)	-	-	$4.93^{+0.38}_{-0.55}$	808^{+43}_{-27}	-	-
Oreshenko et al., 2020: AMES-cond (SML)	-	-	$5.27^{+0.43}_{-0.67}$	878^{+23}_{-78}	-	-
Oreshenko et al., 2020: HELIOS (SML)	-	-	$5.08^{+0.62}_{-0.68}$	800^{+14}_{-100}	-	-
Samland et al., 2017 (FM)	-	$0.94^{+0.04}_{-0.04}$	$4.67^{+0.04}_{-0.04}$	769^{+14}_{-13}	-	-
Filippazzo et al., 2015 (EM)	$37.28^{+24.05}_{-24.05}$	$0.94^{+0.16}_{-0.16}$	$4.90^{+0.50}_{-0.50}$	759^{+63}_{-63}	-	-
Testi, 2009 (FM)	-	-	5.0	900	-	-
Del Burgo et al., 2009 (FM)	-	-	$4.5^{+0.5}_{-0.5}$	948^{+58}_{-58}	-	-
Saumon et al., 2006 (EM, FM)	$42.5^{+4.5}_{-4.5}$	$0.855^{+0.023}_{-0.023}$	5.09-5.23	800-820	-	-
Burgasser et al., 2006 (EM)	-	-	5.1	780-820	-	-

[1] EC FM is Equilibrium Chemistry Forward Model
[2] NEC FM is Non-Equilibrium Chemistry Forward Model
[3] FCR is Free Chemistry Retrieval
[4] ECR is Equilibrium Chemistry Model
[5] SML is Supervised Machine Learning
[6] EM = Evolutionary Model
[7] FM = Forward Model

Table 3.3: Summary of GJ 570D retrieved molecular abundances along with a comparison to previous studies. TW = This work.

	TW, 0.85-2.5μm	TW, 1.2-2.5μm	Kitzmann et al. (2020)	Burningham et al. (2017)	Line et al. (2015)
log(H_20)	$-3.33^{+0.03}_{-0.03}$	$-3.11^{+0.05}_{-0.05}$	$-3.33^{+0.05}_{-0.06}$	$-3.42^{+0.16}_{-0.22}$	$-3.40^{+0.13}_{-0.13}$
log(CH_4)	$-3.39^{+0.03}_{-0.03}$	$-3.34^{+0.05}_{-0.06}$	$-3.28^{+0.06}_{-0.09}$	$-3.44^{+0.20}_{-0.31}$	$-3.45^{+0.10}_{-0.10}$
log(NH_3)	$-4.58^{+0.04}_{-0.04}$	$-4.69^{+0.07}_{-0.09}$	$-4.38^{+0.07}_{-0.10}$	$-4.82^{+0.26}_{-2.47}$	$-4.64^{+0.15}_{-0.15}$
log(CO)	$-7.66^{+3.22}_{-2.86}$	$-7.06^{+4.12}_{-3.12}$	$-7.70^{+2.7}_{-2.4}$	$-7.47^{+3.05}_{-3.04}$	$-7.53^{+2.65}_{-3.07}$
log(CO_2)	$-8.35^{+2.50}_{-2.39}$	$-8.58^{+2.12}_{-2.09}$	$-7.70^{+2.7}_{-2.4}$	$7.86^{+2.67}_{-2.66}$	$-7.76^{+2.23}_{-2.89}$
log(H_2S)	$-8.59^{+2.42}_{-2.26}$	$-3.86^{+0.12}_{-2.26}$	-8.47^{+2}_{-2}	$-8.74^{+2.68}_{-2.20}$	$-8.94^{+2.22}_{-2.11}$
log(Na+K)	$-5.99^{+0.03}_{-0.03}$	$-4.37^{+0.06}_{-0.06}$	$-5.86^{+0.04}_{-0.03}$	$-5.47^{+0.09}_{-0.30}$	$-5.45^{+0.06}_{-0.06}$

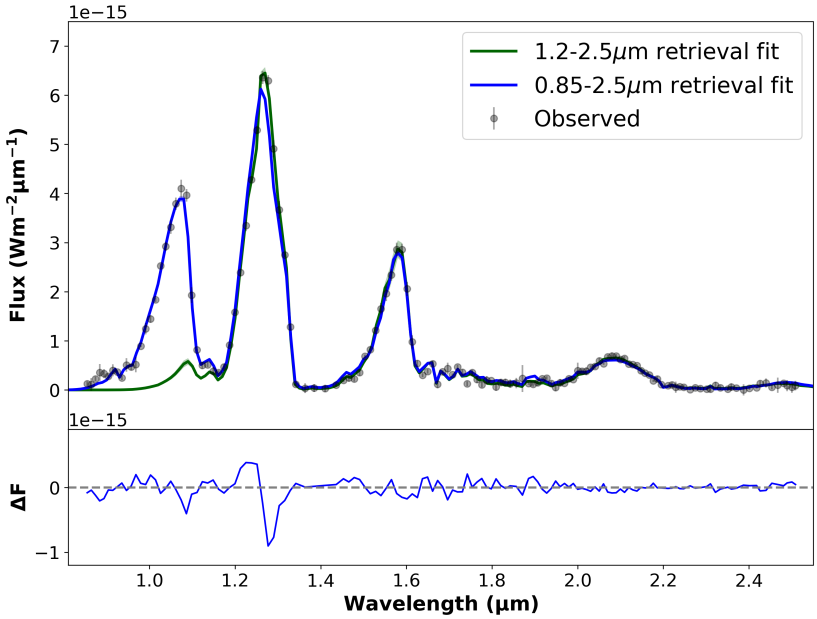

Figure 3.2: GJ 570D retrieval spectral fit

in the analysis listed in Table 3.1.

3.4.1 | Na+K systematic model bias

We encountered a systematic bias in the retrieved estimates for mass and radius when attempting to fit the 0.85-2.5μm spectrum of GJ 570D using a flat prior. This bias resulted in a non-physical radius (see Fortney et al., 2008 and Chabrier et al., 2009 for typical radii) of 1.4 to 1.55 R_{Jup}, along with a mass value that converged to the prior's upper boundary. The mass was also found to increase with the radius, likely in an effort to maintain the best fit surface gravity.

To investigate this effect, we ran retrievals with varying absolute flux calibrations and also employed the Madhusudhan and Seager (2009) temperature-pressure profile. Neither of these approaches negated the systematic bias. The application of a tight Gaussian prior on the radius was also tested, but in this case the mass was still seen to converge to the upper boundary of its flat prior. We find this systematic issue to be sensitive to the sodium and potassium (Na+K) cross sections, a dominating source of contribution in near-infrared model fitting

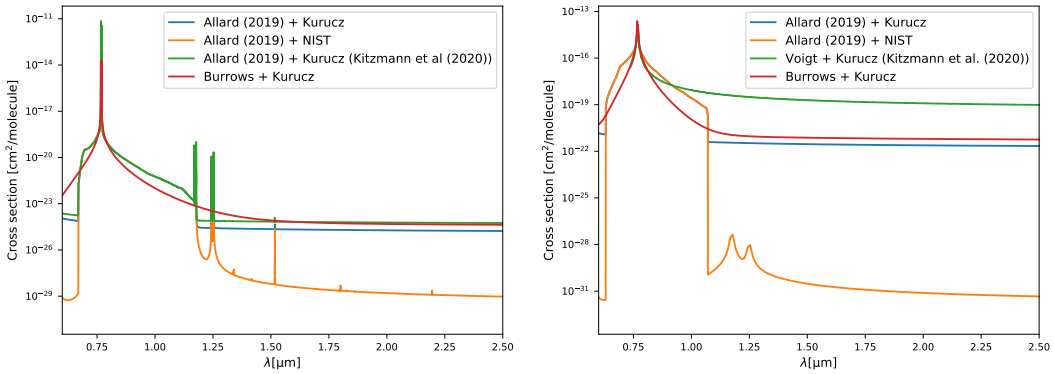

Figure 3.3: A comparison of different methods used to compute the resonance doublet and non-resonance lines of Na and K. The first panel gives cross sections for K computed at $T = 1000$ K, $P = 0.1$ bar, and the second panel the cross sections for K computed at $T = 600$ K, $P = 10$ bar. The cross sections in green are those which were used in Kitzmann et al. (2020). All other combinations shown (using either Burrows et al. (Burrows and Volobuyev, 2003) or Allard et al. (Allard et al., 2016, 2019) for the computation of the resonance doublets, and either NIST (Kramida et al., 2013) or Kurucz (Kurucz and Bell, 1995) for the non-resonance lines) were tested in the present study.

as shown in Line et al. (2015), Burningham et al. (2017) and Oreshenko et al. (2020).

It is noteworthy that this issue seems most prevalent when fitting the whole 0.85 - 2.5 μm spectrum. The resonance doublets of K and Na are at $\sim$0.77 μm and $\sim$0.59 μm respectively. We encountered examples when the bias issue would not be present when fitting only 0.85 - 1.2 μm ($\sim$0.77 μm K / $\sim$0.59 μm Na resonance doublet impacted region), or 1.2 - 2.5 μm (non-resonance lines/resonance doublet line wings region). This indicates a potential issue with either the combination of the resonance doublets and non-resonance lines within the Na+K cross sections, or with the extent of the broadening of the resonance doublets. Some different combinations of computing the cross sections of the resonance doublet and non-resonance lines of K are illustrated in Figure 3.3. The resonance doublets tested in the present study were either treated using the broadening parameters of Burrows et al. (Burrows and Volobuyev, 2003) or Allard et al. (Allard et al., 2016, 2019). The non-resonance lines from both the NIST (Kramida et al., 2013) or Kurucz (Kurucz and Bell, 1995) databases were also tested. Testing various combinations didn't negate the aforementioned bias. We again note that the

results presented in this study (Tables and Figures) were retrieved using the broadening parameters of Allard et al. and non-resonance lines from the Kurucz database. The issues related to the Na and K cross sections are discussed further in Section 3.6.

We therefore present two separate retrieval analyses for GJ 570D. First, to avoid the impact of this systematic bias but to still attain a set of values for the scaling factors (radius, distance and $S_{\rm cal}$) along with the mass (and by extension the inferred surface gravity) we ran a retrieval fitting only the 1.2 - 2.5 μm part of the spectrum. This cut-off of the potassium resonance doublet impacted region of the spectrum allowed for physically credible results for the mass and radius using flat priors. We then used these values as fixed (non-fitted) priors in a subsequent retrieval to infer the chemical properties of the atmosphere. This was necessary as extending the fit of the 1.2 - 2.5 μm retrieval to the 0.85 - 1.2 μm data showed a significant mismatch between the model fit and the observed SED in this region, as shown in Figure 3.2. This two-step approach leads to the most credible values for the retrieved parameters but does lead to a very slightly lower Bayesian Evidence value (see section 2.1.8) due to a slightly worse fit of the J band peak.

While this strategy did derive results consistent with previous studies it does have its limitations and imperfections. Firstly, the assumptions of flat priors while also truncating the data is not an ideal approach. The temperature pressure profile, which is fit in the second retrieval, is significantly constrained as the scaling factors, with which it is intricately linked, are fixed. The same can be said for the alkali abundance, which is strongly correlated to surface gravity. While our approach derives an alkali abundance consistent with previous studies, likely as a result of being able to make use of the alkali dominated wavelength region, we acknowledge this has been driven to an extent by our constraint on this parameter.

3.4.2 | Scaling factors and bulk parameters

The model posteriors for the mass, radius, S_{cal} and distance, along with the inferred surface gravity, can see seen in Figure 3.4, along with the spectral fit

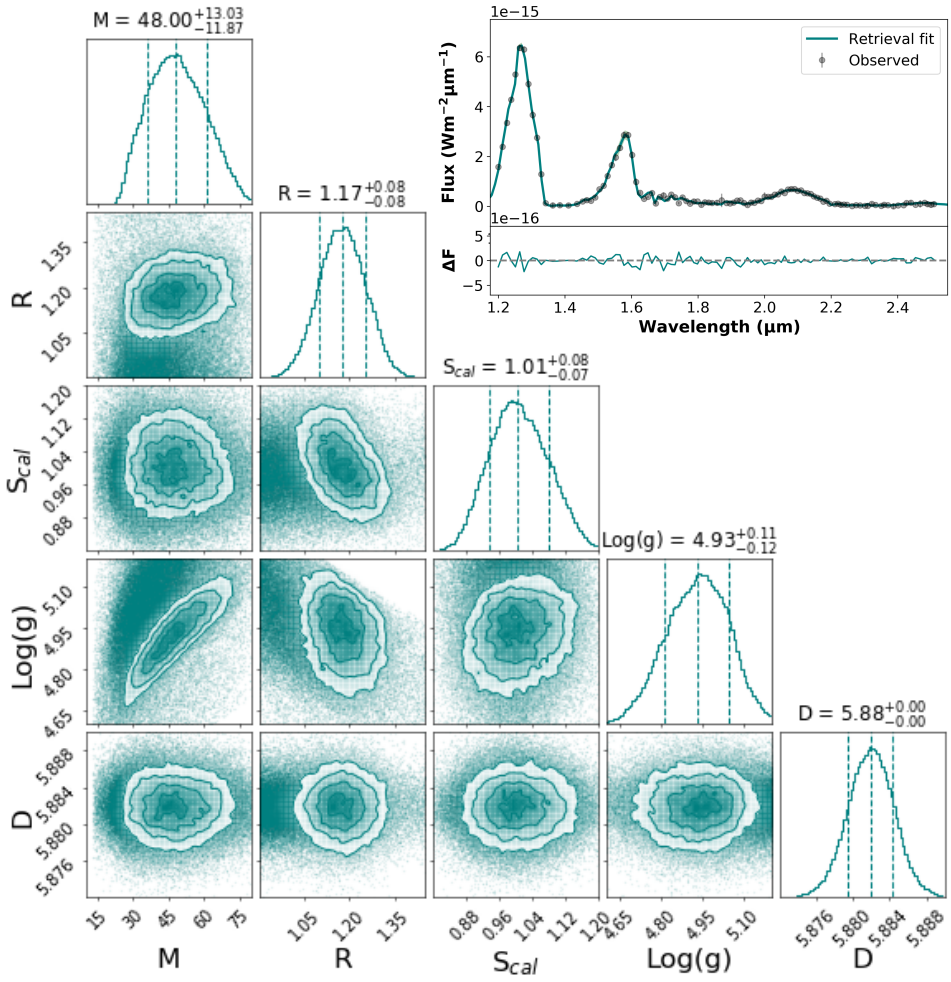

Figure 3.4: GJ 570D bulk parameter posterior probability distributions for the spectral fit of the 1.2-2.5μm data used.

to the data used. These results are also summarised in Table 3.2. In general, the retrieved parameter values are consistent with previous studies. Values from previous studies can also be seen in Table 3.2. Mass is consistent with all previous studies outlined in the table, apart from the equilibrium chemistry retrieval presented in Kitzmann et al. (2020). Radius is consistent with all previous free chemistry retrievals quoted in the table, and is 2σ consistent with the slightly lower radii presented in the equilibrium chemistry retrieval from Kitzmann et al. (2020) and non-retrieval analysis conducted in previous studies. As mass and radius are largely consistent with previous studies, so too is the inferred surface gravity. As the distance prior is well-constrained because of the precise Gaia measurements (Gaia Collaboration et al., 2016, 2018), the distance parameter does not play a significant role in the scaling of the spectrum. Our retrieved effective temperature matches well with all previously conducted retrieval studies, whilst some other studies such as Saumon et al. (2006) and Burgasser et al. (2006) have obtained slightly higher values for this parameter.

3.4.3 | Abundances

The posterior distributions for the retrieved abundances are shown in Figure 3.5, and listed in Table 3.3. The resulting SED fit, derived combining these retrieved abundances along with the locked scaling parameters outlined previously, is shown in Figure 3.2. These show that the three most abundant molecules are H_2O, CH_4 and NH_3, whilst Na+K is also well constrained.

The abundance for Na+K that we retrieve is similar to that from Kitzmann et al. (2020) but noticeably different from the values presented in Line et al. (2015) and Burningham et al. (2017), which we ascribe to the use of the broadening coefficients from Allard et al. (2016) and Allard et al. (2019) in our analysis and that from Kitzmann et al. (2020).

Overall, these abundances (and by extension the C/O and [M/H] ratio) are similar to those from previous retrieval studies of this object presented in Line et al. (2015), Burningham et al. (2017) and Kitzmann et al. (2020). Our super-solar $0.87^{+0.08}_{-0.07}$ C/O ratio for GJ 570D is in good agreement with the reported 0.65 –

0.97 C/O for its host star presented in Line et al. (2015). Our value is slightly lower than that derived in Line et al. (2015)'s and Kitzmann et al. (2020)'s free chemistry retrievals, but is consistent with Kitzmann et al. (2020)'s equilibrium chemistry model. We do note however that this comparison is imperfect, as our inferred C/O value only considers the pure gas phase and this neglects the elemental losses dues to condensation.

3.4.4 | Temperature-Pressure profile

Our retrieved temperature-pressure profile is very similar to that obtained in the Kitzmann et al. (2020) study (see Figure 3.5 for comparison, where the blue band marks the one sigma error on our derived profile). The agreement in the $1-10$ bar pressure region is particularly close, as expected in this region which contributes most to the spectral emission profile. We are further encouraged that this good agreement continues up into the stratospheric region where the constraining influence of the spectral emission is smaller.

3.5 Results: 51 Eri b

In this section we outline our results for 51 Eri b, compared to previous studies, all of which required clouds to produce the observed SED. Here, we find that inverse retrieval methods can recreate the observed SED with cloud-free atmospheres but using a more flexible (*npoint*) temperature-pressure profile. We also present retrievals including clouds (power law) combined with a less flexible (Lavie et al., 2017) temperature-pressure profile for comparison. We also compare our results for 51 Eri b to those for GJ 570 D (which is a close match in spectral type). We also find evidence of an ammonia detection.

We ran retrievals on the SPHERE Y, J, and H band data and separately on the GPI J and H band data. For both retrievals, we adopted the GPI $K1$ and $K2$ data. We present comparison posteriors in Figure 3.7, with the results from the individual data sets shown in Figures 7.1 and 7.2. As Samland et al. (2017)

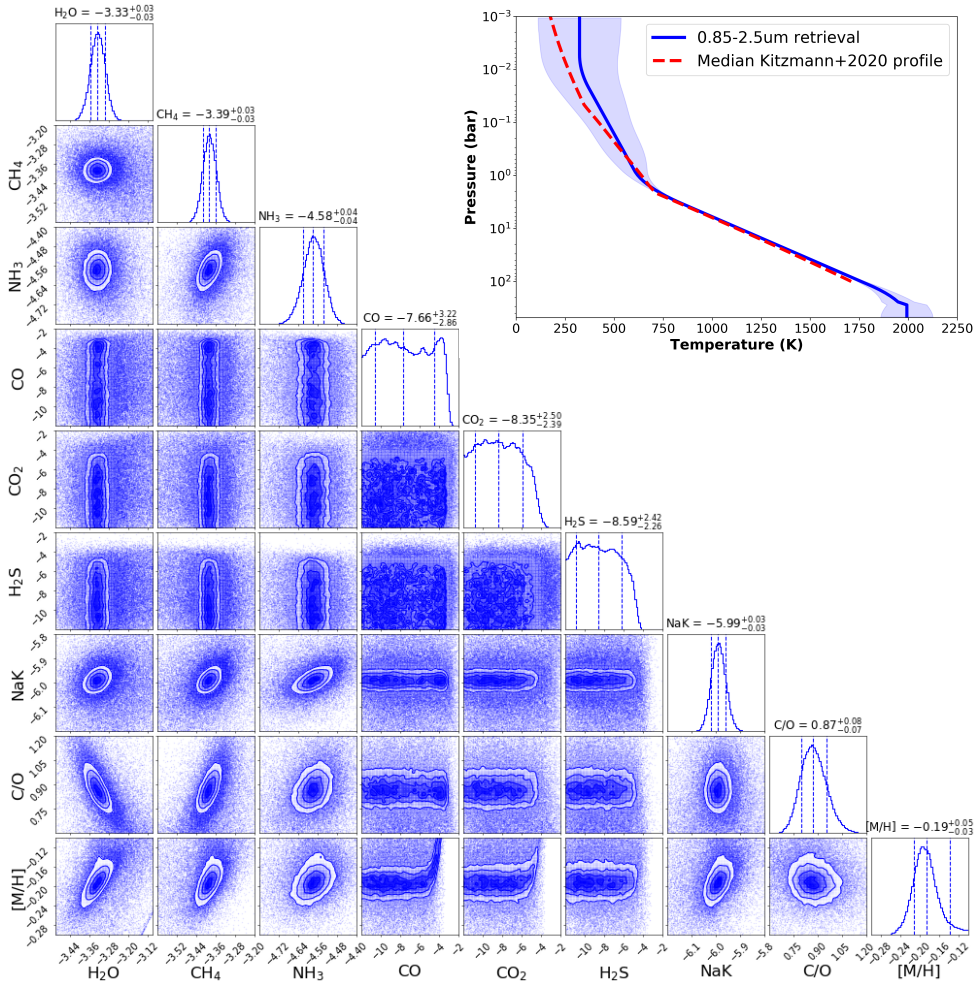

Figure 3.5: GJ 570D mixing ratio posteriors. C/O and [M/H] posteriors are inferred parameters, while all the other parameters are sampled as part of the retrieval. The retrieved temperature-pressure profile is also shown along with a comparison to the median profile retrieved in the Kitzmann et al. (2020) study

.

did not fit the GPI $K1$ and $K2$ data in their study, we also present retrieval results using only the SPHERE Y, J and H band data. The posteriors for these results are presented in figure 7.3. We do note here, however, that Samland et al. (2017) included SPHERE and GPI photometry in their fitting which was a driving component of the high metallicity they derive.

The retrieval priors used in this analysis are presented in Table 3.1, with an overall summary of the retrieval results in Tables 3.4 and 3.5. The following subsections focus on the retrievals which used the *npoint* temperature-pressure profile and omitted clouds as these derived the highest Log(Ev). We then discuss the cloudy retrievals in a subsequent subsection.

Table 3.4: Summary of retrieved bulk parameters for 51 Eri b. Values from previous studies are also included for comparison. L17: Lavie et al. (2017). GPI all: GPI $J, H, K1, K2$ data. SPHERE & GPI: SPHERE Y, J, H & GPI $K1, K2$ data. SPHERE only: SPHERE Y, J, H data. U: Uniform clouds coverage. P: Patchy cloud coverage

	TP Profile Type	Log(Ev)	Mass (M_{Jup})	Radius (R_{Jup})	log(g)	T_{eff} (K)	C/O	[M/H]
TW, Cloudless (GPI $J, H, K1, K2$ data)	npoint, flexible	5596.02	$8.50^{+2.86}_{-3.44}$	$1.09^{+0.11}_{-0.11}$	$4.26^{+0.16}_{-0.23}$	769^{+37}_{-41}	$0.92^{+0.19}_{-0.27}$	$-0.26^{+0.66}_{-0.18}$
TW, Cloudless (SPHERE Y, J, H & GPI $K1, K2$ data)	npoint, flexible	5141.33	$7.93^{+3.22}_{-3.54}$	$1.18^{+0.12}_{-0.12}$	$4.16^{+0.18}_{-0.26}$	700^{+42}_{-45}	$0.97^{+0.09}_{-0.20}$	$-0.04^{+0.95}_{-0.49}$
TW, Cloudless (SPHERE Y, J, H data)	npoint, flexible	2330.45	$8.25^{+3.01}_{-3.33}$	$1.31^{+0.12}_{-0.11}$	$4.09^{+0.15}_{-0.23}$	909^{+37}_{-50}	$0.40^{+0.26}_{-0.15}$	$-0.66^{+0.14}_{-0.11}$
Nielsen et al., 2019			$2.6^{+0.3}_{-0.3}$	-	-	-	-	-
Samland et al., 2017 (PTC-uniform clouds)[1]			$9.1^{+4.9}_{-3.3}$	$1.11^{+0.16}_{-0.14}$	$4.26^{+0.25}_{-0.25}$	760^{+20}_{-20}	-	-
Samland et al., 2017 (PTC-patchy clouds)[1]			$14.5^{+8.7}_{-5.6}$	$1.11^{+0.16}_{-0.14}$	$4.47^{+0.24}_{-0.26}$	757^{+24}_{-24}	-	-
Samland et al., 2017 (PTC-clear)[1]			$14.5^{+4.7}_{-3.1}$	$0.40^{+0.02}_{-0.02}$	$5.35^{+0.15}_{-0.12}$	982^{+18}_{-15}	-	-
Samland et al., 2017 (Morley et al., 2012 clouds)			$64.9^{+19.1}_{-15.6}$	$1.01^{+0.07}_{-0.06}$	$5.19^{+0.10}_{-0.11}$	684^{+16}_{-20}	-	$1.03^{+0.102}_{-0.11}$
Rajan et al., 2017 (Iron-silicate, patchy clouds)			-	$0.68^{+0.13}_{-0.14}$	3.25	737^{+39}_{-46}	-	-
Rajan et al., 2017 (Sulfide, salt, uniform clouds)			-	$0.90^{+0.23}_{-0.26}$	$4.05^{+0.36}_{-0.35}$	605^{+61}_{-66}	-	-
Macintosh et al., 2015 (cloud-free)			67	0.76	5.5	750	-	-
Macintosh et al., 2015 (partial-cloud)			2	1	3.5	700	-	-

Table 3.5: Summary of 51 Eri b retrieved molecular abundances , C/O ratio and metallicity [M/H] with a comparison to our retrieved values for GJ 570D. These are the values from the highest Log(Ev) (cloudlesss, npoint TP) retrievals.

	51 Eri b (1)[1]	51 Eri b (2)[2]	GJ 570D
log(H_20)	$-3.52^{+0.16}_{-0.16}$	$-3.50^{+0.16}_{-0.19}$	$-3.33^{+0.03}_{-0.03}$
log(CH_4)	$-3.63^{+0.12}_{-0.13}$	$-3.60^{+0.09}_{-0.11}$	$-3.39^{+0.03}_{-0.03}$
log(NH_3)	$-4.85^{+0.15}_{-0.18}$	$-4.61^{+0.11}_{-0.14}$	$-4.58^{+0.04}_{-0.04}$
log(CO)	$-3.32^{+1.13}_{-5.68}$	$-5.10^{+2.27}_{-4.54}$	$-7.66^{+3.22}_{-2.86}$
log(Na+K)	$-9.52^{+1.69}_{-1.59}$	$-7.65^{+2.58}_{-2.83}$	$-5.99^{+0.03}_{-0.03}$
C/O	$0.97^{+0.09}_{-0.20}$	$0.92^{+0.19}_{-0.27}$	$0.87^{+0.08}_{-0.07}$
[M/H]	$-0.04^{+0.95}_{-0.49}$	$-0.26^{+0.66}_{-0.18}$	$-0.19^{+0.05}_{-0.03}$

[1] 51 Eri b (1) refers to results retrieved using SPHERE Y, J, H and GPI $K1$, $K2$ band data.
[2] 51 Eri b (2) refers to results retrieved using GPI J, H, $K1$ and $K2$ band data

3.5.1 | Scaling factors and bulk parameters

Our highest Log(Ev) posterior probability distributions for the Mass, Radius, $S_{\rm cal}$ and Distance, along with the inferred surface gravity are presented in Figure 3.7. We find that our retrieval analysis is able to produce excellent fits to 51 Eri b's observed SED (see Figure 3.5) while deriving physically credible mass and radius values. This is the case when analysing each data set as outlined previously.

The S_{cal} factors derived indicate a preference for a brighter K band absolute flux calibration in both retrievals where this data is employed. In the cases of the SPHERE data being employed within the retrieval, an S_{cal} $\sim$1 is derived, indicating a model preference for this absolute flux calibration given the priors set. All the derived S_{cal} values can be found in Figure 7.1, 7.2 and 7.3

We note that the cloudless models used in the previous studies did not fit the SED particularly well. The cloudless models (Saumon and Marley, 2008) in Macintosh et al. (2015) derived a barely sub-stellar mass of 67 $M_{\rm Jup}$ with a low radius of 0.76 $R_{\rm Jup}$ while Samland et al. (2017)'s cloudless model (Mollière et al., 2015, 2017)

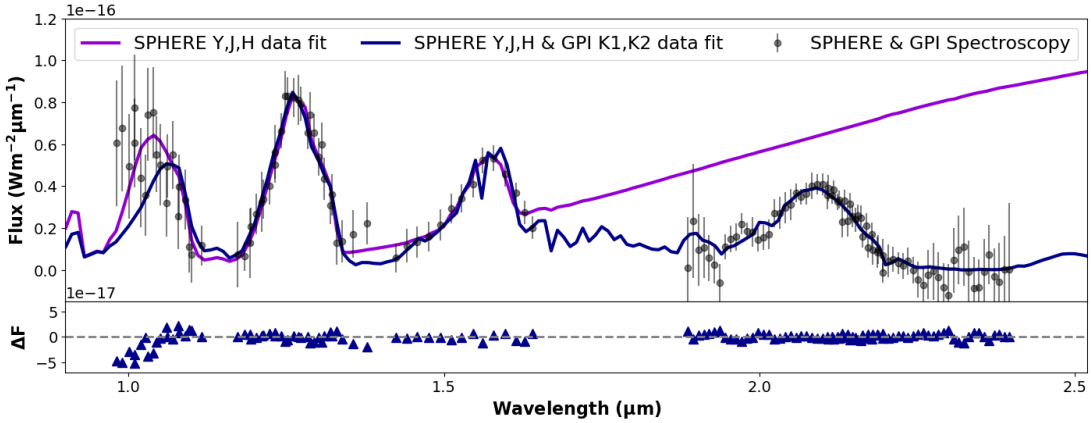

(a)

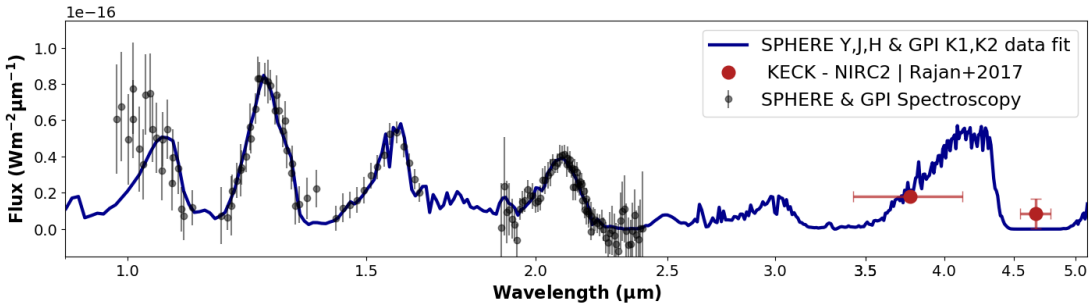

(b)

Figure 3.5: 51 Eri b SED fits via cloudless retrievals. (a) illustrates the model fit for retrievals including the SPHERE data where the dark violet fit shows the retrieval fit to only the SPHERE Y, J and K band data and the dark blue fit shows the retrieval fit when the SPHERE data is combined with the GPI $K1$ and $K2$ data. (b) shows the SPHERE Y,J,H and GPI $K1$ and $K2$ data fit extrapolated to longer wavelengths, with the inclusion of KECK-NIRC2 photometry.

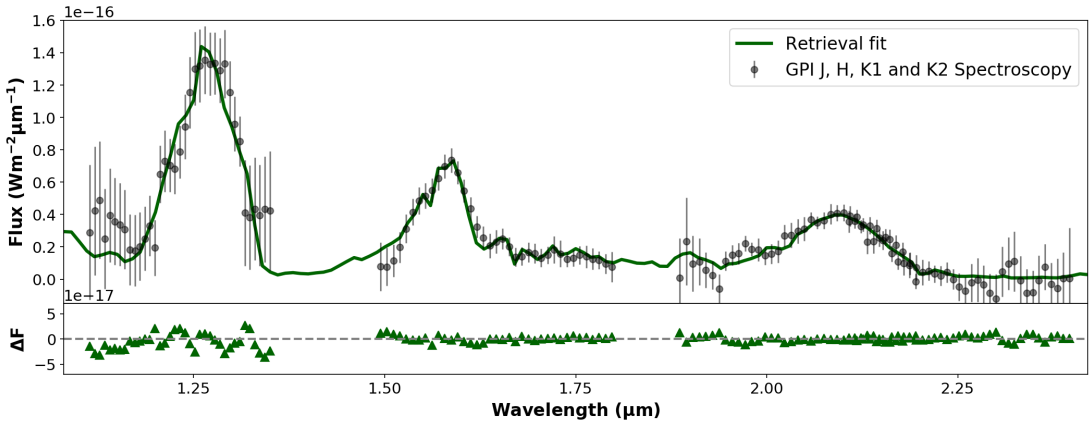

(c)

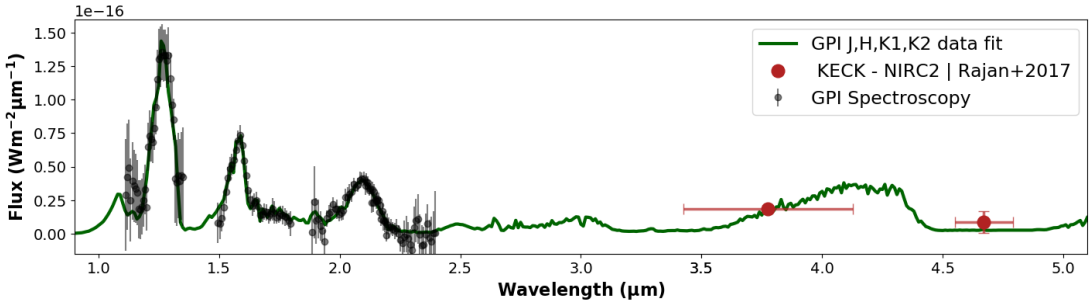

(d)

Figure 3.5: 51 Eri b SED fits via cloudless retrievals. (c) illustrates the model fit for the retrieval using the GPI J, H, $K1$ and $K2$ data. (b) shows the GPI J, H, $K1$, $K2$ data fit extrapolated to longer wavelengths, with the inclusion of KECK-NIRC2 photometry.

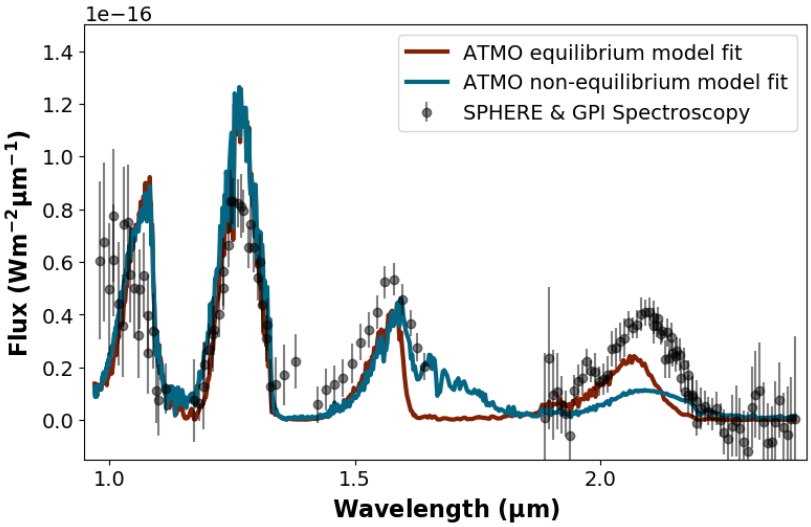

Figure 3.6: 51 Eri b spectral fit using ATMO

derived a mass that was $1\,\sigma$ consistent with that of a planetary mass object, but had an improbably small radius of 0.40 R_{Jup} for a Jovian exoplanet, violating electron degeneracy pressure laws for an object such as this (Chabrier et al., 2009). We attempted to fit the SED of 51 Eri b using a cloudless ATMO grid model as shown in Figure 3.6 and Figure 7.0, illustrating that these grid models are unable to explain the SED of this object or to constrain its surface gravity, radius or effective temperature, using both chemical equilibrium and chemical disequilibrium assumptions as shown in Figures 7.0.

Our retrieved effective temperature values are consistent with expectations for a T dwarf except in the case of the retrieval using only the SPHERE data as longer wavelength data is neglected in this instance. This resulting SED fit is, however, inaccurate when extrapolated to the K band as shown in Figure 3.5a.

3.5.2 | Abundances, tentative ammonia detection

The highest Log(Ev) posterior distributions for the retrieved abundances are shown in Figure 3.7 while retrieved abundances are shown in Table 3.5. Comparison with GJ 570D shows that the abundances of 51 Eri b and GJ 570D match to within 1σ, not unexpected given their similar spectral types (51 Eri b:

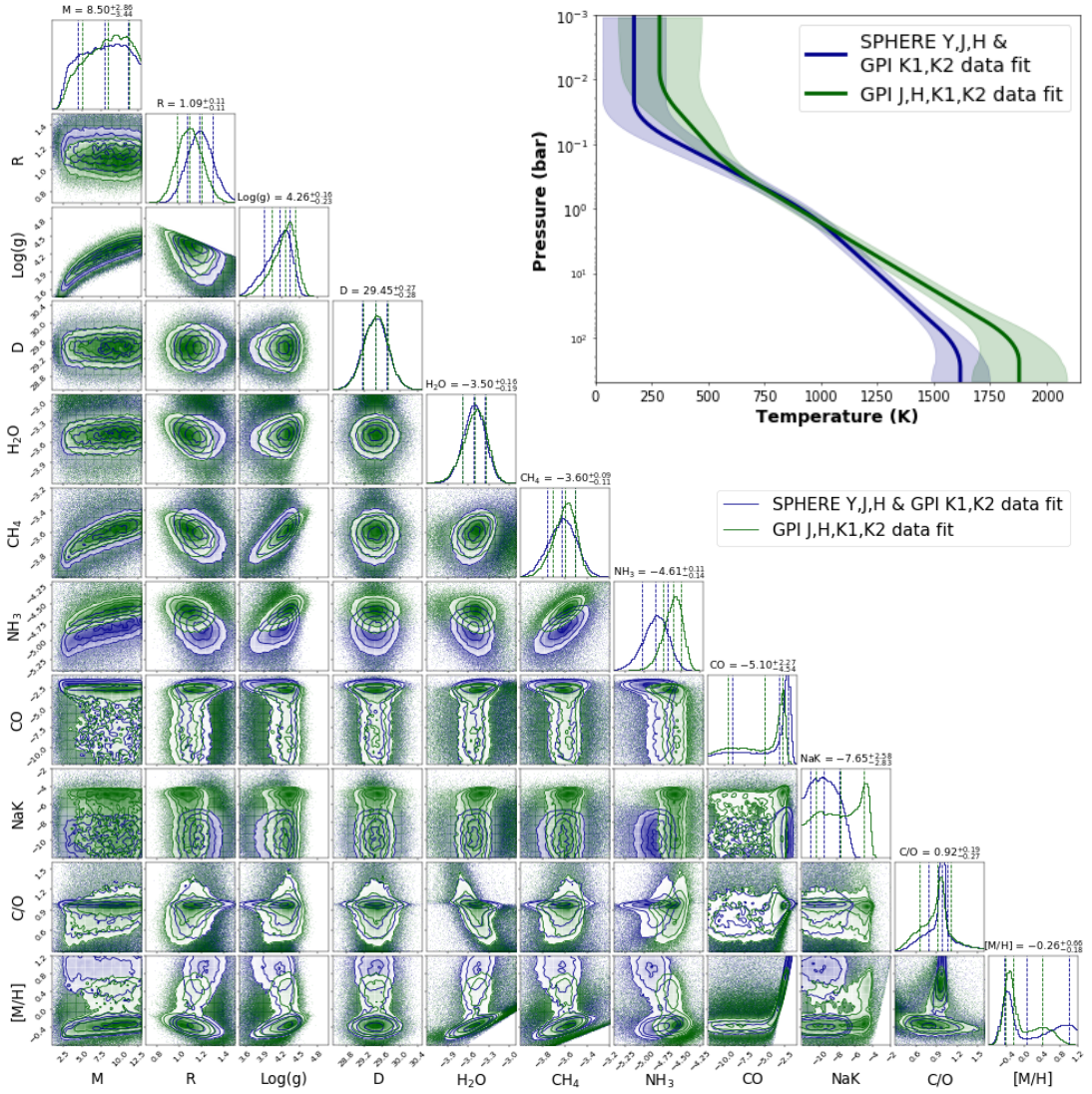

Figure 3.7: 51 Eri b posteriors. Blue indicates the retrieved values from the SPHERE Y,J,H and GPI $K1$,$K2$ data set. Green indicates the retrieved values from the GPI J,H,$K1$,$K2$ data set. Log(g), C/O and [M/H] posteriors are inferred parameters, while all the other parameters are sample as part of the retrieval. A comparison of the retrieved temperature-pressure profiles from each respective data set are also shown.

T6.5±1.5, GJ 570D: T7.5). We see that the derived [M/H] values for 51 Eri b, while consistent with GJ 570 D, have large uncertainties. This can also be seen in the large posterior tails for [M/H] shown in Figure 3.7. This appears to be a result of the large uncertainties see in the retrieved CO abundances.

As presented in Table 3.5, the retrieved Na+K abundance for 51 Eri b is the only abundance which is not 1-σ consistent with that retrieved for GJ 570D. This could either be a physical effect due to 51 Eri b's much lower surface gravity, or it could be related to the Na and K cross sections used in our retrievals. It could also be an impact of absent data below $\sim$1μm where this species plays a key role in contribution. We combine the Na and K cross sections together at solar abundance ratios, which could be an incorrect assumption for one or both of these objects. However, we found a minimal change in the retrieval results when separate Na and K cross sections (not combined at solar ratios) were used.

We report a tentative detection of ammonia in the atmosphere of 51 Eri b. This is another example of similar characteristics between 51 Eri b and GJ 570 D. This detection is at a confidence of $\sim 2.7\sigma$ ($log(b) = 2.36$) for the data set combining SPHERE and GPI obervations, and at 2.5σ confidence ($log(b) = 1.95$) for the data set employing only GPI observations. This was done using a Bayes factor to sigma conversion (Trotta, 2008). If verified, this would be the first detection and constraint on the presence of ammonia in a directly imaged exoplanet. This molecular species is present in planet forming, or protoplanetary disks (Salinas et al., 2016) and has long been included in models of substellar atmosphere (Ackerman and Marley, 2001, Saumon et al., 2012). It is also been shown to be present in Jupiter's atmosphere (Becker et al., 2020).

We also tested a de-correlated data set, where we attempted to negate the impact of possible covariance noise by only analysing one of every three data points (as done for the GJ 570 analysis, as outlined in Section 3.2.1.1). Despite this, the ammonia detection was still present in the retrieval result.

We note, however, that this detection in both retrievals presented in Figure 3.7 and Table 3.5 are driven by the GPI $K1$ and $K2$ band data. We do not detect ammonia when only analysing the Y, J and H band data as shown in Figure 7.3. Also, as noted previously, this analysis does not account for potential cross

correlated noise, which could reduce the confidence of this detection.

3.5.3 | Temperature-Pressure profile

The derived npoint temperature-pressure profiles, retrieved with each data set are shown in Figure 3.7. We also tested the Madhusudhan and Seager, 2009 profile but found that the model preferred the npoint profile in each case, deriving a higher Log Evidence.

Despite the differing spectral data inputs, the results are similar and are consistent at the 2-sigma level. We attribute the hotter profile between ∼20 to 100 bar when using only GPI data due to this having a brighter J band peak compared to the SPHERE J band peak as shown in Figure 3.0b.

We do not include the temperature-pressure profile retrieved using only the SPHERE data as this is an imperfect solution, as mentioned previously (given its inability to explain the GPI $K1$ and $K2$ data). This is a symptom of neglecting data, photometric and spectroscopic, at the longer wavelengths in the case of this particular retrieval. Samland et al. (2017) avoided such an issue by employing photometric data points at longer wavelengths. The similarities in atmospheric properties between 51 Eri b and GJ 570D, as highlighted in the previous subsection, also encompass the temperature-pressure profile. This is shown in Figure 3.8, where the temperature gradients of both objects are similar but 51 Eri b has a slightly steeper, and thus more isothermal, temperature gradient.

In Figure 3.9 we show how our retrieved temperature-pressure profile differs mainly in the Y and J-band photospheric contributions regions when compared to the radiative-convective equilibrium profile from the `ATMO` 2020 grid models. In other words, our retrieval analysis derives cooler Y and J-band photospheric temperatures.

The differences between profiles derived for 51 Eri b compared to the GJ 570 D retrieval (see Figure 3.8) and `ATMO` 2020 fitting (see Figure 3.9) may indicate the presence of an unmodelled cloud as the profile departs from an adiabatic gradient

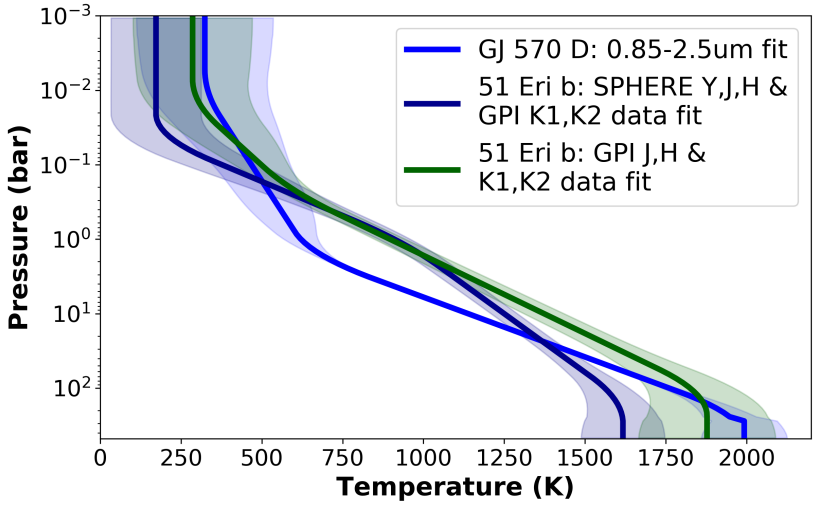

Figure 3.8: Retrieved 51 Eri b TP profile compared to the GJ 570D TP profile.

and becomes more isothermal. This kind of behaviour has been noted in previous retrieval studies such as Burningham et al., 2017 and Mollière et al., 2020 when a cloudless retrieval attempted to account for clouds included in mock data by making the profile more isothermal. As we noted above, our retrieved profile acts to produce a cooler Y and J photosphere and as such may be inadvertently mimicking the presence of a cloud layer. Alternatively, reduced, non-adiabatic temperature gradients triggered by chemical transitions have been suggested as an explanation for the SEDs of brown dwarfs (Tremblin et al., 2016, 2019). Thus, the retrieved non-adiabatic temperature profile could also be indicative of thermo-compositional convection taking place in the atmosphere of 51 Eri b.

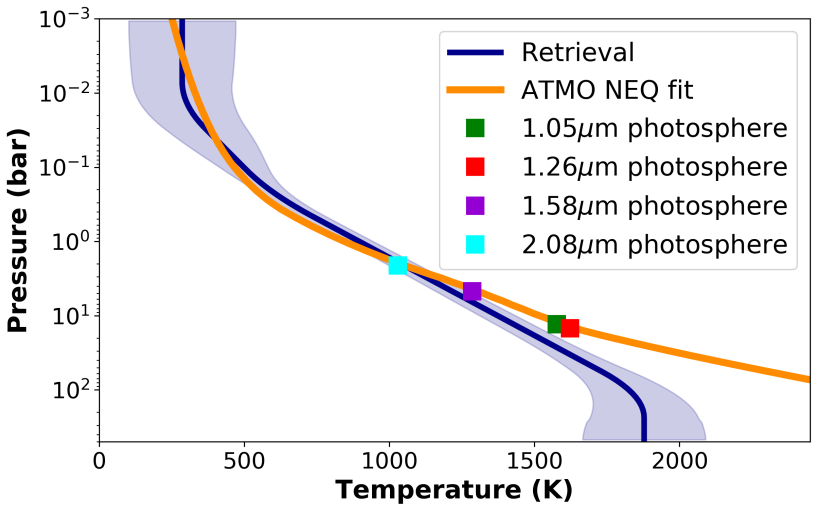

Figure 3.9: Temperature-pressure profile comparison between profiles derived by TauREx3 and ATMO 2020 for 51 Eri b.

3.5.4 | The question of formation

Parameters derived from retrieval analysis can allow us to peer into the formation history of exoplanets (Gravity Collaboration et al., 2020). Here, one can attempt to differentiate between possible formation mechanisms for 51 Eri b, primarily gravitational instability (GI) (Bodenheimer, 1974, Boss, 1997, Durisen et al., 2007) or core accretion (Pollack et al., 1996, Lissauer and Stevenson, 2007). GI is a rapid mechanism that has similarities with the general star formation process. When the system is very young, the disk may become massive enough to become gravitationally unstable, producing spiral density waves that may collapse to form bound objects, which could then slowly contract to produce planetary-mass bodies. Core accretion is a process by which a initially formed solid core slowly accretes gas and planetesimals within a disk. Once this solid core passes a critical mass, "runaway gas accretion" occurs, resulting in a rapid gain of material. Overall, the timescale of core accretion is much longer than that of GI.

All our derived radii values are consistent with the classical cold start and hot start planetary thermal evolution models from Fortney et al. (2008) (updated models from Marley et al. (2007)) as outlined in Figure 3.10, using age estimates from Macintosh et al. (2015) or Rajan et al. (2017). Figure 3.10 also shows that

our derived surface gravity values are consistent with both classical cold start and hot start model predictions at the 2-sigma level. As such, with the current uncertainties derived from retrievals such as that presented in this study, we are unable to differentiate between formation pathways using these models.

However, using carbon and oxygen abundances from Luck (2017) (Identifier: c Eri, Carbon $\log \varepsilon = 8.41$, Oxygen $\log \varepsilon = 8.80$) we derive a C/O ratio of $\sim$0.41 for 51 Eri. Therefore, the large mass retrieved for 51 Eri b, its $\sim$13 AU separation, both coupled with a super-stellar C/O ratio could point towards formation via GI (e.g., Vigan et al., 2017). A core accretion pathway would happen on a much longer timescale resulting in planetesimal enrichment (Mordasini et al., 2016), thus lowering the initial C/O ratio (Espinoza et al., 2017). However, Ilee et al. (2017) illustrate that even GI could produce a wide range of possible atmospheric abundances and so one should interpret the C/O ratio with caution. We also note that a super-stellar C/O ratio for a T dwarf could also be due to oxygen depletion via condensate processes and the formation of clouds below the photosphere (Lodders and Fegley, 2006, Burrows and Sharp, 1999). Therefore, the use of inferred C/O ratio informing on possible formation pathways should be approached with caution for T dwarf exoplanets.

3.6 Discussion

We have presented retrieval results which are consistent with previous studies and often provide improvements relative to forward models used in non-retrieval studies. This can mainly be attributed to the increased flexibility of model parameters, especially in the free chemistry retrievals. However, consistency between retrieval studies is encouraging when taking into account the use of different samplers, temperature-pressure prescriptions and differing cross-section inputs. The success of these studies demonstrates the scope for application of these tools to both the extensive archival data and future planned observations of brown dwarfs and directly imaged giant exoplanets.

There are, of course, limitations and imperfections in our retrieval analysis as

we make assumptions such as isoprofile (constant) mixing ratios, something not expected to be the case in real atmospheres. However, adding additional capabilities to existing retrieval frameworks, such as non-isoprofile mixing ratios, will certainly be probed in future work using both archival and future observation of directly-imaged exoplanets and brown dwarfs. In fact, the current quality and quantity of brown dwarf observations offer a perfect testbed for new modelling parameterisations.

Retrieval analysis is also quite computationally intensive, often requiring computing clusters to run within a reasonable time frame when compared to simply iterating over a grid of forward models. This could become increasingly problematic when significantly higher resolution and increased spectral coverage observations from JWST allow for further parameters to be probed, increasing the overall parameter space and, hence, the computational expense. Recently, however, efforts have been made to use machine learning for the model selection, showing the possibilities for significant gains in computational efficiency (Zingales and Waldmann, 2018).

Based on our analysis of the GJ 570D spectrum, we found that different approaches when considering the Na+K line broadening can have a significant effect on the retrieved abundances. This seems to have knock-on effects with other retrieved parameters, such as radius and mass, seemingly in an attempt to preserve surface gravity for a larger object whilst driving up the metallicity.These parameters have been found to be degenerate in other studies such as Kitzmann et al. (2020). Some potential reasons for the issues caused by the Na and K cross sections are outlined below.

- The profiles of Allard et al. (2016) and Allard et al. (2019) are only considered valid up to a H_2 density of 10^{21} cm^{-3}. They therefore breakdown at pressures above 10-100 bar. Kitzmann et al. (2020) took the approach here of switching back to Voigt profiles at these high pressures. The difference in cross sections computed using these varying approaches is illustrated in Figure 3.3. It can be seen that the divergence between the computed cross sections used in this work and those of Kitzmann et al. (2020) are much higher at larger pressures for this reason. We would not

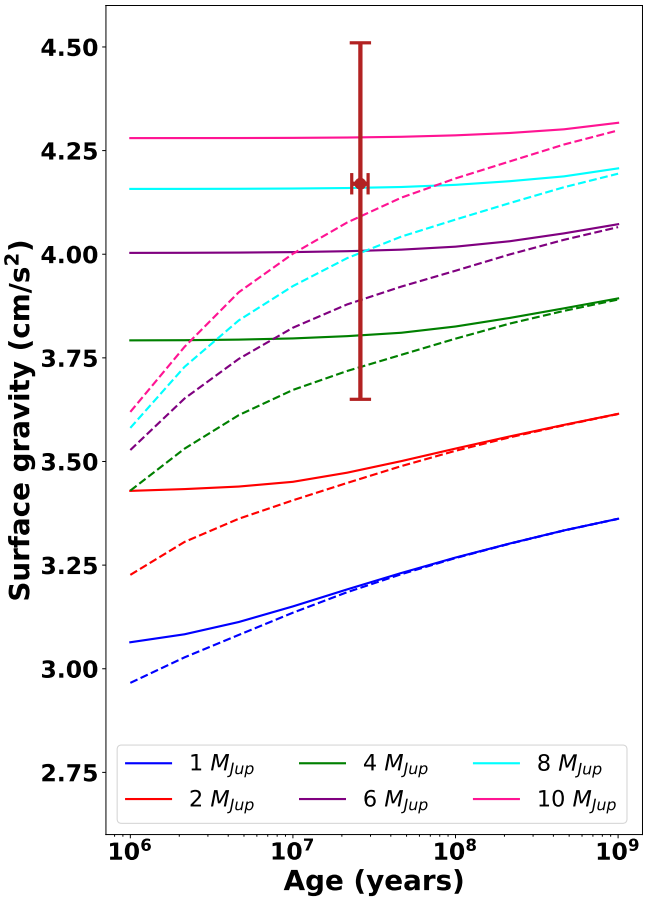

Figure 3.10: Planetary thermal evolution tracks for different planet masses from Fortney et al. (2008), updated from Marley et al. (2007). Dotted lines indicate hot start planets. Solid lines indicate cold start planets. Purple highlighted region indicates the age of 51 Eri b, as stated in Rajan et al. (2017). The error bar indicates the retrieved 2 sigma confidence boundary for surface gravity from the SPHERE Y, J, H and GPI $K1$, $K2$ data set with the age estimate from Rajan et al. (2017).

expect the deviations at such larger pressures to have such an impact, but it is worth looking into this more in the future.

- The line cores of Na and K, based on the data of Allard et al. (2016) and Allard et al. (2019), are computed considering Lorentzian broadening only, with the effects of Doppler broadening not taken into consideration. It is possible this has some effect and is worthy of further investigation.

- We considered the effects due to using both different sources and different line-wing cutoffs for the non-resonance lines of Na and K. We compared using lines from the NIST (Kramida et al., 2013) and the Kurucz (Kurucz and Bell, 1995) databases, and found Kurucz contains more lines for both Na and K. The effects of these various approaches for different pressures and temperatures can be seen in Figure 3.3. The larger number of non-resonance lines in the Kurucz database leads to a larger overall opacity when pressure-broadening is taken into account, with more pronounced effects at higher pressures. However, the use of the different sources for the non-resonance data was found to have negligible effect on the retrieval results.

- We tried using a completely different scheme for treating the line profiles of the Na and K resonance doublets; that of Burrows and Volobuyev (2003). The use of these cross sections did show some effects in terms of the retrieved parameters of Na+K abundance, radius, and mass. However, they still did not give physically plausible radius and mass values, which led us to proceed with the method of splitting the spectra into two regions, as outlined in Section 3.4.1

- We only use H_2-broadening and not He-broadening for the Na and K resonance doublets. As the contribution from H_2-broadening is much higher than from He, this is thought to be a good approximation. However, it would be worth looking into He-broadening in the future, as outlined in Peach et al. (2020) and Peach (2017).

- We did not implement an instrument profile within our analysis as used in Kitzmann et al. (2020). Such a profile can account for flux being spread across instrument pixels. TauREx3 does not account for such a spread when binning the higher resolution forward model to the resolution of

the observation. Such an instrument profile could explain why Helios-R (Kitzmann et al., 2020) was able to fit the heavily alkali influenced J band peak more successfully than TauREx3 and thus may have helped negate the bias issue we experienced in this study. This was also one of the few differences in our retrieval approach and that outlined in the (Kitzmann et al., 2020) study.

We could not identify the exact source of the issue causing unrealistic radius and mass values to be retrieved when the full wavelength coverage spectrum is used. However, it is apparent that the Na+K cross sections used in the retrievals can have a significant impact on the retrieved parameters.

We note there are currently three studies that have used the updated broadening coefficients from Allard et al. (2016) and Allard et al. (2019) in analysis of T dwarf spectra. One of these studies, Kitzmann et al. (2020), did not encounter this issue for GJ 570D. Oreshenko et al. (2020) negated these known issues when modeling the 0.85 - 1.2 μm region by neglecting this wavelength region in their analysis. Piette and Madhusudhan (2020) modulated their K cross sections with a multiplicative factor within their retrieval while only analysing data >1.1 μm. This topic warrants further investigation in the future, but we note that it may be less prevalent when studying data from JWST, which will benefit from having wider wavelength spectral coverage, down-weighting the problematic Na+K dominated region when carrying out retrieval analysis. Further studies of the broadening behaviour of Na and K lines in laboratory settings would likely prove invaluable.

More dynamical (model independent) constraints for directly imaged exoplanets and brown dwarfs will help reduce the volume of parameter space explored by the retrieval method. Such measurements have been carried out for Gl 229B (Brandt et al., 2019), ultracool binaries (Dupuy and Liu, 2017) and Beta Pic b (Snellen and Brown, 2018a, Dupuy et al., 2019a), with HST monitoring campaigns also underway for cool brown dwarfs (Dupuy, 2018, Dupuy et al., 2020a). This would significantly improve constraints on retrieval mass priors, and may also help constrain the radius values retrieved in various studies as surface gravity plays a key role in shaping the SED. Retrieval analyses have, quite often,

returned physically improbable radius values, both in the results presented here (which we attribute to the issues of the Na+K opacities) and in other studies (Kitzmann et al., 2020). Additionally, the temperature-pressure structure would also likely be better constrained, as radius and effective temperature are inversely correlated. During this study we have seen examples of pressure-temperature profiles changing as a result of varying radii whilst maintaining a similar surface gravity, demonstrating a significant and problematic degeneracy. Dynamical and model independent mass measurements for objects in the directly-imaged regime will help constrain the parameter space significantly. Better parallax measurements, such as from Gaia, help constrain the scaling factor (radius) further. For example, both our and the Kitzmann et al. (2020) study benefited from better distance constraints versus that of Line et al. (2015) and Burningham et al. (2017). The narrowing of parameter space for these model drivers may result in the ability to better probe other, more elusive, properties, and will also reduce the computational expense of retrieval analyses.

We retrieved very similar effective temperatures and abundances for both 51 Eri b and GJ 570D. This further supports the use of brown dwarfs as proxies for the harder-to-observe cohort of planetary mass companions. Another example of a close exoplanet analogue is PSO J318.5-22, a free-floating planetary mass brown dwarf with a spectrum which closely matches those of the atmospheres of the HR 8799 planets (Bonnefoy et al., 2016, Liu et al., 2013, Miles et al., 2018). These free floating objects are much easier to observe and can offer a window into their characteristic counterpart exoplanets, as we can make use of the superior quality of spectral data availability for these objects. Therefore, in the same way PSO 318 has long been documented to have overlapping properties with the same spectral type HR 8799 planets, 51 Eri b also has striking chemical similarities to the benchmark T dwarf GJ 570D and other late T dwarfs from the Line et al. (2015) and Line et al. (2017) studies.

The atmospheric similarities between the bona fide exoplanet 51 Eri b and late-T field brown dwarfs extends to mixing ratios, most notably that of ammonia. We acknowledge, though, that such a tentative detection, motivated by the GPI K band data, needs further observations to provide a higher confidence detection. This could be achieved using VLT-GRAVITY (Gravity Collaboration et al.,

2017), Subaru-REACH (Lozi et al., 2018, Kotani et al., 2018) or KECK-KPIC (Pezzato et al., 2019). These instruments deliver higher-resolution observations than that provided by SPHERE and GPI. This would allow us to detect more subtle features. The high-resolution data from REACH and KPIC would allow us to probe individual lines using both retrievals and cross-correlation methods (Hoeijmakers et al., 2018, Brogi and Line, 2019).

We only employed a single scaling S_{cal} factor for 51 Eri b when considering data take from a single instrument and two in the case of the SPHERE plus GPI combination. However, this may be an imperfect approach in the case of using only the GPI data as this spectrum is stitched together from different bands which can employ different data reduction pipelines and photometric calibrations. Such an approach of allowing each band to scale independently was a successfully strategy adopted in Nowak, M. et al. (2020) when combining observations of Beta Pic b. Crucially, such flexibly appears employable when using a high quality data set, as in the case of the GRAVITY Beta Pic b data used in the Nowak, M. et al. (2020), with this data appearing to anchor the model and deriving very small uncertainty for the GRAVITY data scaling factor. Our 51 Eri b data quality from GPI data is such that we didn't find this necessary, given the large uncertainties present in the data we analyse in this study. Future studies should be able to allow for scaling factors in each band when improved data becomes available for this exoplanet. The S_{cal} factor is directly correlated to the retrieved radii and can act to help the retrievals to maintain a physically sensible and higher radii instead of purely accounting for possible calibration imperfections, creating a degeneracy. This behaviour is likely exacerbated by the trend of retrievals deriving small radii (Burningham et al., 2021). Our experience of this factor with the data sets used in this study is that it commonly acted to scale down the model ($S_{cal}<1$) which can then be counterbalanced by a higher radius, especially given the priors we applied in the case of 51 Eri b. This is why we placed a Gaussian prior on this parameter when also employing one on the radius parameter, in an effort to restrict this degeneracy and the ability for the retrieval to simply use S_{cal} to retrieve our set radius prior. This will likely be a continued issue for retrievals going forward, where scaling factors designed for flux calibration and possible variability considerations could mask the documented inability of models to derive expected radii values, especially when using flat priors.

Unlike previous studies, we were able to fit the spectral profile of 51 Eri b without clouds, with the retrievals showing a Bayesian preference for this over our cloudy retrievals. This is an interesting and important result as previous studies all employed cloud models within grid modelling, often based on more rigidly parameterised temperature-pressure profile assumptions (e.g. radiative-convective equilibrium) and chemistry. We acknowledge and stress, however, that our ability to fit the data with a preference for a cloudless modelling may be due to our flexible temperature-pressure profile being able to mimic and account for the presence of an unmodelled cloud. Our result matches with that from Burningham et al. (2017) and Mollière et al. (2020), where synthetic data of cloudy L dwarfs was successfully fit due to the use of a flexible temperature-pressure profile. Mollière et al. (2020) also showed that when an incorrect cloud model was employed to fit synthetic cloudy data the retrieval determines a preference for a cloudless fit. The degenerate ability for a flexible temperature-pressure profile to account for clouds in the absence of any cloud modelling within a retrieval may be negated in the future by employing data across a wider wavelength range, when such data becomes available. Retrieval analysis including clouds will be explored in future work.

Our ability to fit the 51 Eri b data without clouds may have also been assisted by the free chemistry nature of the retrieval, where grid-model are often much more constrained based on coarse parameter sampling or solar abundance ratios. In the case of abundances, for example, exoplanets have been shown to possess a variety of chemical compositions, often deviating from norms seen in our own solar system. For example, exoplanets can possess C/O ratios much higher than that present in our solar system (Madhusudhan et al., 2012, Moses et al., 2013). This is further shown by the super-stellar C/O ratio we retrieved for 51 Eri b. This parameter allows us to hypothesise possible formation pathways. Due to 51 Eri b's large retrieved mass, measured orbital separation and retrieved C/O ratio, we suggest this may hint at formation via gravitational instability (Vigan et al., 2017). Further observations of 51 Eri b, using instruments such as GRAVITY, may help further constrain the C/O ratio via higher resolution K band data and permit a more in depth analysis of possible formation scenarios for this exoplanet.

Overall, we suggest the best approach is using a combination free-retrieval

and self-consistent modelling, as performed in this study, when characterisation self-luminous objects. Ideally, when improved data becomes available from instruments aboard JWST, GPI2 and SPHERE+, the results derived from this different approaches should converges to agreement.

3.7 Summary

We introduce TauREx3 which we have modified to be suitable for directly imaged objects, and apply it to the benchmark brown dwarf GJ 570D and the cool exoplanet 51 Eri b.

We discuss issues with the Na+K cross sections when applied to T dwarf spectra. The retrievals converged to a high mass and radius, likely due to biases introduced by the methods used to compute these cross sections. This issue was overcome by splitting the retrieval into two parts. Part 1 retrieved the mass, radius, distance and S_{cal} using the 1.2-2.5μm data, while part 2 retrieved the chemical profile of the atmosphere using the 0.85-2.5μm data. This allowed for more plausible results.

We compared our GJ 570 D results with other studies that performed retrieval analyses of this object (Kitzmann et al., 2020, Line et al., 2015, Burningham et al., 2017). The different analysis of GJ 570D, across various retrieval codes, shows an encouraging stability of most parameters, especially relating to the atmospheric chemistry as well as the temperature-pressure profile. We therefore successfully demonstrate TauREx3's suitability for brown dwarf emission analysis.

We also carried out free chemistry and cloudless retrieval analyses on all published spectroscopy observations of 51 Eri b, while comparing our results to previous studies that used grid modelling. The main results of our 51 Eri b retrieval analysis are:

- Our retrievals result in excellent fits to the observations without requiring cloud scattering, deriving a higher Log(Ev) when compared to retrievals

including power law clouds. This is in contrast to the cloudy atmosphere conclusions made in all previous studies (Macintosh et al., 2015, Samland et al., 2017, Rajan et al., 2017) who employed grid model fitting. However, this could be due to our flexible temperature-pressure profile being able to account for un-modelled clouds with this behaviour also being seen in Burningham et al. (2017) and Mollière et al. (2020).

- We confirm and constrain the presence of H_2O and CH_4.
- We find tentative evidence of NH3 in the atmosphere of 51 Eri b, to a $\sim$2.7 sigma confidence. Further observations are required to confirm this.
- We retrieve a super-solar C/O ratio, and a solar consistent [M/H] for 51 Eri b.
- Our surface gravity values are consistent with both classical hot-start and cold-start planetary thermal evolution models from Fortney et al. (2008).
- We demonstrate the importance of the K-band observations for constraining the effective temperature and temperature-pressure profile.
- Our highest Log(Ev) retrieve literature consistent radius values of $1.18^{+0.12}_{-0.12}\mathrm{R_{Jup}}$ and $1.09^{+0.11}_{-0.11}\mathrm{R_{Jup}}$ for our two data sets. This is despite not employing cloud modelling, something previous studies struggled to do.
- Our analysis highlights strong similarities between the retrieved molecular mixing ratios and temperature-pressure profiles of 51 Eri b and GJ 570D. The slight gradient differences in temperature-pressure profiles is attributed to possibly accounting for an un-modelled cloud structure in the case of 51 Eri b's retrieval by adopting a more isothermal gradient.
- Our retrieved *npoint* temperature-pressure profiles for 51 Eri b adopts a much more isothermal profile compared to the adiabatic profile employed in the unsuccessful `ATMO` 2020 grid model fit. This more isothermal profile, again, could account for the impact of an unmodelled photospheric cloud structure, or alternatively could be indicative of diabatic convection triggered by the CO/CH_4 chemical transition (Tremblin et al., 2016, 2019) in the atmosphere of 51 Eri b.

- Our retrieved super-stellar C/O ratio, coupled with our retrieved mass and previously measured orbital separation, hints at a possible formation pathway of gravitational instability for 51 Eri b. However, this conclusion is tentative and higher quality data is required for a more thorough analysis of the possible formation history of 51 Eri b.

CHAPTER 4

Retrieval study of low surface gravity L dwarfs

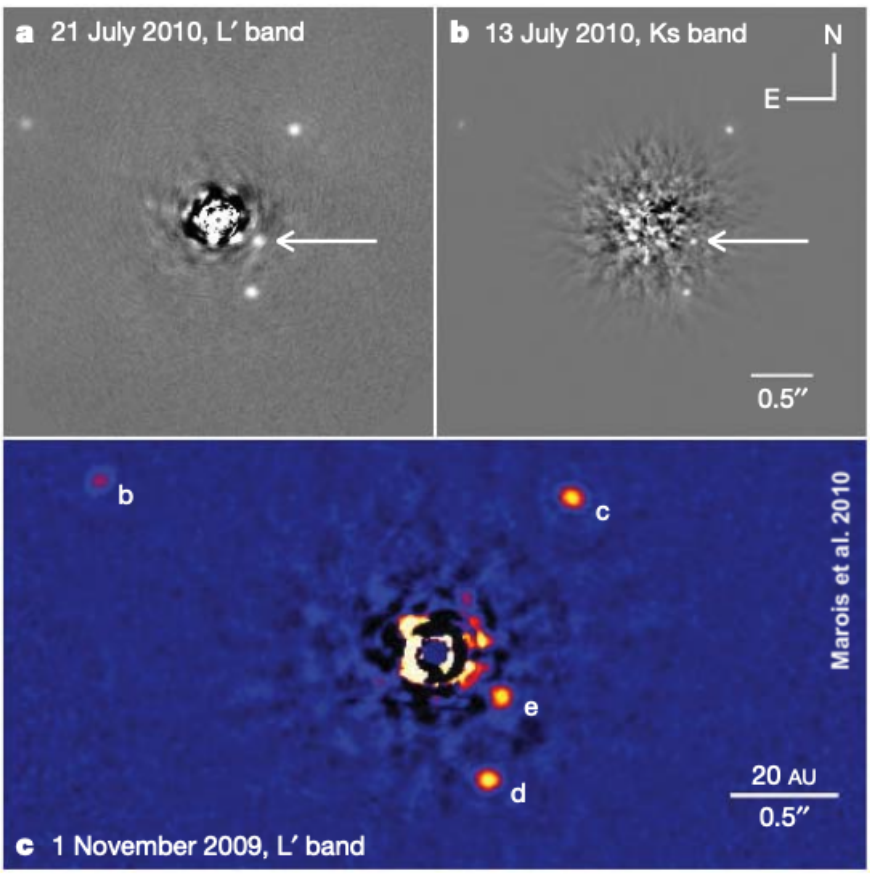

4.1 Introduction

Characterising gas giant planet and brown dwarf atmospheres requires a complex and delicate combination of chemistry and physics to explain the observational data. These are all webbed together in the form of radiative transfer, convection, clouds, opacities and the many other physical processes that dictate their atmospheric emission spectrum. Modelling clouds remains amongst the most significant challenges for modelling atmospheres, both in and beyond our solar system. However, correctly modelling clouds is vital for understanding the evolution and properties of giant exoplanets as well as brown dwarfs (Marley and Robinson, 2015, Gao et al., 2021, Morley et al., 2012, 2014, Lew et al., 2020, Helling, 2019, Marley et al., 2013, Gao et al., 2020, Helling, 2020). Low surface gravity L dwarfs, which are the focus of this study, sit in the ∼1100 to 2200 K temperature range with masses $<30 M_{Jup}$. These objects regularly display evidence of cloud coverage in the form of muted absorption features (flattened spectra) caused by the presence of cloud scattering (Gao et al., 2021). The presence of clouds is also supported by the photometric and spectroscopic variability commonly seen in the objects (Bowler et al., 2020, Zhou et al., 2020, Biller et al., 2021, Apai et al., 2013, 2021, Biller et al., 2018, Vos et al., 2019, 2020), thought to be the result of evolving patchy cloud coverage.

Retrieval models that take into account the optical properties of clouds are now commonly used to fit exoplanet transmission spectra (Tsiaras et al., 2018, MacDonald and Madhusudhan, 2017, Barstow and Heng, 2020, Fisher and Heng, 2018). However, the application of cloudy frameworks within retrievals applied to emission spectra of directly imaged exoplanets is still a largely unexplored and novel territory. There have been extensive retrieval studies of Y and T dwarfs (Line et al., 2015, 2014, 2017, Zalesky et al., 2019) which did not require clouds. Burningham et al. (2017) and Burningham et al. (2021) have used retrievals to probe the atmospheres of cloudy L dwarfs. The former used a cloud modelling approach such as the power law slab and deck, where the cloud opacity is set via a simple power law relative to the wavelength, to model the mid-L and high mass brown dwarfs 2MASS J05002100+0330501 and 2MASSW J2224438−015852. The

latter then explored a much more in depth and complex multi-cloud layered analysis of 2MASSW J2224438-015852. This is the most statically robust cloud investigation into a brown dwarf to date, demonstrating the power of high quality data across the near and mid infrared. Gonzales et al. (2020) applied a power law slab and deck cloud framework to both SDSS J1416+1348AB L+T and high mass binary components. The cloudy HR 8799 planets have also been the focus of several retrieval studies using clouds (Lavie et al., 2017, Mollière et al., 2020, Lee et al., 2013, Wang et al., 2020). These studies collectively show the applicability of retrieval analysis to directly imaged exoplanets and brown dwarfs of different spectral types and the ability to probe their cloud properties using various cloud parameterisation approaches.

Cloudless explanations for the observed spectra have been explored in Tremblin et al. (2016, 2017, 2015), who demonstrated that a reduced atmospheric temperature gradient can reproduce the spectra of late L and T type brown dwarfs, without the need to invoke clouds. This is done via modelling carbon chemistry moving from CO to CH_4 dominance through the transition from L to the T dwarf, triggering a diabatic convection which reduces the temperature gradient (Tremblin et al., 2019). However, Burningham et al. (2021) shows the ability to detect specific species and compositions of clouds when high quality data are available in the case of L dwarf 2MASSW J2224438-015852, detecting layers of enstatite and quartz clouds. The cloud vs cloudless debate will likely be settled when high quality data become available from James Webb Space Telecope (JWST), with the possibility of both theories playing important roles.

Our work is motivated by two factors. First, we wish to test TauREx3's Al-Refaie et al. (2019) applicability to L dwarf spectra using observations from multiple cloudy exoplanets and low mass brown dwarfs. Our sample of targets allows us to both benchmark our results against previous studies while also applying a retrieval framework to several new objects. Second, the launch of JWST Gardner et al. (2006) will define a new era of infrared astronomy, fueling new discovers much like Hubble has for the previous decades. Such data quality will require well tested and calibrated modelling approaches. Several of the objects we have included in our sample will have either JWST Early Release Science (ERS) and Guaranteed Time Observations (GTO) data, so we aim to test our approach using

already existing ground-based data for these objects. In the following section we give brief summaries of the current knowledge of each object in our sample and highlight which data we used. We then outline the retrieval approach setup in the following section before moving on to outlining the results and an overall discussion of our findings.

4.2 Targets and data

In this section we outline the objects we include within our retrieval analysis and also outline the data we use for each. Our sample encompasses PSO 318, VHS 1256b, HR 8799cde and Beta Pic b. This sample includes mid-late L dwarfs with low surface gravities and estimated masses <30 MJup (and down to planetary masses in several cases). These objects together provide a good test bed for our cloud retrieval analysis, offering different data qualities to exploit and test. Some, having been included in previous retrieval studies offer the ability to benchmark TauREx3 against these codes. The properties of the objects included in our sample are discussed in the following subsections and outlined in Table 4.3. An overview of the data used for each object is given in Figure 4.2 along with the relevant references.

4.2.1 | PSO 318

PSO 318 is a free floating, 8.3±0.5 MJup (Allers et al., 2016) late-L dwarf with low surface gravity (Liu et al., 2013). This object is also one of the reddest L dwarfs known (see Figure 4.1). It has an age 20-25 MYr (based on membership of the Beta Pic moving group)Allers et al. (2016). L band spectroscopy has indicated the presence of Methane (Miles et al., 2018). This object has been extensively studied in regards to variability (Biller et al., 2018, Vos et al., 2019, Biller et al., 2015) which has suggested variations as high as 7-10 % in the J band. Such variability is a strong indication of clouds and hints at the possibility of an evolving patchy cloud structure in the photosphere. PSO 318 is a spectral and

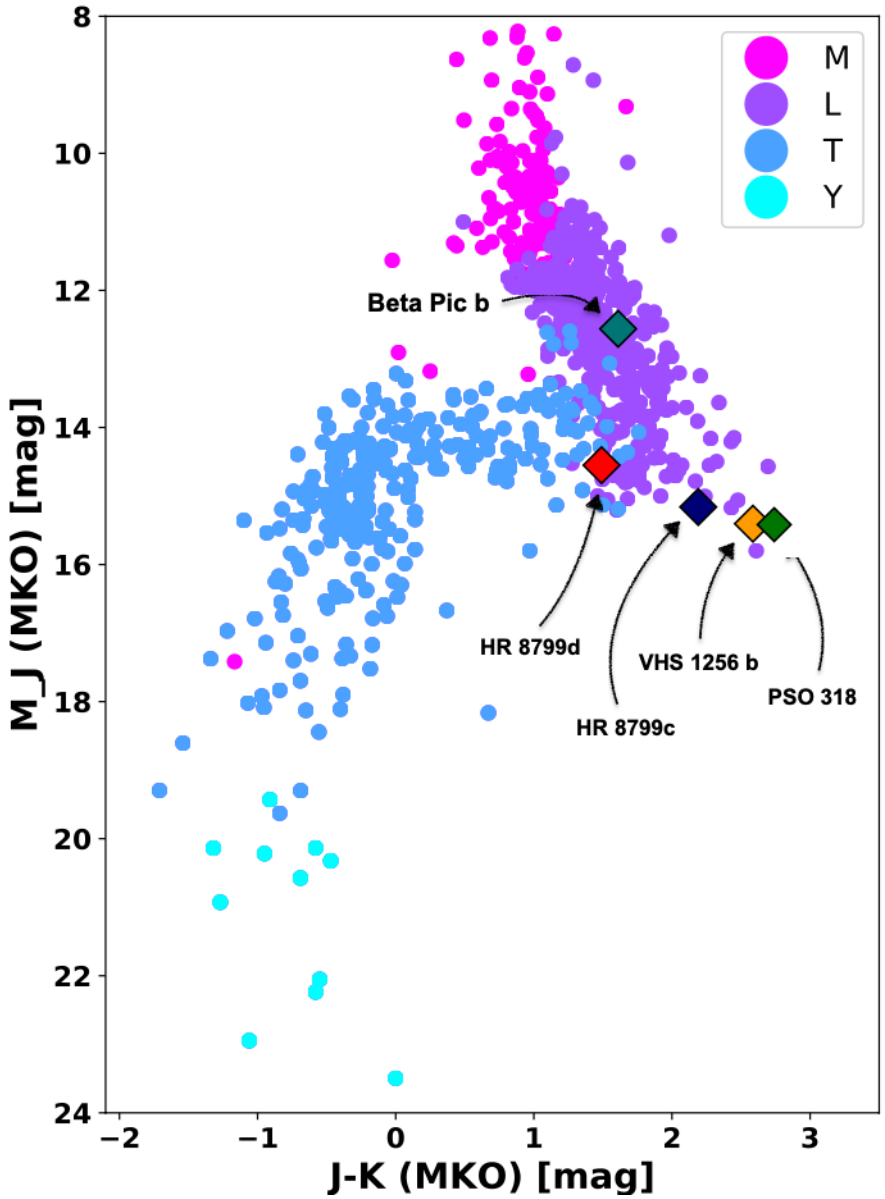

Figure 4.1: Color magnitude diagram of field dwarfs spanning M, L, T and Y dwarfs. PSO 318, VHS 1256b, Beta Pic b and HR 8799cde are indicated. Data used to compile this figure are from Best et al. (2020a) catalogue which is a compilation of Dupuy and Liu (2012), Dupuy and Kraus (2013), Liu et al. (2016), Best et al. (2018) and Best et al. (2020b). The figure highlights the red nature of the mid-late L dwarfs.

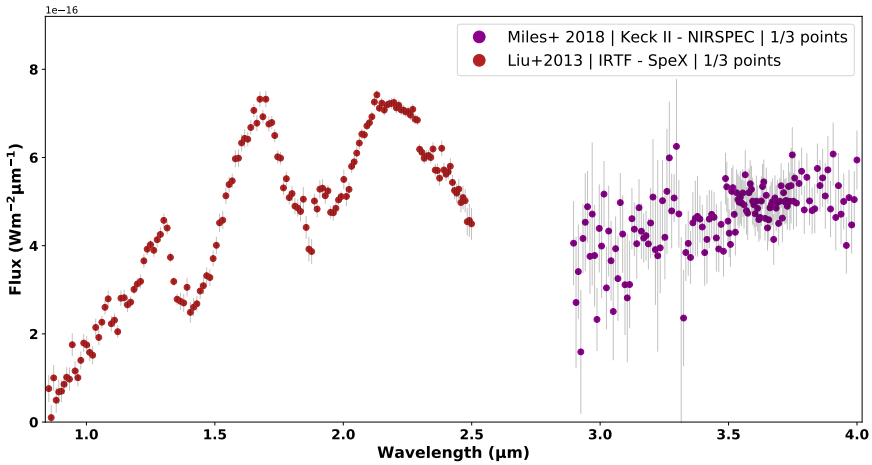

(a) PSO 318

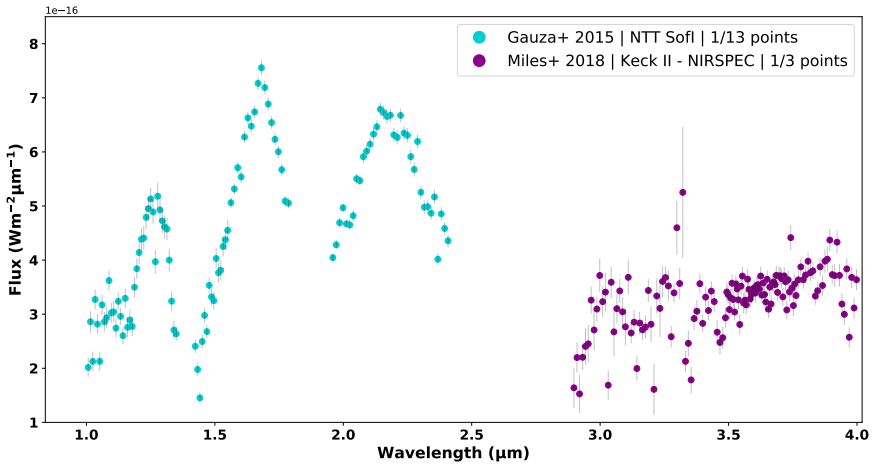

(b) VHS 1256 b

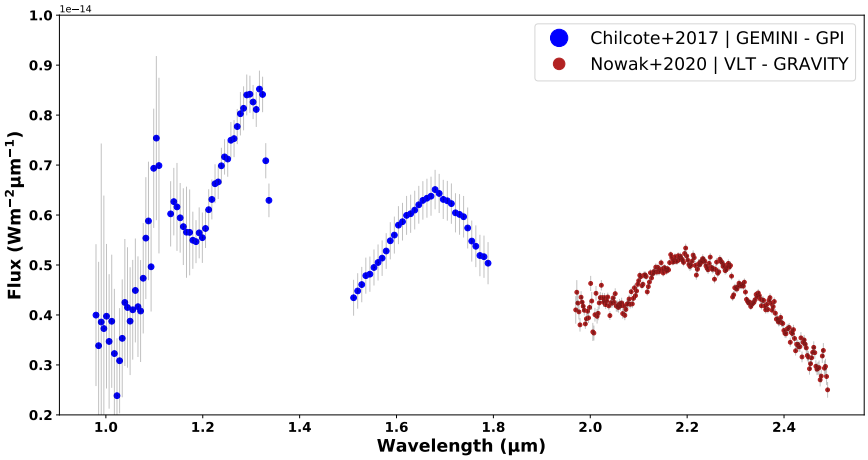

(c) Beta Pic b

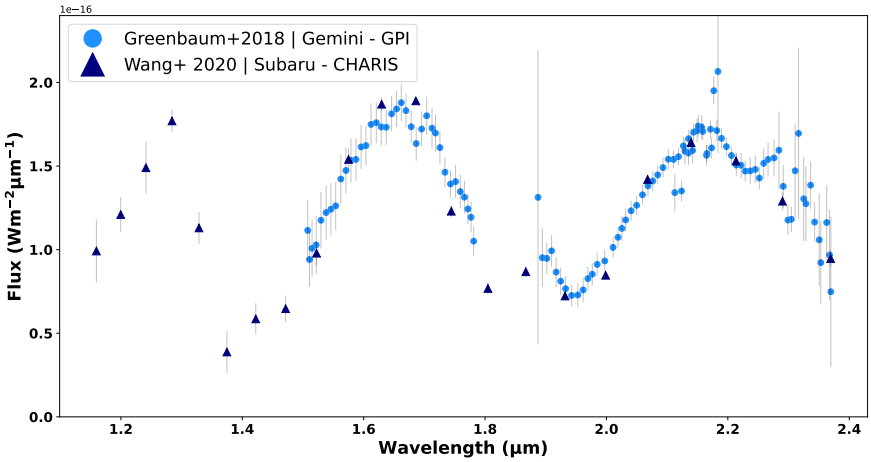

(d) HR 8799c

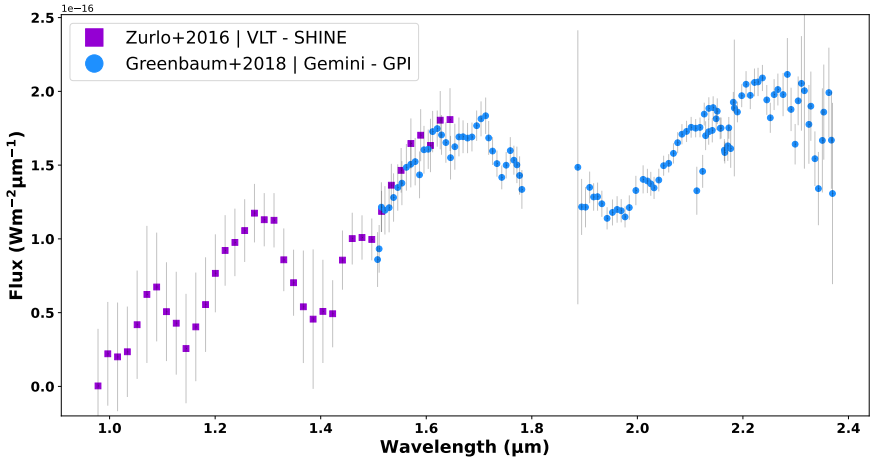

(e) HR 8799d

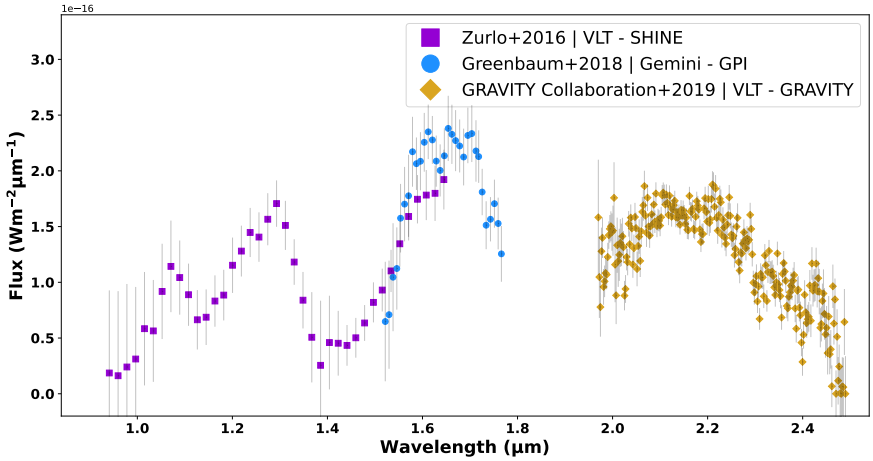

(f) HR 8799e

Figure 4.2: (a) PSO 318 data from Liu et al. (2013) and Miles et al. (2018). (b) VHS 1256 b data from Gauza et al. (2015) and Miles et al. (2018). (c) HR 8799 c data from Greenbaum et al. (2018), (Wang et al., 2020) and (Konopacky et al., 2013). (d) HR 8799 d data from Zurlo et al. (2016) and Greenbaum et al. (2018) (e) HR 8799 e data from Zurlo et al. (2016), Greenbaum et al. (2018) and Gravity Collaboration et al. (2019). (f) Beta Pic b data from Greenbaum et al. (2018) and Nowak, M. et al. (2020).

characteristic analogue to many young, directly imaged exoplanets, particularly those in the HR 8799 system Bonnefoy et al. (2016). This makes it an ideal laboratory to test models given the high quality data we have available for this object.

For our analysis of PSO 318 we employ SpeX spectrograph (Rayner et al., 2003) J, H, and K spectroscopy (Liu et al., 2013) combined with NIRSPEC (McLean et al., 1998) L band spectroscopy (Miles et al., 2018). For the SpeX data and as outlined in Line et al. (2015), neighbouring pixels may not be statistically independent, due to the duplication of flux information. Therefore, when employing this data set we only use every third data point (pixel) for our model fitting. We then de-resolved the NIRSPEC data down to the approximate resolution of the SpeX data in ensure similar spectral resolution of data in each band. The data used is shown in Figure 4.2a

4.2.2 | VHS 1256b

VHS 1256b is a low surface gravity 19±5 MJup (Dupuy et al., 2020b) , very red, late-L dwarf companion of the M dwarf binary VHS1256-1257AB with a wide 8" separation (Gauza et al., 2015, Stone et al., 2016).Dupuy et al. (2020b) places this object at a separation of $22.2^{+1.1}_{-1.2}$ pc. With favourable angular separation for observing and characteristics similar to many young directly imaged exoplanets, such as the HR8799 planets Bonnefoy et al. (2016), VHS 1256b is another ideal laboratory to test and calibrate models models for objects with lower signal-to-noise observations. Spectroscopy of this object has shown weaker alkali features and a h band shape consistent with a low surface gravity object with a young age (Gauza et al., 2015). Rich et al. (2016) showed evidence of thick cloud coverage on this object via model fitting of photometry across 0.8-5μm. VHS 1256b is the most variable of the low surface gravity cohort, with variability amplitudes of >25% over an 8-hour long HST observation (Bowler et al., 2020, Zhou et al., 2020), making it one of the most variable substellar objects ever observed. and thus a prime candidate for the presence of evolving patchy clouds. L band spectroscopy, as with PSO 318, has indicated the presence of Methane (Miles et al., 2018).

For our analysis of VHS 1256 b we employ SofI J, H, and K spectroscopy combined with NIRSPEC L band spectroscopy (Miles et al., 2018). Both the SofI and NIRSPEC data were de-resolved to the approximate resolution of the SpeX data used for PSO 318. The data used is shown in Figure 4.2b

4.2.3 | HR 8799cde

Consisting of four (currently known) planets (Marois et al., 2008, 2010, Currie et al., 2011), HR 8799 system is one of the most intensively studied systems in exoplanet science (Lavie et al., 2017, Zurlo et al., 2016, Bonnefoy et al., 2016, Gravity Collaboration et al., 2019, Konopacky et al., 2013, Wang et al., 2021, Mollière et al., 2020, Lee et al., 2013, Wang et al., 2020, Marley et al., 2012, Greenbaum et al., 2018, Skemer et al., 2012, Oppenheimer et al., 2013, Skemer et al., 2014, Ingraham et al., 2014, Barman et al., 2015, Rajan et al., 2015, Wang et al., 2018, Petit dit de la Roche et al., 2020). It remains the only system with more than two confirmed exoplanets that have been directly imaged. The system is located at a distance of 41.29 $\pm$ 0.15pc (Gaia Collaboration et al., 2018) with an estimated age of $\sim$30 Myr (derived via on possible membership of Columba). The planets orbit within 15 and 72 au from the host start (Wang et al., 2018). Model fitting has suggested that the HR8799 planets may process patchy cloud coverage (Marois et al., 2008, Marley et al., 2010) as well as non equilibrium chemistry (Mollière et al., 2020, Skemer et al., 2012). This system, given its spectral similarities with VHS 1256 b and PSO 318, has also been the target of a variability monitoring campaign (Biller et al., 2021). As a multi-planet system, it offers a unique test bed for probing formation relations to mass, separation and migration. HR 8799cde have spectral types of $\sim$L6-L8 (Zurlo et al., 2016) however they possess the same red colour as VHS 1256 b and PSO 318 (see Figure 4.1). The HR 8799 planets have been the focus of several previous retrieval studies: Lavie et al. (2017) carried out retrieval analysis of all four planets using HELIOS; Wang et al. (2020) focused on on HR 8799c using petitRADTRANS while Mollière et al. (2020) also used petitRADTRANS for analysis of HR 8799e.

For HR 8799d we employ YH band data from the VLT-SPHERE (Beuzit et al., 2008, 2019) Integral Field Spectrograph (IFS) (Zurlo et al., 2016) combined with

H, $K1$ and $K2$ data from GEMINI-GPI's (Macintosh et al., 2014, Greenbaum et al., 2018) IFS (Greenbaum et al., 2018).

For HR 8799c we employ J, H and K band data from the Subaru-CHARIS IFS (Wang et al., 2020) combined with H, $K1$ and $K2$ data from GEMINI-GPI's (Macintosh et al., 2014, Greenbaum et al., 2018) IFS (Greenbaum et al., 2018).

For HR 8799e we combined YH data from SPHERE with GPI H band data along with VLT-GRAVITY (Gravity Collaboration et al., 2017) K band spectroscopy (Gravity Collaboration et al., 2019). The data used for these objects is shown in Figure 4.2d, 2d and 2e.

4.2.4 | Beta Pic b

Beta Pic b was one of the original exoplanets to be directly-imaged (Lagrange et al., 2010) and has an early to mid L dwarf spectral type (see Figure 4.1).The Beta Pic system has an age of 24±3 Myrs (Bell et al., 2015). Beta Pic b resides at a distance of 19.44± 0.05 pc from its host. (Gray et al., 2006). It is housed within an edge-on circumstellar disk (Smith and Terrile, 1984) in which it has a non-circular orbit (Nowak, M. et al., 2020). The combination of this disk, along with well documented age constraints and mass measurements (Brandt et al., 2021b), make this object an ideal laboratory system for probing formation pathways and evolution. The photometric colors and luminosity of this exoplanet overlap with those of early-type brown dwarfs (see Figure 4.1) but its mass estimate of $9.3^{+2.6}_{-2.5}$ Mjup (Brandt et al., 2021b) places it in the planetary mass regime. Beta Pic b has also been the focus of previous retrieval studies. Nowak, M. et al. (2020), using petitRADTRANS, have inferred an approximately stellar C/O ratio of Beta Pic b's atmosphere. Beta Pic b's high mass, when combined with this inferred C/O ratio, may suggest a core accretion pathway accompanied by significant planetesimal enrichment (Nowak, M. et al., 2020, Öberg et al., 2011, Öberg and Bergin, 2021). A second exoplanet, Beta Pic c, has now also been discovered in this system (Gravity Collaboration et al., 2020, Lagrange et al., 2019).

Within this study we make use of the Y, J and H band spectroscopy from GEMINI-GPI's IFS (Macintosh et al., 2014, Chilcote et al., 2017) and the VLT-

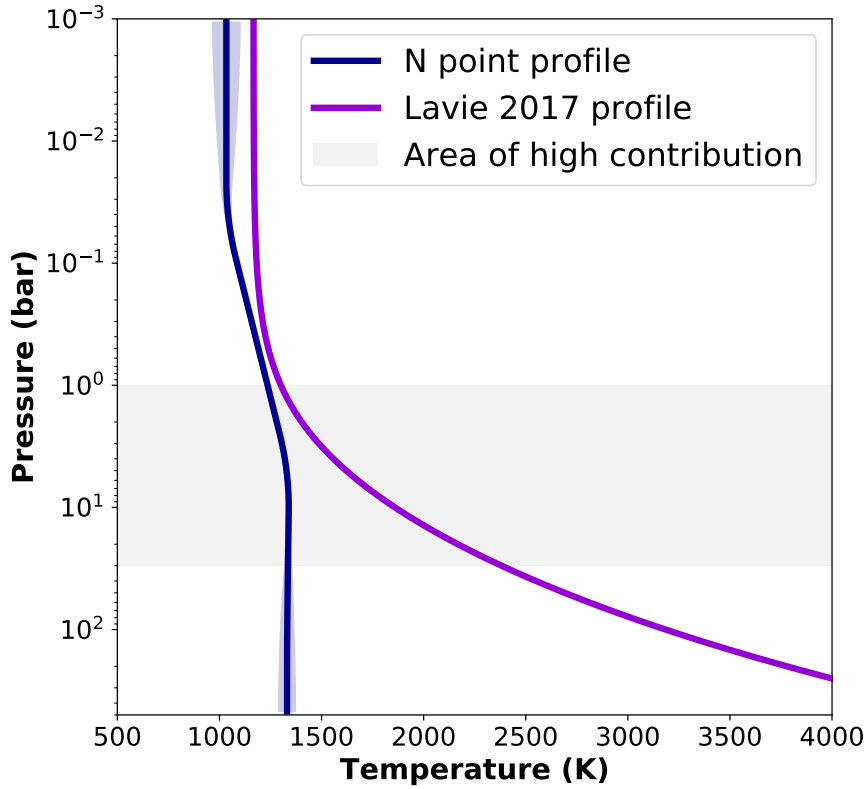

Figure 4.3: Comparison of flexible npoint (Waldmann et al., 2015a) vs relatively inflexible Lavie et al. (2017) temperature-pressure profile when employed in retrieval of cloudy L dwarf spectra. PSO 318 was used for this example.

GRAVITY (Gravity Collaboration et al., 2017) K band spectroscopy (Nowak, M. et al., 2020). The data used is shown in Figure 4.2c.

4.3 TauREx3 setup

4.3.0.1 | Retrieval setup

Previous retrieval studies have shown the ability of a flexible temperature-pressure profile to account for or mimic the presence of clouds by adopting an isothermal gradient (Mollière et al., 2020, Burningham et al., 2017). We also tested TauREx3's flexible npoint profile using L dwarf data and this was

again the case as shown in Figure 4.3. For this reason, within our retrievals we employed a relatively inflexible temperature-pressure profile which determined the temperature in each model layer via the same parameterisation outlined in Lavie et al. (2017) which acts to enforce a radiative equilibrium gradient.

The molecular trace-gas mixing ratio profiles (as a function of pressure), in the forward model are set as isoprofiles (constant with pressure). The atmospheric forward model is described in Waldmann et al. (2015a) and Al-Refaie et al. (2019). We consider a model atmosphere with pressures ranging from 10^{-3} to 500 bar, with 100 layers uniformly sampled in log-space. We assume a hydrogen dominated atmosphere with a H_2 and He mixing ratio He/H_2 = 0.17567. In our study we include the line lists for H_2O (Polyansky et al., 2018), CO (Li et al., 2015), CO_2 (Yurchenko et al., 2020) and CH_4 (Yurchenko et al., 2017) as these are the dominant absorbers in the near-IR. Collision induced absorption (CIA) of H_2–H_2 and H_2–He (Abel et al., 2011, Fletcher et al., 2018, Abel et al., 2012) is also included.

We employ the Lee Mie and BH mie cloud opacity parameterisations within our retrievals (see Chapter 2). Given the expectation of silicate clouds being the dominant source of cloud opacity for the objects considered in this work, we set $\mathcal{Q}_0$=10 when employing the Lee Mie cloud parameterisation as this is representative of "astro silcate" Lee et al. (2013). For the BH mie cloud opacity we test both the lognormal and "cloud" particle size distributions (see Chapter 2), as well as modelling a variety of condensate species.

In this work we employ linear scaling factors for different bands of data when there are spectroscopic gaps between data, similar to the approach employed in Mollière et al. (2020), Gravity Collaboration et al. (2020) and Burningham et al. (2021).

4.3.0.2 | Priors

The priors and prior bounds set for the retrieval analysis performed in this work were either uniform, log-uniform or Gaussian priors based on values from previous published studies (when such values were available). See Table 4.1 for a full

overview of the priors set.

We adopted a Gaussian prior of 1.2±0.1R_{Jup} for the objects in our sample apart from PSO 318, where we use 1.4±0.1R_{Jup} based on the assumption of a more inflated object (Miles et al., 2018, Allers et al., 2016). For mass we set a planetary mass flat prior of 1-13M_{Jup} for PSO 318 and HR 8799c and d. For VHS 1256 b we set a low surface gravity assumption via a flat 1-25M_{Jup} prior. For HR 8799e and Beta Pic b we set Gaussian priors based on measured dynamical masses of 9.6±1.9 M_{Jup} (Brandt et al., 2021b) and 9.6±2.6 M_{Jup} (Brandt et al., 2021a) respectively.

4.3.1 | TEA - Thermochemical equilibrium abundances

In order to compare the retrieved abundances in the free chemistry mode of TauREx3 to those predicted by equilibrium chemistry, we employ the open-source[1] Thermochemical Equilibrium Abundances (TEA) code. The code ingests the retrieved temperature-pressure profile and derives the abundances that satisfy the thermochemical equilibrium requirement. This allows us to determine if the retrieved abundance significantly deviates from those derived by TEA, enabling inference of chemical equilibrium vs disequilibrium. This can be done by comparing the molecules with the best constraints on their abundances. As this study focuses on cool T dwarfs, we expect that the three best constrained molecules should be H_2O, CO, CO $_2$ and CH_4.

4.4 Exo-REM setup

In addition to our free retrieval with TauREx3, described in section 4.3, we performed further analysis by comparing a grid of self-consistent model emission spectra with the data. This grid was obtained using the self-consistent 1D radiative-equilibrium model Exo-REM[2] (Charnay et al., 2018, Baudino et al.,

[1]TEA: `https://github.com/dzesmin/TEA`
[2]Exo-REM 2.2.0: `https://gitlab.obspm.fr/dblain/exorem`

Table 4.1: Priors used for retrieval analysis.

Retrieved parameter	Distribution Type	PSO 318	VHS 1256b	HR 8799c	HR 8799d	HR 8799e	Beta Pic b
log(*Active Species*)	Log-Uniform	1e-12 - 1e-1	1e-12 - 1e-1	1e-12 - 1e-1	1e-12 - 1e-1	1e-12 - 1e-1	1e-12 - 1e-1
Radius R	Gaussian	1.4 ± 0.1 R_{Jup}	1.2 ± 0.1 R_{Jup}	1.2 ± 0.1 R_{Jup}	1.2 ± 0.1 R_{Jup}	1.2 ± 0.1 R_{Jup}	1.2 ± 0.1 R_{Jup}
Mass M	Uniform	1-13 M_{Jup}	1-25 M_{Jup}	1-13 M_{Jup}	1-13 M_{Jup}	9.6 ± 1.9 M_{Jup}	9.6 ± 2.6 M_{Jup}
D_{planet}	Gaussian	22.2 ± 0.8	22.2 ± 1.2	41.29 ± 0.15	41.29 ± 0.15	41.29 ± 0.15	19.3 ± 0.2
S_{cal} factors	0.8-1.2	0.8-1.2	0.8-1.2	0.8-1.2	0.8-1.2	0.8-1.2	0.8-1.2
T_{int}	Uniform	10, 2000	10, 2000	10, 2000	10, 2000	10, 2000	10, 2500
K_O	Log-Uniform	1e-15 - 1	1e-15 - 1	1e-15 - 1	1e-15 - 1	1e-15 - 1	1e-15 - 1
r_{Lee}	Log-Uniform	0.1 - 1000 μm	0.1 - 1000 μm	0.1 - 1000 μm	0.1 - 1000 μm	0.1 - 1000 μm	0.1 - 1000 μm
χ	Log-Uniform	1e-20 - 1e-4	1e-20 - 1e-4	1e-20 - 1e-4	1e-20 - 1e-4	1e-20 - 1e-4	1e-20 - 1e-4
P_{top}	Log-Uniform	1e-3 - 5e2 bar	1e-3 - 5e2 bar	1e-3 - 5e2 bar	1e-3 - 5e2 bar	1e-3 - 5e2 bar	1e-3 - 5e2 bar
P_{top}	Log-Uniform	1e-3 - 5e2 bar	1e-3 - 5e2 bar	1e-3 - 5e2 bar	1e-3 - 5e2 bar	1e-3 - 5e2 bar	1e-3 - 5e2 bar
r_c	Log-Uniform	0.1 - 1000 μm	0.1 - 1000 μm	0.1 - 1000 μm	0.1 - 1000 μm	0.1 - 1000 μm	0.1 - 1000 μm
χ_c	Log-Uniform	1e-20 - 1e-4	1e-20 - 1e-4	1e-20 - 1e-4	1e-20 - 1e-4	1e-20 - 1e-4	1e-20 - 1e-4
P_{top}	Log-Uniform	1e-3 - 5e2 bar	1e-3 - 5e2 bar	1e-3 - 5e2 bar	1e-3 - 5e2 bar	1e-3 - 5e2 bar	1e-3 - 5e2 bar
P_{top}	Log-Uniform	1e-3 - 5e2 bar	1e-3 - 5e2 bar	1e-3 - 5e2 bar	1e-3 - 5e2 bar	1e-3 - 5e2 bar	1e-3 - 5e2 bar
σ	Uniform	1.01 - 3	1.01 - 3	1.01 - 3	1.01 - 3	1.01 - 3	1.01 - 3
C_{frac}, cloud fraction	Uniform	0-1	0-1	0-1	0-1	0-1	0-1

2015, Baudino et al., 2017, Blain, D. et al., 2021). Our Exo-REM models assume no external light source, and solar elemental abundances (Lodders, 2019). Species abundances are determined using non-equilibrium chemistry (see Blain, D. et al., 2021, for details about the Exo-REM implementation).

The atmosphere is modelled using the plane-parallel approximation and 81 levels uniformly spaced in log-space between 10^2 and 10^{-6} bar. The modelled emission spectra are calculated from 40 to 30 000 cm^{-1} (0.3 to 250 μm) with a step of 20 cm^{-1} and includes the gas opacities of CH_4, CO, CO_2, FeH, H_2O, H_2S, HCN, K, Na, NH_3, PH_3, Ti and VO, collision-induced absorption of H_2–H_2, H_2–He and H_2O–H_2O, as well as Rayleigh scattering from CH_4, CO, CO_2, H_2, H_2O, N_2, NH_3, He and the other noble gases.

We included absorption and scattering by clouds – calculated from the extinction coefficient, single scattering albedo, and asymmetry factor interpolated from pre-computed tables for a set of wavelengths and particle radii (Charnay et al., 2018). For simplicity, only the radiative and opacity contributions of Mg_2SiO_4 and Fe clouds – assuming $C_{\rm frac} = 1$ – were included, although most temperature profiles obtained cross the condensation curve of other species. The vertical distribution of the cloud masses are modelled following the approach of Ackerman and Marley (2001), which assumes an equilibrium between the cloud condensation and sedimentation, determined by the vertical eddy diffusion coefficient K_{zz} and the free parameter $f_{\rm sed}$. In all our Exo-REM models, we assumed $f_{\rm sed} = 1$, while K_{zz} was self-consistently determined using mixing length theory.

For our Exo-REM models, the metallicity M/H is obtained by keeping the H, He, and other noble gases elemental abundances fixed at their solar value, while multiplying all the other elemental abundances, except C, by M/H. The different C/O ratios are obtained by changing the elemental abundance of C.

Our grid is constructed by changing the gravity at 1 bar, the effective temperature $T_{\rm eff}$ (since the effect of external light sources are negligible, $T_{\rm eff}$ is equal to the intrinsic temperature), the M/H and the C/O ratio. The parameters for our grid of models, their ranges and the step used are displayed in Table 4.2. The C/O ratio grid points were 0.3, 0.55 (i.e. $\approx$ the solar C/O), and 0.75. We used the exact same model grid for all targets.

Table 4.2: Exo-REM atmospheric model grid fitted on the targets

Parameter	Range	Step
$\log_{10}(g)$ (cm/s^2)	3.5–4.5	0.5
$T_{\rm eff}$ (K)	1050–1400	50
[M/H] ($\times$ solar)	-0.5–1	0.5
C/O	0.3–0.75	*see text*

Once the grid is generated, we re-bin the modelled spectra to the wavelengths of the observed spectrum. We then find the distance between the planet and the observer that minimises the reduced χ^2 between each re-binned modelled spectrum and the observed spectrum. Finally, we compare the models using these minimised reduced χ^2 values. Our results are presented in Table 4.3.

4.5 TauREx3 results

In the following subsections we summarise our retrieval results for each of the objects considered. A summary of the bulk parameters retrieved or inferred is shown in Table 4.3 which also includes and extensive collection of values derived from previous studies of these objects. A statistical comparison of the various cloud parameterisations and species tested is shown in Table 4.4. The posteriors (corner plots) shown are those from the retrievals which determined the highest log(Ev) value.

4.5.1 | PSO318

Our best fit model spectrum for PSO 318 is shown in Figure 4.4. The best fit model spectrum replicates the SpeX data well, but fails to fit the L band NIRSpec data. The poor fit to the NIRSpec data is likely due to the low S/N ratio of these data compared to the higher S/N ratio of the SpeX data. This issue persists despite allowing for error inflation in the SpeX data with possesses the higher

signal-to-noise ratio (SNR).

Our retrieval constrains well the presence of H_2O and CO but is unable to constrain the presence of CH_4 and CO_2 (see Figure 7.4). Despite the methane non-detection here, Miles et al. (2018) present evidence for the presence of CH_4 from fits to the L band NIRSpec data. However, our retrievals are likely unable to detect this due to the SpeX data driving the fit for PSO 318 while Miles et al. (2018) fit the L band NIRSPEC data separately. We derive a C/O ratio of $0.44^{+0.05}_{-0.06}$ but as PSO 318 is a free floating object a comparison with a host is not possible. We derive a metallicity [M/H] of $0.2^{+0.8}_{-0.8}$ making it largely unconstrained.

Our retrieved radius of $1.25^{+0.01}_{-0.01}\mathrm{R_{Jup}}$ is well constrained but we note this parameter was informed by a Gaussian prior (see Table 4.1), possibly introducing significant bias. This radius is slightly lower than the $\sim$1.4$\mathrm{R_{Jup}}$ radius derived in the Allers et al. (2016) study but is close to the Miles et al. (2018) best fit of 1.3$\mathrm{R_{Jup}}$, using the same data as used in the Miles et al. (2018) study. We retrieved a mass of $11.01^{+0.87}_{-1.28}\mathrm{M_{Jup}}$ for PSO 318. However, we enforced a planetary mass prior of $<13\mathrm{M}_{Jup}$, with the posterior probability distribution partially converging near the upper edge of this prior. This value is larger than the value determined in Allers et al. (2016), (Miles et al., 2018) and Liu et al. (2013) (see Table 4.3). As a result, our derived surface gravity of $4.27^{+0.05}_{-0.09}$ is also slightly higher than values stated in these studies. Our derived effective temperature of 1259^{+14}_{-12} K is consistent at 2-4 σ with previous studies of this object and is 2 σ consistent with Miles et al. (2018) which used the same data coupled with grid forward modelling.

The best fit cloud model, determined via the largest Log(Ev), for PSO 318 employed a BH Mie Fe cloud together with the "cloud" particle size distribution. However, the log evidence of this best-fit retrieval is barely larger than for the retrieval employing Mg_2SiO_4 cloud with a log-normal particle size distribution. Our fits show a very strong $\log(b) > 160$ (where log(b) is Δlog(Ev) between retrievals, see Table 2.1) preference for including clouds over excluding clouds. We are able to constrain well the position of the top of the cloud layer while the cloud bottom position is much less well constrained. Our effective cloud particle radius is poorly constrained, with values from 1 to 100 μm being consistent within 1σ. Our cloud fraction converged to $\sim$100%, despite the expectation of

fractional cloud coverage for this object given its large variability (Biller et al., 2018). The posteriors for these parameters are shown in Figure 4.5 as is our retrieved temperature-pressure profile for this object.

4.5.2 | VHS 1256b

Our best fit model spectrum for VHS 1256 b is shown in Figure 4.6. Unlike for PSO 318, our best fit model spectrum fits both the SpeX and NIRSpex data well. This is likely due to the higher SNR of the L band data for VHS 1256 b, where the retrieval will have weighted this area of the spectrum higher than in the case of PSO 318.

Our retrieval constrain the presence of H_20 and CO while unable to place such constraints on the presence of CH_4 and CO_2 (see Figure 7.5). Despite the higher SNR for the L band data used here compared to PSO 318, the retrieval is still unable to probe the apparent CH_4 feature (Miles et al., 2018).

We derive a high C/O ratio of $0.83^{+0.04}_{-0.04}$ for VHS 1256b but as it orbits a M-dwarf binary a comparison with its hosts is currently not possible. We also derive a high metallicity of $0.91^{+0.15}_{-0.13}$.

Our retrieved radius of $1.15^{+0.04}_{-0.03}$ R_{Jup} is well constrained but, as before, we note this parameter had a Gaussian prior (see Table 4.1). This is higher than the values of ~ 0.9 R_{Jup} derived in the Miles et al. (2018) study and can be explained by our use of the updated distance of 22.2pc (Dupuy et al., 2020b) while Miles et al. (2018) used 17.1pc (Rich et al., 2016). We retrieved a mass of $11.76^{+5.36}_{-3.38}$ M_{Jup} for VHS 1256 b. However, we note that a low surface gravity prior of < 25 M_{Jup} was enforced. Our retrieved radius is consistent with the value determined in (Gauza et al., 2015), thus we find that this object remains a planetary mass candidate. Our derived surface gravity of $4.36^{+0.16}_{-0.14}$ is also slightly higher than values stated in these studies. Our derived effective temperature of 1276^{+14}_{-12} is consistent within 2 σ Miles et al. (2018), which employed the same data.

The best fit cloud model for VHS 1256 b employed a BH Mie Mg2SiO4 cloud together with the "cloud" particle size distribution. However, the the retrievals

was unable to clearly demonstrate a preference for Fe vs MgSiO3 clouds. Our firs again show a very strong $\log(b) > 115$ preference for including clouds over excluding clouds. We are again able to well constrain the position of the top of the cloud layer while the cloud bottom position is much less constrained. Our effective cloud particle radius is poorly constrained, with values from 1 to 100 μm being consistent within 1σ. Our cloud fraction converged to $\sim$99%, again despite the expectation of fractional cloud coverage for this object given its large variability (Bowler et al., 2020, Zhou et al., 2020). The posteriors for these parameters are shown in Figure 4.7 as is our retrieved temperature-pressure profile.

4.5.3 | HR 8799c

Our best fit model spectrum for HR 8799c is shown in Figure 4.8. We successfully fit the J, H and K band spectroscopy. Our retrieval constrains the presence of H_2O (see Figure 7.6). However, the constraints placed on the CO and CH_4 abundances is much broader. We expect our retrieval analysis to be able to better detect and constrain CO compared to CH_4; the strong CH4 constraint found for HR 8799c may point towards a systematic issue with the GPI K band data for this object. We note Wang et al. (2020) was able to retrieval the aforementioned expectation as they made use of OSIRIS data which we have not employed.

As a knock on affect of the retrieved CO and CH_4 abundances, we derive a suspect and unreliable C/O ratio of $0.15^{+0.12}_{-0.12}$ for HR 8799c, placing it as a very sub solar (0.55) and sub stellar result. This value is suspect given the unexpected chemical constraints we retrieve. Wang et al. (2020) places a constraint of $0.54^{+0.12}_{-0.09}$ which is in agreement with the 0.65 value offered by Konopacky et al. (2013) (see Table 4.3). This shows the importance of the high-resolution K band OSIRIS data for HR 8799c (Konopacky et al., 2013) . We derive a metallicity of -$0.11^{+0.11}_{-0.09}$.

Our retrieved radius of $1.11^{+0.03}_{-0.02}R_{Jup}$ is well constrained but we again note this parameters had a Gaussian prior (see Table 4.1). This value is consistent with the PHOENIX model fit from Greenbaum et al. (2018) and the Exo-REM fit from Bonnefoy et al. (2016) but is higher than many other model fits which are listed in Table 4.3.

We retrieved a mass of $12.31^{+0.44}_{-0.75}$M$_{\rm Jup}$ for HR 8799c. However, given the < 13 M$_{\rm Jup}$ prior, the mass fit has simply converged towards the upper boundary of the allowed parameter space. Our derived surface gravity is $4.41^{+0.02}_{-0.02}$, placing it higher than most values derived from the Greenbaum et al. (2018) and Bonnefoy et al. (2016) studies. Our derived effective temperature of 1352^{+25}_{-31} K is higher than expected for this exoplanet and thus higher than most values from previous studies. This is possibly due to the use of low resolution data across the J band (see Figure 4.2d) as this effective temperature is higher than the other 4 mid to late L dwarfs effective temperatures that we have retrieved in this study. Our other objects possess the higher resolution spectroscopy of either GPI or SPHERE in the J band, providing a better platform for the retrieval to determine more reliable constraints on parameters such as effective temperature.

The best fit cloud model for HR 8799c employed a BH Mie $MgSiO_3$ cloud together with the "cloud" particle size distribution. The log evidence of this retrieval is, however, barely larger than several other cloud retrievals with four falling within a Bayes Factor of 1. Our fits again show a very strong $\log(b) > 180$ preference for including clouds over excluding clouds. We are able to well constrain the position of the top of the cloud layer while the cloud bottom position is much less constrained. Our effective cloud particle radius is again unconstrained, with values from 1 to 100 μm being consistent with 1σ. Our cloud fraction converged to $\sim$91%. This is, by far, the lowest of any objects we analysed in this study but may be the result of the low resolution data employed (as mentioned previously in relation to effective temperature) as the retrieval has more fitting freedom due to the usage of less spectral data points. The posteriors for these parameters are shown in Figure 4.9 as is our retrieved temperature-pressure profile.

4.5.4 | HR 8799d

Our best fit model spectrum for HR 8799 d is shown in Figure 4.10. We successfully fit the J, H and K band.

Our retrieval constrains well the presence of H_2O (see Figure 7.7). However, much like in the case of the HR 8799c, we are unable to constrain the presence

of CO. This result paired with the convergence of the final model with too an unexpectedly high amount of CO_2. The retrieval is, however, unable to place a tight constraint on the abundance of CO_2, instead suggesting an upper limit on the abundance of this molecule. These CO and CO_2 result are likely caused by the the GPI data used, which has significant systematic issues due to large uncertainties at wavelengths >2.3μm (See figure 4.2e). This wavelength region is crucial for constraining CO, with a feature present ∼2.3μm, exactly where these data have systematic issues.

Due to these surprising abundances, we derive a very low C/O ratio of $0.07^{+0.06}_{-0.07}$ for HR 8799d placing it as a very sub solar (0.55) and sub stellar result. Wang et al. (2020) places a constraint of $0.54^{+0.12}_{-0.09}$ for HR 8799. We also derive a high metallicity of $0.05^{+0.15}_{-0.11}$. These chemical values should be treated with caution due to the problematic K band data. Studies such as Konopacky et al. (2013) and Wang et al. (2021), who used high resolution K band data (Konopacky et al., 2013), have shown the presence of CO in the atmosphere of HR 8799 d making our retrieved chemistry results, using lower resolution data, suspect and likely incorrect.

Our retrieved radius of $1.20^{+0.05}_{-0.05}\mathrm{R_{Jup}}$ is well constrained but we again note this parameter had a Gaussian prior (see Table 4.1). This value is consistent with the PHOENIX model fit from Greenbaum et al. (2018) and the Exo-REM fit from Bonnefoy et al. (2016) but is higher than the values from many other model fits, listed in Table 4.3. We retrieved a mass of $10.40^{+1.38}_{-1.75}\mathrm{M_{Jup}}$ for HR 8799d. Our derived surface gravity of $4.27^{+0.06}_{-0.09}$ is higher than several values derived from the Greenbaum et al. (2018) and Bonnefoy et al. (2016) studies. Our derived effective temperature of 1244^{+22}_{-21} K is consistent with many previous studiesand overlaps within 1σ with the effective temperatures derived for VHS 1256b and PSO 318, further demonstrating the similarities with these between these late-L objects.

The best fit cloud model for HR 8799d employed a BHMie Fe cloud together with the "cloud" particle size distribution, the same best-fit cloud model found for PSO 318. The log evidence of this retrieval is, however, barely larger than several other cloud retrievals with four falling within a Bayes Factor of 1. Our fits show a very strong $\log(b) > 38$ preference for including clouds over excluding

clouds. We are again able to well constrain the position of the top of the cloud layer while the cloud bottom position is much less constrained. Our effective cloud particle radius is unconstrained, with values from 1 to 100 μm consistent within 1σ. Our cloud fraction converged to $\sim$98%.The posteriors for these parameters are shown in Figure 4.11 as is our retrieved temperature-pressure profile.

4.5.5 | HR 8799e

Our best fit model spectrum for HR 8799e is shown in Figures 4.12a and 4.12b. We successfully fit the J, H and K band despite thee varying SNRs and resolutions of these data. We do not experience any issues with the GRAVITY data dominating the fit over the GPI and SPHERE data. We do note a poor fit to the data at $\sim$2.45-2.5μm. This feature is, however, not present in the updated and re-reduced spectrum in Mollière et al. (2020) so may be a systematic issue with the initial data from the Gravity Collaboration et al. (2019). The Exo-REM model fit of this data from Gravity Collaboration et al. (2019) also missed this feature.

Our retrieval places very precise constraints on the presence of H_2O and CO (see Figure 7.8). Unlike in the case of HR 8799c and d, there is a visible CO feature $\sim$2.3μm in the GRAVITY data which the retrieval is able to use to constrain CO. CO_2 and CH_4 are not well constrained, much like in several of the previous retrievals.

We derive a C/O ratio of $0.67^{+0.05}_{-0.04}$ for HR 8799e placing it as as slightly above solar (0.55) and consistent with the stellar C/O ratio from Wang et al. (2020). This C/O value is also consistent with the $0.60^{+0.07}_{-0.08}$ C/O value from Mollière et al. (2020) which used the same SPHERE and GPI data as well as an updated version of the GRAVITY spectrum. We do note here, however, that their approach fit C/O directly in their chemical equilibrium retrieval which was coupled with a quench pressure to account for chemical disequilibrium. We used free chemistry isoprofiles for our chemical input and infer C/O from these abundances. This is therefore an encouraging demonstration that these differing modelling approaches can derive the same C/O ratio when employed on the same data.

Our retrieved radius of $1.10^{+0.03}_{-0.02}R_{Jup}$ is well constrained but, as before, we note

this parameters had a Gaussian prior (see Table 4.1). Our value is once again consistent with the retrieval radius from Mollière et al. (2020). This radius value is also largely consistent with the radii derived via Exo-REM grid model fits to GRAVITY data of this exoplanet as listed in Table 4.3.

We retrieved a mass of $9.88^{+1.05}_{-0.97}\mathrm{M_{Jup}}$ for HR 8799e with derived surface gravity of $4.32^{+0.05}_{-0.05}$. As in the case of HR8799d, this value places it higher than the values derived from the Greenbaum et al. (2018) and Bonnefoy et al. (2016) studies. However, our value is within 2σ of mass values from other studies that employed GRAVITY data (Gravity Collaboration et al., 2019, Mollière et al., 2020), as outlined in 4.3. Our derived effective temperature of 1223^{+12}_{-13} is largely consistent with previous studies and overlaps at the 1σ level with the effective temperatures we derive for PSO 318 and HR 8799d. Our effective temperature is also consistent with the effective temperature found in the retrieval analysis of Mollière et al. (2020).

The best fit cloud model for HR 8799e employed a BHMie $MgSiO_3$ cloud together with the lorgnormal particle size distribution. This model has a Bayes Factor at least $\log(b) > 2$ compared to all other models, presenting itself as a strong candidate for the dominant cloud species present in the atmosphere of HR 8799e. Our fits show a very strong $\log(b) > 349$ preference for including clouds over excluding clouds. We are again able to well constrain the position of the top of the cloud layer while the cloud bottom position is much less constrained. Our effective cloud particle radius is poorly constrained, with values from 1 to 100 μm consistent within 1σ. Our cloud fraction converged to $\sim$99%. The posteriors for these cloud parameters are shown in Figure 4.13 as is our retrieved temperature-pressure profile.

4.5.6 | Beta Pic b

Our best fit model spectrum for Beta Pic b is shown in Figures 4.14a and 4.14b. We were able to fit the K band successfully but our fit to the rest of the data in the J and H band is less successful. The fit is particularly poor in the 1.15 - 1.35 μm region. Nowak, M. et al. (2020) also found a poor fit in the same wavelength

region. As we have seen in our study, such issues are can arise when combining data from different instruments with different resolutions. Our retrieval misses the small absorption feature at $\sim$ 1.03 μm. To try to fit this feature, we ran retrievals including more molecules. The retrievals including TiO were able to successfully fit this feature. However, our confidence in this fit is rather low, as it was based on only a few data points. It is also not clear if this feature is a systematic issue with the data, as such a feature is not present in the YJ band SPHERE data of Beta Pic b (private communication with Dr. Faustine Cantalloube).

Our retrieval places very precise constraints on the presence of H_2O, CO and CO_2 (see Figure 7.8). CH_4 is unconstrained, much like in the previous retrievals outlined.

We derive a C/O ratio of $0.30^{+0.02}_{-0.02}$ for Beta Pic b placing it as sub solar (0.55). As there is currently no measurement of the C/O ratio of the host star Beta Pic, we cannot compare the C/O ratio of the companion to its star.. Our retrieved C/O value is also lower than the $0.43^{+0.05}_{-0.05}$ C/O value from Nowak, M. et al. (2020), even though we used the same data. Nowak, M. et al. (2020), however, fit C/O and M/H via a chemical equilibrium model combined with quench pressure (as in the case of HR 8799e) while we used a free chemistry approach. Our lower C/O ratio is likely driven by the high abundance of CO_2. Such a constraint, however, is always suspect using ground based data due to telluric contamination from Earths atmosphere and/or systematic issues with the data.

Our retrieved radius of $1.13^{+0.03}_{-0.03}\mathrm{R_{Jup}}$ is well constrained but, as before, we note this parameter had a Gaussian prior (see Table 4.1). Our value is lower than the retrieved $1.36^{+0.01}_{-0.01}\mathrm{R_{Jup}}$ radius from Nowak, M. et al. (2020).

We retrieved a mass of $17.32^{+1.40}_{-1.53}\mathrm{M_{Jup}}$ for Beta Pic b with a derived surface gravity of $4.49^{+0.04}_{-0.04}$. As in the case of several of the previous objects, this value places it higher than most values derived in Chilcote et al. (2017) (see Table 4.3). However, our value is consistent within 2σ of Nowak, M. et al. (2020) which employed GRAVITY data. Our derived effective temperature of 1872^{+16}_{-15} K is higher than previous studies, placing it $>$ 100 K higher than the petitRADTRANS retrieval and $\sim$300K higher than the Exo-REM fit from Nowak, M. et al. (2020). This

is likely due the lower radius we retrieved which is inversely linked to effective temperature.

The best fit cloud model for Beta Pic b employed a BHMie TiO cloud together with the lognormal particle size distribution. This model has a Bayes Factor of only $\log(b) > 1.1$ over all other models. However, several other cloud species had similar log(Ev) including Al_2O_3 and Mg_2SiO_4. Our fits show a very strong $\log(b) > 450$ preference for including clouds over excluding clouds. We are again able to well constrain the position of the top of the cloud layer while the cloud bottom position is much less constrained. Our effective cloud particle radius is poorly constrained, with values from 1 to 100 μm consistent within 1σ. Our cloud fraction converged to $\sim$100%. The posteriors for these cloud parameters are shown in Figure 4.15 as is our retrieved temperature-pressure profile.

Table 4.3: Summary of retrieval bulk parameters for sample along with values from previous studies.

Object	Study	Mass (M_{Jup})	Radius (R_{Jup})	log(g) (cm/s^2)	T_{eff} (K)	C/O	[M/H]
PSO 318	TW, TauREx3	$11.01^{+1.14}_{-2.04}$	$1.24^{+0.02}_{-0.01}$	$4.27^{+0.05}_{-0.09}$	1259^{+14}_{-12}	$0.46^{+0.05}_{-0.05}$	$0.24^{+0.08}_{-0.09}$
	TW, Exo-REM	6.5 (asm)	1.27 (der)	4	1150	0.55	1
	Miles et al. 2018	1.03	1.3	3.2	1240	-	-
	Biller et al. 2018, Exo-REM	-	1.39	3.3	1150	0.0	-
	Biller et al. 2018, M11	-	-	4.0	1200	-	-
	Biller et al. 2018, BT-Settl	-	-	3.5	1600	-	-
	Allers et al., 2016, AMES-COND	7.9 ± 0.4	1.358 ± 0.010	4.03 ± 0.03	1176^{+26}_{-24}	-	-
	Allers et al., 2016, AMES-DUSTY	8.7 ± 0.4	1.417 ± 0.007	4.00 ± 0.02	1154^{+25}_{-27}	-	-
	Allers et al., 2016, Saumon+(2008) CL	7.9 ± 0.4	1.373 ± 0.010	4.04 ± 0.03	1164^{+26}_{-27}	-	-
	Allers et al., 2016, Saumon+(2008) f_{sed}=2	8.3 ± 0.5	1.464 ± 0.010	4.01 ± 0.03	1127^{+24}_{-26}	-	-
	Liu et al., 2013	$6.5^{+1.3}_{-1.0}$	$1.53^{+0.02}_{-0.03}$	$3.8^{+0.10}_{-0.08}$	1160^{+30}_{-40}	-	-
VHS 1256 b	TW, TauREx3	$11.76^{+5.36}_{-3.38}$	$1.15^{+0.04}_{-0.03}$	$4.36^{+0.16}_{-0.14}$	1279^{+25}_{-26}	$0.83^{+0.04}_{-0.04}$	$0.91^{+0.15}_{-0.13}$
	TW, Exo-REM	19 (asm)	3.86 (der)	2.5	1100	0.55	0
	Miles et al. 2018	0.5	0.9	3.2	1240	-	-
	Gauza et al. 2015	$11.2^{+9.2}_{-1.8}$	-	$4.24^{+0.35}_{-0.10}$	880^{+140}_{-110}	-	-
HR 8799c	TW, TauREx3	$12.31^{+0.44}_{-0.75}$	$1.11^{+0.03}_{-0.02}$	$4.41^{+0.02}_{-0.02}$	1352^{25+}_{-31}	$0.15^{+0.12}_{-0.12}$	$-0.11^{+0.11}_{-0.09}$
	Wang et al. 2020, pRT	-	-	-	-	-	-
	Wang et al. 2020, pRT	-	-	-	-	-	-
	Wang et al. 2020, pRT	-	-	-	-	-	-
	Greenbaum et al. 2018, Phoenix	-	1.2	3.5	1100	-	-
	Greenbaum et al. 2018, Saumon+(2008)	-	0.8	3.75	1100	-	-
	Greenbaum et al. 2018, Cloud-AE60	-	0.75	3.5	1300	-	-
	Greenbaum et al. 2018, BT-Settl	-	0.7	3.5	1350	-	-
	Bonnefoy et al., 2016, BT-Settl	-	0.6	3.5	1350	-	0.0
	Bonnefoy et al., 2016, Exo-REM	-	1.0	3.9	1200	-	0.5
	Bonnefoy et al., 2016, Cloud AE-60	-	1.1	3.5	1100	-	0.0
	Konopacky et al., 2013	-	-	4.0	1100	-	0.65

[3] FCR is Free Chemistry Retrieval

Table 4.3 continued...

Object	Study	Mass (M_{Jup})	Radius (R_{Jup})	log(g) (cm/s^2)	T_{eff} (K)	C/O	[M/H]
HR 8799d	TW, TauREx3	$10.40^{+1.38}_{-1.75}$	$1.20^{+0.05}_{-0.05}$	$4.27^{+0.06}_{-0.09}$	1244^{+22}_{-21}	$0.07^{+0.06}_{-0.07}$	$0.05^{+0.15}_{-0.11}$
	Greenbaum et al. 2018, Phoenix	-	1.2	3.5	1100	-	-
	Greenbaum et al. 2018, Saumon+(2008)	-	0.8	4.0	1100	-	-
	Greenbaum et al. 2018, Cloud-AE60	-	0.65	3.5	1400	-	-
	Greenbaum et al. 2018, BT-Settl	-	0.65	3.5	1600	-	-
	Bonnefoy et al., 2016, BT-Settl	-	0.6	3.5	1650	-	0.0
	Bonnefoy et al., 2016, Exo-REM	-	1.1	4.4	1200	-	0.5
	Bonnefoy et al., 2016, Cloud AE-60	-	0.8	3.5	1300	-	0.0
HR 8799e	TW, TauREx3	$9.88^{+1.05}_{-0.97}$	$1.10^{+0.03}_{-0.02}$	$4.32^{+0.05}_{-0.05}$	1223^{+12}_{-13}	$0.67^{+0.05}_{-0.04}$	$-0.03^{+0.09}_{-0.07}$
	Brandt et al., 2021b	$9.6^{1.9}_{-1.8}$	-	-	-	-	
	Mollière et al. 2020, pRT	$4.81^{+8.78}_{-3.33}$	$1.12^{+0.09}_{-0.09}$	$4.0^{+0.46}_{-0.52}$	1154^{+49}_{-48}	$0.60^{+0.07}_{-0.08}$	$0.48^{+0.25}_{-0.29}$
	Mollière et al. 2020, Exo-REM	-	$1.32^{+0.15}_{-0.17}$	$3.82^{+0.26}_{-0.13}$	1071^{+61}_{-50}	<0.3	>0.5
	Gravity Collaboration et al. 2019, Exo-REM	10^{+7}_{-4}	$1.17^{+0.13}_{-0.11}$	4.3 ± 0.3	1150 ± 50	-	-
	Greenbaum et al. 2018, Phoenix	-	1.3	3.5	1100	-	-
	Greenbaum et al. 2018, Saumon+(2008)	-	0.9	3.75	1300	-	-
	Greenbaum et al. 2018, Cloud-AE60	-	1.15	3.5	1100	-	-
	Greenbaum et al. 2018, BT-Settl	-	0.6	3.5	1650	-	-
	Bonnefoy et al., 2016, BT-Settl	-	0.7	3.5	1300	-	0.0
	Bonnefoy et al., 2016, Exo-REM	-	1.0	3.7	1200	-	0.5
	Bonnefoy et al., 2016, Cloud AE-60	-	0.9	3.5	1200	-	0.0

Table 4.3 continued...

Object	Study	Mass (M_{Jup})	Radius (R_{Jup})	log(g) (cm/s^2)	T_{eff} (K)	C/O	[M/H]
Beta Pic b	TW, TauREx3	$17.32^{+1.40}_{-1.53}$	$1.20^{+0.02}_{-0.02}$	$4.49^{+0.04}_{-0.04}$	1872^{+16}_{-15}	$0.30^{+0.02}_{-0.02}$	$-0.03^{+0.03}_{-0.03}$
	Brandt et al., 2021b	$9.3^{+2.6}_{-2.5}$	-	-	-	-	
	Dupuy et al., 2019b	13 ± 3	-	-	-	-	
	Snellen and Brown, 2018b	11 ± 2	-	-	-	-	
	Nowak, M. et al. 2020, pRT	$15.43^{+2.91}_{-2.79}$	$1.36^{+0.01}_{-0.01}$	$4.34^{+0.08}_{-0.09}$	1742 ± 10	$0.43^{+0.04}_{-0.03}$	$0.68^{+0.11}_{-0.08}$
	Nowak, M. et al. 2020, Exo-REM	12.4	1.76	4.0	1590 ± 20	0.43 ± 0.05	0.5
	Chilcote et al. 2017, AMES Dusty	-	1.17	3.5	1800	-	-
	Chilcote et al. 2017, BT Stettl	-	1.22	3.5	1800	-	-
	Chilcote et al. 2017, Drift Phoenix	-	1.41	4.0	1700	-	-
	Allers et al., 2016	12.8 ± 0.2	1.576 ± 0.010	4.135 ± 0003	1583^{+30}_{-33}	-	-
	Morzinski et al., 2015	-	1.45 ± 0.02	4.2	1780 ± 23	-	-
	Baudino et al., 2015	4.0	1.76 ± 0.24	3.5 ± 1	1550 ± 150	-	-
	Chilcote et al. 2015	-	-	3.5-4.5	1600-1700	-	-
	Bonnefoy et al. 2014	<20	1.5 ± 0.2	<4.7	1650 ± 150	-	-
	Bonnefoy et al. 2013	9-10	1.5-1.6	4.0 ± 0.5	1700 ± 100	-	-
	Currie et al., 2013	1.65 ± 0.06	6.9	3.8 ± 0.2	1575	-	-

4.6 Discussion

4.6.1 | Surface gravity / Masses

We employed either uniform planetary mass ($1 - 13$ M_{Jup}) or low surface gravity ($1 - 25$ M_{Jup}) priors for objects where dynamical masses were not available. In the cases of HR 8799e and Beta Pic b we used of Gaussian priors via the current dynamical mass measurements. Via these we retrieve masses and derive surface gravities that are largely consistent with previous literature values. The clearest exception to this would be Beta Pic b where our retrieved mass deviated from the dynamical mass, preferring instead to select a larger value. In the case of HR 8799c we note that the mass simply converged to the edge of the allowed parameter space possibly due to the fact we used data with systematic issues present.

4.6.2 | Inability to clearly distinguish between cloud species

Burningham et al. (2021) recently used retrieval analysis to differentiate between possible cloud species for the red field L-dwarf 2M2244-0158. For the sample considered here, our retrievals were unable to identify a clear preference for a particular cloud species present in the atmospheres of our low surface gravity L dwarfs. This is likely because for all retrievals attempted here, the effective particle size remained unconstrained, with 1 to 100 μm particles all consistent at the 1σ level. However, for every object in our sample, the retrieval fits did find a preference for the inclusion of cloud opacity over clear models. Burningham et al. (2021) found that mid-IR data was crucial to constrain cloud species.

The ability to distinguish between species is closely linked to the ability to tightly constrain the cloud constituent particle radii and particle size distributions. In all of our best-fit retrievals, the effective particle size is essentially unconstrained, rendering it impossible to distinguish between cloud species. We also do not

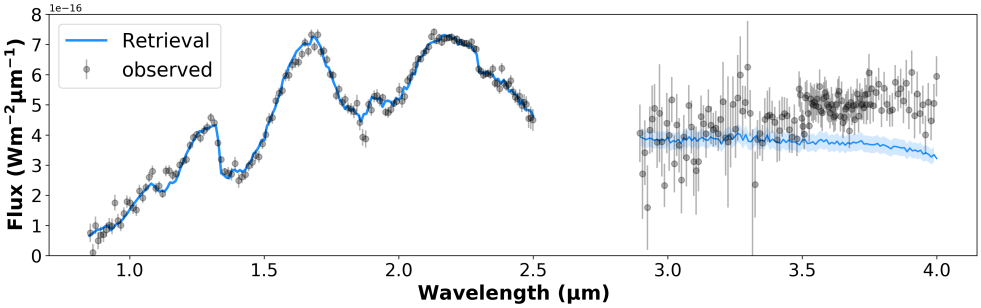

Figure 4.4: PSO 318 retrieval spectral fit.

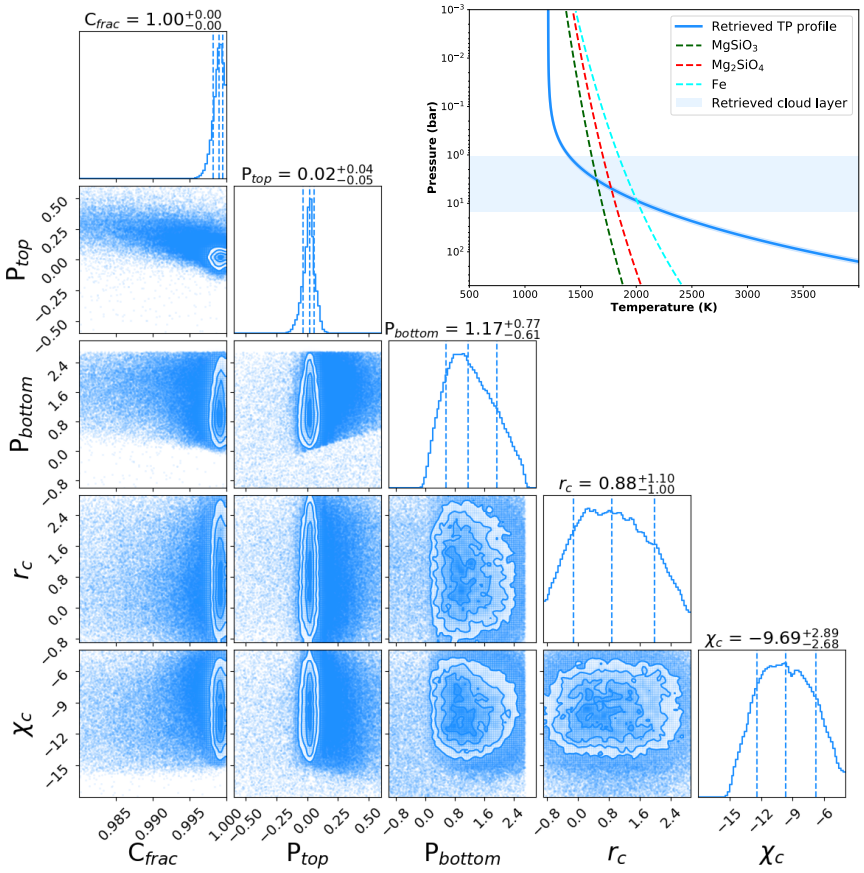

Figure 4.5: PSO 318 corner plot of the best-fit model's retrieved cloud parameters. The retrieved temperature pressure profile is also shown along with condensate curves of MgSiO3, Mg2SiO4 and Fe as well as the retrieved cloud.

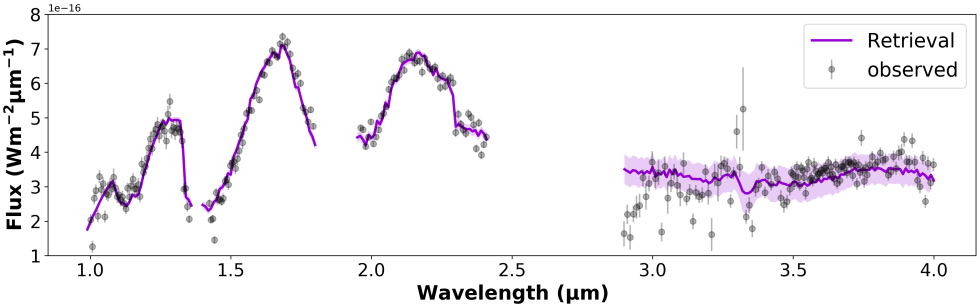

Figure 4.6: VHS 1256 b retrieval spectral fit.

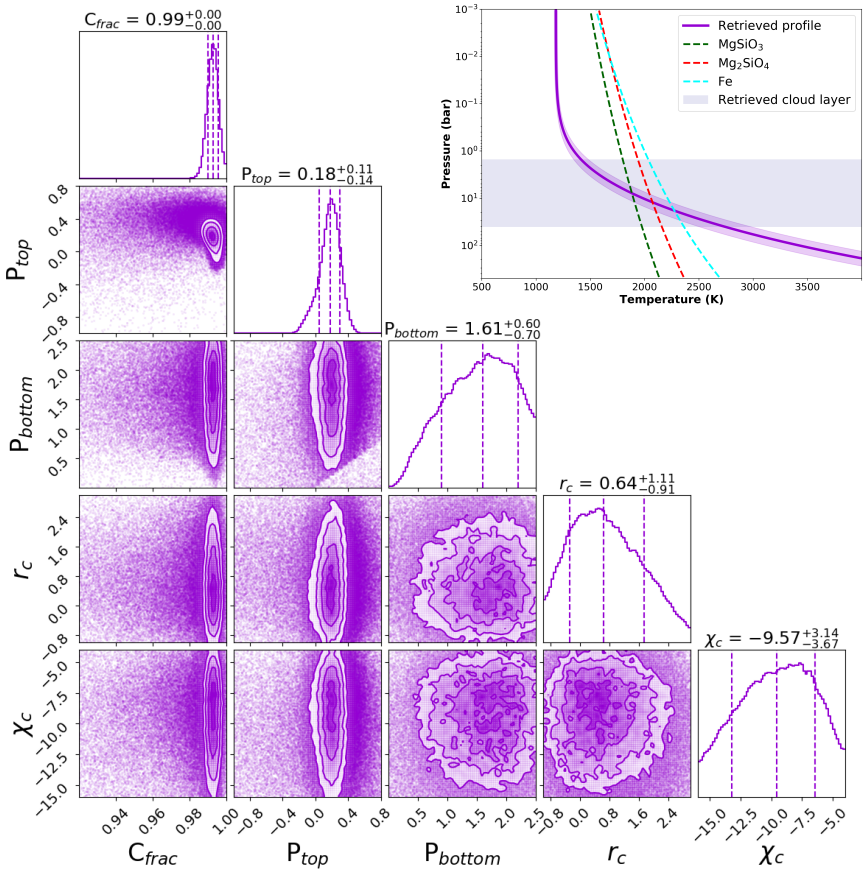

Figure 4.7: VHS 1256 b corner plot of the best-fit model's retrieved cloud parameters. The retrieved temperature pressure profile is also shown along with condensate curves of MgSiO3, Mg2SiO4 and Fe as well as the retrieved cloud.

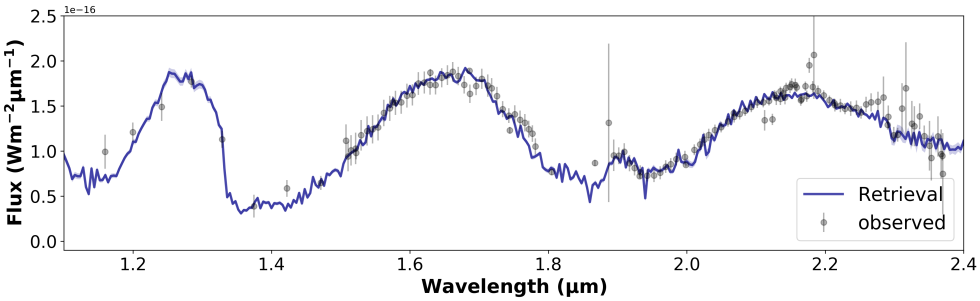

Figure 4.8: HR8799c retrieval spectral fit.

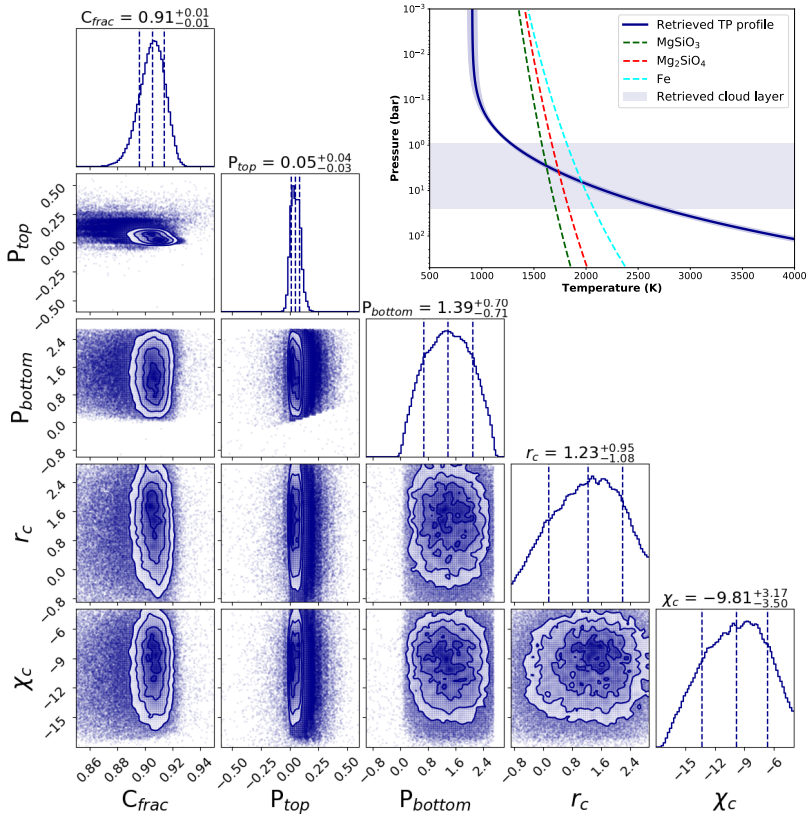

Figure 4.9: HR 8799c corner plot of the best-fit model's retrieved cloud parameters. The retrieved temperature pressure profile is also shown along with condensate curves of MgSiO3, Mg2SiO4 and Fe as well as the position of the retrieved cloud.

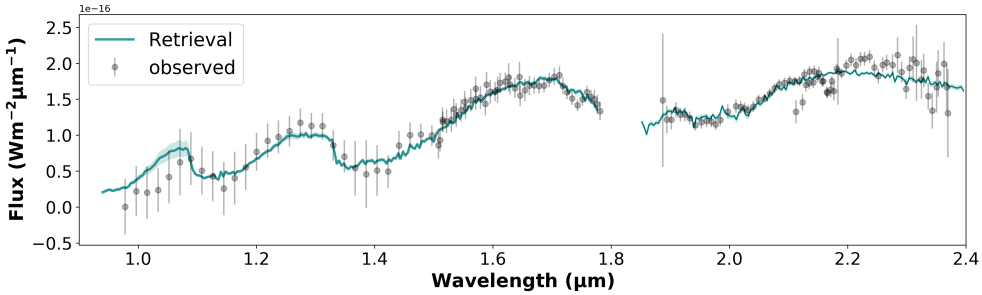

Figure 4.10: HR8799d retrieval spectral fit.

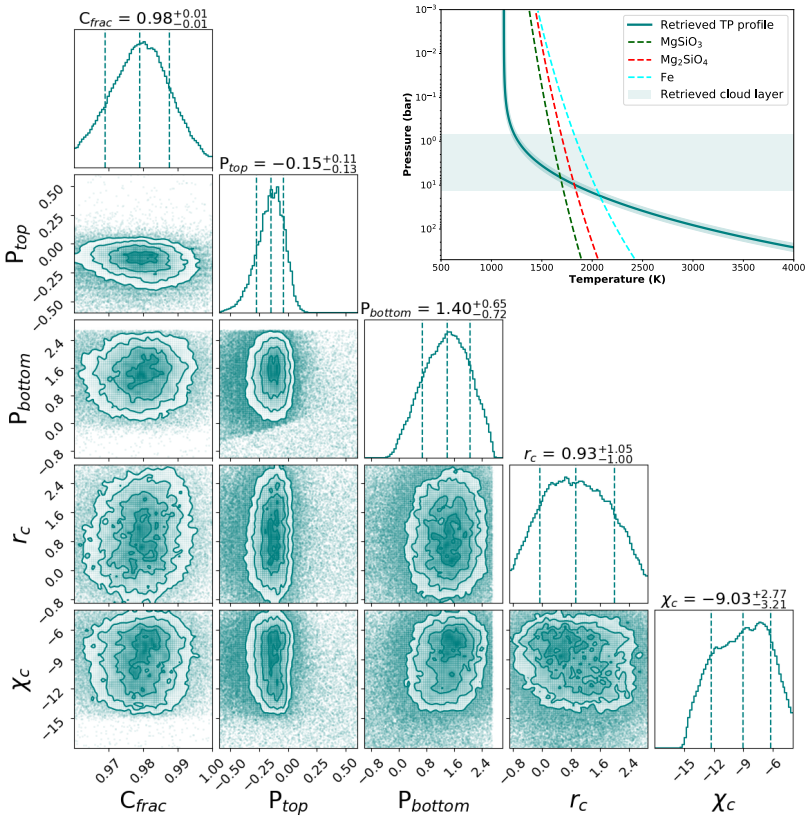

Figure 4.11: HR 8799d corner plot of the best-fit model's retrieved cloud parameters. The retrieved temperature pressure profile is also shown along with condensate curves of MgSiO3, Mg2SiO4 and Fe as well as the the position of the retrieved cloud.

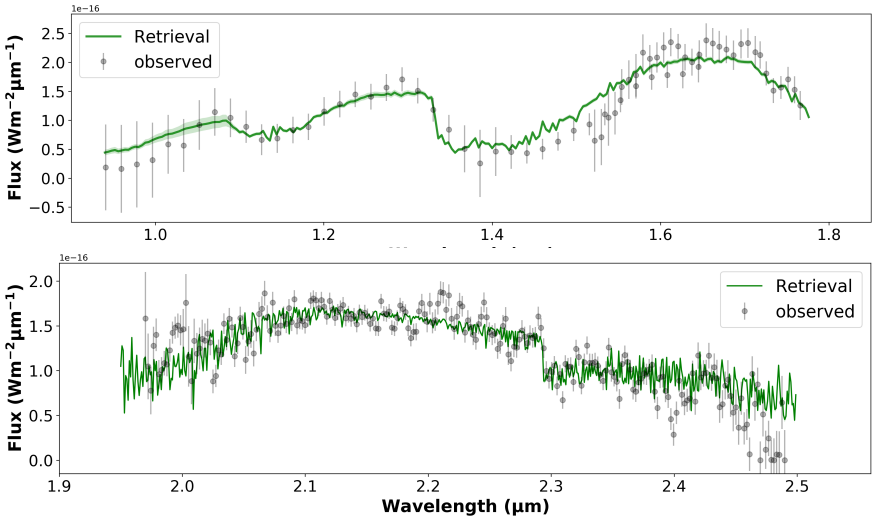

(b)

Figure 4.12: HR8799e retrieval spectral fit.

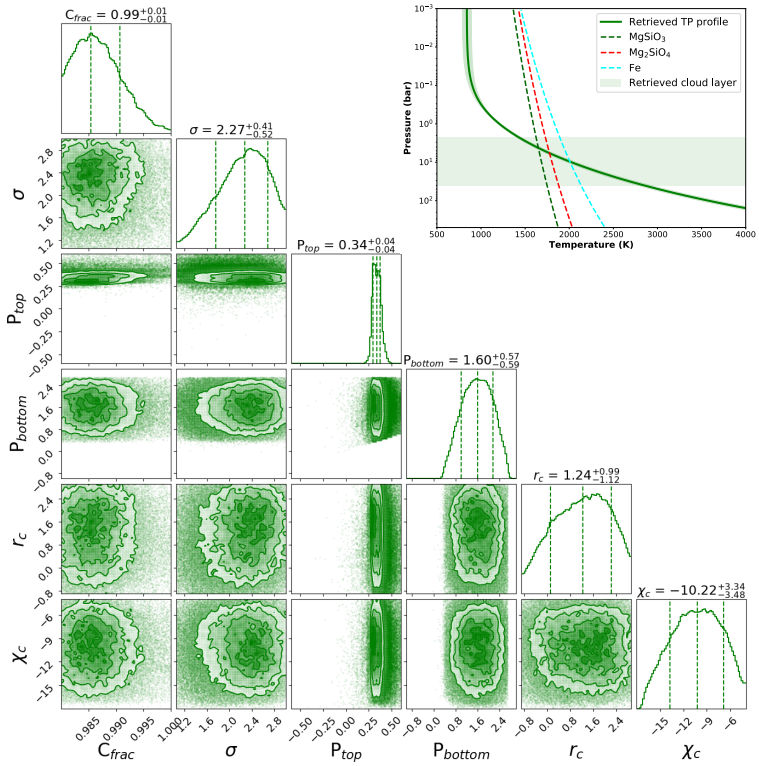

Figure 4.13: HR 8799e corner plot of the best-fit model's retrieved cloud parameters. The retrieved temperature pressure profile is also shown along with condensate curves of MgSiO3, Mg2SiO4 and Fe as well as the position of the retrieved cloud.

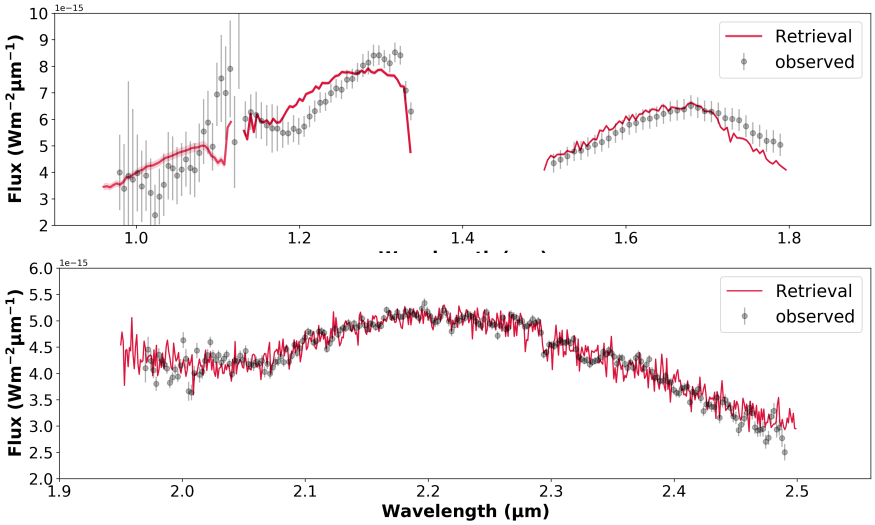

(b) (b)

Figure 4.14: Beta pic b retrieval spectral fit.

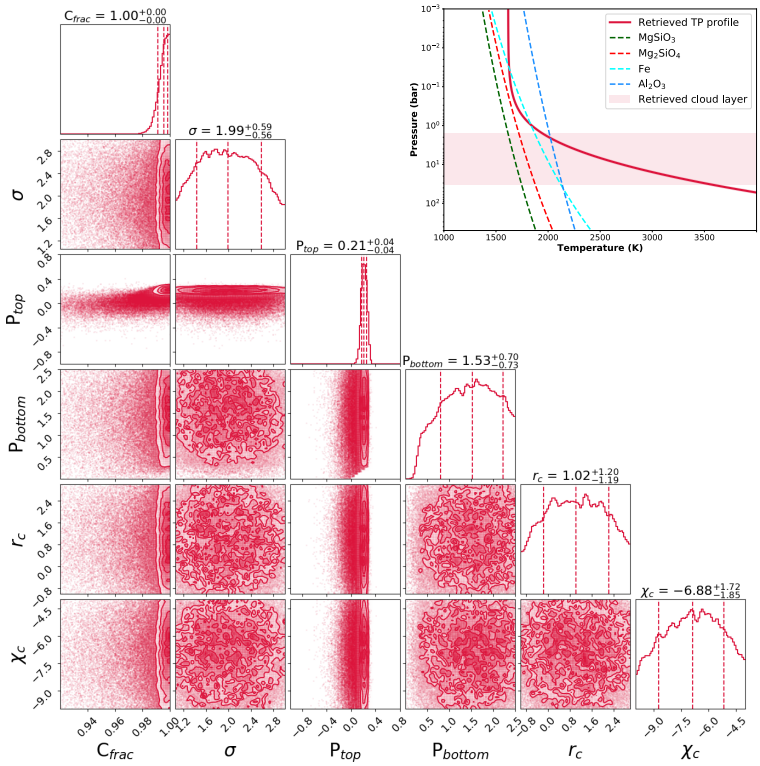

Figure 4.15: Beta Pic b corner plot of the best-fit model's retrieved cloud parameters. The retrieved temperature pressure profile is also shown along with condensate curves of MgSiO3, Mg2SiO4 and Fe as well as the retrieved cloud.

Table 4.4: Bayesian evidence summary of retrievals.

Object	Cloud model	Particle size distribution	Log(Ev)
PSO 318	Cloudless	-	5339.79
	BHmie, $MgSiO_3$	S&B 2007, cloud	5489.12
	BHmie, $MgSiO_3$	A&M 2001, lognormal	5495.35
	BH mie, Mg_2SiO_4	S&B 2007, cloud	5494.64
	BH mie, Mg_2SiO_4	A&M 2001, lognormal	5501.30
	BH mie, Fe	S&B 2007, cloud	**5501.35**
	BH mie, Fe	A&M 2001, lognormal	5486.70
	Lee mie	monodisperse	5499.59
VHS 1256 b	Cloudless	-	5385.77
	BHmie, $MgSiO_3$	S&B 2007, cloud	5501.10
	BHmie, $MgSiO_3$	A&M 2001, lognormal	5498.71
	BH mie, Mg_2SiO_4	S&B 2007, cloud	**5501.19**
	BH mie, Mg_2SiO_4	A&M 2001, lognormal	5500.98
	BH mie, Fe	S&B 2007, cloud	5499.81
	BH mie, Fe	A&M 2001, lognormal	5500.28
	Lee mie	monodisperse	5498.90
HR 8799c	Cloudless	-	4722.91
	BHmie, $MgSiO_3$	S&B 2007, cloud	**4909.67**
	BHmie, $MgSiO_3$	A&M 2001, lognormal	4906.43
	BH mie, Mg_2SiO_4	S&B 2007, cloud	4909.45
	BH mie, Mg_2SiO_4	A&M 2001, lognormal	4907.27
	BH mie, Fe	S&B 2007, cloud	4908.04
	BH mie, Fe	A&M 2001, lognormal	4906.03
	Lee mie	monodisperse	4905.30
HR 8799d	Cloudless	-	5443.87
	BHmie, $MgSiO_3$	S&B 2007, cloud	5489.38
	BHmie, $MgSiO_3$	A&M 2001, lognormal	5489.42
	BH mie, Mg_2SiO_4	S&B 2007, cloud	5488.85
	BH mie, Mg_2SiO_4	A&M 2001, lognormal	5488.31
	BH mie, Fe	S&B 2007, cloud	**5489.71**
	BH mie, Fe	A&M 2001, lognormal	5487.30
	Lee mie	monodisperse	5481.59
HR 8799e	Cloudless	-	10905.48
	BHmie, $MgSiO_3$	S&B 2007, cloud	11241.01
	BHmie, $MgSiO_3$	A&M 2001, lognormal	**11243.17**
	BH mie, Mg_2SiO_4	S&B 2007, cloud	11235.61
	BH mie, Mg_2SiO_4	A&M 2001, lognormal	11236.63
	BH mie, Fe	S&B 2007, cloud	11226.53
	BH mie, Fe	A&M 2001, lognormal	11233.57
	Lee mie	monodisperse	11222.76
Beta Pic b	Cloudless	-	10749.99
	BHmie, $MgSiO_3$	S&B 2007, cloud	11205.83
	BHmie, $MgSiO_3$	A&M 2001, lognormal	11207.18
	BH mie, Mg_2SiO_4	S&B 2007, cloud	11210.79
	BH mie, Mg_2SiO_4	A&M 2001, lognormal	11213.13
	BH mie, Fe	S&B 2007, cloud	11209.58
	BH mie, Fe	A&M 2001, lognormal	11208.18
	BHmie, Al_2O_3	S&B 2007, cloud	11203.53
	BHmie, Al_2O_3	A&M 2001, lognormal	11213.05
	BHmie, TiO_2	S&B 2007, cloud	11211.69
	BHmie, TiO_2	A&M 2001, lognormal	**11214.33**
	Lee mie	monodisperse	11202.89

see a preference for one of the two particle size distribution regimes we tested. Our single-layer cloud modelling is also likely overly simplistic, as Burningham et al. (2021), Manjavacas et al. (2021) have shown that multiple cloud layers are present in objects within this spectral class. Such "cloud busting" approaches, as applied in Burningham et al. (2021), for the objects within our sample will require further data, specifically in the near-IR. We note that the best constrained cloud parameter constrained across this current study was the cloud top P_{top} position, likely due to its position in the observable photosphere.

4.6.3 | Fractional cloud

Despite the expectation of cloudy and clear patches of atmosphere for many objects within our sample we see the cloud fraction parameter converge to 97-100% in all cases. Our approach linearly combined two forward models, one with clouds and one without clouds. Such a high value of cloud coverage was seen in Bowler et al. (2020) who attempted to explain the variability present for VHS 1256 b with a varying cloud free region of 0.775-1.225%. It is likely that the assumption of the exact same non-cloud parameters in both the cloudy and clear is incorrect. It is very probable that, for example, the temperature gradient will differ in these regions. The simplistic approach of our linear combination of the two models is also imperfect. We do note studies have successfully linearly combined cloudy grid models with differing effective temperatures (Skemer et al., 2014). It is still unclear which approach is better or more physically correct with both likely to be overly simplistic. This should become apparent when better and further data becomes available such as variability monitoring of the mid-IR silicate feature via JWST-MIRI or by exploring different retrieval approaches which combine models of differing temperatures as in (Skemer et al., 2014).

4.6.4 | Uncertainties in flux calibrations

Within our retrievals we scale the flux between different spectral bands to account for uncertainties in flux calibration between bands. This practice has become common in retrieval studies to allow for the accounting of possible calibration

imperfections. We adopted a unifrom prior for this parameter within this study, ranging from 0.8 to 1.2 as was also adopted by Nowak, M. et al. (2020) and Mollière et al. (2020). However, the drawback of such an approach is it allows a flexibility within the model which is not necessarily representative of the object's true characteristics. This parameter essentially allows for the colours of the objects to vary. The assumption of the same flux scaling across multiple bands also not ideal our confidence may vary in the flux calibration between bands. This parameter will not be as necessary, however, when data becomes available from JWST as its spectroscopic observation bands tend to overlap with each other. The will permit better calibration of flux between bands from the overlap regions

4.6.5 | The challenge of combining data

We combined data from many instruments within this study. The benefit of this is clearly that it allows up to cover a larger wavelength range, allowing for the improved constraint of many parameters. The importance of this has been well documented in retrieval modelling (Burningham et al., 2021). However, we have seen issues arise when data have varying resolutions or SNRs or different flux calibrations. For example, in the case of PSO 318 the JHK data greatly outweights the L band data due to the low SNR. For Beta Pic b we see the GRAVITY data drive the fit due to the higher resolution and greater SNR. Combating such an issue is difficult but one approach is to de-resolve the higher resolution data to the approximate resolution of the lowest resolution component of the employed data. This is the approach we adopted for PSO 318 and VHS 1256 b. This does, however, sacrifice data points which is never ideal, especially for such a data driven approach as in the case of retrievals. Combining data is becoming common practice for retrieval studies of directly imaged exoplanets (Lavie et al., 2017, Nowak, M. et al., 2020, Mollière et al., 2020, Wang et al., 2020) but it will be important to investigate the biases and map the issues this approach introduces. This will be the focus of future work.

4.6.6 | Enforcing a radius prior

Previous retrieval studies adopted a diverse set of priors on radius. Burningham et al. (2017) elected to set a wide uniform prior from 0.5 to 2 R_{Jup}. Mollière et al. (2020) set uniform priors but with a lower limit set slightly higher with 0.9 to 2.0 R_{Jup} while Wang et al. (2020) set tight Gaussian priors in order to avoid convergence to problematically small values. We also chose to adopt a Gaussian prior on our radius to help avoid unexpected radii values. Retrievals tend to prefer very small and sometimes nonphysical radii values when applied to brown dwarfs and directly imaged exoplanet data sets. Nonphysical radii values are often linked to increased effective temperature values, as these two parameters are intrinsically correlated.

Mordasini et al. (2012) and Marley et al. (2012) outline that for young and low surface gravity objects, such as those included in our sample, we expect radii > 1 R_{Jup}. Despite these theoretical expectations, retrieval studies of brown dwarfs and direct imaging exoplanets have often found radii below 1 R_{Jup}, as outlined in Table 4.3. With all this in mind, we adopted a universal prior of 1.2 ± 0.1 R_{Jup} for our sample, except for PSO 318, where larger radii values have often been assigned. For this particularly object we instead adopted 1.4 ± 0.1 R_{Jup}, based on the findings of an inflated atmosphere from Allers et al. (2016). This approach did successfully result in best fit radii >1 R_{Jup} for all of our best fit models. However, despite retrieved radii values > 1 R_{Jup} we still find effective temperature values $\sim$ 100K higher than expected, as as similarly found by Mollière et al. (2020).

We note also that enforcing any kind of radius prior within a retrieval constricts and introduces a bias to the inferred effective temperature. Thus, constraining the model prior of both radius and temperature, this will have a knock-on effect of potentially biasing other model factors such as the cloud parameters. Future work could explore retesting the retrievals we carried out within this study using a flat prior to explore and map these biases.

4.6.7 | Temperature-pressure profile

Retrieval studies have employed a diverse selection of temperature-pressure profiles. Early approaches, for solar system objects, retrieved the temperature in every layer within the model (Irwin et al., 2008, Rodgers, 2000). A similar approach was adopted in early exoplanet (Lee et al., 2012) and brown dwarf retrievals (Line et al., 2014). However, such an approach is too flexible and high-dimensional for low quality data such as that for directly imaged exoplanets. As such, more recent studies employ temperature-pressure profiles which retrieve temperature at a selected number of pressures (altitudes) which are then connected via linear, spline, or other types of interpolations (Waldmann et al., 2015a, Kitzmann et al., 2020, Line et al., 2015). This greatly reduces the number of free parameters in the fit but lacks the physically motivated constraints of self-consistent modelling. Therefore, more physically motivated temperature pressure profiles have also been developed and routinely employed. A common example of this is the two stream profile (Guillot, 2010). The Madhusudhan and Seager (2009) profile is a further example, allowing for a parameterisation of the atmospheres that permits or excludes temperature inversions (which can often been seen in hot-jupiter atmospheres). The Madhusudhan and Seager (2009) profile has often been employed for retrievals studies encompassing brown dwarfs (Burningham et al., 2021, Gonzales et al., 2020, Burningham et al., 2017) and directly-imaged exoplanets. Mollière et al. (2020) outlines a similar approach, which constrains a physically motivated profile split into different altitude sections. Many studies, particularly of transmission spectroscopy, simply employ an isothermal profile as these studies probe a thin layer of the atmosphere (Edwards et al., 2020, Skaf et al., 2020, Pluriel et al., 2020).

Given the diversity of approaches, choosing the most appropriate profile is difficult. Retrieval studies of brown dwarfs and directly-imaged exoplanets have also demonstrated a trend of using flexible temperature-pressure profile parameterisations to produce a very isothermal structure to account for cloud opacity (Mollière et al., 2020, Burningham et al., 2017). As such, we elected to employ a temperature-pressure profile from Lavie et al. (2017) that is physically motivated but still restrictive enough that it would not permit such behaviour.

While we retrieved adiabatic profiles via this parameterisation, this approach may be overly restrictive. A comparison using several of the different possible profiles with the same data is an important next step to explore the biases which different temperature-profile choices may introduce to the overall results. We certainly see, for example in the case of HR 8799e, that the Mollière et al. (2020) study retrieves a more isothermal profile than that retrieved in our study. However, Burningham et al. (2021) demonstrated the corrective power of mid-IR data, where the same Madhusudhan and Seager (2009) parameterisation within the retrieval adopted an adiabatic gradient compared to the earlier Burningham et al. (2017) study. Retrievals on high quality, and broadband data, should lead to a convergence of different parameterisations to the same profile, even with differing degrees of flexibility being permitted.

4.6.8 | Chemical equilibrium vs disequilibrium: comparing retrieved abundances to TEA

Comparing our retrieved abundances to those predicted by an equilibrium model such as TEA can potentially yield evidence for disequilibrium chemistry in our low-gravity, L dwarf sample. Figure 4.16 shows the comparison of our retrieved molecular abundances to those predicted by TEA.

CH_4 has been a molecule of focus, with a depletion of CH_4 seen in mid-late L dwarfs. This depletion may be caused by disequilibrium chemistry driven by significant vertical mixing of cooler CH_4-rich gas regions with warmer CO-rich gas regions (Barman et al., 2011a, Zahnle and Marley, 2014, Miles et al., 2018, Barman et al., 2011b). However, for VHS1256b, PSO 318, HR8799c, d and e, the constraints on CH_4 abundances are too loose to to constrain whether or not the atmosphere is in chemical equilibrium or disequilibrium. This is largely due to the retrieval's inability to robustly probe clear CH_4 features in the data. In the case of Beta Pic b, our retrieved abundance for CH_4 is consistent with predicted by TEA, indicating a chemical state of equilibrium which matches the findings of Nowak, M. et al. (2020). In particular, Nowak, M. et al. (2020) find that the the impact of their retrieval quench point was negligible, indicating that their model did not require disequilibrium chemistry.

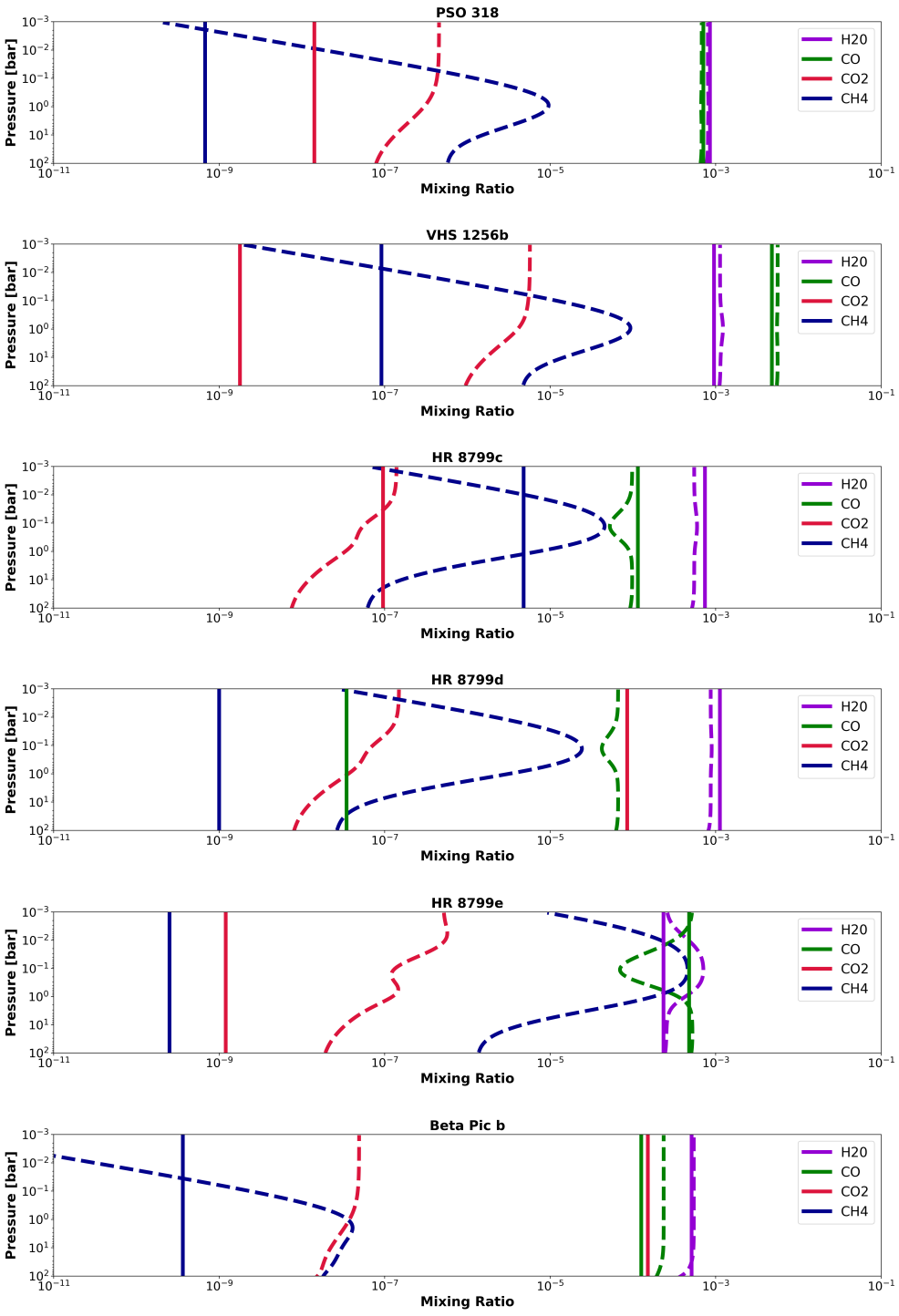

Figure 4.16: Retrieved isoprofile abundances (solid lines) compared to TEA abundance profiles (dashed line).

4.6.9 | Consistency between retrieval codes?

We analyse data from Beta Pic b and HR 8799e which has been previously explored by retrieval approaches but which employed equilibrium chemistry combined with a quench pressure to account for disequilibrium chemistry present within these exoplanets (Nowak, M. et al., 2020, Mollière et al., 2020). On the other hand, we used a free chemistry retrieval approach with isoprofile abundances. Despite these differing approaches, we derive results largely consistent with other retrievals. Encouragingly, we derived a C/O ratio for HR 8799e consistent with that from Mollière et al. (2020). In the case of Beta Pic b, we derived a C/O value slightly lower that of Nowak, M. et al. (2020) seemingly due to a high abundance of CO_2 retrieved. The C/O ratio has been used as an important constraint on formation mechanisms for these objects. Thus, robust determinations of C/O from different modelling approaches are mandatory to test formation mechanism.

4.6.10 | C/O ratio as a formation tracer

Model fit C/O values for exoplanets are increasingly being used to make predictions about the formation pathways. Measurements of the C/O ratio for low surface gravity objects are shown in Figure 4.17. We tested the consistency of C/O values between different modelling codes and approaches while also providing a retrieval C/O value for PSO 318 and VHS 1256 b. We also find that our retrieved chemistry, and by extension C/O, is largely independent of which cloud model or species is being employed, consistent with the results of Burningham et al. (2021) and Mollière et al. (2020). One flaw with determining C/O via retrievals is that the impact of cloud condensates on this characteristic are neglected. Silicate clouds remove some of the O from the atmosphere, which could lead to some uncertainties on the true atmospheric C/O. However, Burningham et al. (2021) suggest that the impact of condensates are negligible due to the position of the observable photosphere relative to the condensation zone for L dwarfs. We can therefore adopt the current values for L dwarfs with a reasonable degree of confidence, and begin to probe trends in C/O ratio as a function of a given

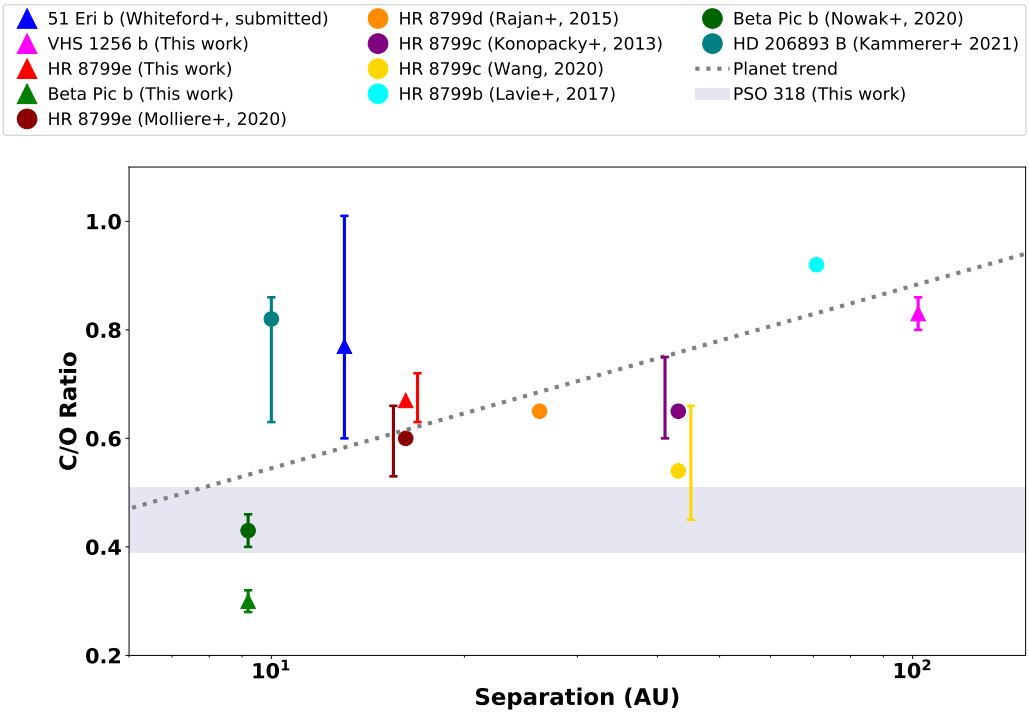

Figure 4.17: Currently inferred C/O ratios for low surface gravity objects.

object's separation from its host star. The current tentative trend, shown in Figure 4.17, may indicate an increase in C/O with increased separation. It has been suggested that the impact of ice lines relative to formation location is an important driving factor for this characteristic, showing that C/O of both solid and gaseous material within a formation disk increases with separation (Öberg et al., 2011).

4.6.11 | Importance of K band

Similar to the discussion in Lavie et al. (2017), we see the importance of the K band spectroscopy for the retrieval analysis. Its importance for deriving the inferred C/O ratio cannot be overstated, given the CO and CH_4 features present in this wavelength range. Konopacky et al. (2013) first demonstrated the power of K band spectroscopy in regards to probing C/O while Lavie et al. (2017) outlined how the omission of K band spectroscopy hampered their ability to meaningfully retrieve carbon chemistry. The studies of Nowak, M. et al. (2020) and Mollière

et al. (2020) also demonstrate the power of the GRAVITY K band data in regards to probing formation and chemical disequilibrium. In this study we see the impact of high vs low SNR in the data employed. For example, with HR 8799 c and d we see an inability to properly constrain the presence and expected abundances of CO, resulting in questionable C/O ratios for these exoplanets. This is in contrast to the other objects where we employed K band spectroscopy with high SNR, where we experience no such issues.

4.6.12 | Outlook to future work

Despite the novel results now being produced by retrievals of directly imaged exoplanets and brown dwarfs, there are still many improvements to be made and tests to be carried out. As alluded to previously, the selection of temperature-pressure profile can have a significant impact on the retrievals results. Therefore, an in-depth comparison of the various temperature-pressure approaches outlined earlier should be explored using both high and low quality data set to explore biases and map the impacts of differing assumptions. Combining data presented challenges within this study. This practice is becoming common due to the desire to use as much data as possible over the widest available wavelength range. However, a common problem is the biasing of the retrieval to the highest SNR, or highest resolution, section of data. Exploring different ways of combining data, particularly including single band photometric points, will be an important area to explore in the future.

It will be key to further explore different cloud parameterisations within retrievals. For example, we explored heterogeneous cloud coverage using a simple linear combination of cloudy and cloudless models. All other parameters were the same for these models, however, it is unlikely this is truly the case. Testing a diverse set of temperature-pressure profiles in the cloudy and cloudless regions of the atmosphere warrants further exploration. L and M band spectroscopy will aid this endeavour, as these wavelength regions may bear signatures of fractional cloud properties. This will also be assisted by ongoing and future variability monitoring of L dwarfs in different spectral bands which may offer definitive proof or further compelling evidence for the presence of patchy clouds.

Mid-IR spectroscopy will be a treasure trove for unlocking the cloudy mysteries of L dwarfs. Specifically, we will be able to probe multi-layer cloud structures and constrain multiple species (Burningham et al., 2021). Such data will hopefully become available for many of the objects included in this study courtesy of JWST.

More measurements of dynamical masses for young, low-surface gravity objects will lead to the ability to more more confident constraints on the chemical makeup of these objects. By placing a dynamical constraint on mass we strongly constrain the surface gravity and by extension metallicity.

New instrumentation will prove vital for improving retrievals. For example, higher resolution data from VLT-CRIRES+ and JWST will offer chances to combine retrieval analysis with cross-correlation analysis (Brogi and Line, 2019, Patapis et al., 2021). Future instrumentation, such as GPI2 and SPHERE+, may lead to further discoveries of the class of objects which is the focus of this study. Such discoveries may allow for a more in depth demographic look the properties of gas giant exoplanets by increasing the sample pool.

4.7 Summary

We apply TauREx3 to six low surface gravity L dwarf spectra. Our sample of objects includes PSO 318, VHS 1256b, HR8799cde and Beta Pic b. We test TauREx3's cloud capabilities using this sample, namely an Mie opacity approximation regime from Lee et al. (2013) and a more rigorous species dependant Mie opacity regime from Bohren & Huffman. We also tested an exponential potential vs a lognormal particle size distribution for our Bohren & Huffman mie opacity. The main results of our L dwarf sample retrieval analysis are:

- We show a Bayes Factor preference for clouds to be included in the retrieval for all our objects.
- For each object, we have a Bayes factor preference for the Bohren &

Huffman mie opacity over the Lee et al. (2013) mie opacity approximation regime.

- We are unable to clearly distinguish a preference for a cloud species for any of our objects.
- We are unable to tightly constrain a particle size distribution for any of our objects and we cannot identify a clear preference for either the "cloud" or lognormal distribution types.
- We are able to well constrain the cloud top pressure but unable to place such constraints on the cloud bottom pressure.
- We derive radii $>$ 1Rjup for all our objects but this is likely due to the enforcement of a 1.2 $\pm$ 0.1 Rjup prior.
- We derive retrieval C/O ratios for PSO 318 ($0.44^{+0.05}_{-0.06}$) and VHS 1256 b ($0.83^{+0.04}_{-0.04}$) for the first time.
- We derived unexpectedly low C/O ratio ratios for HR 8799c and d, likely due to incorrectly retrieved chemical abundances stemming from systematic issues in the GPI K band spectroscopy for these objects.
- We demonstrated spectral fitting issues which arise when combing data of differing resolutions or SNRs.
- We tested fractional cloud coverage with our retrievals generally showing a preference to converge to a coverage $\sim$97-100%.

CHAPTER 5

JWST and retrievals

5.1 Introduction

Jame Webb Space Telescope (JWST) (Gardner et al., 2006) will soon provide novel observing capabilities, opening up new mid-IR wavelength regions and offer medium resolution capabilities with the benefits of space based observing. Specifically, it will offer unparalleled potential for characterising low surface gravity brown dwarfs and gas giant exoplanets. JWST (Gardner et al., 2006) will define a new era for astronomy. By combining the spectroscopic capabilities of the Mid Infrared Instrument (MIRI) (Rieke et al., 2015a, Wright et al., 2015, Bouchet et al., 2015, Kendrew et al., 2015, Boccaletti et al., 2015, Wells et al., 2015, Rieke et al., 2015b, Ressler et al., 2015, Glasse et al., 2015, Gordon et al., 2015) and Near infrared Spectrograph (NIRSpec) [1], we will be be able to rigorously detect and catalogue atmospheric spectral features from $\sim 0.5-28\mu m$. This wavelength coverage will offer the ability to probe new chemical features, chemical state and cloud signatures (Luna and Morley, 2021).

Currently, most studies of low surface gravity brown dwarfs and gas giant exoplanets have been limited to $\sim 0.9-4\mu m$ spectroscopy (Macintosh et al., 2015, Zurlo et al., 2016, Samland et al., 2017, Chilcote et al., 2017, Rajan et al., 2017, Gravity Collaboration et al., 2019, Nowak, M. et al., 2020, Miles et al., 2020, Liu et al., 2013, Miles et al., 2018, Greenbaum et al., 2018, Ingraham et al., 2014, Burgasser et al., 2010, Zhang et al., 2021) combined with photometric points at wavelengths $<5\mu m$. There is also currently a very limited amount of spectroscopic data with $R > 500$ (Konopacky et al., 2013, Wang et al., 2021). Therefore, we cannot robustly characterise the true chemical state of the atmospheres of these objects. Such constraints will prove invaluable as the chemical makeup of these atmospheres is increasingly used to trace back the formation pathways of such objects using ratios such as C/O and N/O (Öberg et al., 2011, Öberg and Bergin, 2021, Cridland et al., 2020, Schneider and Bitsch, 2021).

Numerous JWST Early Release Science (ERS), Guaranteed Time Observation (GTO) and Guest Observer (GO) programs planned will explore the atmospheric

[1] `https://jwst-docs.stsci.edu/near-infrared-spectrograph`

characteristics of substellar objects. However, the behaviour and capability of our model fitting approaches when applied to such novel data is still unknown. These programs seek to answer science questions such as: What is the exact chemical makeup of their atmospheres? Are these atmospheres in a state of chemical equilibrium or non-equilibrium? What cloud condensate species and structures are present? Can we robustly constrain the true temperature-pressure structure present? Can we use precise and robust chemical ratio measurements, such as C/O and N/O, to trace back the formation stories of these objects?

Retrievals, where a flexible forward model attempts to best fit an observed spectrum whilst guided by Bayes theorem, will be a key tool to characterise these objects using JWST data, building upon their application to currently available data (Lavie et al., 2017, Kitzmann et al., 2020, Line et al., 2015, Burningham et al., 2017, Lee et al., 2013, Line et al., 2017, Zalesky et al., 2019). Recent retrieval studies have shown the power of using ground based data with $R \sim 500$ (Nowak, M. et al., 2020, Mollière et al., 2020) to probe C/O and disequilibrium chemistry while Burningham et al. (2021) demonstrating the power and impact of employing high SNR data covering mid-IR wavelength regions in relation to constrain L dwarf cloud properties.

In this work we will investigate the capabilities of the retrieval method when applied to simulated JWST data of a cloudless T dwarf and cloudy L dwarf. We seek to test the extent to which our retrievals can extract the input chemistry along with other characteristics such as the temperature pressure profile, mass and radius. In Section 5.2 we outline how we create our simulated observations and how we set up our retrievals. We then outline our main results in Section 5.3. We discuss these results and outline our plans for future work in Section 5.4

5.2 Method

We perform this test by first employing the forward modelling tool Exo-REM (Charnay et al., 2018, Baudino et al., 2015, Blain, D. et al., 2021) to produce a self consistent forward models of low surface gravity brown dwarfs based on

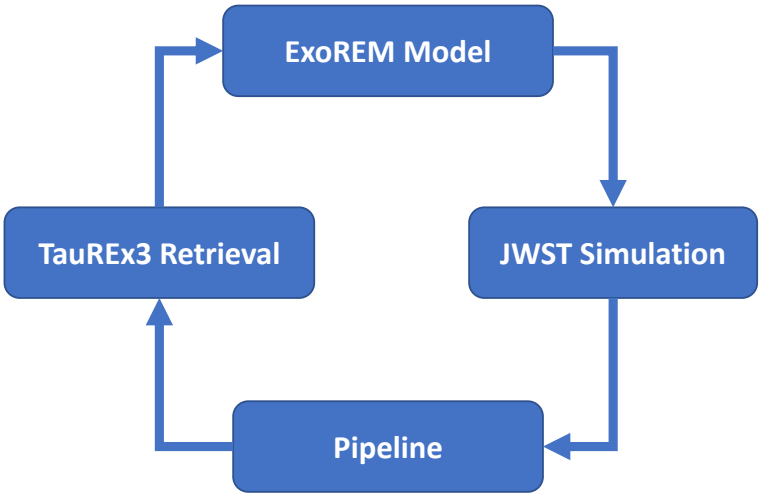

Figure 5.1: Flowchart outlining project overview and methods process.

the characteristics of VHS 1256 b and Ross 458 c. These characteristics are outlined in Section 5.2.1. The simulations of NIRSpec and MIRI observation were created using the JWST Exposure Time Calculator (ETC) and Mid-Infrared Instrument Simulator (MIRISim). We have chosen these "mock" objects as these are an JWST Early Release Science (VHS 1256b, ID: 1386[2]) and Guaranteed Time Observation (Ross 458 c, ID: 1277[3]) targets. This will also allow us to test a retrievals response to a benchmark example of a cloudy L dwarf and a non-cloudy T dwarf. We used TauREx3 to perform the retrieval analysis of the mock observations. Figure 5.1 outlines the overall process followed for this study. Our main focus was testing how successfully the retrieval can extract the chemistry of the input Exo-REM model. We outline the various components of our analysis in the following subsections.

5.2.1 | Simulated Objects

[2]https://www.stsci.edu/jwst/science-execution/approved-programs/dd-ers/program-1386

[3]https://www.stsci.edu/jwst/science-execution/program-information.html?id=1277

5.2.1.1 | A cloudy L dwarf: VHS 1256 b

VHS 1256b is a low surface gravity, very red, late-L dwarf companion of the M dwarf VHS1256-1257 with a wide 8" separation (Gauza et al., 2015, Stone et al., 2016). Given its favourable separation and its characteristic similarities with many young directly imaged exoplanets, such as the HR8799bc planets (Bonnefoy et al., 2016), VHS 1256b is an ideal laboratory to test giant exoplanet atmospheric models. Rich et al. (2016) showed evidence of thick cloud coverage on this object. VHS 1256b is amongst the most variable substellar objects known with variability amplitudes of >25% over an 8-hour long HST observation (Bowler et al., 2020), likely due to the presence of evolving patchy clouds. Miles et al. (2018), via L band spectroscopy, presented evidence of a Methane absorption feature.

5.2.1.2 | A cloudless T dwarf: Ross 458 c

Ross 458 c is a low surface gravity, cool T dwarf. It is a wide orbit companion to the M0.5+M7 binary system Ross 458AB with a separation of 1168.0 AU (Goldman et al., 2010, Burningham et al., 2011). Spectral analysis from Burningham et al. (2011) derived an effective temperature of ∼695K, a surface gravity of log(g)=4.0-4.7, a mass of 5-20 $M_{\rm Jup}$, and a spectral type of T8.5p. Burningham et al. (2011) also found evidence of CO-CO2 non-equilibrium chemistry. Both Burgasser et al. (2010) and Burningham et al. (2011) provided evidence for the presence of condensate cloud species. However, to test a simple cloudless model within our analysis scheme, we neglected to include any cloud condensates for the simulated data of this object.

5.2.2 | Exo-REM Model

Our input models were obtained using the self-consistent 1D radiative-equilibrium model Exo-REM[4] (Charnay et al., 2018, Baudino et al., 2015, Baudino et al., 2017, Blain, D. et al., 2021). Table 5.2 outlines the bulk parameter inputs.

[4]Exo-REM 2.2.0: `https://gitlab.obspm.fr/dblain/Exo-REM`

Our Exo-REM models assume no external light source, and solar elemental abundances (Lodders, 2019). Species abundances are determined using non-equilibrium chemistry (see Blain, D. et al., 2021, for details about the Exo-REM implementation). The atmosphere is modelled using the plane-parallel approximation with 81 levels uniformly spaced in log-space between 10^2 and 10^{-6} bar. The modelled emission spectra are calculated from 40 to 30000 cm^{-1} (0.3 to 250 μm) with a step of 20 cm^{-1} and includes the gas opacities of H_2O, CH_4, CO, CO_2, NH_3, H_2S, HCN, PH_3, K, and Na. HCN was excluded for VHS 1256 b. Collision-induced absorption of H_2–H_2, H_2–He and H_2O–H_2O was also included.

For Ross 458 c we assumed a cloudless atmosphere. For VHS 1256b we included absorption and scattering by clouds – calculated from the extinction coefficient, single scattering albedo, and asymmetry factor interpolated from pre-computed tables for a set of wavelengths and particle radii (Charnay et al., 2018). For simplicity, only the radiative and opacity contributions of Mg_2SiO_4 – assuming $C_{\rm frac} = 0.99$ – were included. The vertical distribution of the cloud masses are modelled following the approach of Ackerman and Marley (2001), which assumes an equilibrium between the cloud condensation and sedimentation, determined by the vertical eddy diffusion coefficient K_{zz} and the parameter $f_{\rm sed}$. In all our Exo-REM models, we assumed $f_{\rm sed} = 2$ for VHS 1256 b, with K_{zz} set at 10^8 for both objects. For our Exo-REM models, the metallicity [M/H] and C/O was set to solar.

5.2.3 | MIRI simulations

In order to produce simulated observations of the two objects for the MRS, the MIRI Instrument Simulator (Klaassen et al., 2021, MIRISim) is used. The simulator takes as input the observation parameters, instrument configuration and the spectra of the astronomical objects in the scene, to produce the same data product as the real instrument. The simulation incorporates instrument specifications such as the spatial and spectral resolution, photon to electron conversion efficiency, wavelength coverage and point spread function. It simulates instrumental effects such as geometric distortion and detector fringing, as well as detector level noise components of photon noise, readout noise, dark current, pixel

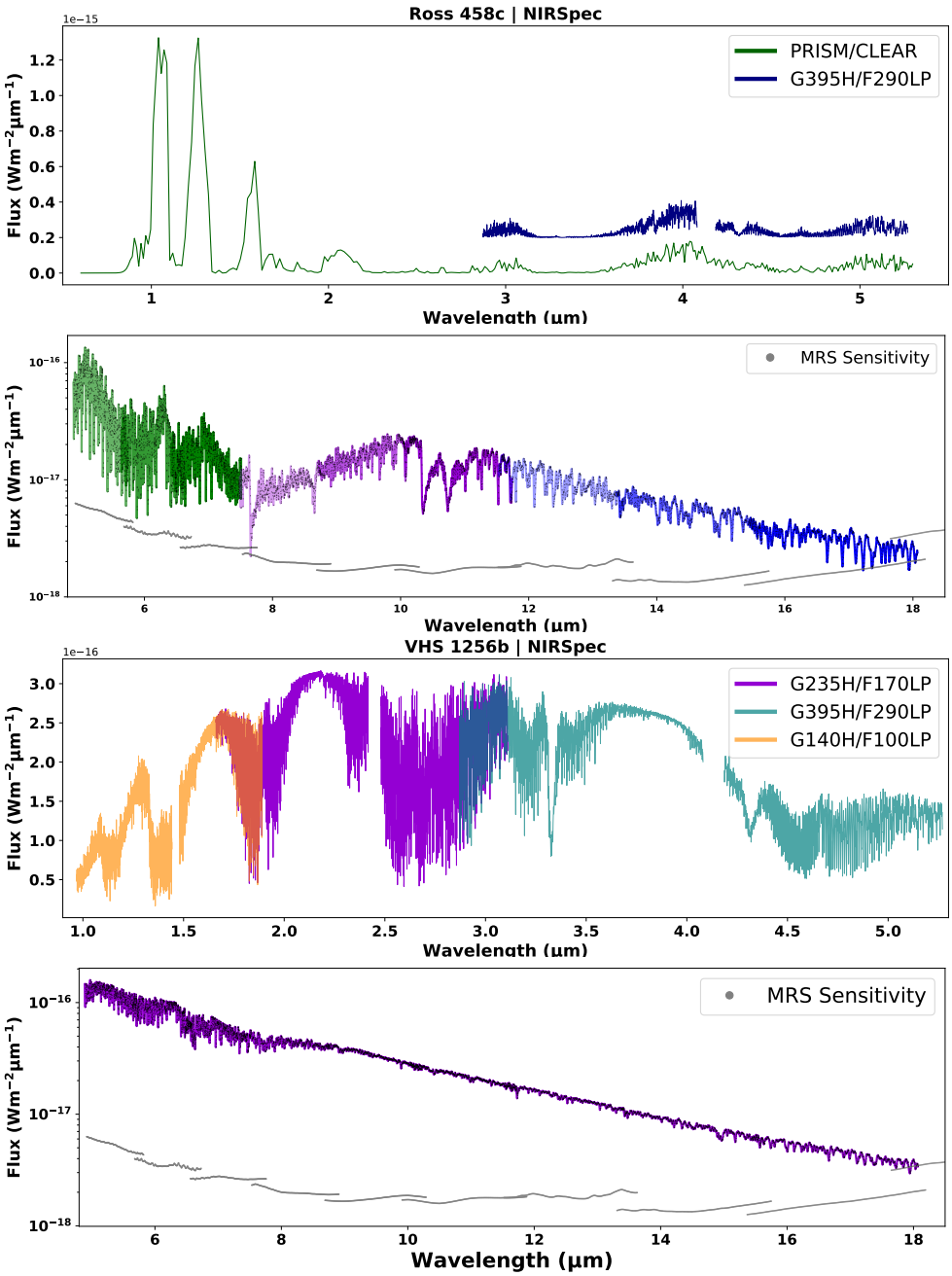

Figure 5.2: Simulated JWST spectra of VHS 1256 b and Ross 458 c

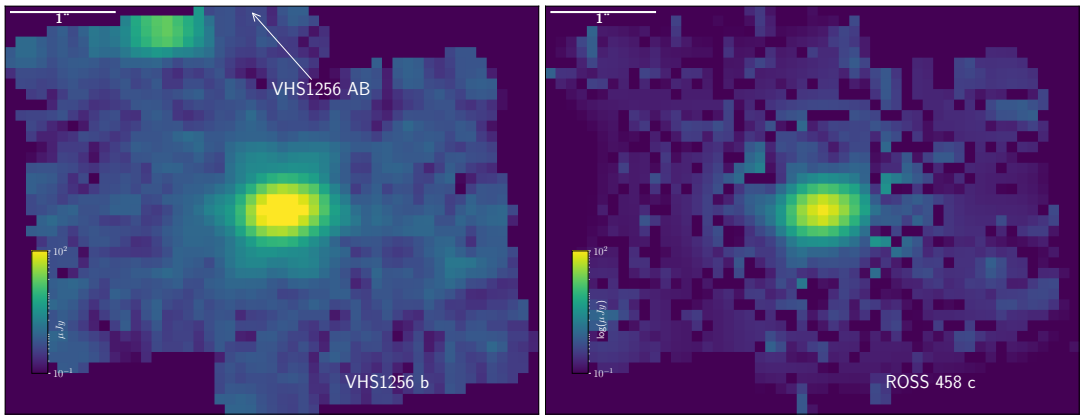

Figure 5.3: MIRISim simulated data of VHS1256 b (left) and ROSS 458 ABc (right) after processing them with the `JWST` pipeline.

gain and non-linearity of the detector ramps.

We adopt the observation parameters from the corresponding APT file of the Guaranteed Time Observation (GTO) program for Ross 458 ABc , and Early Release Science (ERS) program for VHS 1256 b. The parameters include the number of groups per exposure, number of exposures and dither pattern. Since both targets are isolated from their host star(s), the companion is placed in the centre of the Field of View (FoV) itself. The observations of ROSS458 ABc will use 200 groups/integration with a two point dither pattern for all MRS Channels, for a total exposure time of 3300 seconds. The observations of VHS1256 b will use 260 groups/integration and the two point dither pattern as well, for a total exposure time of 4332 seconds. Dithering ensures that the MRS is properly sampled in both the spatial and spectral coordinates. The `Exo-REM` modelled spectra described in Section 5.2.2 were used as input for the simulator.

The output of MIRISim consists of a series of FITS files with uncalibrated Level 1 data. These files can directly be fed to the `JWST` pipeline[5] where three stages of the pipeline process the MRS data to produce the reconstructed and photometrically calibrated data cubes (Labiano-Ortega et al., 2016). In Figure 5.3 a slice of the processed data is shown for MIRI's sub-band 1A over a small wavelength range.

The output spectrum of the MIRISim possesses discontinuities due to various

[5] `https://jwst-pipeline.readthedocs.io/en/latest/`

different instrumental effects. As such, a calibration step is required. We simply scale the MIRISim flux back to the flux scale of the input Exo-REM model. The is done using a linear interpolation of the ExoREM model to the wavelength grid of MIRI. Such a process will not be possible for real observations, where we will instead make use of calibration observations/libraries to understand the relative behaviour of the instrument once it is launched and commissioned. Spectrophotometric calibration observation during commissioning should yield an accuracy around 10%. Additionally, one could use the wavelength overlap between the bands to correct for systematic offsets. The process of spectrum "stitching" is still under development and will be finalised during commissioning. The final simulated MIRI spectroscopy is shown in Figure 5.2.

5.2.4 | NIRSpec simulations

In order to generate simulated observations of our two targets for JWST NIRSpec we have employed the JWST Exposure Time Calculator [6] (ETC) which is built upon Pandeia (Pontoppidan et al., 2016). There is currently no publicly available instrument specific simulator for NIRSpec. The ETC, much like MIRISim, produces simulated spectra using a combination of observation parameters, instrument setup and modelled spectral input of the object of interest. Unlike MIRISim, however, this simulator does not fully replicate the observational data products from real observations. There was therefore no need for the JWST pipeline to be used in this instance.

The ETC employs a pixel-based 3-dimensional approach to simulate a small user-defined scene. It accounts for spatial and wavelength dimensions, making used of realistic point spread functions produced via WebbPSF (Perrin et al., 2015) for each instrument mode. The ETC accounts for effects such as correlated read noise, inter-pixel capacitance and saturation. Via the signal and noise modelling for each pixel, the ETC replicates many of the real steps that will be performed when reducing and calibrating the real JWST observations (JWST ETC User Documentation, 2022). As such, this is an ideal tool for the purposes of our analysis, offering an efficient platform producing realistic signal-to-noise

[6] `https://jwst-docs.stsci.edu/jwst-exposure-time-calculator-overview`

simulations of our ERS and GTO targets.

Within the modeled scenes, the ETC includes sources of noise such as cosmic rays and the interstellar medium. Within our simulations, we elected for the medium option of background noise. We again adopted the observational parameters specified in the relevant GTO and ERS program APT files.

For VHS 1256 b (ERS target) we used 36 groups/integrations for each filter and grating combination along with a two point dither pattern. The grating/filters used are G235H/F170LP, G395H/F290LP and G140H/F100LP which a total combined observation time of 3238.7 seconds.

For Ross 458 c (GTO target) we used 10 groups/integrations for PRISM/-CLEAR grating/filter combination with 2 integrations per exposure. For the G395H/F290LP grating/filter combination we also used 10 groups/integrations with only one integration per exposure. These strategies also made use of a two point dither pattern. In total these Ross 458 c observations tally to 1838.2 seconds. Both the VHS 1256 b and Ross 458 c observations employ the NRSIRS2RAPID readout pattern.

We employed the same scaling calibration approach for the simulated NIRSpec observations as was employed for the MIRI simulation (which are outlined in the previous subsection). The final simulated NIRSpec spectroscopy is shown in Figure 5.2.

5.2.5 | TauREx3 setup

For our retrieval analysis we employed TauREx3 (Al-Refaie et al., 2019) Using MultiNest, we sampled the parameter space using 3000 live points at a sampling efficiency of 0.8. We employed a relatively inflexible temperature-pressure profile for this study which follows the same parameterisation outlined in Lavie et al. (2017). This was in order to reduce the dimensionality of our retrievals in order to reduce retrieval run times. This profile acts to enforce a radiative equilibrium gradient. We assume a hydrogen dominated atmosphere with a H_2 and He mixing ratio $He/H_2 = 0.17567$. We consider a model atmosphere with pressures ranging

Table 5.1: Priors used for retrieval analysis.

Retrieved parameter	Distribution Type	Ross 458c	VHS 1256b
log(*Active Species*)	Log-Uniform	1e-12 - 1e-1	1e-12 - 1e-1
$Radius, R$	Uniform	0.5 - 2.0 R_{Jup}	0.5 - 2.0 R_{Jup}
$Mass, M$	Uniform	1-40 M_{Jup}	1-40 M_{Jup}
$T_{\rm int}$	Uniform	10, 2000 K	10, 2000 K
κ_0	Log-Uniform	1e-15 - 1	1e-15 - 1 (msk)
$r_{\rm c}$	Log-Uniform	-	0.1 - 1000 μm
χ	Log-Uniform	-	1e-20 - 1e-4
$P_{\rm top}$	Log-Uniform	-	1e-3 - 5e2 bar
$P_{\rm bottom}$	Log-Uniform	-	1e-3 - 5e2 bar
σ	Uniform	-	1.01 - 3
C_{frac}	Uniform	-	0-1

from 10^{-3} to 500 bar, with 100 layers uniformly sampled in log-space. In our study we include the line lists for H_2O, CO, CO_2, CH_4, NH3, H2S, PH3, HCN, Na and K as these are the molecules included in our input Exo-REM model. Collision induced absorption (CIA) of H_2–H_2 and H_2–He (Abel et al., 2011, Fletcher et al., 2018, Abel et al., 2012) is also included. In this work we do not use linear scaling factors as our mock data is calibrated such that there are no discontinuities (see Section 5.2.3). The priors and prior bounds set for the retrieval analysis performed in this study were all uniform or log-uniform. See Table 5.1 for a full overview of the priors set. We adopted wide priors for the radius of 0.5-2.0R_{Jup} and mass of 1-40M_{Jup} in order to investigate the retrieval's ability to correctly constrain these parameters given the extensive and novel wavelength coverage without the bias of Gaussian priors. For the distance we set this parameter to the literature values used for the observation simulations. In the case of VHS 1256 b we used the BH Mie scattering model (Bohren and Huffman, 1983) within TauREx3 using the refractory indices of Mg_2SiO_4 with a lognormal particle size distribution.

Table 5.2: Exo-REM model input and retrived values.

Object	Parameter	Exo-REM Input	Retrieval (MIRI)	Retrieval (NIRSpec and MIRI)
Ross 458 c	Radius,R	1.12	0.98	1.10
	log(g)	4.4	5.04,	4.93,
	C/O	0.55, solar	$2.05^{+0.01}_{-0.01}$	$0.35^{+0.00}_{-0.00}$
	[M/H]	0, solar	$-0.01^{+0.00}_{-0.00}$	$0.30^{+0.00}_{-0.00}$
VHS 1256 b	Radius, R	0.9	0.97	0.96
	log(g)	3.2	5.06,	5.04,
	C/O	0.55, solar	$0.44^{+0.01}_{-0.01}$	$0.59^{+0.00}_{-0.00}$
	[M/H]	0, solar	$0.71^{+0.05}_{-0.05}$	$1.90^{+0.00}_{-0.00}$
	C_{frac},	0.99	$0.72^{+0.18}_{-0.24}$	$0.69^{+0.00}_{-0.00}$
	r_c	1.7	$1.04^{+1.26}_{-1.31}$	$0.98^{+1.38}_{-1.35}$

5.3 Results

In the following subsections we outline the results of our retrieval analysis of the mock JWST observations. We note here that we tested a retrieval on only MIRI simulated data followed by a retrieval of both the MIRI and NIRSpec simulated data combined. The overall results are shown in Table 5.2 as well as the corner plots shown in Figures 5.11 and 5.12.

5.3.1 | Ross 458 c

For Ross 458 c we obtain reasonable fits to the simulated data, both when using the MIRI simulation alone and when it was paired with the NIRSpec simulations. This is shown in Figures 5.5 and 5.4. We note, however, that the goodness of the fit from 1-2.5μm suffers due to lower resolution of the spectral data in this wavelength region. This is due to the retrieval prioritising the wavelength regions with higher resolutions in order to maximise the Bayesian evidence.

There is a slight continuum misalignment visible when only MIRI mock data is fit, in the $\sim$9.5-12μm wavelength region in Figure 5.4. The retrieval is unable to correctly fit the depth of a CH_4 feature present at $\sim$7.7μm for both simulated Ross 458 c retrieval inputs.

In neither case of of the two retrievals of the mock Ross 458 c data was the retrieval able to successfully constrain a value for mass. In both cases the retrieval result simply converged to the upper boundary of uniform prior space ($40M_{Jup}$) acting to push the derived surface gravity much higher than the input model. However, the retrievals did constrain a radius value successfully. When using both the NIRSpec and MIRI mock data, the retrieval returned a value of $1.1R_{Jup}$ very close to with the $1.12R_{Jup}$ value set in the input Exo-REM model. The retrieval was not as successful when only MIRI data was used, instead retrieving a radius of $0.98R_{Jup}$.

The overall retrieved molecular abundances compared to mock data molecular

input was successful in most cases. This is shown in Figure 5.7 and 5.8. CO_2 is incorrectly constrained when retrieving using both NIRSpec and MIRI simulated data, likely due to incorrectly fitting the CO_2 features in the lower resolution PRISM/CLEAR data points for NIRSpec. We see in the case of H_2S that NIRSpec data is needed in order to derive a tight posterior as shown in Figure 5.12. The posteriors of Na and K both acted to converge to the bottom end of the abundance prior space in the case of combining MIRI and NIRSpec data. Figure 5.12 clearly shows that the posteriors shift when NIRSpec data is added to the retrieval. Many molecules move towards the input truth such as CO and CH4. However, the addition of NIRSpec data acted to move some posteriors further from the input truth such as H2O and CO_2. It is crucial to note here that this, again, could be a symptom of different data resolutions across the NIRSpec data, where the retrieval will prioritise G395H/F290LP grating/filter data over that of PRISM/CLEAR in order to maximise $\log(Ev)$.

Neither retrieval for Ross 458 c was able to correctly retrieve the input solar C/O ratio. In the case of the retrieval using only MIRI data, the retrieval did derive a metallicity consistent with the input model, while the retrieval with NIRSpec and MIRI simulated data overestimated the metallicity when applied to both NIRSpec and MIRI data.

The retrieved temperature-pressure profile for the simulated Ross 458 c data, shown in Figure 5.13, is offset by ∼100-600K in temperature compared to the input Exo-REM model. Employing NIRSpec and MIRI combined vs only MIRI simulated data did not have an impact on the temperature-pressure profile, as both of these retrieved profiles almost perfectly overlap.

5.3.2 | VHS 1256 b

For VHS 1256b we again obtain good fits to most of the simulated data, both when using the MIRI simulated data alone and when paired with the NIRSpec simulated data. This is shown in Figures 5.4 and 5.6. We see, however, that the goodness of the fit from 0.95-1.3μm is poor. This mismatch could be due to a mismatch in alkali cross sections between the input model of Exo-REM and the

retrieval model of TauREx3.

For VHS 1256 b, we again find that the retrievals are unable to constrain a mass value. In both cases the retrieval result simply converged to the upper boundary of uniform prior space(40 M_{Jup}). This again acted to push the derived surface gravity log(g) to a much higher value than the input model. However, the retrievals did again constrain a radius value successfully. These values of $0.96R_{Jup}$ and $0.97R_{Jup}$ are higher than the $0.9R_{Jup}$ value of the input Exo-REM model. This also suggests the accuracy of the retrieval did not benefit at all from the addition of the NIRSpec data where the radius barely changed and actually acted to converge further from the true input value.

The overall retrieval of molecular abundances compared to simulated data molecular input was again reasonably successful in most cases. This is shown in Figure 5.9 and 5.10. We see in this case that the combination of NIRSpec and MIRI simulted data acted to sharpen the posteriors of many molecular abundances, such as CH_4, PH_3 and H_2S, leveraging the spectral information encoded in the more feature rich NIRSpec simulated data. We see that NH_3 is poorly constrained, especially in the case of retrieving via the combined NIRSpec and MIRI simulated data. The retrieval greatly underestimates the abundance, likely due to the inability to make use of the NH_3 features which has been flattened out due to the presence of a cloud opacity. Generally, however, the addition of NIRSpec data acted to push the retrieved abundances closer to that of the input model. For the simulated data of VHS 1256b, we encounter issues with the retrieved abundance for Na and K. First, when using only MIRI simulations we obtained a K abundance that was much higher than that of the input model. Then, in the case of the NIRSpec and MIRI simulation combination we retrieved a Na abundances that was much higher than than input Exo-REM model. This could be caused by the difference in the treatment of alkali cross sections.

The retrieval for VHS 1256b, which included both MIRI and NIRSpec simulated data, derived a C/O ratio of 0.59 which is close of that of the input value of 0.55 . However. the retrieval underestimated the C/O ratio when only using MIRI simulated data as an input. Both retrievals of VHS 1256 b overestimated the metallicity, deriving values inconsistent with the input.

The retrieved temperature-pressure profile for the simulated VHS 1256 b data, shown in Figure 5.13, shows than when both NIRSpec and MIRI data is retrieved we get almost an exact match in profiles. In the case of solely employing MIRI simulated data, we see a significant mismatch at higher pressures.

For VHS 1256 b's retrievals, given the difference in cloud modelling approachs between Exo-REM's input and TauREx3's retrieval, it is difficult to make a like-for-like comparison of cloud parameters. However, there are two common parameters between the models: the cloud fraction C_{frac} and cloud particle radius r_c . We see that the cloud coverage fraction of the retrievals significantly varies from that of of the input model as shown in Table 5.2. Our retrievals were also incapable of constraining a cloud particle radius, with these values also shown in Table 5.2.

5.4 Discussion

5.4.1 | Our results

We have shown the power that JWST will offer retrieval models in terms of tightly constraining a diverse chemical catalogue for giant exoplanets and brown dwarfs. The retrieval output generally closely matches the molecular chemistry of the input model. However, while we derive precise constraints, they are not necessarily universally consistent with the input model. There are a number of factors which could motivate this result such as slightly differing input cross sections. These mismatches do, however, represent the unavoidable mismatches that will inevitably be present between the theoretical models and the real data which JWST will provide. A good example is the temperature-pressure profile mismatch for Ross 458 c, despite the huge wavelength coverage and high quality of the simulated data. Degeneracies likely played a key role here, such as temperature's degeneracy with radius. Thus, these mismatches offer a invaluable insight into model behaviours and highlight areas where caution should be exercised. Retrievals, when applied to real JWST data will inevitably present

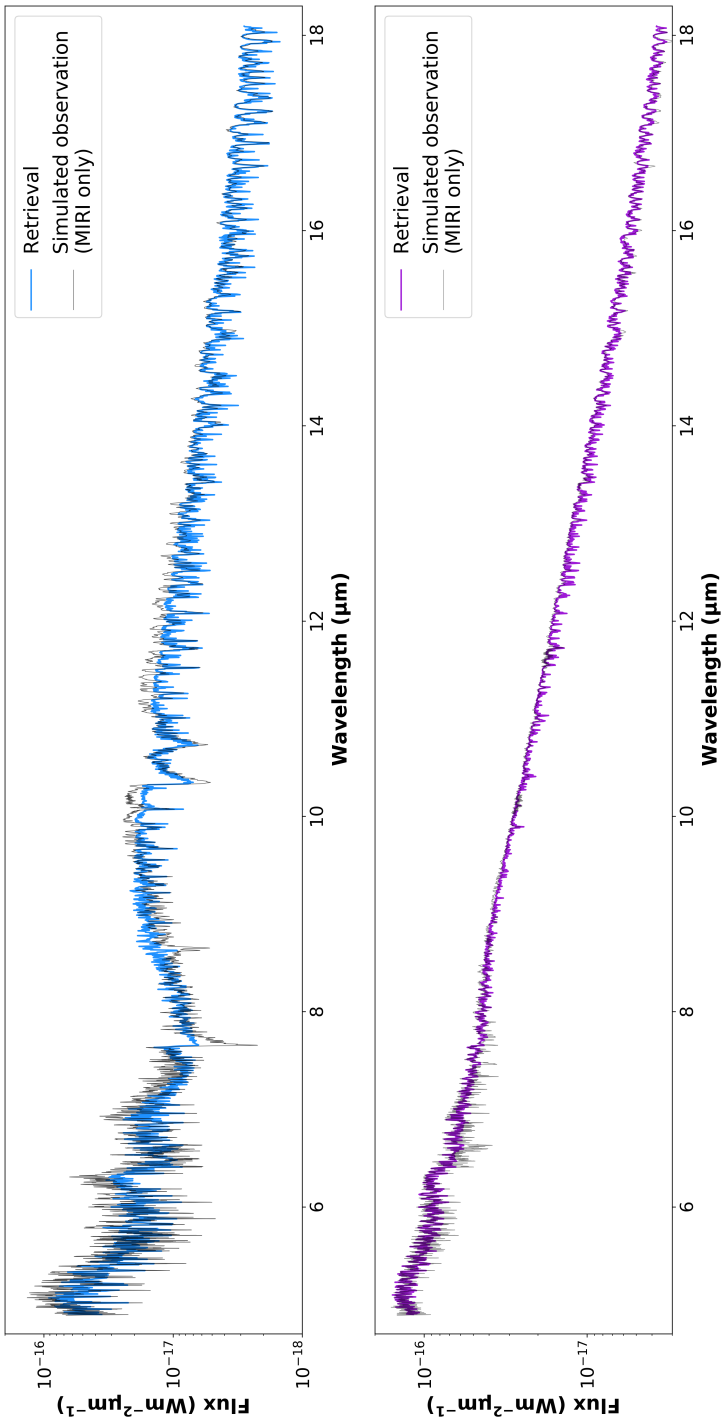

Figure 5.4: Retrieval fits of MIRI simulated observations of Ross 458 c and VHS 1256 b. These fits were performed using only MIRI simulations.

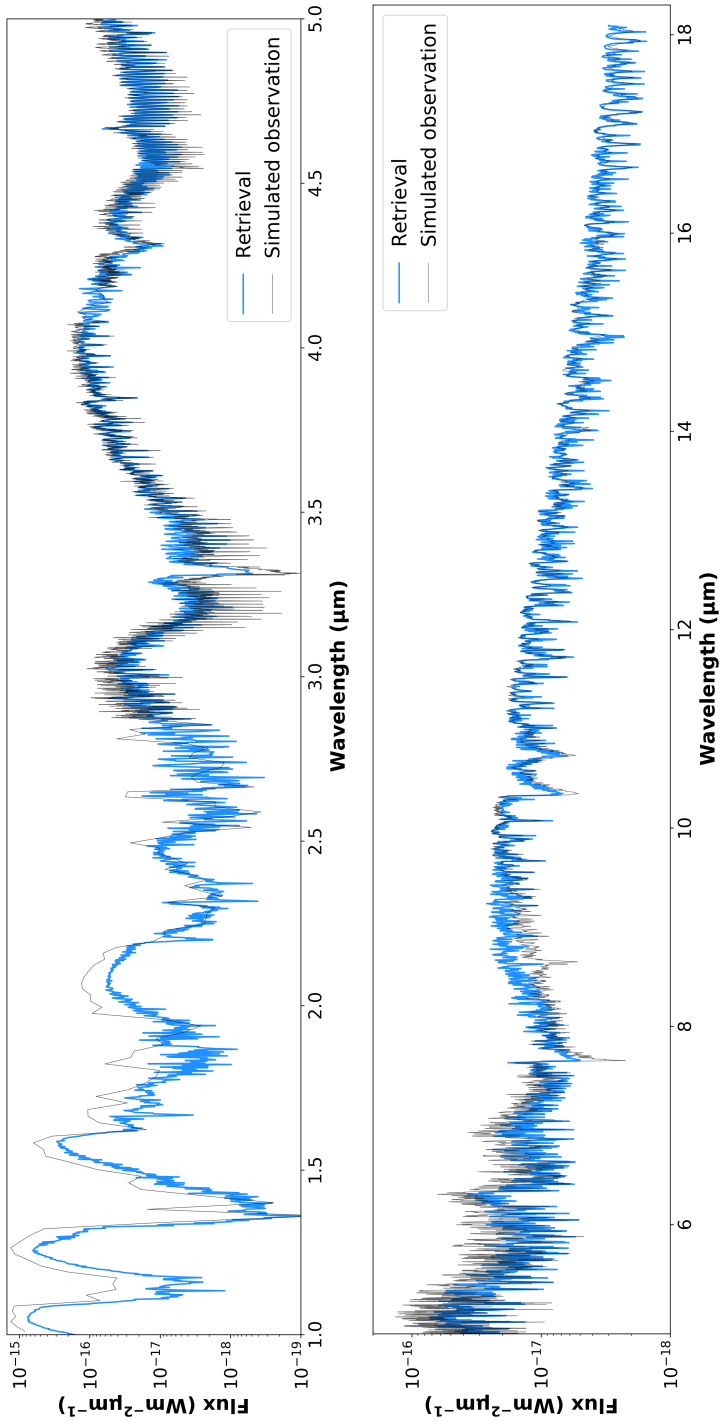

Figure 5.5: Retrieval fits of NIRSpec and MIRI simulated observations of Ross 458 c. These fits were performed using the combination of NIRSpec and MIRI data.

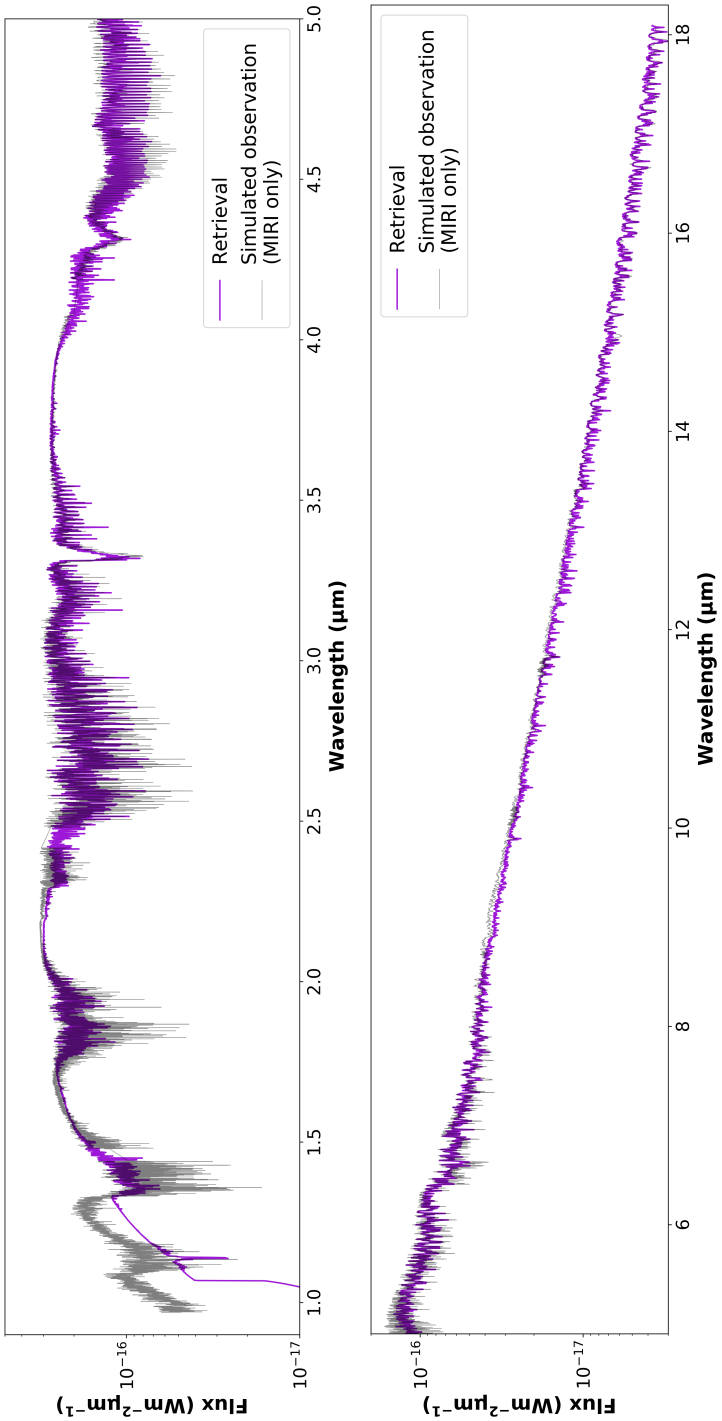

Figure 5.6: Retrieval fits of NIRSpec and MIRI simulated observations of VHS 1256 b. These fits were performed using the combination of NIRSpec and MIRI data.

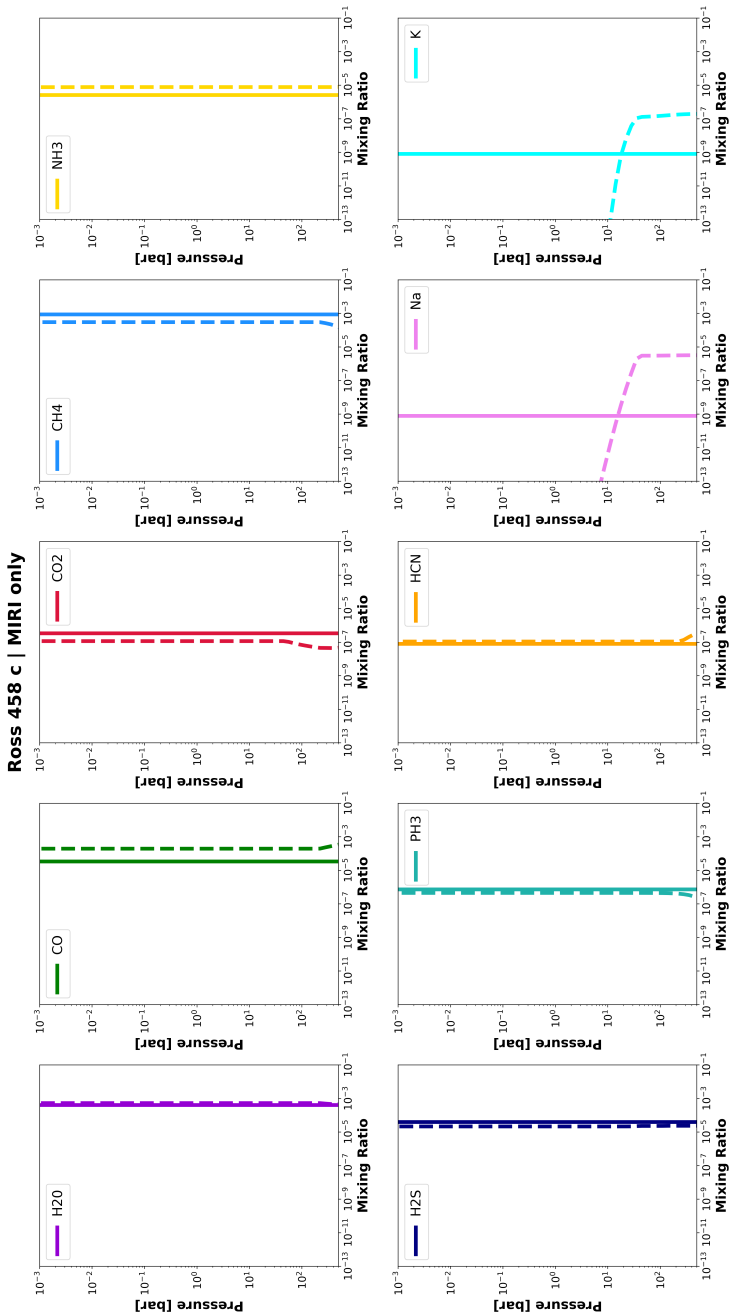

Figure 5.7: Molecular abundance profiles from simulated Ross 458 c observations via Exo-REM (dashed line) and the retrieved molecular abundance isoprofiles. This result is using simulated MIRI data only.

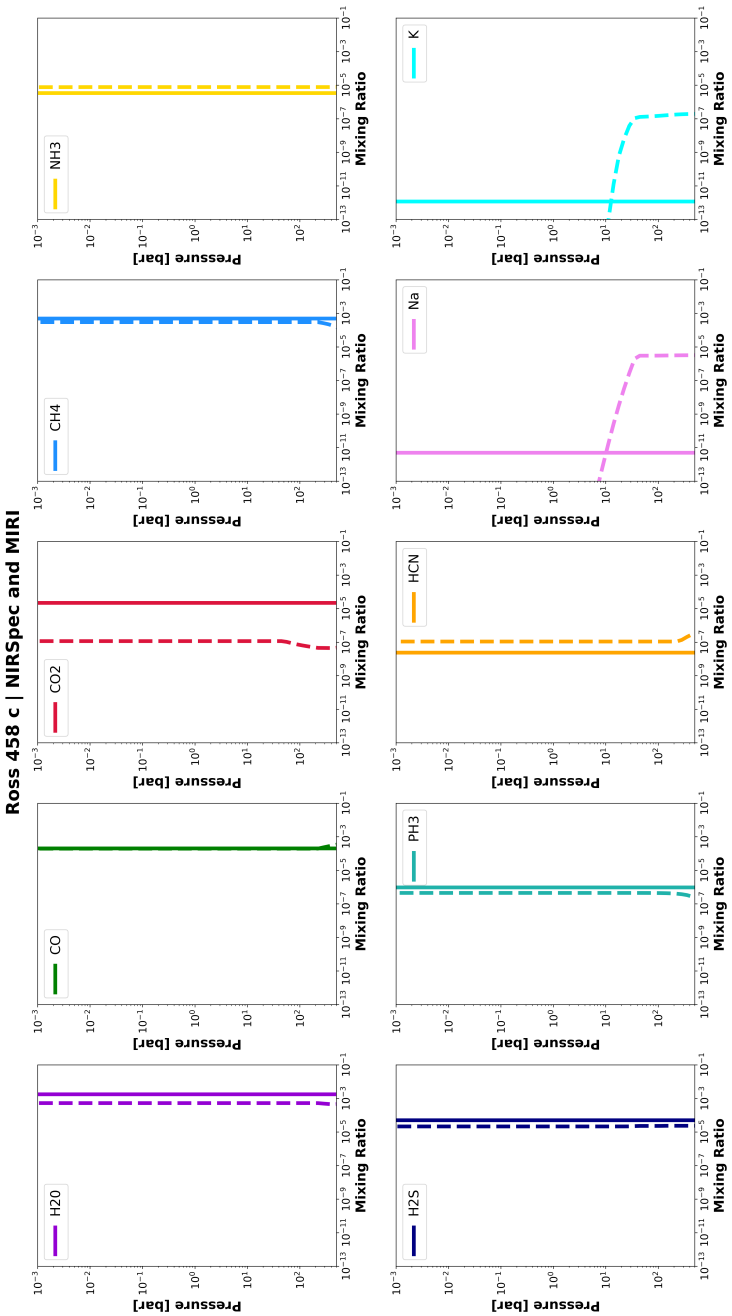

Figure 5.8: Molecular abundance profiles from simulated Ross 458 c observations via Exo-REM (dashed line) and the retrieved molecular abundance isoprofiles. This result is using simulated NIRSpec and MIRI data.

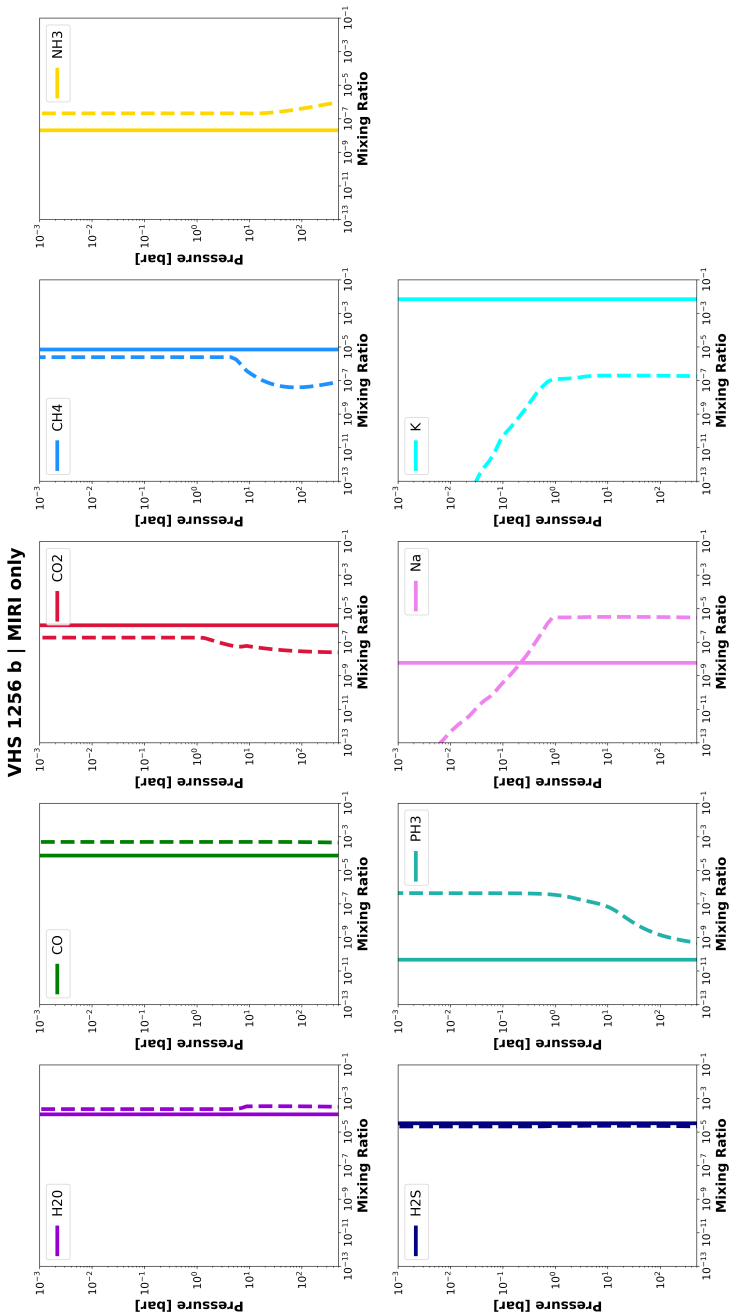

Figure 5.9: Molecular abundance profiles from simulated VHS 1256b observations via Exo-REM (dashed line) and the retrieved molecular abundance isoprofiles. This result is using simulated MIRI data only

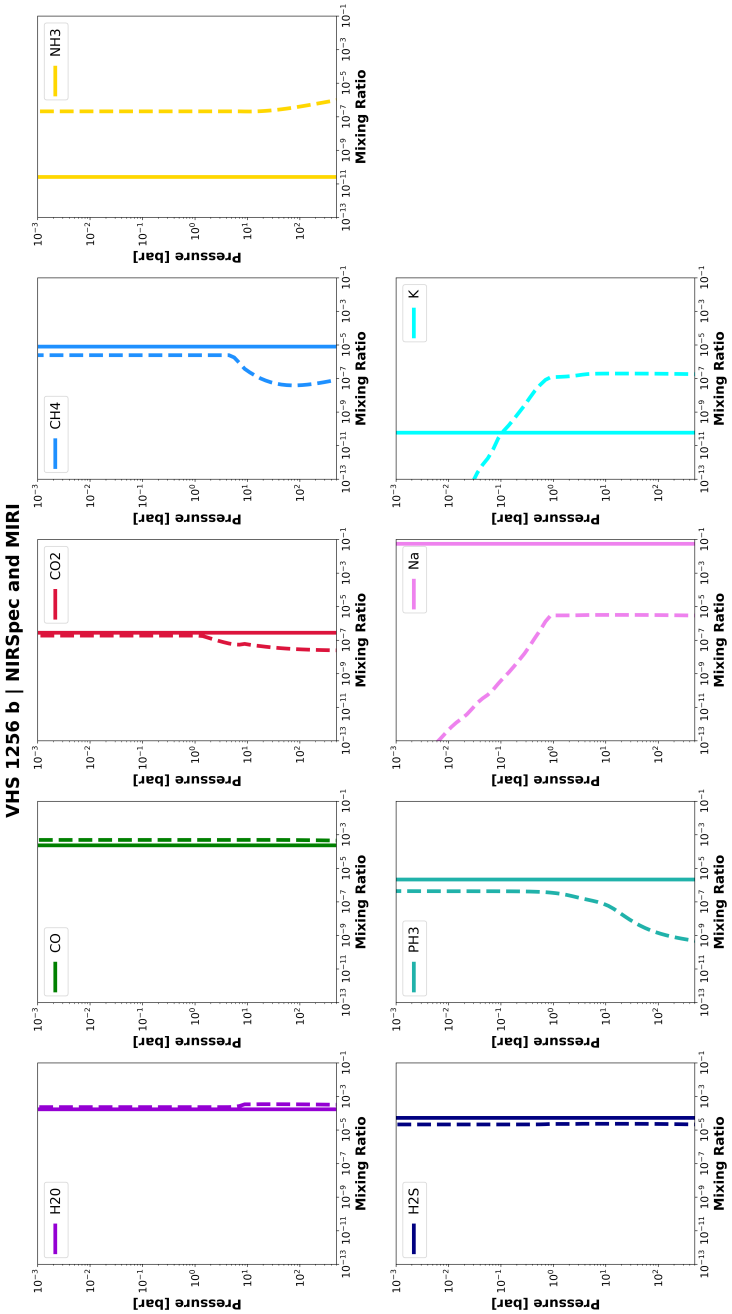

Figure 5.10: Molecular abundance profiles from simulated VHS 1256 b observations via Exo-REM (dashed line) and the retrieved molecular abundance isoprofiles. This result is using simulated NIRSpec and MIRI data.

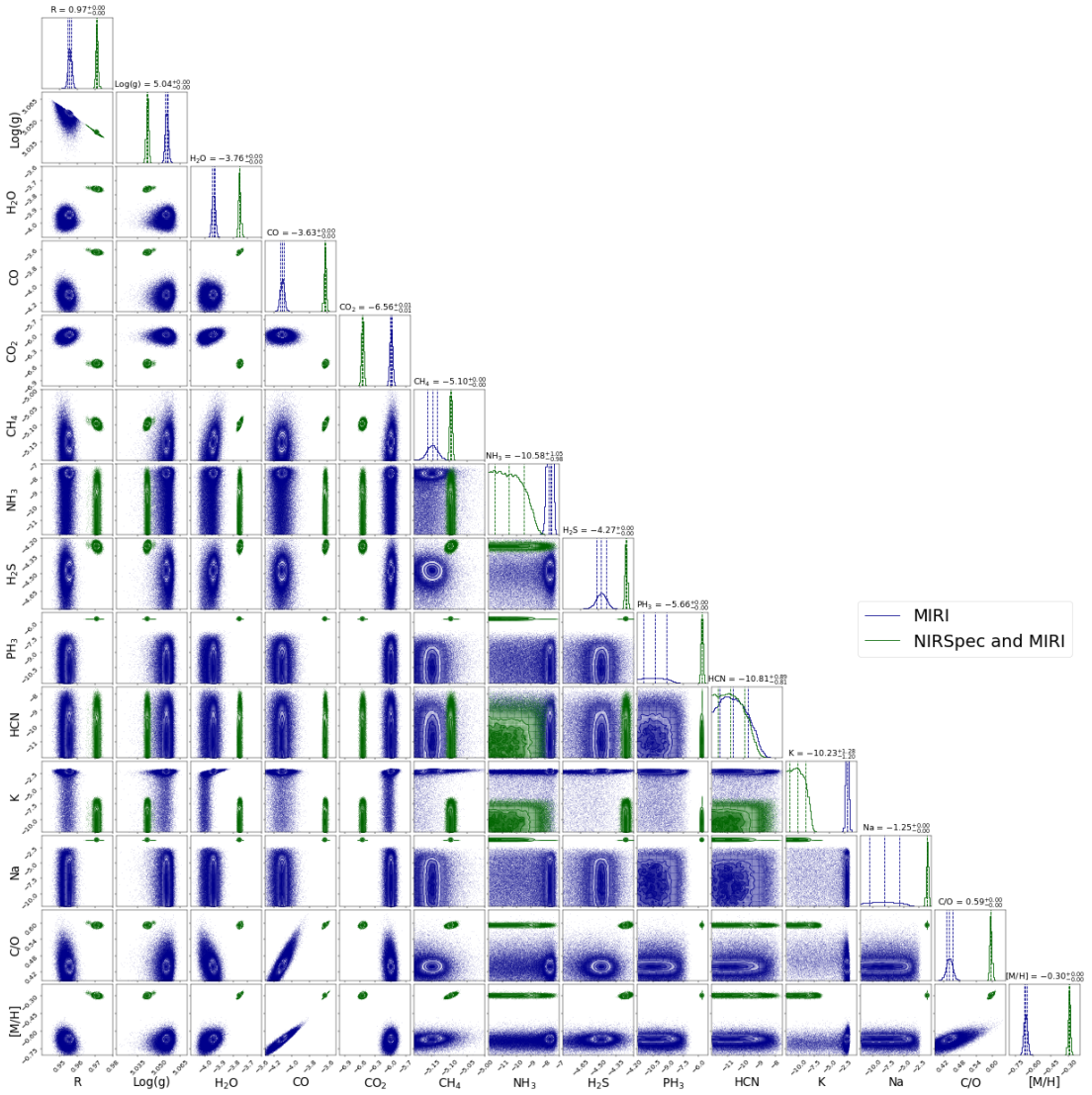

Figure 5.11: VHS 1256 b retrieval posterior comparison.

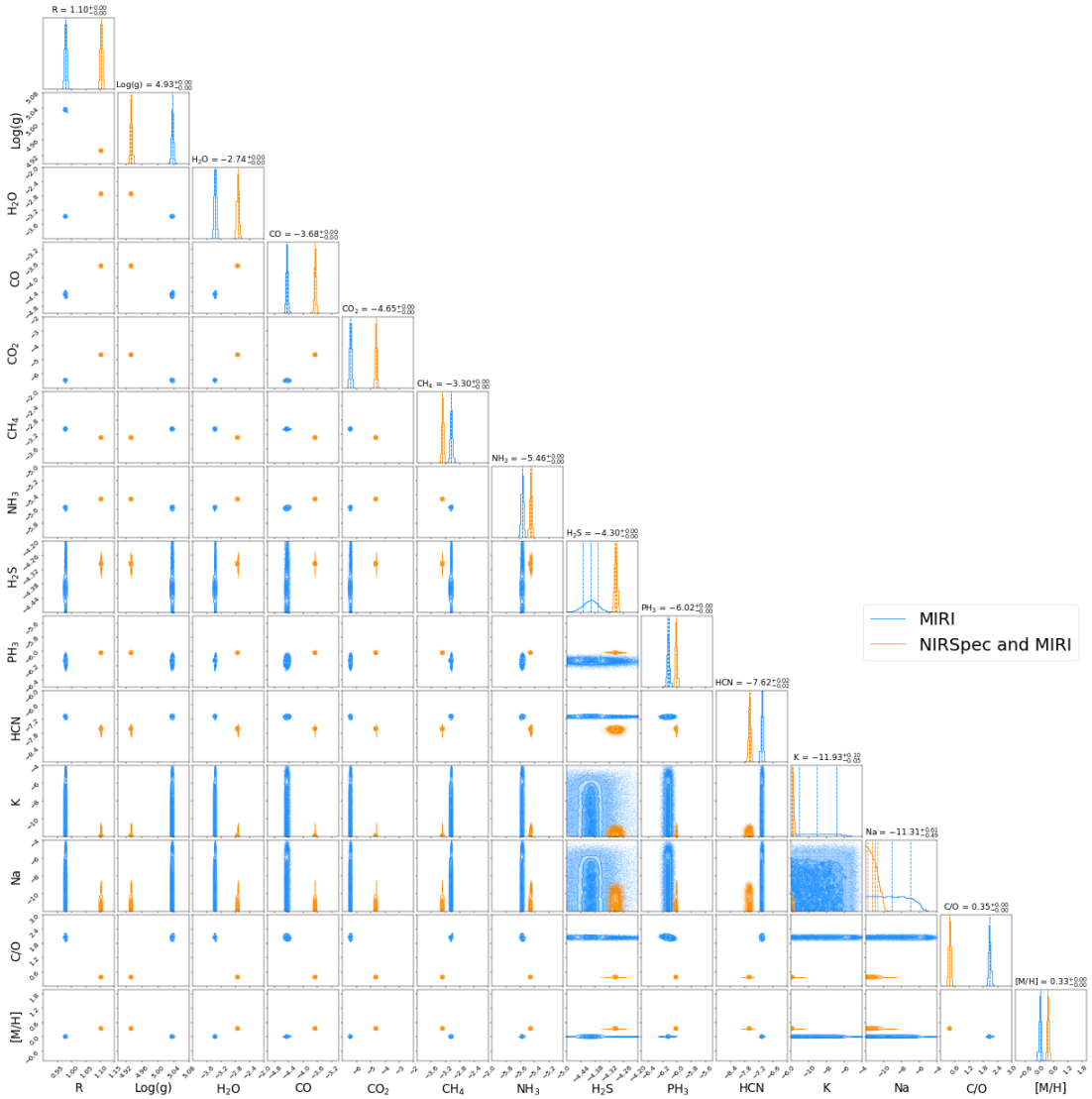

Figure 5.12: Ross 458 c retrieval posterior comparison.

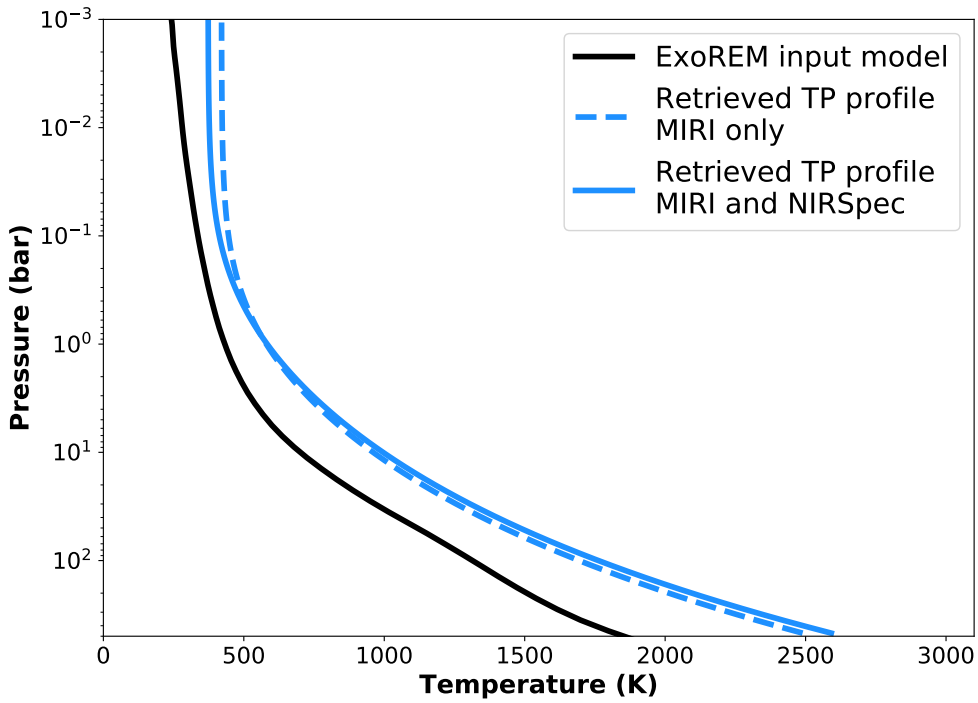

(a) Ross 458 c

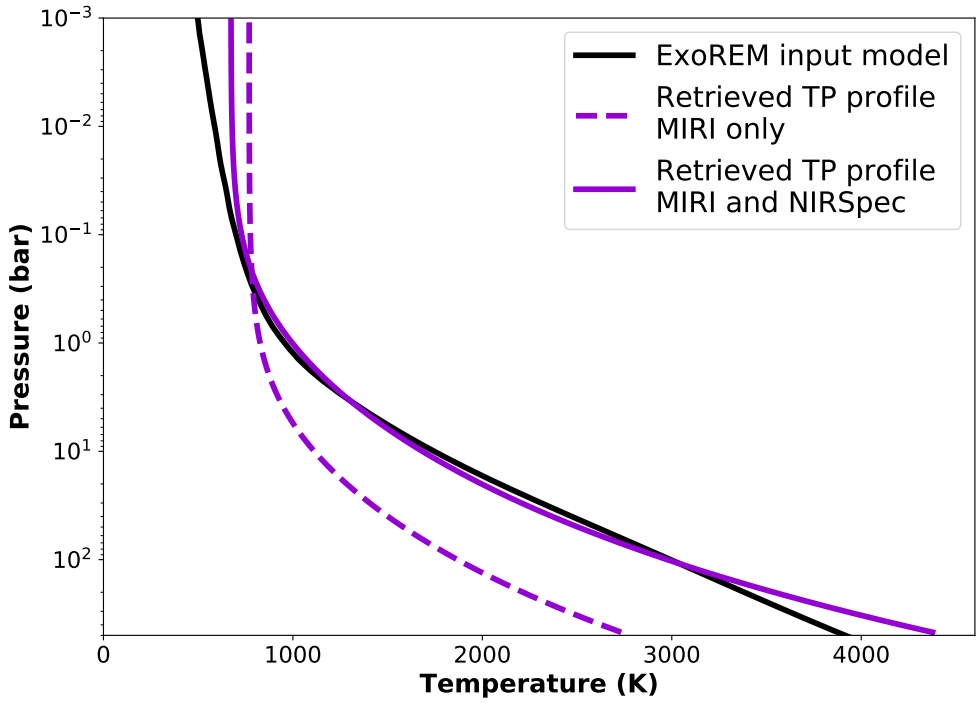

(b) VHS 1256 b

Figure 5.13: Temperature-pressure profiles for simulated observations (black solid line) with the retrieved profile using only MIRI simulations (dashed non black line) and profile retrieved using NIRSpec and MIRI simulations (solid non black line). The 1σ bounds are also plotted but not visible as they are so narrow.

precise results, which is primarily demonstrated by the minute uncertainties our retrievals places on many parameters, but which may not represent the absolute truth. One of the most important areas with which to exercise caution is likely to be the derived C/O ratio. We see deviation between input model and retrieved model, but still very precise constraints. Given the weight a C/O ratio is given in relation to tracing formation, our results suggest that caution should be applied to these values.

5.4.2 | Future work

5.4.2.1 | Testing different temperature-pressure profiles

We see that our the retrievals were not always able to match the input temperature-pressure profile (see Figure 5.13. In most cases the temperature gradient was well matched. However, our retrieval used a temperature-pressure profile we knew could replicate the gradient trend of the input model, despite only have two free parameters. Such a simple parameterisation within the retrieval, however, may not capture the true profile when applied to future data. For this reason, we will first test if a more flexible parameterisation such as that from Madhusudhan and Seager (2009) or Mollière et al. (2020) can replicate the input of Exo-REM. Second, we will test the impact of introducing differing structures, such as temperature inversions and sharp changes in temperature gradient, to test how different retrieval parameterisations respond and the possible issues or biases this could introduce. Another test will be to explore how a more flexible profile performs with the cloudy simulated data of VHS 1256b. We have often found that a retrieval employs a more isothermal gradient in order to account for, or mimic, clouds. However, Burningham et al. (2021) demonstrated the importance of mid-IR data for breaking this degeneracy. We would aim to show that MIRI data is crucial for breaking this modelling degeneracy.

5.4.2.2 | Testing alkali cross sections

We suspect that mismatches in alkali cross sections between the Exo-REM input and the TauREx3 retrieval resulted in issues for the retrieval of these molecules. Exo-REM uses the a combination of approaches from Burrows et al. (2000) and Baudino et al. (2015) for the Na and K cross section. This differs from our cross section for Na and K which were computed using updated methods described in Allard et al. (2016) and Allard et al. (2019). Motivated by this, we will replicate the analysis performed here using the same cross sections setup for these molecules. However, retrievals commonly encounter difficulties with these particular molecules. Our analysis, with an alkali cross section mismatch included, may indicate the possibly issues that will be encountered with real JWST data.

5.4.2.3 | Retrieving same cloud model

We used differing cloud models for our input model (F_{sed}) and retrieval model (Mie scattering). For that reason, we neglected to focus on how the retrieval extracted the cloud parameters apart from the common component of particle size and cloud fraction. Retrieving clouds will be a key aim of modelling brown dwarfs and exoplanets during the JWST era. Therefore, we will explore if we are able to accurately and precisely retrieve different cloud parameterisations using simulated JWST data. For this, we will add further cloud models, such as that from Ackerman and Marley (2001) and Charnay et al. (2018), so we can more directly compared the same input model and retrieval parameters. Further tests could involve, for example, exploring the ability of the retrieval to extract differing types of particle size distributions and cloud species.

5.4.2.4 | Attempting to retrieve multiple cloud layers

Burningham et al. (2021) and Manjavacas et al. (2021) have shown evidence for the presence of multiple cloud layers in brown dwarfs. Such structures will likely be present in many substellar objects that will be observed with JWST. Most

retrievals of substellar objects have employed only a single layer of clouds (Lavie et al., 2017, Mollière et al., 2020, Gonzales et al., 2020). This will undoubtedly change in the era of JWST, with multiple cloud layer modelling becoming the norm. However, the extent to which we can constrain the presence of such atmospheric structures, using JWST data, is currently unexplored. Therefore, we will create simulated JWST data sets with cloud layering of different condensate species, motivated primarily by the results of (Burningham et al., 2021) and Manjavacas et al. (2021), and explore if a retrieval can accurately and precisely replicate such a structure.

5.4.2.5 | Retrieving variability?

Variability is a common characteristic of low surface gravity substellar objects (Vos et al., 2019). Particularly, VHS 1256 b exhibits such significant variability that it may experience up to $\sim$ 10% variability during the JWST ERS observations. Motivated by this, we will explore if retrievals detect this variability if the dimension of time is added. We would primarily test if evolution in cloud coverage and structure during the period of a JWST observations could be retrieved.

5.4.2.6 | Testing NIRSpec by itself

Within our retrieval analysis we tested the simulated data of MIRI plus MIRI and NIRSpec simulated data combined. However, we have not yet tested a retrieval solely using NIRSpec data. This test will help to further probe which wavelength regions are key for different parameters, especially different molecular abundances. NIRSpec covers the feature dense region of the near and mid IR while MIRI uniquely covers molecular features inaccessible to NIRSpec. Therefore, we will probe which characteristics we can constrain using solely NIRSpec data and demonstrate when the addition of MIRI data proves vital.

5.4.2.7 | Reducing retrieval run times

Retrievals require a significant amount of computational time. As resolution and wavelength coverage increases so too do the retrieval run time. The combined resolution and coverage of JWST, especially when combining MIRI and NIRSpec data, is extremely challenging in terms of compuational expense. For example, our analysis of our simulated data of VHS 1256b, combining MIRI and NIRSpec, took approximately a week to run on 540 cores for a single retrieval. We also expect that the number of parameters included in retrievals of the real data sets for this object will likely be higher due to modelling expansions. This could be due to employing more flexible temperature-pressure profile, additional cloud layers or condensates, as well as considering characteristics such as variability. This will act to further increase the computational time, greatly restricting the ability to run many retrievals. This will place practical limits how much time can be spent testing and calibrating different model setups, which is common practice in retrieval studies. Motivated by this, we will explore the impact of de-resolving JWST data to a lower resolution and testing retrievals using only windows of the JWST wavelength coverage. We would aim to demonstrate that accurate retrievals could be performed with less computing time by using a more computationally efficient approach.

5.5 Summary

Motivated by the imminent data of JWST, we test the ability of retrievals to characterise brown dwarfs and giant exoplanet chemical catalogues and bulk parameters. We first used Exo-REM to make a model of Ross 458 c and VHS 1256 b, targets which are included within JWST GTO and ERS programs. Using these forward models, we employed MIRISim and the JWST ETC to simulate mock observations of these objects. We then performed retrievals on these mock observations using TauREx3. The main results of this study are:

- Using ExoREM, we created a forward model of a cloudy L dwarf (VHS

1256b) and a cloudless T dwarf (Ross 458c).

- Using the ExoREM forward models, we created a simulation of JWST NIRSpec and MIRI observations for VHS 1256 b and Ross 458c via MIRISim and the JWST ETC.
- Using TauREx3, we performed a retrieval analysis of this simulated data.
- These retrievals produce very precise, but not always accurate, constraints on molecular abundances.
- The retrievals encounters issues accurately constraining alkali abundances, likely due to cross section mismatches between the ExoREM model and TauREx3 model.
- The retrievals were consistently unable to constrain surface gravity (and by extension, mass)
- In the case of the VHS 1256b simulated data, which included clouds, the retrieval was unable to constrain any cloud paramters, likely due to a modelling mismatch between ExoREM and TauREx3.
- Most retrievals of the simulated data were unable to accurately replicate the temperature-pressure structure of the input ExoREM model.

CHAPTER 6

Summary and outlook

6.1 Summary of chapter 2

Here, we outlined TauREx3 (Waldmann et al., 2015a,b, Al-Refaie et al., 2019), the Bayesian retrieval code, including several additions and adaptations that were made in order to accommodate the aims of this work. These included:

- Addition of a new emission flux mode, allowing directly-imaged spectra to be analysed.
- Addition of an error inflation considerations for the spectroscopic data (Line et al., 2015).
- Addition of a scaling factor capability to account for potential photometric inaccuracies or photometric mismatches between difference spectral bands (Oreshenko et al., 2020, Mollière et al., 2020).
- Addition of 3 new cloud parameterisations includes a power law deck, power law slab (Burningham et al., 2017) and power law infinity deck.
- Addition of the lognormal particle size distributions for the Mie cloud opacity parameterisations (Ackerman and Marley, 2001)
- Addition of a fractional cloud consideration.
- Additions of 2 new temperature-pressure structure parameterisations. This includes the three layer structure outlined in Madhusudhan and Seager (2009) and the radiative equilibrium structure from Lee et al. (2013) and Lavie et al. (2017).

6.2 Summary of chapter 3

Here, we presented results for the cool exoplanet 51 Eri b, the first application of a free chemistry retrieval analysis to this object, using spectroscopic observations from GPI and SPHERE. While our retrieval analysis is able to explain

spectroscopic and photometric observations without employing cloud scattering, we conclude this could be a result of employing a flexible temperature-pressure profile which is able to mimic their presence. We present Bayesian evidence for an ammonia detection with a 2.7σ confidence, the first indication of ammonia in an exoplanetary atmosphere. This is consistent with this molecule being present in brown dwarfs of a similar spectral type. We retrieve a super-stellar C/O ratio which tentatively hints at formation via gravitational instability. We also demonstrate TauREx3's applicability to sub-stellar atmospheres by presenting results for brown dwarf benchmark GJ 570D which are consistent with previous retrieval studies, whilst also exhibiting systematic biases associated with the presence of alkali lines. Finally, we demonstrate the chemical similarities between 51 Eri b and GJ 570D in relation to their retrieved molecular mixing ratios.

6.2.1 | Future Work

With the implementation of several new cloud paramaterisations in TauREx3, we will now compare our cloudless analysis from this study to a novel cloud retrieval study for this object. This will aim to rigorously test if clouds are statically preferred and how the addition of clouds affects the constraints of the other parameters such as the chemical abundances. Such work will be enhanced by the data taken by JWST GTO program 1412, which will observe 51 Eri b via NIRCam's Coronagraphic imaging mode.

6.3 Summary of chapter 4

We used TauREx3 for analysis of near-infrared spectroscopy for a sample of directly imaged gas giant exoplanets and low surface gravity brown dwarfs, including Beta Pic b, HR 8799cde, PSO 318 and VHS 1256 b. Using this sample, which spans the L spectral types, we have probed a range of cloud species. We also explored the implementation of non-uniform clouds and the impact of using different cloud particle size distributions. We show a Bayes Factor preference for

clouds to be included in retrieval for all our objects but are unable to clearly determine a preference for a specific cloud species for any of our objects. This is linked to the inability to tightly constrain a cloud particle size distribution for any of our objects. We derive retrieval C/O ratios for PSO 318 ($0.44^{+0.05}_{-0.06}$) and VHS 1256 b ($0.83^{+0.04}_{-0.04}$) for the first time. We derived unexpectedly low C/O ratio ratios for HR 8799c and d, likely due to incorrectly retrieved chemical abundances stemming from systematic issues in the GPI K band spectroscopy for these objects. We demonstrated spectral fitting issues which arise when combining data of differing resolutions or signal-to-noise ratios. We tested fractional cloud coverage with our retrievals generally showing a preference to converge to a coverage ∼97-100%. We show that a possible trend in retrieved atmospheric C/O with separation may exist as predicted by formation disk composition models. However, this is extremely tentative trend and will require much better C/O constraints and a more populated parameter space to explore in more detail. This testing of retrieval frameworks is essential given the upcoming launch of JWST and the subsequent high-quality data it will provide.

6.3.1 | Future work

This study omitted the inclusion of any photometric points within the retrieval analysis. Future work will include this data. Our study also enforced a Gaussian radius prior in each case. Future work could compare results in the case a uniform prior is used instead. Omitting the problematic K band data points in retrievals for HR 8799c and d retrievals will also be explored. This study included only 4 molecules within the retrieval, therefore, further analysis will be conducted by employing further molecules. We also enforced an inflexible radiative equilibrium temperature-pressure profile for the retrievals within this study. Therefore, future work could include allowing for a more flexible profile such as the Madhusudhan and Seager (2009) parameterisation.

6.4 Summary of chapter 5

We employed ExoREM to create a forward model of a cloudy L dwarf and a cloudless T dwarf. These models were then run through the JWST ETC and MIRISim observation simulators in order to create a simulated data set of the upcoming ERS and GTO spectroscopic observations of VHS 1256b and Ross 458c. Using TauREx3, we then ran a set of retrievals on this simulated data, primarily in order to test the precision and accuracy of the retrieved chemistry. We found that these chemical constraints are often very precise, but not always accurate. We also encountered issues correctly constraining the alkali abundances, along with surface gravity (and mass).

6.4.1 | Future work

We employed an inflexible radiative equilibrium temperature pressure profile in our retrievals of the simulated observations. Future work will explore the ability of different temperature-pressure profiles, with varying degrees of flexibility, to correctly match the input ExoREM model. As we encountered issues correctly constraining the alkali abundances, likely due to cross section mismatches in the models of ExoREM and TauREx3. We will test this theory by using the same alkali cross sections in the forward model for the simulations and the retrieval model. We also didn't explore if cloud parameters could be correctly constrained, due again to a model mismatch between ExoREM and TauREx3. Using the same, or more similar cloud modelling approaches between the observation forward model and the retrieval model, we will test the retrieval's ability to constrain the simulated observation input model's cloud setup. As an extension of this work, we will also test the limits of a retrieval's ability to detect and constrain multiple cloud layers when using JWST data. For simplicity, VHS 1256b's extensive variability was neglected in the observation simulation. However, future work will test if a retrieval can constrain parameters related to the variability of such as object, such as an evolving cloud structure or changing cloud coverage. In our study, we focused on using MIRI data or MIRI data combined with NIRSpec

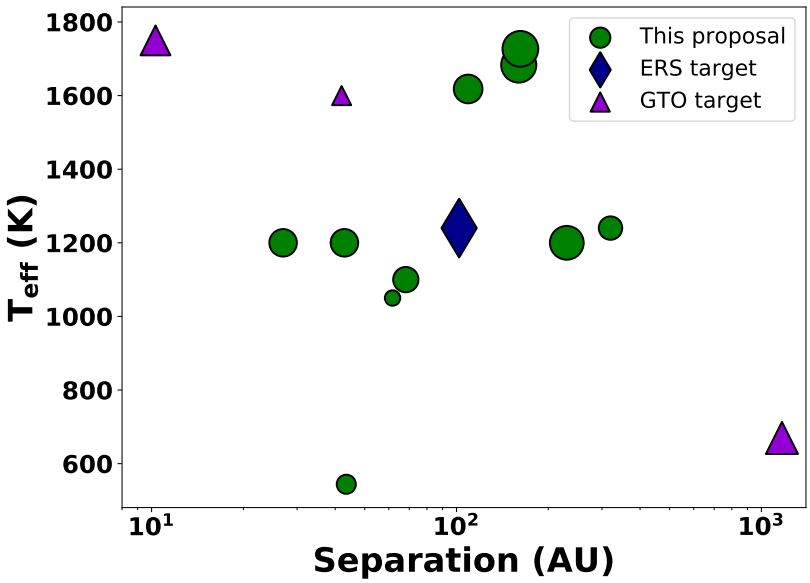

Figure 6.1: PLATFORM sample of directly imaged planets covers both separation and temperature, allowing us to systematically approach atmospheric chemistry and links to formation. Marker size indicates mass.

data. Therefore, future work will test retrievals using only NIRSpec data. Finally, we will test ways of decreasing the retrievals computational run times. Such tests will involve using specific spectral windows and/or using de-resolved spectra.

6.5 A JWST GO program: PLanetary Abundance Tracing to constrain FORmation in the mid-IR - PLATFORM

PIs: Polychronis Patapis, Niall Whiteford, Evert Nasedkin

With no spectroscopic observations for directly-imaged exoplanets beyond 5μm we are limited in our ability to perform extensive chemical characterisations of brown dwarfs and exoplanets. Thus, many key questions remain unanswered:

- What is the chemical makeup of exoplanet atmospheres?

- Can we use their atmospheres to trace the story of their formation?

These questions will remain open until we begin to demographically study this class of young exoplanets via observations extending to the uncharted mid-IR range covered by JWST. Using JWST observations, we aim to tell the formation stories of these objects via the in depth characterisation of novel chemistry which is only accessible through a space-based mid-IR mission.

Studies (Öberg et al., 2011, Öberg and Bergin, 2021, Cridland et al., 2020) have attempted to link exoplanet composition back to the protoplanetary disk environment, as pebble drift and iceline location will lead to regions that are enriched in certain chemical species. However, such studies lack observational constraints with which to rigorously test these predictions. By combining disk formation models with the giant exoplanet atmospheric measurements provided by this program, we can start to probe their formation histories, possibly even chemically differentiating between core-accretion and gravitational instability pathways.

With many past, present and future instruments populating the near-IR with observations (Biller and Bonnefoy, 2018, Zurlo et al., 2016, Bonnefoy et al., 2016, Samland et al., 2017, Rajan et al., 2017, Gravity Collaboration et al., 2019, Nowak, M. et al., 2020, Konopacky et al., 2013, Greenbaum et al., 2018, Ingraham et al., 2014) JWST is the unique solution to probe the mid-IR range and will remain so until the mid-IR instruments become available on extremely large telescopes. The mid-IR offers access to the many novel spectral features. We propose to use the MIRI Medium Resolution Spectrometer (MRS) to observe the emission spectrum of a representative sample of 10 planetary mass companions across a range of separations and temperatures. MIRI is, and will be, the only instrument to which the mid-IR wavelength range is accessible for at least a decade to come.

With currently only a small handful of observations with R>500 for some of these objects making the MRS mode ideal for this program. Therefore, our JWST-MRS GO program would yield transformative observations and will build on the Guaranteed Time GTO and ERS direct imaging programs. This would be the first mid-IR survey of directly-imaged exoplanets, and will provide a wealth of

data with which to improve atmospheric and formation models.

- **Goal 1:** Systematically study atmospheric properties across our sample, quantifying the abundances of carbon and nitrogen bearing molecules together with silicate condensates.
- **Goal 2:** Probe the formation history of exoplanets via their chemistry, determining their formation pathways and the search for chemical proto-planetary disk imprints.
- **Goal 3:** Construct a legacy library of observations across novel mid-IR wavelengths which will serve as a powerful benchmarks for atmospheric models.

6.6 Final thoughts

The next decade of exoplanet science will likely revolutionise our understanding of exoplanets and their atmospheres. With the recent successful launch of JWST, an exciting era of astronomy lies ahead. Observations from this telescope will require and permit dramatic expansion of modelling techniques in order to fully exploit and investigate the new data, where the retrieval method explored in this work will play a key role. Beyond JWST, the ELTs will offer further ground breaking detection, observation and characterisation capabilities, helping to further our understanding of these alien worlds.

CHAPTER 7

Appendix

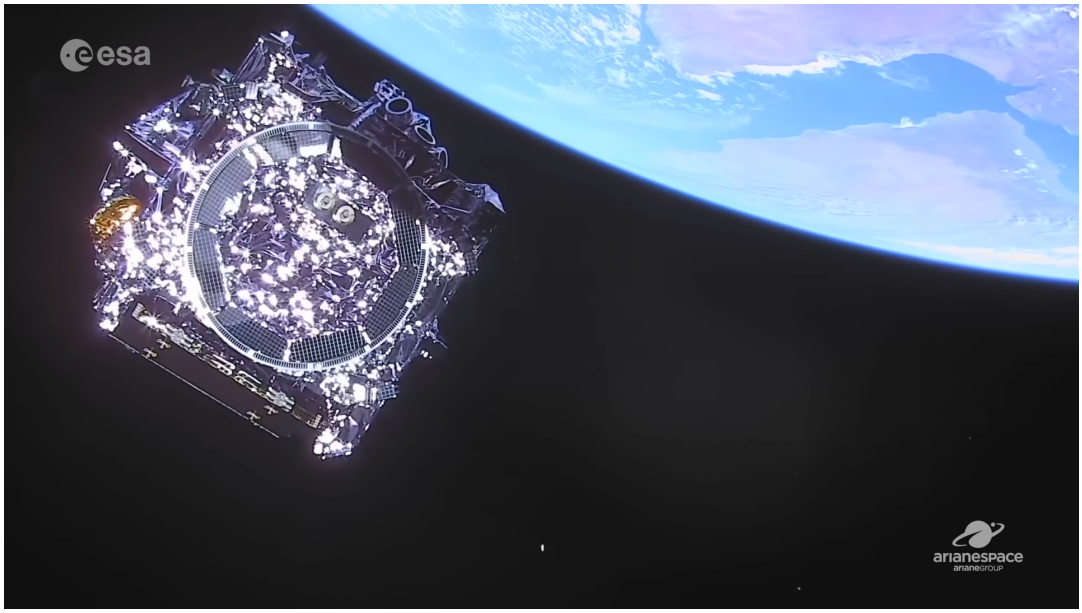

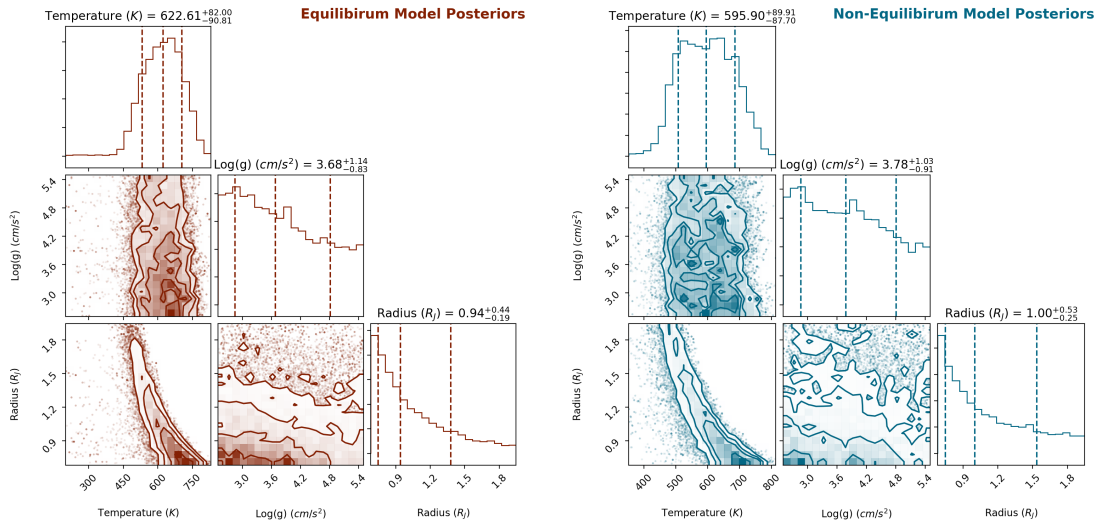

(a) (a) (b) (b)

Figure 7.0: ATMO posteriors plots for 51 Eri b. Left: Equilibrium chemisty model. Right: Non-equilibrium chemistry model.

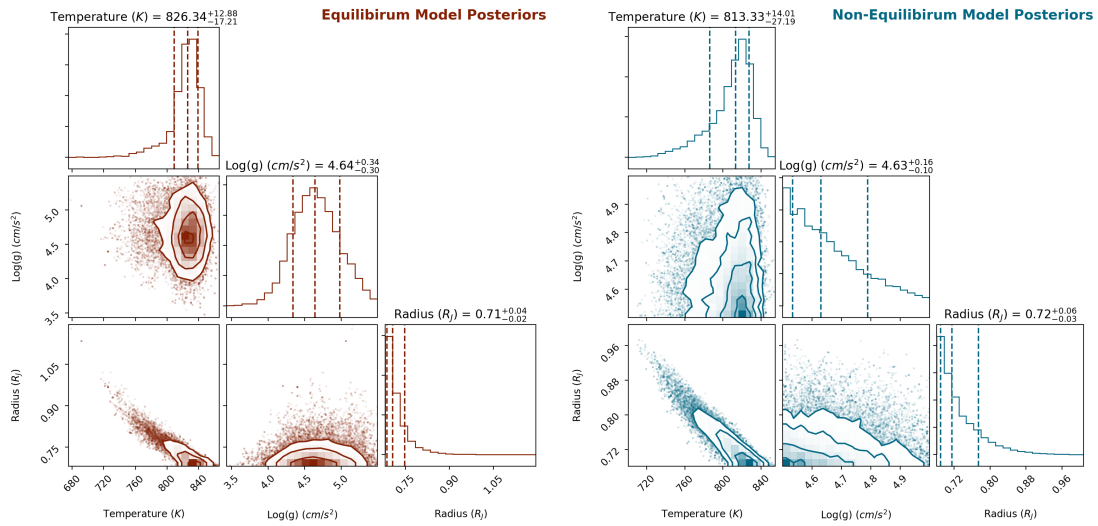

(a) (a) (b) (b)

Figure 7.0: ATMO posteriors plots for GJ 570D. Left: Equilibrium chemisty model. Right: Non-equilibrium chemistry model.

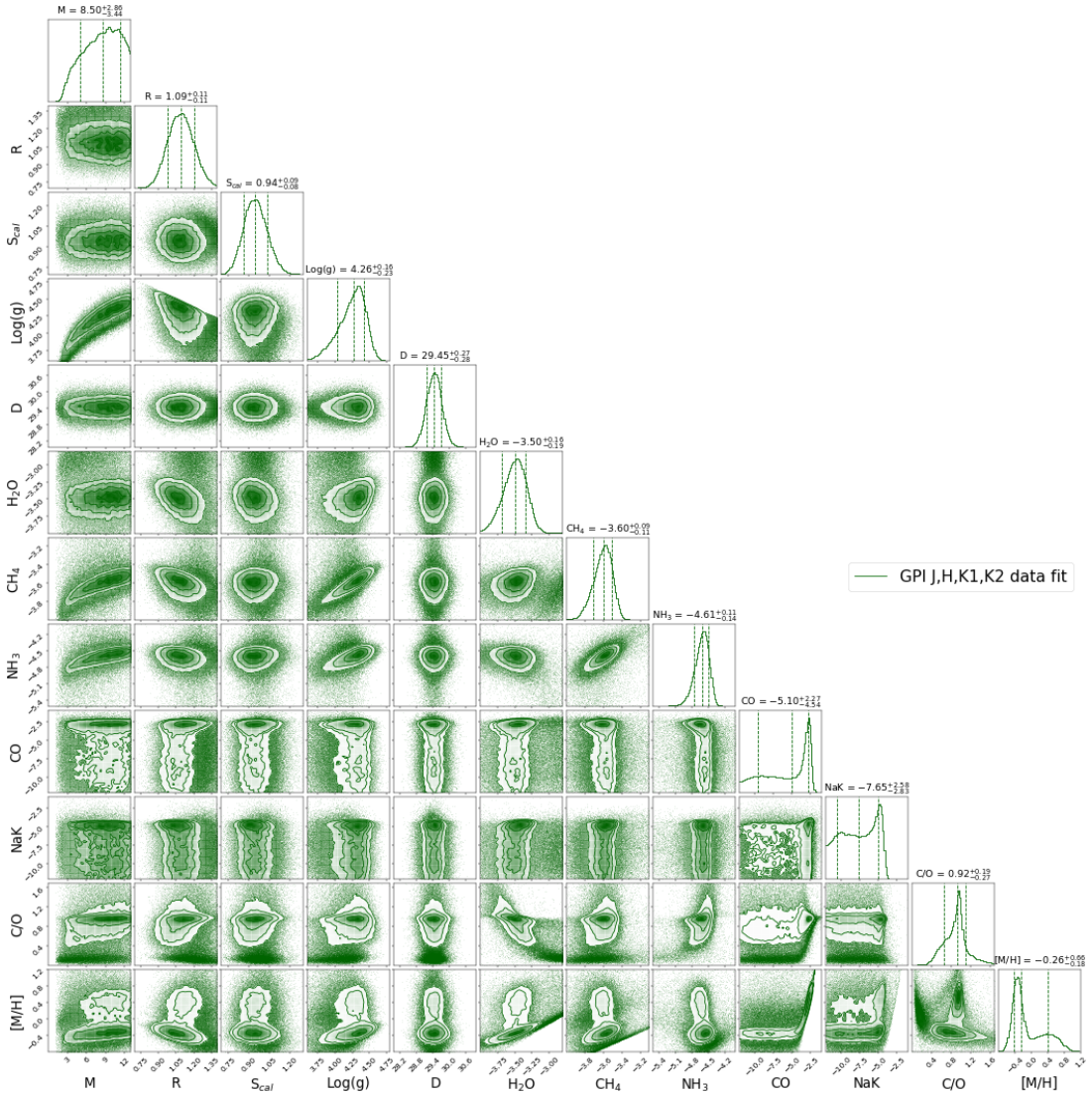

Figure 7.1: 51 Eri b posteriors for GPI J, H and K band data. Log(g), C/O and [M/H] posteriors are inferred parameters, while all the other parameters are sample as part of the retrieval.

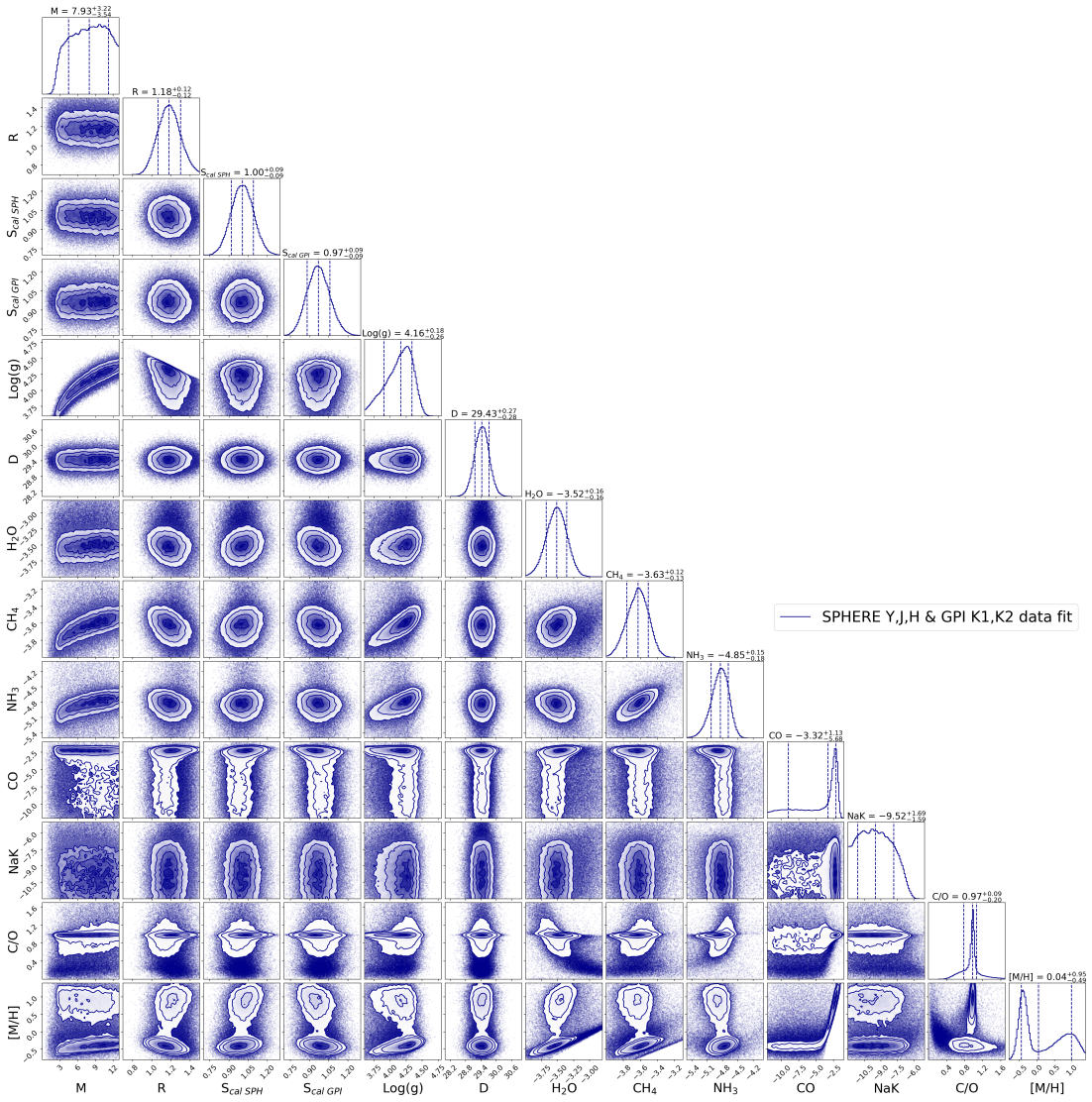

Figure 7.2: 51 Eri b posteriors for SPEHRE Y, J, H and GPI K band data. Log(g), C/O and [M/H] posteriors are inferred parameters, while all the other parameters are sample as part of the retrieval. We note the bi-modal distribution of [M/H] with one of the modes overlapping with the [M/H] derived in Samland et al. (2017).

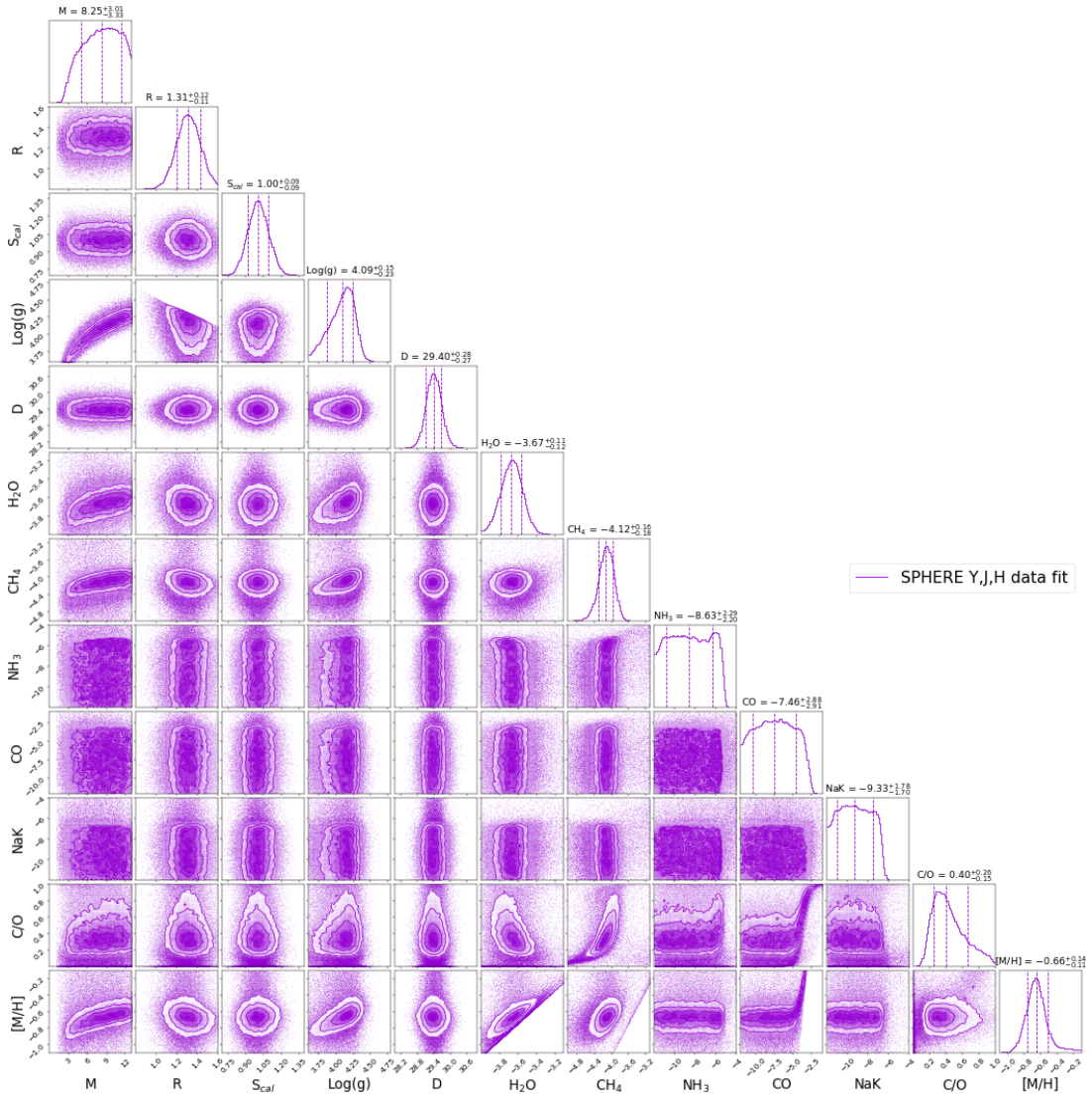

Figure 7.3: 51 Eri b posteriors for SPHERE Y, J and H band data. Log(g), C/O and [M/H] posteriors are inferred parameters, while all the other parameters are sample as part of the retrieval. We note the bi-modal distribution of [M/H] with one of the modes overlapping with the [M/H] derived in Samland et al. (2017).

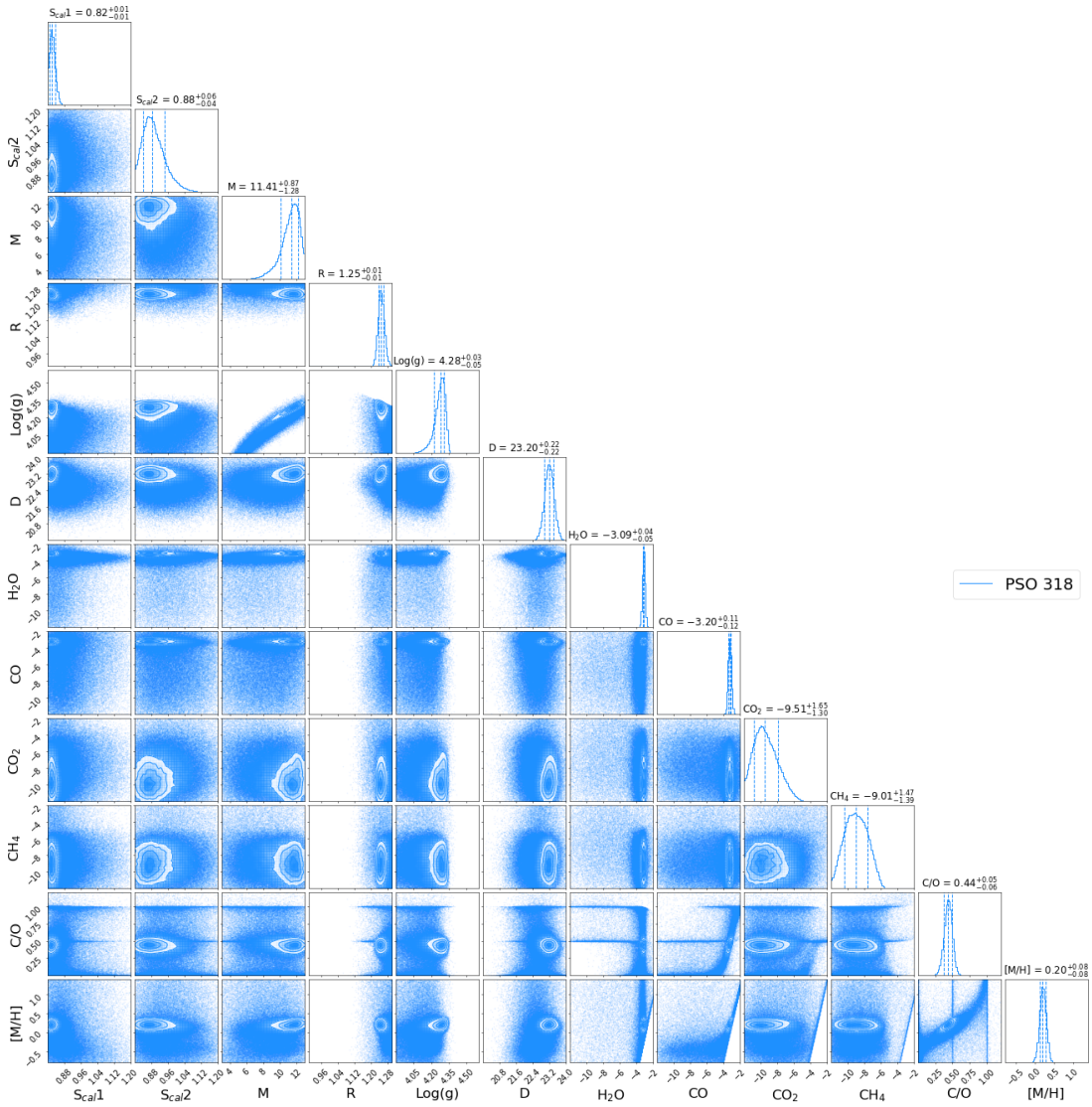

Figure 7.4: PSO 318 corner plot showing the best-fit model retrieved parameters. Log(g), C/O and [M/H] posteriors are inferred parameters, while all the other parameters are sample as part of the retrieval.

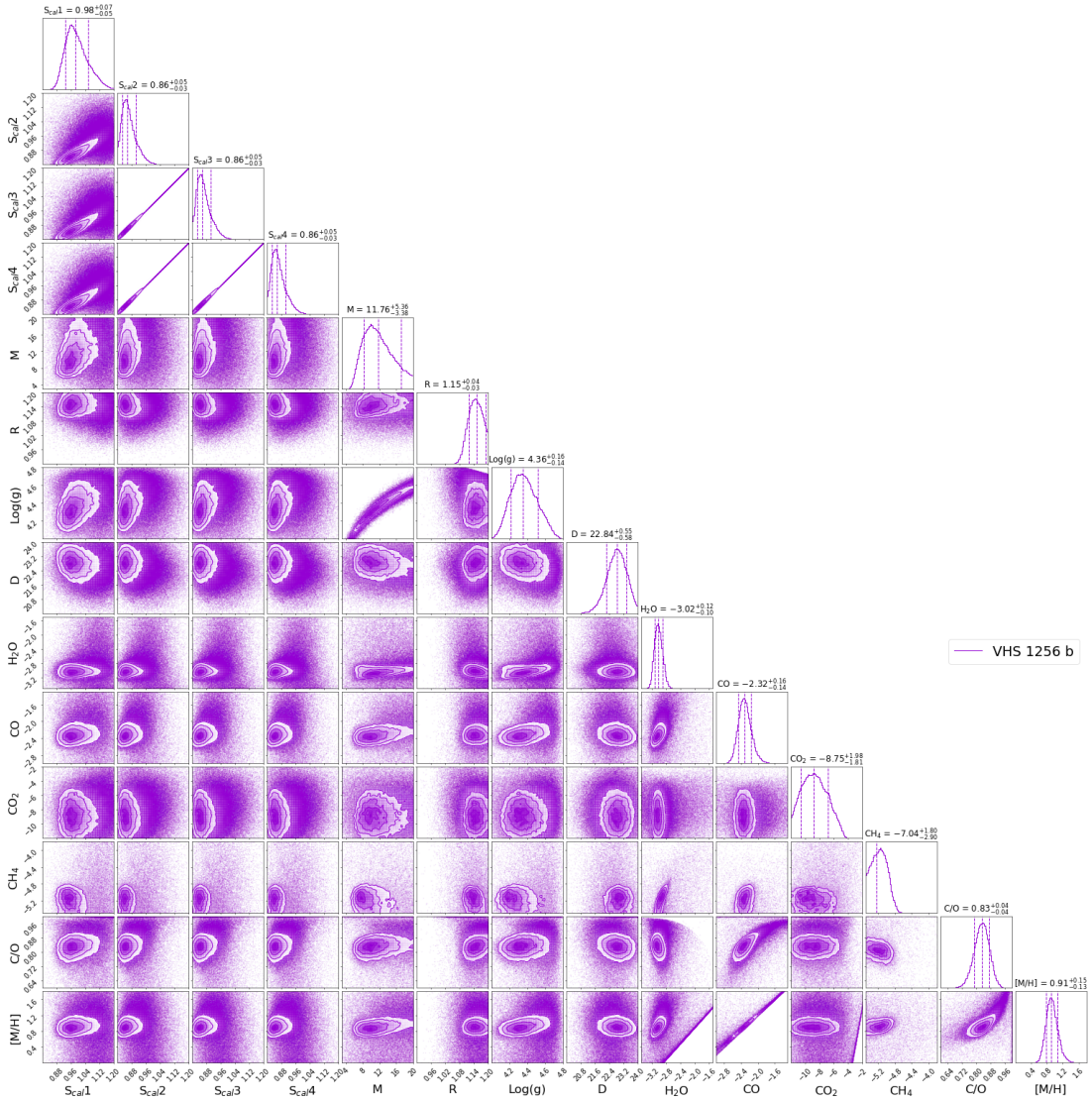

Figure 7.5: VHS 1256 b corner plot showing the best-fit model retrieved parameters. Log(g), C/O and [M/H] posteriors are inferred parameters, while all the other parameters are sample as part of the retrieval.

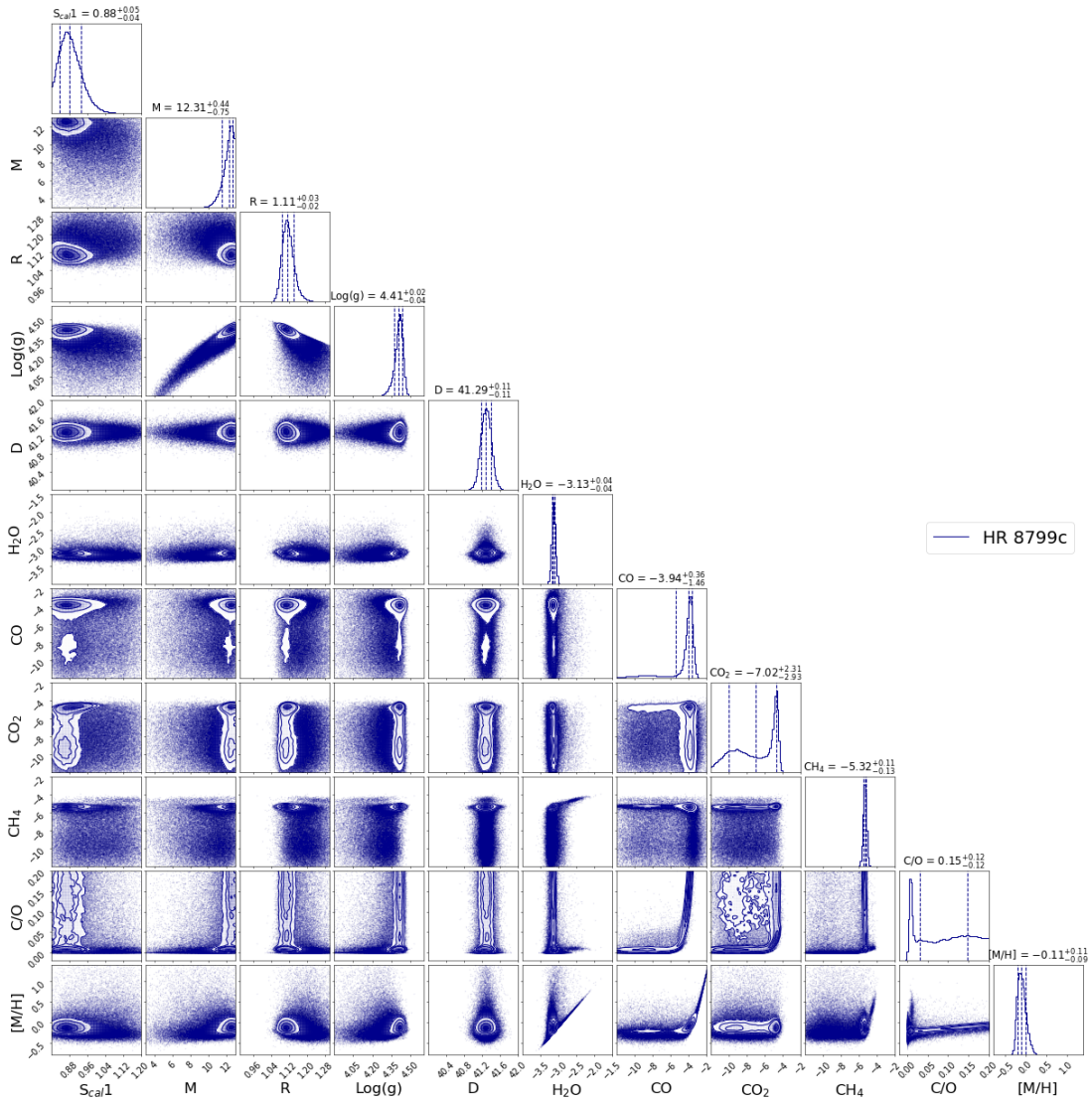

Figure 7.6: HR 8799c corner plot showing the best-fit model retrieved parameters. Log(g), C/O and [M/H] posteriors are inferred parameters, while all the other parameters are sample as part of the retrieval.

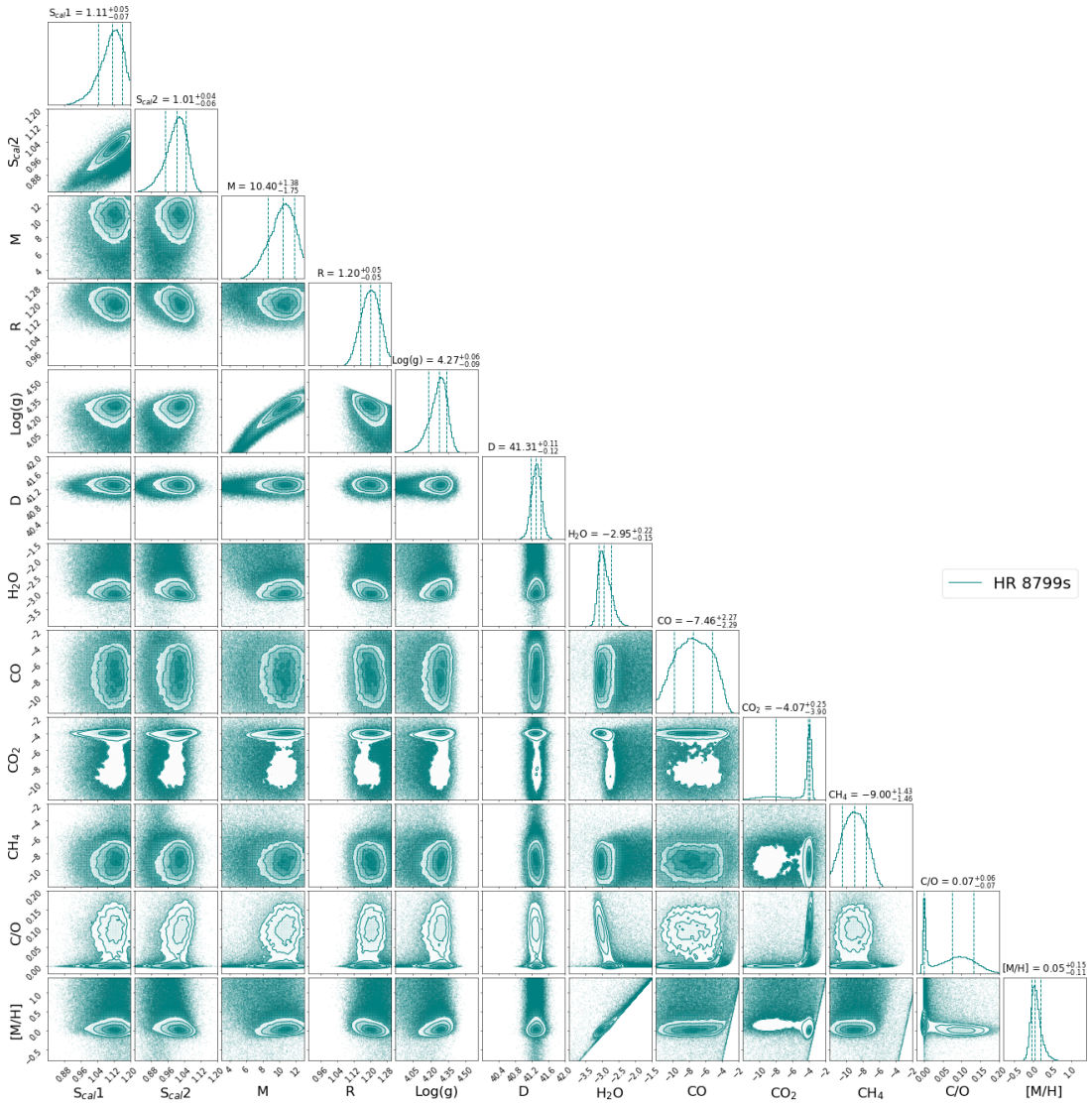

Figure 7.7: HR 8799d corner plot showing the best-fit model retrieved parameters. Log(g), C/O and [M/H] posteriors are inferred parameters, while all the other parameters are sample as part of the retrieval.

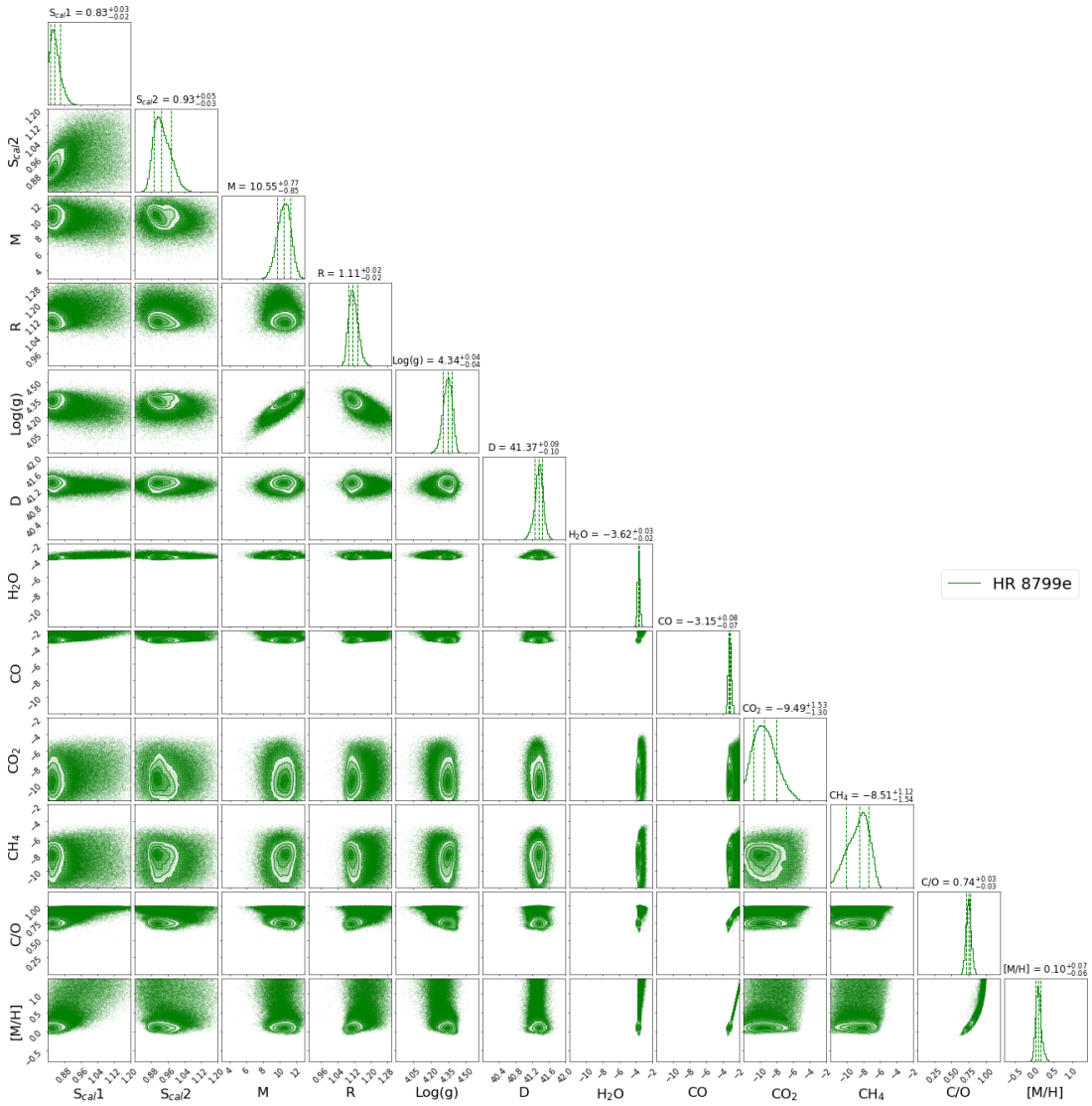

Figure 7.8: HR 8799e corner plot showing the best-fit model retrieved parameters. Log(g), C/O and [M/H] posteriors are inferred parameters, while all the other parameters are sample as part of the retrieval.

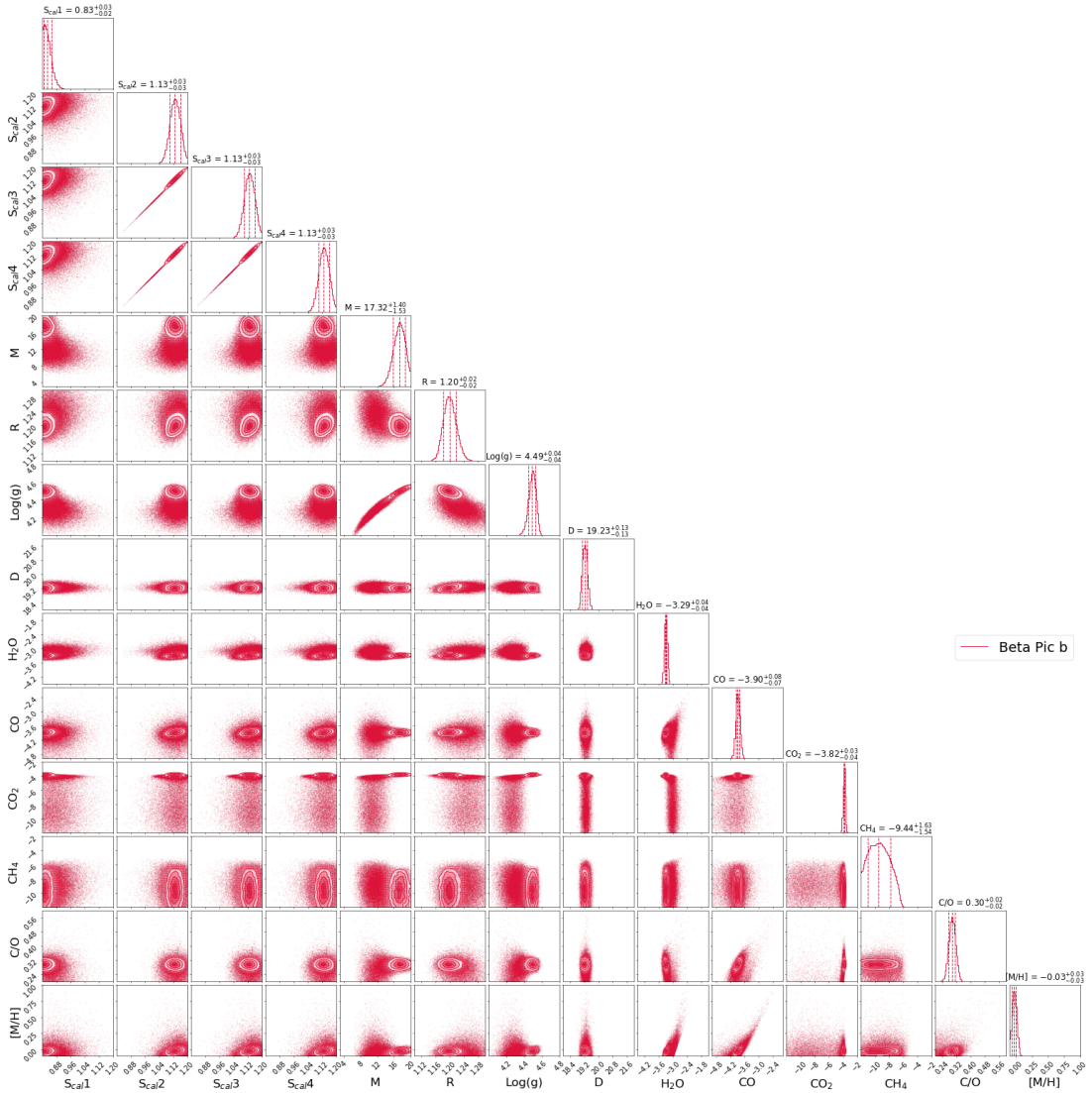

Figure 7.9: Beta Pic b corner plot showing the best-fit model retrieved parameters. Log(g), C/O and [M/H] posteriors are inferred parameters, while all the other parameters are sample as part of the retrieval.

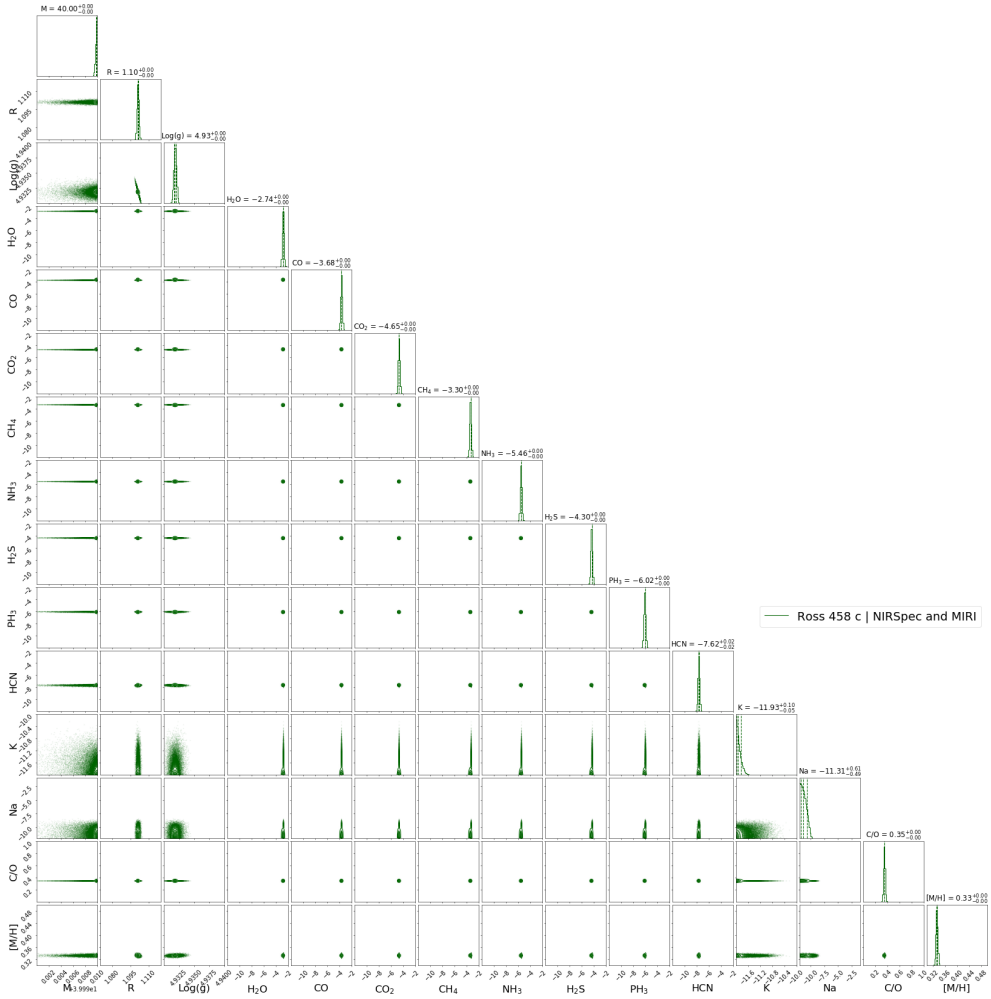

Figure 7.10: Ross 458 c corner plot for NIRSpec and MIRI simulations

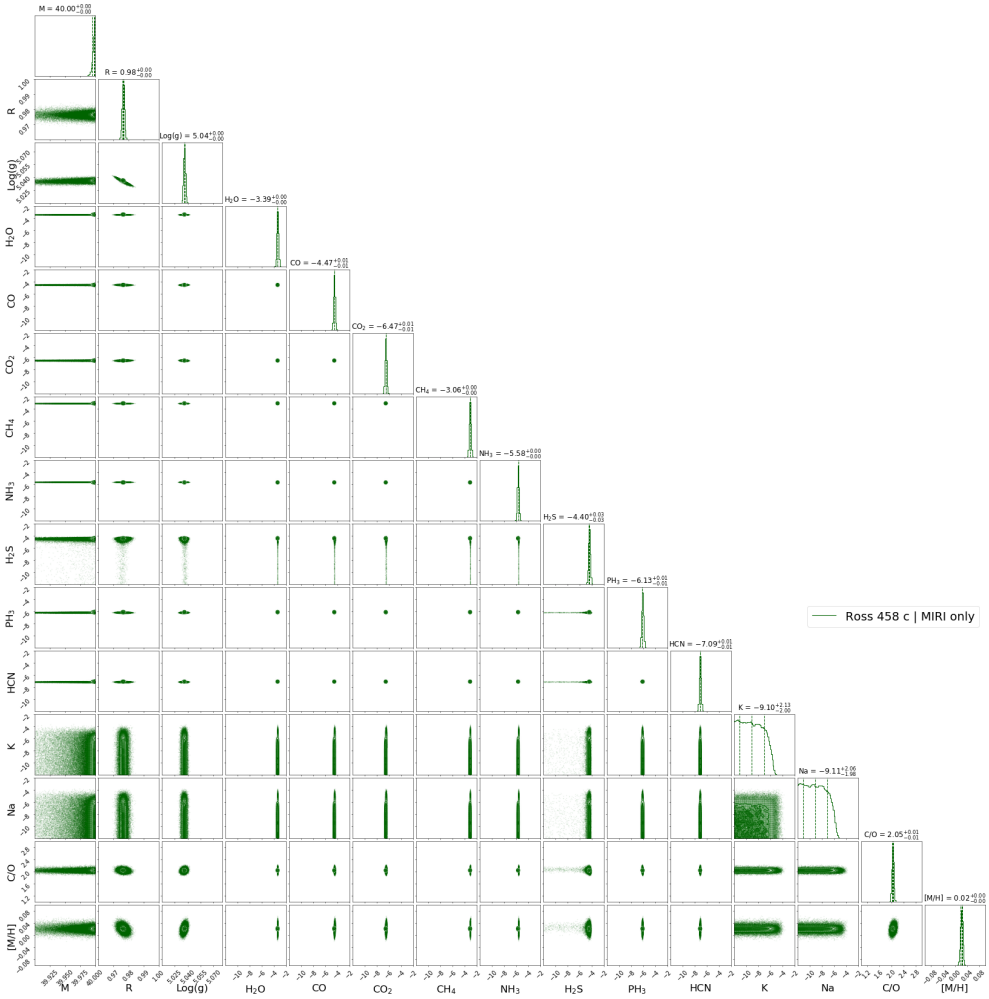

Figure 7.11: Ross 458 c corner plot for MIRI simulations

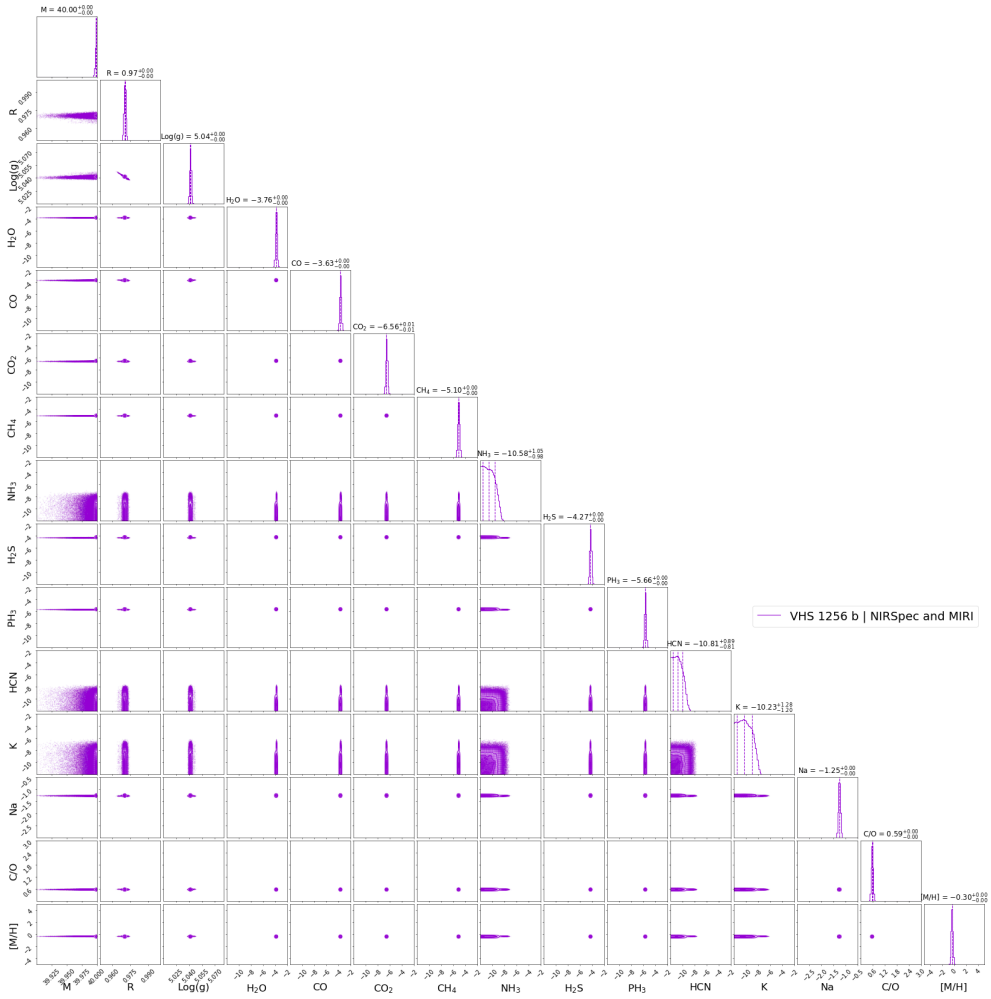

Figure 7.12: VHS 1256 b corner plot for NIRSpec and MIRI simulations

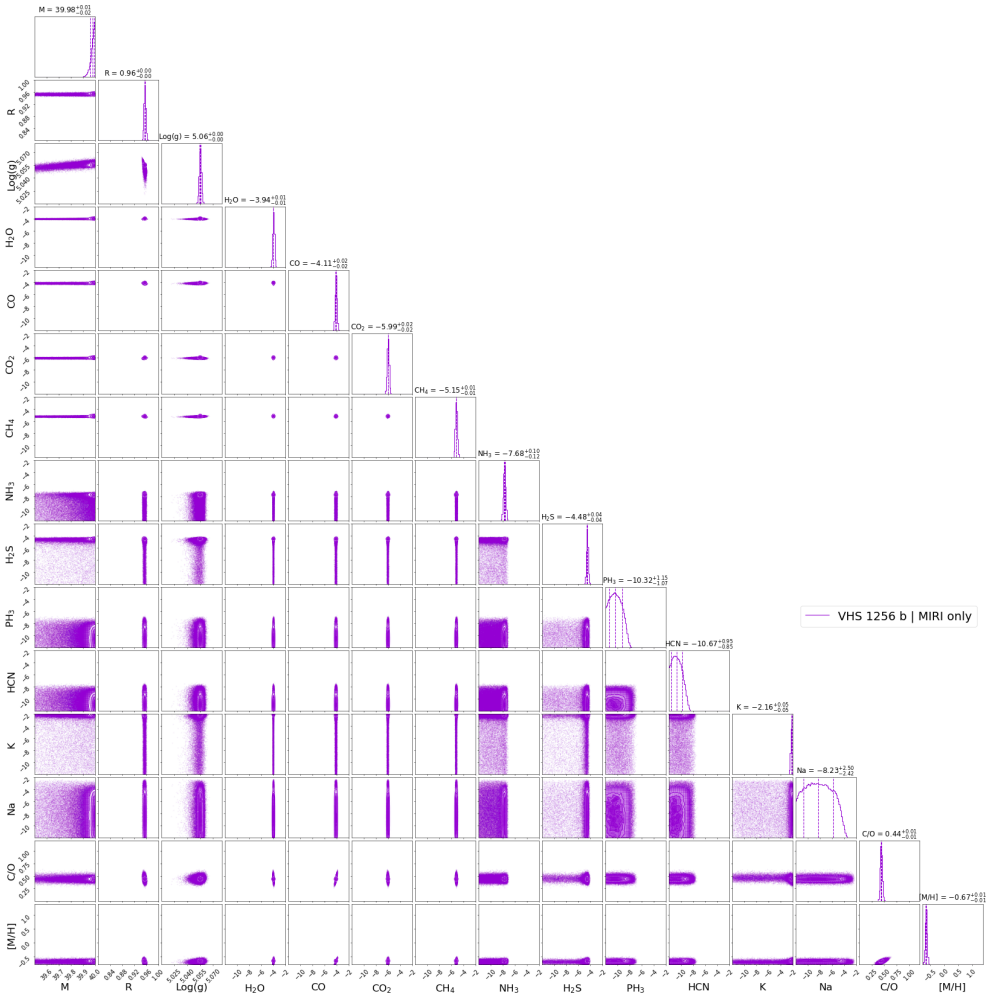

Figure 7.13: VHS 1256 b corner plot for MIRI simulation

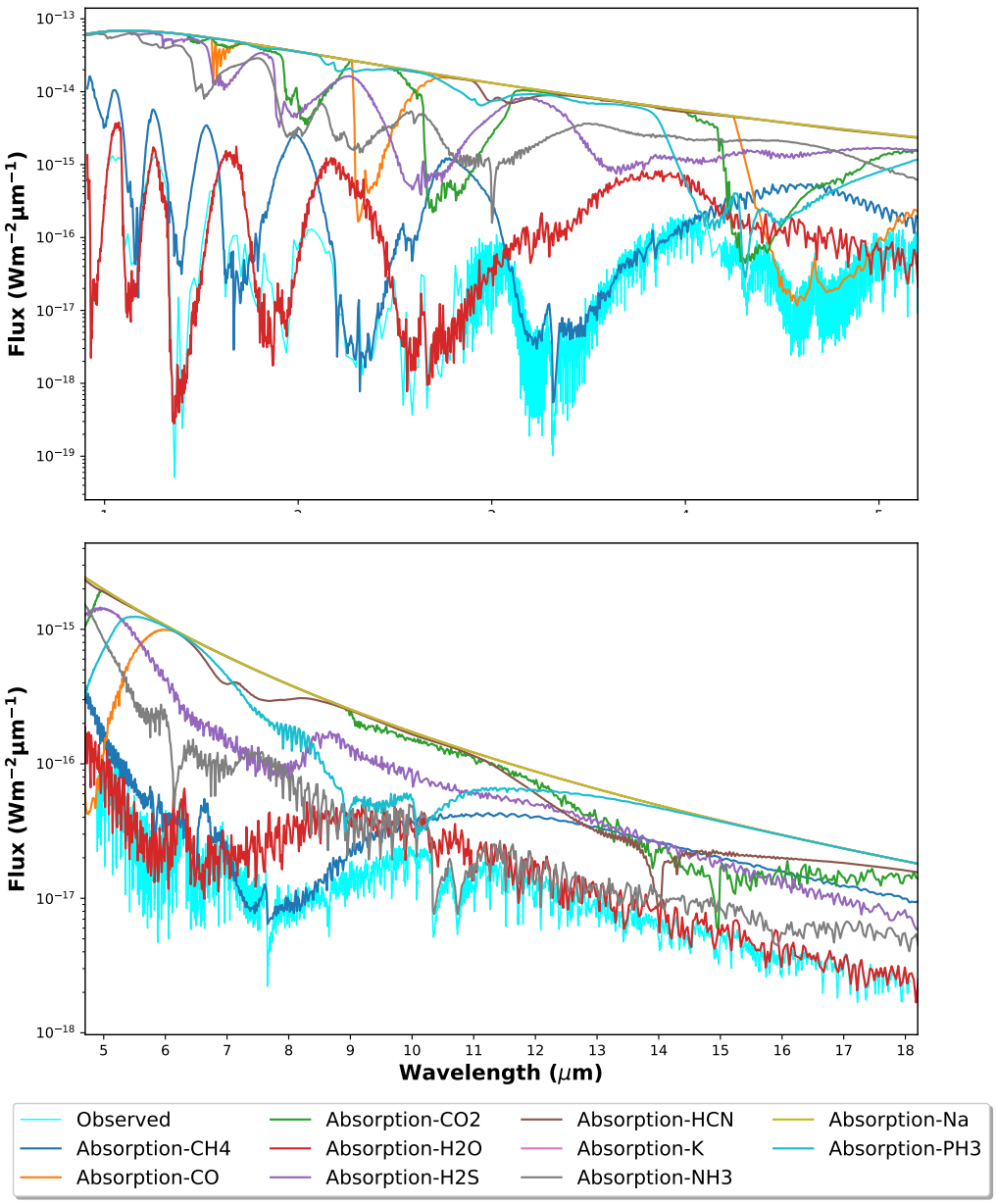

Figure 7.14: Demonstration of Ross 458 c retrieval molecular contribution used across of NIRSpec (Top) and MIRI (bottom) wavelength ranges.

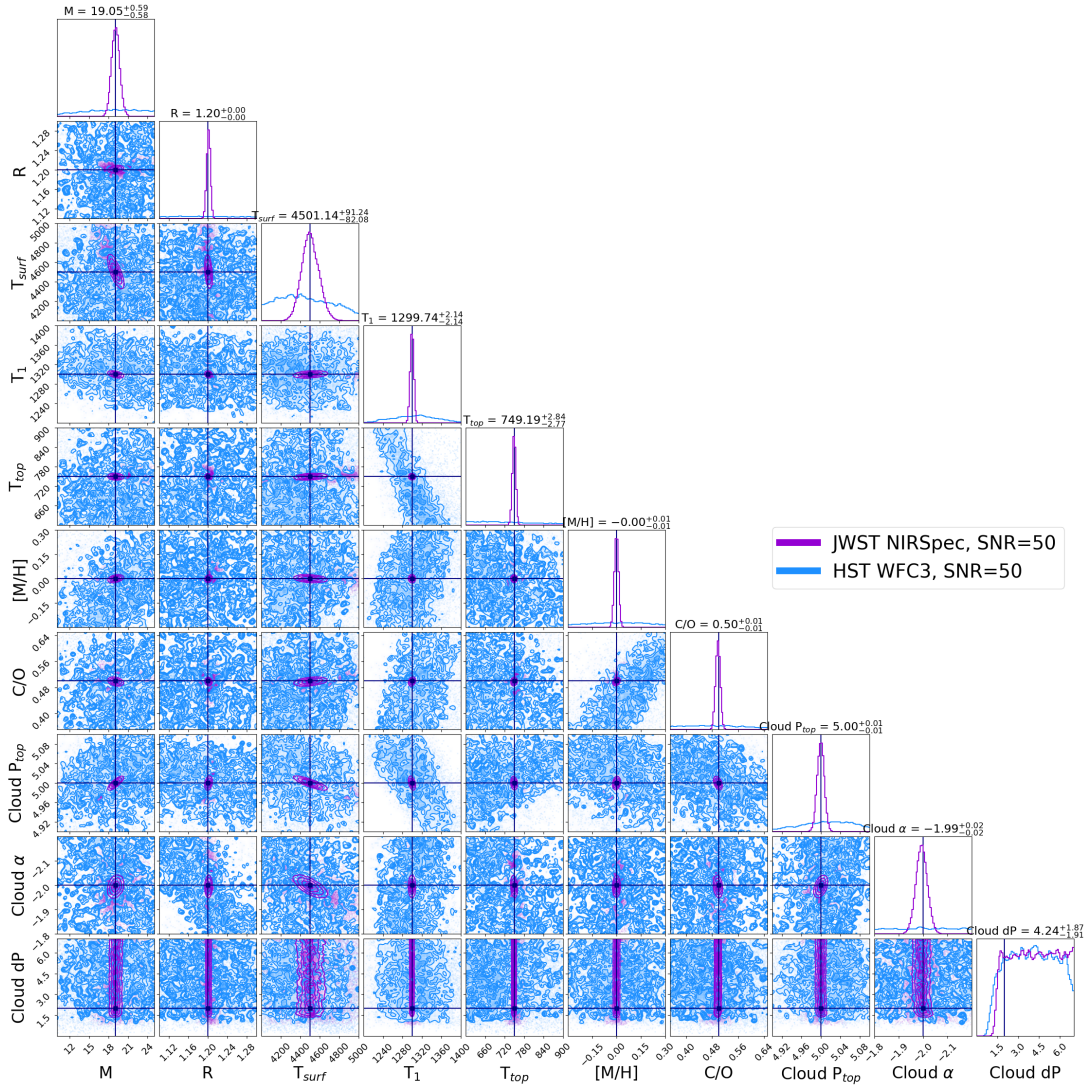

Figure 7.15: HST vs JWST retrieval precision comparison

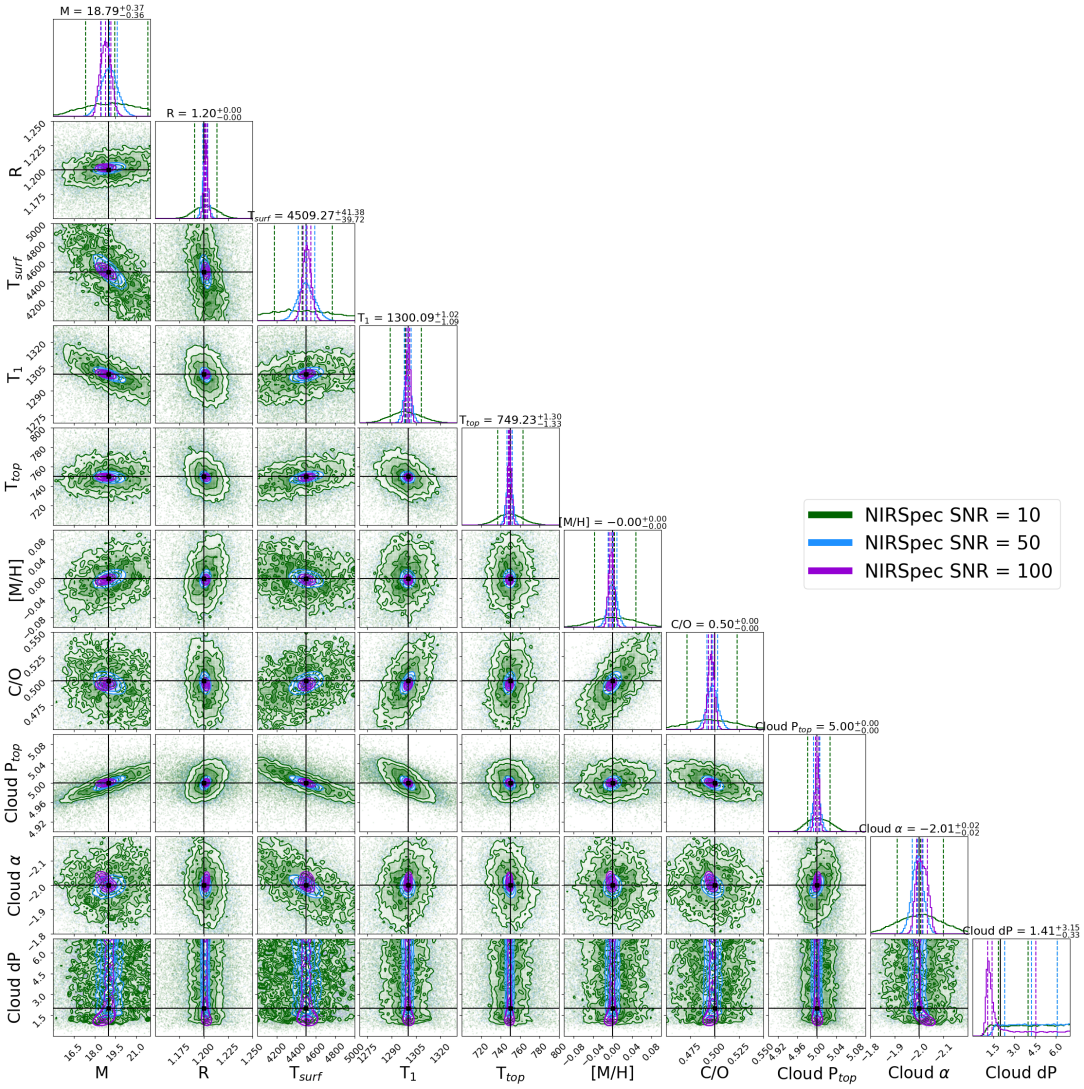

Figure 7.16: JWST retrieval precision at different signal-to-noise rations.

Bibliography

N. Madhusudhan and S. Seager. A Temperature and Abundance Retrieval Method for Exoplanet Atmospheres. ApJ, 707:24–39, December 2009. doi: 10.1088/0004-637X/707/1/24.

Baptiste Lavie, João M. Mendonça, Christoph Mordasini, et al. HELIOS-RETRIEVAL: An Open-source, Nested Sampling Atmospheric Retrieval Code; Application to the HR 8799 Exoplanets and Inferred Constraints for Planet Formation. AJ, 154:91, Sep 2017. doi: 10.3847/1538-3881/aa7ed8.

Michel Mayor and Didier Queloz. A Jupiter-mass companion to a solar-type star. *nat*, 378:355–359, November 1995. doi: 10.1038/378355a0.

NASA Exoplanet Archive. NASA Exoplanet Archive, NASA Exoplanet Science Institute. `https://exoplanetarchive.ipac.caltech.edu/docs/counts_detail.html`, 2022. [Online; accessed 19-July-2019].

Brendan P. Bowler. Imaging Extrasolar Giant Planets. PASP, 128(968):102001, October 2016. doi: 10.1088/1538-3873/128/968/102001.

S. Seager, R.Ž. Dotson, and L.P. Institute. *Exoplanets*. Space Science Series. University of Arizona Press, 2010. ISBN 9780816529452. URL `https://books.google.co.uk/books?id=7dVOXyaP2MoC`.

Jason T. Wright and B. Scott Gaudi. *Exoplanet Detection Methods*, page 489. 2013. doi: 10.1007/978-94-007-5606-9_10.

D. A. Fischer, A. W. Howard, G. P. Laughlin, et al. Exoplanet Detection Techniques. In Henrik Beuther, Ralf S. Klessen, Cornelis P. Dullemond, and Thomas Henning, editors, *Protostars and Planets VI*, page 715, January 2014. doi: 10.2458/azu_uapress_9780816531240-ch031.

M. Perryman. *The Exoplanet Handbook*. Cambridge University Press, 2014. ISBN 9781107668560. URL https://books.google.co.uk/books?id=j5mQngEACAAJ.

Michael Perryman. *The Exoplanet Handbook*. Cambridge University Press, 2 edition, 2018. doi: 10.1017/9781108304160.

J. L. Birkby. Exoplanet Atmospheres at High Spectral Resolution. *arXiv e-prints*, art. arXiv:1806.04617, June 2018.

C. Lovis and D. Fischer. Radial Velocity Techniques for Exoplanets. In S. Seager, editor, *Exoplanets*, pages 27–53. 2010.

C. Lovis, M. Mayor, F. Bouchy, et al. The HARPS search for southern extra-solar planets. III. Three Saturn-mass planets around HD 93083, HD 101930 and HD 102117. A&A, 437(3):1121–1126, July 2005. doi: 10.1051/0004-6361:20052864.

M. Mayor, F. Pepe, D. Queloz, et al. Setting New Standards with HARPS. *The Messenger*, 114:20–24, December 2003.

Rosario Cosentino, Christophe Lovis, Francesco Pepe, et al. Harps-N: the new planet hunter at TNG. In Ian S. McLean, Suzanne K. Ramsay, and Hideki Takami, editors, *Ground-based and Airborne Instrumentation for Astronomy IV*, volume 8446 of *Society of Photo-Optical Instrumentation Engineers (SPIE) Conference Series*, page 84461V, September 2012. doi: 10.1117/12.925738.

Yuri Netto, Diego Lorenzo-Oliveira, Jorge Meléndez, et al. Radial-velocity Precision of ESPRESSO Through the Analysis of the Solar Twin HIP 11915. AJ, 162(4):160, October 2021. doi: 10.3847/1538-3881/ac1bb5.

F. Pepe, S. Cristiani, R. Rebolo, et al. ESPRESSO at VLT. On-sky performance and first results. A&A, 645:A96, January 2021. doi: 10.1051/0004-6361/202038306.

Maciej Konacki, Guillermo Torres, Saurabh Jha, and Dimitar D. Sasselov. An extrasolar planet that transits the disk of its parent star. Nature, 421(6922): 507–509, January 2003. doi: 10.1038/nature01379.

D. L. Pollacco, I. Skillen, A. Collier Cameron, et al. The WASP Project and the SuperWASP Cameras. PASP, 118(848):1407–1418, October 2006. doi: 10.1086/508556.

Joshua Pepper, Richard W. Pogge, D. L. DePoy, et al. The Kilodegree Extremely Little Telescope (KELT): A Small Robotic Telescope for Large-Area Synoptic Surveys. PASP, 119(858):923–935, August 2007. doi: 10.1086/521836.

William J. Borucki, David Koch, Gibor Basri, et al. Kepler Planet-Detection Mission: Introduction and First Results. *Science*, 327(5968):977, February 2010. doi: 10.1126/science.1185402.

William J. Borucki, David G. Koch, Gibor Basri, et al. Characteristics of Planetary Candidates Observed by Kepler. II. Analysis of the First Four Months of Data. ApJ, 736(1):19, July 2011. doi: 10.1088/0004-637X/736/1/19.

Steve B. Howell, Charlie Sobeck, Michael Haas, et al. The K2 Mission: Characterization and Early Results. PASP, 126(938):398, April 2014. doi: 10.1086/676406.

George R. Ricker, Joshua N. Winn, Roland Vanderspek, et al. Transiting Exoplanet Survey Satellite (TESS). *Journal of Astronomical Telescopes, Instruments, and Systems*, 1:014003, January 2015. doi: 10.1117/1.JATIS.1.1.014003.

Michaël Gillon, Emmanuël Jehin, Susan M. Lederer, et al. Temperate Earth-sized planets transiting a nearby ultracool dwarf star. Nature, 533(7602):221–224, May 2016. doi: 10.1038/nature17448.

Michaël Gillon, Amaury H. M. J. Triaud, Brice-Olivier Demory, et al. Seven temperate terrestrial planets around the nearby ultracool dwarf star TRAPPIST-1. *nat*, 542:456–460, February 2017. doi: 10.1038/nature21360.

A. Santerne, R. F. Díaz, C. Moutou, et al. SOPHIE velocimetry of Kepler transit candidates. VII. A false-positive rate of 35% for Kepler close-in giant candidates. A&A, 545:A76, September 2012. doi: 10.1051/0004-6361/201219608.

Peter W. Sullivan, Joshua N. Winn, Zachory K. Berta-Thompson, et al. The Transiting Exoplanet Survey Satellite: Simulations of Planet Detections and Astrophysical False Positives. ApJ, 809(1):77, August 2015. doi: 10.1088/0004-637X/809/1/77.

J. N. Winn. *Exoplanet Transits and Occultations*, pages 55–77. 2010.

A. Udalski. The Optical Gravitational Lensing Experiment. Real Time Data Analysis Systems in the OGLE-III Survey. Acta Astron., 53:291–305, December 2003.

I. A. Bond, F. Abe, R. J. Dodd, et al. Real-time difference imaging analysis of MOA Galactic bulge observations during 2000. MNRAS, 327(3):868–880, November 2001. doi: 10.1046/j.1365-8711.2001.04776.x.

R. L. Akeson, X. Chen, D. Ciardi, et al. The NASA Exoplanet Archive: Data and Tools for Exoplanet Research. PASP, 125(930):989, Aug 2013. doi: 10.1086/672273.

Beth Biller. Detecting and Characterizing Exoplanets with Direct Imaging: Past, Present, and Future. In Mark Booth, Brenda C. Matthews, and James R. Graham, editors, *Exploring the Formation and Evolution of Planetary Systems*, volume 299, pages 1–11, January 2014. doi: 10.1017/S1743921313007667.

Christian Marois, Bruce Macintosh, Travis Barman, et al. Direct Imaging of Multiple Planets Orbiting the Star HR 8799. *Science*, 322(5906):1348, Nov 2008. doi: 10.1126/science.1166585.

Christian Marois, B. Zuckerman, Quinn M. Konopacky, et al. Images of a fourth planet orbiting HR 8799. Nature, 468(7327):1080–1083, Dec 2010. doi: 10.1038/nature09684.

A. M. Lagrange, M. Bonnefoy, G. Chauvin, et al. A Giant Planet Imaged in the Disk of the Young Star β Pictoris. *Science*, 329(5987):57, Jul 2010. doi: 10.1126/science.1187187.

J. Rameau, G. Chauvin, A. M. Lagrange, et al. Confirmation of the Planet around HD 95086 by Direct Imaging. ApJ, 779(2):L26, December 2013. doi: 10.1088/2041-8205/779/2/L26.

B. Macintosh, J. R. Graham, T. Barman, et al. Discovery and spectroscopy of the young jovian planet 51 Eri b with the Gemini Planet Imager. *Science*, 350:64–67, Oct 2015. doi: 10.1126/science.aac5891.

N. Madhusudhan, H. Knutson, J. J. Fortney, and T. Barman. Exoplanetary Atmospheres. In *Protostars and Planets VI, Henrik Beuther, Ralf S. Klessen, Cornelis P. Dullemond, and Thomas Henning (eds.), University of Arizona Press, Tucson, 914 pp., p.739-762*, page 739, January 2014. doi: 10.2458/azu_uapress_9780816531240-ch032.

David J. Stevenson. The search for brown dwarfs. ARA&A, 29:163–193, January 1991. doi: 10.1146/annurev.aa.29.090191.001115.

Michael C. Liu, Zahed Wahhaj, Beth A. Biller, et al. The Gemini NICI Planet-Finding Campaign. In Brent L. Ellerbroek, Michael Hart, Norbert Hubin, and Peter L. Wizinowich, editors, *Adaptive Optics Systems II*, volume 7736 of *Society of Photo-Optical Instrumentation Engineers (SPIE) Conference Series*, page 77361K, July 2010. doi: 10.1117/12.858358.

Beth A. Biller, Michael C. Liu, Zahed Wahhaj, et al. The Gemini/NICI Planet-Finding Campaign: The Frequency of Planets around Young Moving Group Stars. ApJ, 777(2):160, November 2013. doi: 10.1088/0004-637X/777/2/160.

Eric L. Nielsen, Michael C. Liu, Zahed Wahhaj, et al. The Gemini NICI Planet-Finding Campaign: The Frequency of Giant Planets around Young B and A Stars. ApJ, 776(1):4, October 2013. doi: 10.1088/0004-637X/776/1/4.

S. Desidera, E. Covino, S. Messina, et al. The VLT/NaCo large program to probe the occurrence of exoplanets and brown dwarfs in wide orbits. I. Sample definition and characterization. A&A, 573:A126, January 2015. doi: 10.1051/0004-6361/201323168.

G. Chauvin, A. Vigan, M. Bonnefoy, et al. The VLT/NaCo large program to probe the occurrence of exoplanets and brown dwarfs at wide orbits. II. Survey description, results, and performances. A&A, 573:A127, January 2015. doi: 10.1051/0004-6361/201423564.

M. Reggiani, M. R. Meyer, G. Chauvin, et al. The VLT/NaCo large program to probe the occurrence of exoplanets and brown dwarfs at wide orbits . III. The frequency of brown dwarfs and giant planets as companions to solar-type stars. A&A, 586:A147, February 2016. doi: 10.1051/0004-6361/201525930.

A. Vigan, J. Patience, C. Marois, et al. The International Deep Planet Survey. I. The frequency of wide-orbit massive planets around A-stars. A&A, 544:A9, August 2012. doi: 10.1051/0004-6361/201218991.

R. Galicher, C. Marois, B. Macintosh, et al. The International Deep Planet Survey. II. The frequency of directly imaged giant exoplanets with stellar mass. A&A, 594:A63, October 2016. doi: 10.1051/0004-6361/201527828.

Bruce Macintosh, James R. Graham, Patrick Ingraham, et al. First light of the Gemini Planet Imager. *Proceedings of the National Academy of Science*, 111 (35):12661–12666, Sep 2014. doi: 10.1073/pnas.1304215111.

Eric L. Nielsen, Robert J. De Rosa, Bruce Macintosh, et al. The Gemini Planet Imager Exoplanet Survey: Giant Planet and Brown Dwarf Demographics from 10 to 100 au. AJ, 158(1):13, Jul 2019. doi: 10.3847/1538-3881/ab16e9.

G. Chauvin, S. Desidera, A. M. Lagrange, et al. SHINE, The SpHere INfrared survey for Exoplanets. In C. Reylé, P. Di Matteo, F. Herpin, et al., editors, *SF2A-2017: Proceedings of the Annual meeting of the French Society of Astronomy and Astrophysics*, page Di, December 2017.

S. Desidera, G. Chauvin, M. Bonavita, et al. The SPHERE infrared survey for exoplanets (SHINE). I. Sample definition and target characterization. A&A, 651:A70, July 2021. doi: 10.1051/0004-6361/202038806.

M. Langlois, R. Gratton, A. M. Lagrange, et al. The SPHERE infrared survey for exoplanets (SHINE). II. Observations, data reduction and analysis, detection performances, and initial results. A&A, 651:A71, July 2021. doi: 10.1051/0004-6361/202039753.

A. Vigan, C. Fontanive, M. Meyer, et al. The SPHERE infrared survey for exoplanets (SHINE). III. The demographics of young giant exoplanets below 300 au with SPHERE. A&A, 651:A72, July 2021. doi: 10.1051/0004-6361/202038107.

A. J. Bohn, M. A. Kenworthy, C. Ginski, et al. The Young Suns Exoplanet Survey: Detection of a wide-orbit planetary-mass companion to a solar-type Sco-Cen member. MNRAS, 492(1):431–443, February 2020. doi: 10.1093/mnras/stz3462.

Trent J. Dupuy and Michael C. Liu. Individual Dynamical Masses of Ultracool Dwarfs. ApJS, 231(2):15, August 2017. doi: 10.3847/1538-4365/aa5e4c.

I. A. G. Snellen and A. G. A. Brown. The mass of the young planet Beta Pictoris b through the astrometric motion of its host star. *Nature Astronomy*, 2:883–886, August 2018a. doi: 10.1038/s41550-018-0561-6.

Timothy D. Brandt, Trent J. Dupuy, Brendan P. Bowler, et al. A Dynamical Mass of 70 $\pm$ 5 Jupiter Masses for Gliese 229B, the First T Dwarf. *arXiv e-prints*, art. arXiv:1910.01652, October 2019.

G. Mirek Brandt, Timothy D. Brandt, Trent J. Dupuy, et al. The First Dynamical Mass Measurement in the HR 8799 System. ApJ, 915(1):L16, July 2021a. doi: 10.3847/2041-8213/ac0540.

G. Mirek Brandt, Timothy D. Brandt, Trent J. Dupuy, et al. Precise Dynamical Masses and Orbital Fits for beta Pic β and β Pic c. AJ, 161(4):179, April 2021b. doi: 10.3847/1538-3881/abdc2e.

M. Keppler, M. Benisty, A. Müller, et al. Discovery of a planetary-mass companion within the gap of the transition disk around PDS 70. A&A, 617:A44, September 2018. doi: 10.1051/0004-6361/201832957.

S. Y. Haffert, A. J. Bohn, J. de Boer, et al. Two accreting protoplanets around the young star PDS 70. *Nature Astronomy*, 3:749–754, June 2019. doi: 10.1038/s41550-019-0780-5.

J. J. Fortney, M. S. Marley, D. Saumon, and K. Lodders. Synthetic Spectra and Colors of Young Giant Planet Atmospheres: Effects of Initial Conditions and Atmospheric Metallicity. ApJ, 683(2):1104–1116, August 2008. doi: 10.1086/589942.

Ian J. M. Crossfield. Observations of Exoplanet Atmospheres. PASP, 127(956): 941, October 2015. doi: 10.1086/683115.

Beth A. Biller and Mickaël Bonnefoy. *Exoplanet Atmosphere Measurements from Direct Imaging*, page 101. 2018. doi: 10.1007/978-3-319-55333-7_101.

Laura Kreidberg. *Exoplanet Atmosphere Measurements from Transmission Spectroscopy and Other Planet Star Combined Light Observations*, page 100. 2018. doi: 10.1007/978-3-319-55333-7_100.

Vivien Parmentier and Ian J. M. Crossfield. *Exoplanet Phase Curves: Observations and Theory*, page 116. 2018. doi: 10.1007/978-3-319-55333-7_116.

Nikku Madhusudhan. Exoplanetary Atmospheres: Key Insights, Challenges, and Prospects. ARA&A, 57:617–663, August 2019. doi: 10.1146/annurev-astro-081817-051846.

David Charbonneau, Timothy M. Brown, Robert W. Noyes, and Ronald L. Gilliland. Detection of an Extrasolar Planet Atmosphere. *apj*, 568:377–384, March 2002. doi: 10.1086/338770.

A. Tsiaras, M. Rocchetto, I. P. Waldmann, et al. Detection of an Atmosphere Around the Super-Earth 55 Cancri e. ApJ, 820(2):99, April 2016. doi: 10.3847/0004-637X/820/2/99.

A. Tsiaras, I. P. Waldmann, T. Zingales, et al. A Population Study of Gaseous Exoplanets. AJ, 155(4):156, April 2018. doi: 10.3847/1538-3881/aaaf75.

S. Seager and D. D. Sasselov. Theoretical Transmission Spectra during Extrasolar Giant Planet Transits. ApJ, 537(2):916–921, July 2000. doi: 10.1086/309088.

Timothy M. Brown. Transmission Spectra as Diagnostics of Extrasolar Giant Planet Atmospheres. ApJ, 553(2):1006–1026, June 2001. doi: 10.1086/320950.

Jonathan J. Fortney. The effect of condensates on the characterization of transiting planet atmospheres with transmission spectroscopy. MNRAS, 364 (2):649–653, December 2005. doi: 10.1111/j.1365-2966.2005.09587.x.

David K. Sing, Jonathan J. Fortney, Nikolay Nikolov, et al. A continuum from clear to cloudy hot-Jupiter exoplanets without primordial water depletion. Nature, 529(7584):59–62, January 2016. doi: 10.1038/nature16068.

Zachory K. Berta, David Charbonneau, Jean-Michel Désert, et al. The Flat Transmission Spectrum of the Super-Earth GJ1214b from Wide Field Camera 3 on the Hubble Space Telescope. ApJ, 747(1):35, March 2012. doi: 10.1088/0004-637X/747/1/35.

David Charbonneau, Lori E. Allen, S. Thomas Megeath, et al. Detection of Thermal Emission from an Extrasolar Planet. *apj*, 626:523–529, June 2005. doi: 10.1086/429991.

Drake Deming, Sara Seager, L. Jeremy Richardson, and Joseph Harrington. Infrared radiation from an extrasolar planet. Nature, 434(7034):740–743, March 2005. doi: 10.1038/nature03507.

Heather A. Knutson, David Charbonneau, Nicolas B. Cowan, et al. Multiwavelength Constraints on the Day-Night Circulation Patterns of HD 189733b. ApJ, 690(1):822–836, January 2009. doi: 10.1088/0004-637X/690/1/822.

Heather A. Knutson, Nikole Lewis, Jonathan J. Fortney, et al. 3.6 and 4.5 μm Phase Curves and Evidence for Non-equilibrium Chemistry in the Atmosphere of Extrasolar Planet HD 189733b. ApJ, 754(1):22, July 2012. doi: 10.1088/0004-637X/754/1/22.

D. J. Armstrong, E. de Mooij, J. Barstow, et al. Variability in the atmosphere of the hot giant planet HAT-P-7 b. *Nature Astronomy*, 1:0004, December 2016. doi: 10.1038/s41550-016-0004.

Ignas A. G. Snellen, Remco J. de Kok, Ernst J. W. de Mooij, and Simon Albrecht. The orbital motion, absolute mass and high-altitude winds of exoplanet HD209458b. Nature, 465(7301):1049–1051, June 2010. doi: 10.1038/nature09111.

Matteo Brogi, Ignas A. G. Snellen, Remco J. de Kok, et al. The signature of orbital motion from the dayside of the planet τ Boötis b. Nature, 486(7404):502–504, June 2012. doi: 10.1038/nature11161.

J. L. Birkby, R. J. de Kok, M. Brogi, et al. Detection of water absorption in the day side atmosphere of HD 189733 b using ground-based high-resolution spectroscopy at 3.2μm. MNRAS, 436:L35–L39, November 2013. doi: 10.1093/mnrasl/slt107.

H. Jens Hoeijmakers, David Ehrenreich, Kevin Heng, et al. Atomic iron and titanium in the atmosphere of the exoplanet KELT-9b. Nature, 560(7719):453–455, August 2018. doi: 10.1038/s41586-018-0401-y.

Ignas A. G. Snellen, Bernhard R. Brandl, Remco J. de Kok, et al. Fast spin of the young extrasolar planet β Pictoris b. Nature, 509(7498):63–65, May 2014. doi: 10.1038/nature13253.

Jean-Luc Beuzit, Markus Feldt, Kjetil Dohlen, et al. SPHERE: a 'Planet Finder' instrument for the VLT. In Proc. SPIE, volume 7014 of *Society of Photo-Optical Instrumentation Engineers (SPIE) Conference Series*, page 701418, Jul 2008. doi: 10.1117/12.790120.

A. Zurlo, A. Vigan, R. Galicher, et al. First light of the VLT planet finder SPHERE. III. New spectrophotometry and astrometry of the HR 8799 exoplanetary system. A&A, 587:A57, Mar 2016. doi: 10.1051/0004-6361/201526835.

M. Bonnefoy, A. Zurlo, J. L. Baudino, et al. First light of the VLT planet finder SPHERE. IV. Physical and chemical properties of the planets around HR8799. A&A, 587:A58, Mar 2016. doi: 10.1051/0004-6361/201526906.

M. Samland, P. Mollière, M. Bonnefoy, et al. Spectral and atmospheric characterization of 51 Eridani b using VLT/SPHERE. A&A, 603:A57, Jul 2017. doi: 10.1051/0004-6361/201629767.

Jeffrey Chilcote, Laurent Pueyo, Robert J. De Rosa, et al. 1-2.4 μm Near-IR Spectrum of the Giant Planet β Pictoris b Obtained with the Gemini Planet Imager. AJ, 153:182, Apr 2017. doi: 10.3847/1538-3881/aa63e9.

Abhijith Rajan, Julien Rameau, Robert J. De Rosa, et al. Characterizing 51 Eri b from 1 to 5 μm: A Partly Cloudy Exoplanet. AJ, 154(1):10, Jul 2017. doi: 10.3847/1538-3881/aa74db.

Gravity Collaboration, R. Abuter, M. Accardo, et al. First light for GRAVITY: Phase referencing optical interferometry for the Very Large Telescope Interferometer. A&A, 602:A94, June 2017. doi: 10.1051/0004-6361/201730838.

Gravity Collaboration, S. Lacour, M. Nowak, et al. First direct detection of an exoplanet by optical interferometry. Astrometry and K-band spectroscopy of HR 8799 e. A&A, 623:L11, Mar 2019. doi: 10.1051/0004-6361/201935253.

Nowak, M., Lacour, S., Lagrange, A.-M., et al. Direct confirmation of the radial-velocity planet toris c. *A&A*, 642:L2, 2020. doi: 10.1051/0004-6361/202039039. URL `https://doi.org/10.1051/0004-6361/202039039`.

Quinn M. Konopacky, Travis S. Barman, Bruce A. Macintosh, and Christian Marois. Detection of Carbon Monoxide and Water Absorption Lines in an Exoplanet Atmosphere. *Science*, 339(6126):1398–1401, March 2013. doi: 10.1126/science.1232003.

Jason J. Wang, Jean-Baptiste Ruffio, Evan Morris, et al. Detection and Bulk Properties of the HR 8799 Planets with High Resolution Spectroscopy. *arXiv e-prints*, art. arXiv:2107.06949, July 2021.

Brendan P. Bowler, Yifan Zhou, Caroline V. Morley, et al. Strong Near-infrared Spectral Variability of the Young Cloudy L Dwarf Companion VHS J1256-1257 b. ApJ, 893(2):L30, April 2020. doi: 10.3847/2041-8213/ab8197.

Yifan Zhou, Brendan P. Bowler, Caroline V. Morley, et al. Spectral Variability of VHS J1256-1257b from 1 to 5 μm. AJ, 160(2):77, August 2020. doi: 10.3847/1538-3881/ab9e04.

Beth A. Biller, Dániel Apai, Mickaël Bonnefoy, et al. A high-contrast search for variability in HR 8799bc with VLT-SPHERE. MNRAS, 503(1):743–767, May 2021. doi: 10.1093/mnras/stab202.

J. C. Tarter. Brown Dwarfs, Lilliputian Stars, Giant Planets and Missing Mass Problems. In *Bulletin of the American Astronomical Society*, volume 8, page 517, September 1976.

Shiv S. Kumar. The Structure of Stars of Very Low Mass. ApJ, 137:1121, May 1963. doi: 10.1086/147589.

C. Hayashi and T. Nakano. Evolution of Stars of Small Masses in the Pre-Main-Sequence Stages. *Progress of Theoretical Physics*, 30(4):460–474, October 1963. doi: 10.1143/PTP.30.460.

T. Nakajima, B. R. Oppenheimer, S. R. Kulkarni, et al. Discovery of a cool brown dwarf. Nature, 378(6556):463–465, November 1995. doi: 10.1038/378463a0.

B. R. Oppenheimer, S. R. Kulkarni, K. Matthews, and T. Nakajima. Infrared Spectrum of the Cool Brown Dwarf Gl 229B. *Science*, 270(5241):1478–1479, December 1995. doi: 10.1126/science.270.5241.1478.

Katharina Lodders and Bruce Fegley. Atmospheric Chemistry in Giant Planets, Brown Dwarfs, and Low-Mass Dwarf Stars. I. Carbon, Nitrogen, and Oxygen. Icarus, 155(2):393–424, February 2002. doi: 10.1006/icar.2001.6740.

K. Lodders and Jr. Fegley, B. *Chemistry of Low Mass Substellar Objects*, page 1. 2006. doi: 10.1007/3-540-30313-8_1.

Adam Burrows and C. M. Sharp. Chemical Equilibrium Abundances in Brown Dwarf and Extrasolar Giant Planet Atmospheres. ApJ, 512(2):843–863, February 1999. doi: 10.1086/306811.

Travis S. Barman, Bruce Macintosh, Quinn M. Konopacky, and Christian Marois. Clouds and Chemistry in the Atmosphere of Extrasolar Planet HR8799b. ApJ, 733(1):65, May 2011a. doi: 10.1088/0004-637X/733/1/65.

Kevin J. Zahnle and Mark S. Marley. Methane, Carbon Monoxide, and Ammonia in Brown Dwarfs and Self-Luminous Giant Planets. ApJ, 797(1):41, December 2014. doi: 10.1088/0004-637X/797/1/41.

M. S. Marley and T. D. Robinson. On the Cool Side: Modeling the Atmospheres of Brown Dwarfs and Giant Planets. ARA&A, 53:279–323, August 2015. doi: 10.1146/annurev-astro-082214-122522.

Annie J. Cannon and Edward C. Pickering. Spectra of bright southern stars photographed with the 13-inch Boyden telescope as part of the Henry Draper Memorial. *Annals of Harvard College Observatory*, 28:129–P.6, January 1901.

J. Davy Kirkpatrick. New Spectral Types L and T. ARA&A, 43(1):195–245, Sep 2005. doi: 10.1146/annurev.astro.42.053102.134017.

J. Davy Kirkpatrick, Christopher R. Gelino, Michael C. Cushing, et al. Further Defining Spectral Type "Y" and Exploring the Low-mass End of the Field Brown Dwarf Mass Function. ApJ, 753(2):156, Jul 2012. doi: 10.1088/0004-637X/753/2/156.

Michael C. Cushing, J. Davy Kirkpatrick, Christopher R. Gelino, et al. The Discovery of Y Dwarfs using Data from the Wide-field Infrared Survey Explorer (WISE). ApJ, 743(1):50, Dec 2011. doi: 10.1088/0004-637X/743/1/50.

K. Lodders and Jr. Fegley, B. Condensation Chemistry of Circumstellar Grains. In T. Le Bertre, A. Lebre, and C. Waelkens, editors, *Asymptotic Giant Branch Stars*, volume 191, page 279, January 1999.

France Allard, Peter H. Hauschildt, David R. Alexander, et al. The Limiting Effects of Dust in Brown Dwarf Model Atmospheres. ApJ, 556(1):357–372, July 2001. doi: 10.1086/321547.

Katharina Lodders. Titanium and Vanadium Chemistry in Low-Mass Dwarf Stars. ApJ, 577(2):974–985, October 2002. doi: 10.1086/342241.

Mark S. Marley, S. Seager, D. Saumon, et al. Clouds and Chemistry: Ultracool Dwarf Atmospheric Properties from Optical and Infrared Colors. ApJ, 568(1):335–342, March 2002. doi: 10.1086/338800.

Takashi Tsuji. Dust in the Photospheric Environment: Unified Cloudy Models of M, L, and T Dwarfs. ApJ, 575(1):264–290, August 2002. doi: 10.1086/341262.

Christiane Helling and Sarah Casewell. Atmospheres of brown dwarfs. A&A Rev., 22:80, November 2014. doi: 10.1007/s00159-014-0080-0.

Peter Gao, Hannah R. Wakeford, Sarah E. Moran, and Vivien Parmentier. Aerosols in Exoplanet Atmospheres. *Journal of Geophysical Research (Planets)*, 126(4):e06655, April 2021. doi: 10.1029/2020JE006655.

Cleménce Fontanive. *Brown Dwarfs and Giant Exoplanets: Bridging Observations and Theory with Statistical Methods*. PhD thesis, University of Edinburgh, 2019.

Adam J. Burgasser, Adam Burrows, and J. Davy Kirkpatrick. A Method for Determining the Physical Properties of the Coldest Known Brown Dwarfs. ApJ, 639(2):1095–1113, March 2006. doi: 10.1086/499344.

Andrew S. Ackerman and Mark S. Marley. Precipitating Condensation Clouds in Substellar Atmospheres. ApJ, 556(2):872–884, August 2001. doi: 10.1086/321540.

Adam J. Burgasser, J. Davy Kirkpatrick, Michael E. Brown, et al. The Spectra of T Dwarfs. I. Near-Infrared Data and Spectral Classification. ApJ, 564(1):421–451, January 2002. doi: 10.1086/324033.

Takashi Tsuji and Tadashi Nakajima. Transition from L to T Dwarfs on the Color-Magnitude Diagram. ApJ, 585(2):L151–L154, March 2003. doi: 10.1086/374388.

Mark S. Marley, Didier Saumon, and Colin Goldblatt. A Patchy Cloud Model for the L to T Dwarf Transition. ApJ, 723(1):L117–L121, Nov 2010. doi: 10.1088/2041-8205/723/1/L117.

Caroline V. Morley, Jonathan J. Fortney, Mark S. Marley, et al. Neglected Clouds in T and Y Dwarf Atmospheres. ApJ, 756:172, September 2012. doi: 10.1088/0004-637X/756/2/172.

Jonathan J. Fortney. Modeling Exoplanetary Atmospheres: An Overview. *ArXiv e-prints*, April 2018.

Nikku Madhusudhan. *Atmospheric Retrieval of Exoplanets*, page 104. 2018. doi: 10.1007/978-3-319-55333-7_104.

I. P. Waldmann, G. Tinetti, M. Rocchetto, et al. Tau-REx I: A Next Generation Retrieval Code for Exoplanetary Atmospheres. *apj*, 802:107, April 2015a. doi: 10.1088/0004-637X/802/2/107.

I. P. Waldmann, M. Rocchetto, G. Tinetti, et al. Tau-REx II: Retrieval of Emission Spectra. *apj*, 813:13, November 2015b. doi: 10.1088/0004-637X/813/1/13.

Ahmed F. Al-Refaie, Quentin Changeat, Ingo P. Waldmann, and Giovanna Tinetti. TauREx III: A fast, dynamic and extendable framework for retrievals. *arXiv e-prints*, art. arXiv:1912.07759, December 2019.

Maria Oreshenko, Daniel Kitzmann, Pablo Márquez-Neila, et al. Supervised Machine Learning for Intercomparison of Model Grids of Brown Dwarfs: Application to GJ 570D and the Epsilon Indi B Binary System. AJ, 159(1):6, January 2020. doi: 10.3847/1538-3881/ab5955.

P. Mollière, T. Stolker, S. Lacour, et al. Retrieving scattering clouds and disequilibrium chemistry in the atmosphere of HR 8799e. *arXiv e-prints*, art. arXiv:2006.09394, June 2020.

Ben Burningham, Jacqueline K. Faherty, Eileen C. Gonzales, et al. Cloud busting: Enstatite and quartz clouds in the atmosphere of 2M2224-0158. MNRAS, May 2021. doi: 10.1093/mnras/stab1361.

Daniel Kitzmann, Kevin Heng, Maria Oreshenko, et al. Helios-r2: A New Bayesian, Open-source Retrieval Model for Brown Dwarfs and Exoplanet Atmospheres. ApJ, 890(2):174, February 2020. doi: 10.3847/1538-4357/ab6d71.

Eileen Gonzales, Ben Burningham, Jackie Faherty, et al. Retrieval of SDSS J1416+1348AB. *arXiv e-prints*, art. arXiv:2010.01224, October 2020.

Martin Asplund, Nicolas Grevesse, A. Jacques Sauval, and Pat Scott. The Chemical Composition of the Sun. ARA&A, 47(1):481–522, September 2009. doi: 10.1146/annurev.astro.46.060407.145222.

Michael R. Line, Johanna Teske, Ben Burningham, et al. Uniform Atmospheric Retrieval Analysis of Ultracool Dwarfs. I. Characterizing Benchmarks, Gl 570D and HD 3651B. ApJ, 807(2):183, Jul 2015. doi: 10.1088/0004-637X/807/2/183.

K. L. Chubb, M. Rocchetto, A. F. Al-Refaie, et al. The ExoMolOP Database: Cross-sections and k-tables for molecules of interest in high-temperature exoplanet atmospheres. *A&A*, 2020. (Submitted).

Jonathan Tennyson and Sergei N. Yurchenko. ExoMol: molecular line lists for exoplanet and other atmospheres. MNRAS, 425(1):21–33, Sep 2012. doi: 10.1111/j.1365-2966.2012.21440.x.

L. S. Rothman, I. E. Gordon, R. J. Barber, et al. HITEMP, the high-temperature molecular spectroscopic database. J. Quant. Spec. Radiat. Transf., 111:2139–2150, Oct 2010. doi: 10.1016/j.jqsrt.2010.05.001.

L. S. Rothman, R. R. Gamache, A. Goldman, et al. The hitran database: 1986 edition. *Appl. Opt.*, 26(19):4058–4097, Oct 1987. doi: 10.1364/AO.26.004058. URL `http://ao.osa.org/abstract.cfm?URI=ao-26-19-4058`.

Peter F Bernath. MoLLIST: Molecular line lists, intensities and spectra. *J. Quant. Spectrosc. Radiat. Transf.*, 240:106687, 2020. ISSN 0022-4073. doi: https://doi.org/10.1016/j.jqsrt.2019.106687.

O. L. Polyansky, A. A. Kyuberis, N. F. Zobov, et al. ExoMol molecular line lists XXX: a complete high-accuracy line list for water. *Mon. Not. R. Astron. Soc.*, 480:2597–2608, 2018. doi: 10.1093/mnras/sty1877.

Gang Li, Iouli E. Gordon, Laurence S. Rothman, et al. Rovibrational line lists for nine isotopologues of the co molecule in the x $^1\Sigma^+$ ground electronic state. *Astrophys. J. Suppl.*, 216:15, 2015. doi: 10.1088/0067-0049/216/1/15.

Sergei N. Yurchenko, Thomas M. Mellor, Richard S. Freedman, and Jonathan Tennyson. ExoMol line lists – XXXIX. Ro-vibrational molecular line list for CO_2. *Mon. Not. R. Astron. Soc.*, page submitted, 2020.

S. N. Yurchenko, D. S. Amundsen, J. Tennyson, and I P Waldmann. A hybrid line list for CH_4 and hot methane continuum. *A&A*, 605:A95, 2017. doi: 10.1051/0004-6361/201731026.

L. K. McKemmish, S. N. Yurchenko, and J. Tennyson. ExoMol Molecular linelists – XVIII. The spectrum of Vanadium Oxide. *Mon. Not. R. Astron. Soc.*, 463: 771–793, 2016. doi: 10.1093/mnras/stw1969.

Laura K McKemmish, Thomas Masseron, H Jens Hoeijmakers, et al. ExoMol molecular line lists – XXXIII. The spectrum of Titanium Oxide. *Mon. Not. R. Astron. Soc.*, 488(2):2836–2854, 07 2019. doi: 10.1093/mnras/stz1818.

A. A. A. Azzam, S. N. Yurchenko, J. Tennyson, and O. V. Naumenko. ExoMol line lists XVI: A Hot Line List for H_2S. *Mon. Not. R. Astron. Soc.*, 460: 4063–4074, 2016. doi: 10.1093/mnras/stw1133.

P. A. Coles, , Sergei N. Yurchenko, and Jonathan Tennyson. ExoMol molecular line lists XXXV: a rotation-vibration line list for hot ammonia. *Mon. Not. R. Astron. Soc.*, 490:4638–4647, 2019. doi: 10.1093/mnras/stz2778.

MichaÃ«l Rey, Andrei V. Nikitin, Yurii L. Babikov, and Vladimir G. Tyuterev. Theorets â an information system for theoretical spectra based on

variational predictions from molecular potential energy and dipole moment surfaces. *Journal of Molecular Spectroscopy*, 327:138–158, 2016. ISSN 0022-2852. doi: https://doi.org/10.1016/j.jms.2016.04.006. URL `https://www.sciencedirect.com/science/article/pii/S0022285216300583`. New Visions of Spectroscopic Databases, Volume II.

N. F. Allard, F. Spiegelman, and J. F. Kielkopf. K-H_2 line shapes for the spectra of cool brown dwarfs. *A&A*, 589:A21, 2016. doi: 10.1051/0004-6361/201628270.

N. F. Allard, F. Spiegelman, T. Leininger, and P. Mollière. New study of the line profiles of sodium perturbed by H_2. *A&A*, 628:A120, 2019. doi: 10.1051/0004-6361/201935593.

A. Kramida, Y. Ralchenko, and J. Reader. NIST atomic spectra database – version 5, 2013. http://www.nist.gov/pml/data/asd.cfm.

R.L. Kurucz and B. Bell. Kurucz molecular database, 1995. http://kurucz.harvard.edu/molecules.html.

Q. Changeat, B. Edwards, I. P. Waldmann, and G. Tinetti. Toward a More Complex Description of Chemical Profiles in Exoplanet Retrievals: A Two-layer Parameterization. ApJ, 886(1):39, November 2019. doi: 10.3847/1538-4357/ab4a14.

T. Guillot. On the radiative equilibrium of irradiated planetary atmospheres. A&A, 520:A27, Sep 2010. doi: 10.1051/0004-6361/200913396.

Ben Burningham, M. S. Marley, M. R. Line, et al. Retrieval of atmospheric properties of cloudy L dwarfs. MNRAS, 470(1):1177–1197, Sep 2017. doi: 10.1093/mnras/stx1246.

Kevin Heng, João M. Mendonça, and Jae-Min Lee. Analytical Models of Exoplanetary Atmospheres. II. Radiative Transfer via the Two-stream Approximation. ApJS, 215(1):4, November 2014. doi: 10.1088/0067-0049/215/1/4.

Scott Tremaine, Karl Gebhardt, Ralf Bender, et al. The Slope of the Black Hole Mass versus Velocity Dispersion Correlation. ApJ, 574(2):740–753, August 2002. doi: 10.1086/341002.

David W. Hogg, Jo Bovy, and Dustin Lang. Data analysis recipes: Fitting a model to data. *arXiv e-prints*, art. arXiv:1008.4686, August 2010.

Daniel Foreman-Mackey, David W. Hogg, Dustin Lang, and Jonathan Goodman. emcee: The MCMC Hammer. PASP, 125(925):306, March 2013. doi: 10.1086/670067.

F. Feroz and M. P. Hobson. Multimodal nested sampling: an efficient and robust alternative to Markov Chain Monte Carlo methods for astronomical data analyses. MNRAS, 384(2):449–463, Feb 2008. doi: 10.1111/j.1365-2966.2007.12353.x.

F. Feroz, M. P. Hobson, and M. Bridges. MULTINEST: an efficient and robust Bayesian inference tool for cosmology and particle physics. MNRAS, 398(4):1601–1614, Oct 2009. doi: 10.1111/j.1365-2966.2009.14548.x.

F. Feroz, M. P. Hobson, E. Cameron, and A. N. Pettitt. Importance Nested Sampling and the MultiNest Algorithm. *arXiv e-prints*, art. arXiv:1306.2144, Jun 2013.

J. Buchner, A. Georgakakis, K. Nandra, et al. X-ray spectral modelling of the AGN obscuring region in the CDFS: Bayesian model selection and catalogue. A&A, 564:A125, April 2014. doi: 10.1051/0004-6361/201322971.

Farhan Feroz, Michael P. Hobson, Ewan Cameron, and Anthony N. Pettitt. Importance Nested Sampling and the MultiNest Algorithm. *The Open Journal of Astrophysics*, 2(1):10, November 2019. doi: 10.21105/astro.1306.2144.

Robert E. Kass and Adrian E. Raftery. Bayes factors. *Journal of the American Statistical Association*, 90(430):773–795, 1995. ISSN 01621459. URL `http://www.jstor.org/stable/2291091`.

Jae-Min Lee, Kevin Heng, and Patrick G. J. Irwin. Atmospheric Retrieval Analysis of the Directly Imaged Exoplanet HR 8799b. ApJ, 778:97, Dec 2013. doi: 10.1088/0004-637X/778/2/97.

Craig F. Bohren and Donald R. Huffman. *Absorption and scattering of light by small particles*. IOP Publishing, 1983.

James E. Hansen. Multiple Scattering of Polarized Light in Planetary Atmospheres Part II. Sunlight Reflected by Terrestrial Water Clouds. *Journal of Atmospheric Sciences*, 28(8):1400–1426, November 1971. doi: 10.1175/1520-0469(1971)028\textless{}1400:MSOPLI\textgreater{}2.0.CO;2.

David Sudarsky, Adam Burrows, and Ivan Hubeny. Theoretical spectra and atmospheres of extrasolar giant planets. *The Astrophysical Journal*, 588(2):1121–1148, may 2003. doi: 10.1086/374331. URL `https://doi.org/10.1086/374331`.

D. Deirmendjian. Scattering and polarization properties of water clouds and hazes in the visible and infrared. *Appl. Opt.*, 3(2):187–196, Feb 1964. doi: 10.1364/AO.3.000187. URL `http://ao.osa.org/abstract.cfm?URI=ao-3-2-187`.

A. Vigan, C. Fontanive, M. Meyer, et al. The SPHERE infrared survey for exoplanets (SHINE). III. The demographics of young giant exoplanets below 300 au with SPHERE. *arXiv e-prints*, art. arXiv:2007.06573, July 2020.

Giovanna Tinetti, Thérèse Encrenaz, and Athena Coustenis. Spectroscopy of planetary atmospheres in our Galaxy. *Astronomy and Astrophysics Review*, 21:63, October 2013. doi: 10.1007/s00159-013-0063-6.

Michael R. Line, Aaron S. Wolf, Xi Zhang, et al. A Systematic Retrieval Analysis of Secondary Eclipse Spectra. I. A Comparison of Atmospheric Retrieval Techniques. ApJ, 775:137, October 2013. doi: 10.1088/0004-637X/775/2/137.

P. G. J. Irwin, N. A. Teanby, R. de Kok, et al. The NEMESIS planetary atmosphere radiative transfer and retrieval tool. J. Quant. Spec. Radiat. Transf., 109:1136–1150, April 2008. doi: 10.1016/j.jqsrt.2007.11.006.

Joseph Harrington, Patricio Cubillos, Jasmina Blecic, et al. A Random Walk on WASP-12b with the Bayesian Atmospheric Radiative Transfer (BART) Code. In *American Astronomical Society Meeting Abstracts #227*, volume 227 of *American Astronomical Society Meeting Abstracts*, page 212.01, January 2016.

Björn Benneke. Strict Upper Limits on the Carbon-to-Oxygen Ratios of Eight Hot Jupiters from Self-Consistent Atmospheric Retrieval. *arXiv e-prints*, art. arXiv:1504.07655, April 2015.

Ryan J. MacDonald and Nikku Madhusudhan. HD 209458b in new light: evidence of nitrogen chemistry, patchy clouds and sub-solar water. MNRAS, 469(2): 1979–1996, August 2017. doi: 10.1093/mnras/stx804.

Siddharth Gandhi and Nikku Madhusudhan. Retrieval of exoplanet emission spectra with HyDRA. MNRAS, 474(1):271–288, February 2018. doi: 10.1093/mnras/stx2748.

P. Mollière, J. P. Wardenier, R. van Boekel, et al. petitRADTRANS. A Python radiative transfer package for exoplanet characterization and retrieval. A&A, 627:A67, July 2019. doi: 10.1051/0004-6361/201935470.

Michael Zhang, Yayaati Chachan, Eliza M. R. Kempton, et al. PLATON II: New Capabilities And A Comprehensive Retrieval on HD 189733b Transit and Eclipse Data. *arXiv e-prints*, art. arXiv:2004.09513, April 2020.

M. Rocchetto, I. P. Waldmann, O. Venot, et al. Exploring Biases of Atmospheric Retrievals in Simulated JWST Transmission Spectra of Hot Jupiters. ApJ, 833 (1):120, December 2016. doi: 10.3847/1538-4357/833/1/120.

Angelos Tsiaras, Ingo P. Waldmann, Giovanna Tinetti, et al. Water vapour in the atmosphere of the habitable-zone eight-Earth-mass planet K2-18 b. *Nature Astronomy*, 3:1086–1091, September 2019. doi: 10.1038/s41550-019-0878-9.

Billy Edwards, Quentin Changeat, Robin Baeyens, et al. ARES I: WASP-76 b, A Tale of Two HST Spectra. *arXiv e-prints*, art. arXiv:2005.02374, May 2020.

Nour Skaf, Michelle Fabienne Bieger, Billy Edwards, et al. ARES. II. Characterizing the Hot Jupiters WASP-127 b, WASP-79 b, and WASP-62b with the Hubble Space Telescope. AJ, 160(3):109, September 2020. doi: 10.3847/1538-3881/ab94a3.

William Pluriel, Niall Whiteford, Billy Edwards, et al. ARES. III. Unveiling the Two Faces of KELT-7 b with HST WFC3. AJ, 160(3):112, September 2020. doi: 10.3847/1538-3881/aba000.

Joanna K. Barstow, Quentin Changeat, Ryan Garland, et al. A comparison of exoplanet spectroscopic retrieval tools. MNRAS, 493(4):4884–4909, April 2020. doi: 10.1093/mnras/staa548.

Joanna K. Barstow and Kevin Heng. Outstanding Challenges of Exoplanet Atmospheric Retrievals. *arXiv e-prints*, art. arXiv:2003.14311, March 2020.

Michael R. Line, Jonathan J. Fortney, Mark S. Marley, and Satoko Sorahana. A Data-driven Approach for Retrieving Temperatures and Abundances in Brown Dwarf Atmospheres. ApJ, 793(1):33, Sep 2014. doi: 10.1088/0004-637X/793/1/33.

Michael R. Line, Mark S. Marley, Michael C. Liu, et al. Uniform Atmospheric Retrieval Analysis of Ultracool Dwarfs. II. Properties of 11 T dwarfs. ApJ, 848 (2):83, October 2017. doi: 10.3847/1538-4357/aa7ff0.

Joseph A. Zalesky, Michael R. Line, Adam C. Schneider, and Jennifer Patience. A Uniform Retrieval Analysis of Ultra-cool Dwarfs. III. Properties of Y Dwarfs. ApJ, 877(1):24, May 2019. doi: 10.3847/1538-4357/ab16db.

Gravity Collaboration, M. Nowak, S. Lacour, et al. Peering into the formation history of β Pictoris b with VLTI/GRAVITY long-baseline interferometry. A&A, 633:A110, January 2020. doi: 10.1051/0004-6361/201936898.

Ji Wang, Jason Wang, Bo Ma, et al. On the Chemical Abundance of HR 8799 and the Planet c. *arXiv e-prints*, art. arXiv:2007.02810, July 2020.

Jonathan P. Gardner, John C. Mather, Mark Clampin, et al. The James Webb Space Telescope. Space Sci. Rev., 123:485–606, April 2006. doi: 10.1007/s11214-006-8315-7.

S. Udry, C. Lovis, F. Bouchy, et al. Exoplanet Science with the European Extremely Large Telescope. The Case for Visible and Near-IR Spectroscopy at High Resolution. *ArXiv e-prints*, November 2014.

Bernhard R. Brandl, Markus Feldt, Alistair Glasse, et al. METIS: the mid-infrared E-ELT imager and spectrograph. In *Proceedings of the SPIE, Volume 9147, id. 914721 18 pp. (2014).*, volume 9147, page 914721, August 2014. doi: 10.1117/12.2056468.

I. J. M. Crossfield, B. Biller, J. E. Schlieder, et al. A global cloud map of the nearest known brown dwarf. *nat*, 505:654–656, January 2014. doi: 10.1038/nature12955.

Brittany E. Miles, Andrew J. I. Skemer, Caroline V. Morley, et al. Observations of Disequilibrium CO Chemistry in the Coldest Brown Dwarfs. AJ, 160(2):63, August 2020. doi: 10.3847/1538-3881/ab9114.

Mark S. Marley, Didier Saumon, Michael Cushing, et al. Masses, Radii, and Cloud Properties of the HR 8799 Planets. ApJ, 754:135, Aug 2012. doi: 10.1088/0004-637X/754/2/135.

Caroline V. Morley, Mark S. Marley, Jonathan J. Fortney, et al. Water Clouds in Y Dwarfs and Exoplanets. ApJ, 787(1):78, May 2014. doi: 10.1088/0004-637X/787/1/78.

B. Charnay, B. Bézard, J. L. Baudino, et al. A Self-consistent Cloud Model for Brown Dwarfs and Young Giant Exoplanets: Comparison with Photometric and Spectroscopic Observations. ApJ, 854(2):172, Feb 2018. doi: 10.3847/1538-4357/aaac7d.

Ben W. P. Lew, Dániel Apai, Mark Marley, et al. Cloud Atlas: Unraveling the vertical cloud structure with the time-series spectrophotometry of an unusually red brown dwarf. *arXiv e-prints*, art. arXiv:2009.10714, September 2020.

Christiane Helling. Exoplanet Clouds. *Annual Review of Earth and Planetary Sciences*, 47:583–606, May 2019. doi: 10.1146/annurev-earth-053018-060401.

P. Tremblin, D. S. Amundsen, G. Chabrier, et al. Cloudless Atmospheres for L/T Dwarfs and Extrasolar Giant Planets. ApJ, 817(2):L19, Feb 2016. doi: 10.3847/2041-8205/817/2/L19.

P. Tremblin, G. Chabrier, I. Baraffe, et al. Cloudless Atmospheres for Young Low-gravity Substellar Objects. ApJ, 850(1):46, Nov 2017. doi: 10.3847/1538-4357/aa9214.

P. Tremblin, T. Padioleau, M. W. Phillips, et al. Thermo-compositional Diabatic Convection in the Atmospheres of Brown Dwarfs and in Earth's Atmosphere and Oceans. ApJ, 876(2):144, May 2019. doi: 10.3847/1538-4357/ab05db.

A. Burrows, M. Marley, W. B. Hubbard, et al. A Nongray Theory of Extrasolar Giant Planets and Brown Dwarfs. ApJ, 491(2):856–875, December 1997. doi: 10.1086/305002.

Michael C. Liu, S. K. Leggett, and Kuenley Chiu. The Late-T Dwarf Companion to the Exoplanet Host Star HD 3651: A New Benchmark for Gravity and Metallicity Effects in Ultracool Spectra. ApJ, 660(2):1507–1516, May 2007. doi: 10.1086/512662.

Adam J. Burgasser, Michael W. McElwain, J. Davy Kirkpatrick, et al. The 2MASS Wide-Field T Dwarf Search. III. Seven New T Dwarfs and Other Cool Dwarf Discoveries. AJ, 127(5):2856–2870, May 2004. doi: 10.1086/383549.

Adam J. Burgasser, J. Davy Kirkpatrick, Roc M. Cutri, et al. Discovery of a Brown Dwarf Companion to Gliese 570ABC: A 2MASS T Dwarf Significantly Cooler than Gliese 229B. ApJ, 531(1):L57–L60, March 2000. doi: 10.1086/312522.

Anjali A. A. Piette and Nikku Madhusudhan. Considerations for atmospheric retrieval of high-precision brown dwarf spectra. MNRAS, 497(4):5136–5154, October 2020. doi: 10.1093/mnras/staa2289.

J. T. Rayner, D. W. Toomey, P. M. Onaka, et al. SpeX: A Medium-Resolution 0.8-5.5 Micron Spectrograph and Imager for the NASA Infrared Telescope Facility. PASP, 115(805):362–382, March 2003. doi: 10.1086/367745.

Adam J. Burgasser. The SpeX Prism Library: 1000+ low-resolution, near-infrared spectra of ultracool M, L, T and Y dwarfs. In *Astronomical Society of India Conference Series*, volume 11 of *Astronomical Society of India Conference Series*, pages 7–16, Jan 2014.

Michael C. Cushing, William D. Vacca, and John T. Rayner. Spextool: A Spectral Extraction Package for SpeX, a 0.8-5.5 Micron Cross-Dispersed Spectrograph. PASP, 116(818):362–376, April 2004. doi: 10.1086/382907.

A. J. Burgasser and Splat Development Team. The SpeX Prism Library Analysis Toolkit (SPLAT): A Data Curation Model. In *Astronomical Society of India Conference Series*, volume 14 of *Astronomical Society of India Conference Series*, pages 7–12, Jan 2017.

M. F. Skrutskie, R. M. Cutri, R. Stiening, et al. The Two Micron All Sky Survey (2MASS). AJ, 131(2):1163–1183, February 2006. doi: 10.1086/498708.

Eric L. Nielsen, Robert J. De Rosa, Jason Wang, et al. Dynamical Mass Measurement of the Young Spectroscopic Binary V343 Normae AaAb Resolved With the Gemini Planet Imager. AJ, 152(6):175, December 2016. doi: 10.3847/0004-6256/152/6/175.

P. Mollière, R. van Boekel, C. Dullemond, et al. Model Atmospheres of Irradiated Exoplanets: The Influence of Stellar Parameters, Metallicity, and the C/O Ratio. ApJ, 813(1):47, November 2015. doi: 10.1088/0004-637X/813/1/47.

P. Mollière, R. van Boekel, J. Bouwman, et al. Observing transiting planets with JWST. Prime targets and their synthetic spectral observations. A&A, 600: A10, April 2017. doi: 10.1051/0004-6361/201629800.

J. L. Beuzit, A. Vigan, D. Mouillet, et al. SPHERE: the exoplanet imager for the Very Large Telescope. A&A, 631:A155, November 2019. doi: 10.1051/0004-6361/201935251.

Ian S. McLean and David Sprayberry. Instrumentation at the Keck observatory. In Masanori Iye and Alan F. M. Moorwood, editors, *Instrument Design and Performance for Optical/Infrared Ground-based Telescopes*, volume 4841 of *Society of Photo-Optical Instrumentation Engineers (SPIE) Conference Series*, pages 1–6, March 2003. doi: 10.1117/12.461785.

Martin Abel, Lothar Frommhold, Xiaoping Li, and Katharine LC Hunt. Collision-induced absorption by h2 pairs: From hundreds to thousands of kelvin. *The Journal of Physical Chemistry A*, 115(25):6805–6812, 2011.

Leigh N Fletcher, Magnus Gustafsson, and Glenn S Orton. Hydrogen dimers in giant-planet infrared spectra. *The Astrophysical Journal Supplement Series*, 235(1):24, 2018.

Martin Abel, Lothar Frommhold, Xiaoping Li, and Katharine LC Hunt. Infrared absorption by collisional h2–he complexes at temperatures up to 9000 k and frequencies from 0 to 20 000 cm- 1. *The Journal of chemical physics*, 136(4): 044319, 2012.

M. W. Phillips, P. Tremblin, I. Baraffe, et al. A new set of atmosphere and evolution models for cool T-Y brown dwarfs and giant exoplanets. A&A, 637: A38, May 2020. doi: 10.1051/0004-6361/201937381.

Jayesh M. Goyal, Nathan Mayne, Benjamin Drummond, et al. A Library of Self-Consistent Simulated Exoplanet Atmospheres. MNRAS, August 2020. doi: 10.1093/mnras/staa2300.

S Gordon and B J McBride. Computer program for calculation of complex chemical equilibrium compositions and applications, 1994.

B. Drummond, P. Tremblin, I. Baraffe, et al. The effects of consistent chemical kinetics calculations on the pressure-temperature profiles and emission spectra of hot Jupiters. *Astronomy and Astrophysics*, 594:A69, October 2016. doi: 10.1051/0004-6361/201628799.

David S Amundsen, Isabelle Baraffe, Pascal Tremblin, et al. Accuracy tests of radiation schemes used in hot Jupiter global circulation models. *Astronomy and Astrophysics*, 564:A59, April 2014.

David S Amundsen, Pascal Tremblin, James Manners, et al. Treatment of overlapping gaseous absorption with the correlated-k method in hot Jupiter and brown dwarf atmosphere models. *Astronomy and Astrophysics*, 598:A97, February 2017.

T J Bueno and F P Bendicho. A Novel Iterative Scheme for the Very Fast and Accurate Solution of Non-LTE Radiative Transfer Problems. ApJ, 455:646, Dec 1995. doi: 10.1086/176612.

B Gustafsson, B Edvardsson, K Eriksson, et al. A grid of MARCS model atmospheres for late-type stars. I. Methods and general properties. *Astronomy and Astrophysics*, 486(3):951–970, August 2008.

D Saumon, G Chabrier, and H M van Horn. An Equation of State for Low-Mass Stars and Giant Planets. *Astrophysical Journal Supplement v.99*, 99: 713–, August 1995.

Joseph C. Filippazzo, Emily L. Rice, Jacqueline Faherty, et al. Fundamental Parameters and Spectral Energy Distributions of Young and Field Age Objects with Masses Spanning the Stellar to Planetary Regime. ApJ, 810(2):158, September 2015. doi: 10.1088/0004-637X/810/2/158.

L. Testi. A low-resolution near-infrared spectral library of M-, L-, and T-dwarfs. A&A, 503(2):639–650, August 2009. doi: 10.1051/0004-6361/200810699.

C. Del Burgo, E. L. Martín, M. R. Zapatero Osorio, and P. H. Hauschildt. Physical parameters of T dwarfs derived from high-resolution near-infrared spectra. A&A, 501(3):1059–1071, July 2009. doi: 10.1051/0004-6361/200810752.

D. Saumon, M. S. Marley, M. C. Cushing, et al. Ammonia as a Tracer of Chemical Equilibrium in the T7.5 Dwarf Gliese 570D. ApJ, 647(1):552–557, August 2006. doi: 10.1086/505419.

Adam Burrows and Maxim Volobuyev. Calculations of the far-wing line profiles of sodium and potassium in the atmospheres of substellar-mass objects. 583 (2):985–995, feb 2003. doi: 10.1086/345412.

G. Chabrier, I. Baraffe, J. Leconte, et al. The mass-radius relationship from solar-type stars to terrestrial planets: a review. In Eric Stempels, editor, *15th Cambridge Workshop on Cool Stars, Stellar Systems, and the Sun*, volume 1094 of *American Institute of Physics Conference Series*, pages 102–111, February 2009. doi: 10.1063/1.3099078.

Gaia Collaboration, T. Prusti, J. H. J. de Bruijne, et al. The Gaia mission. A&A, 595:A1, November 2016. doi: 10.1051/0004-6361/201629272.

Gaia Collaboration, A. G. A. Brown, A. Vallenari, et al. Gaia Data Release 2. Summary of the contents and survey properties. A&A, 616:A1, August 2018. doi: 10.1051/0004-6361/201833051.

D. Saumon and Mark S. Marley. The Evolution of L and T Dwarfs in Color-Magnitude Diagrams. ApJ, 689(2):1327–1344, December 2008. doi: 10.1086/592734.

Roberto Trotta. Bayes in the sky: Bayesian inference and model selection in cosmology. *Contemporary Physics*, 49(2):71–104, March 2008. doi: 10.1080/00107510802066753.

Vachail N. Salinas, Michiel R. Hogerheijde, Edwin A. Bergin, et al. First detection of gas-phase ammonia in a planet-forming disk. NH_3, N_2H^+, and H_2O in the disk around TW Hydrae. A&A, 591:A122, June 2016. doi: 10.1051/0004-6361/201628172.

Didier Saumon, Mark S. Marley, Martin Abel, et al. NEW h2collision-INDUCED ABSORPTION AND NH3opacity AND THE SPECTRA OF THE COOLEST BROWN DWARFS. *The Astrophysical Journal*, 750(1):74, apr 2012. doi: 10.1088/0004-637x/750/1/74. URL `https://doi.org/10.1088%2F0004-637x%2F750%2F1%2F74`.

Heidi N. Becker, James W. Alexander, Sushil K. Atreya, et al. Small lightning flashes from shallow electrical storms on Jupiter. Nature, 584(7819):55–58, August 2020. doi: 10.1038/s41586-020-2532-1.

P. Bodenheimer. Calculations of the Early Evolution of Jupiter. Icarus, 23(3):319–325, November 1974. doi: 10.1016/0019-1035(74)90050-5.

A. P. Boss. Giant planet formation by gravitational instability. *Science*, 276:1836–1839, January 1997. doi: 10.1126/science.276.5320.1836.

R. H. Durisen, A. P. Boss, L. Mayer, et al. Gravitational Instabilities in Gaseous Protoplanetary Disks and Implications for Giant Planet Formation. In Bo Reipurth, David Jewitt, and Klaus Keil, editors, *Protostars and Planets V*, page 607, January 2007.

James B. Pollack, Olenka Hubickyj, Peter Bodenheimer, et al. Formation of the Giant Planets by Concurrent Accretion of Solids and Gas. Icarus, 124(1):62–85, November 1996. doi: 10.1006/icar.1996.0190.

J. J. Lissauer and D. J. Stevenson. Formation of Giant Planets. In Bo Reipurth, David Jewitt, and Klaus Keil, editors, *Protostars and Planets V*, page 591, January 2007.

Mark S. Marley, Jonathan J. Fortney, Olenka Hubickyj, et al. On the Luminosity of Young Jupiters. ApJ, 655(1):541–549, January 2007. doi: 10.1086/509759.

R. Earle Luck. Abundances in the Local Region II: F, G, and K Dwarfs and Subgiants. AJ, 153(1):21, January 2017. doi: 10.3847/1538-3881/153/1/21.

A. Vigan, M. Bonavita, B. Biller, et al. The VLT/NaCo large program to probe the occurrence of exoplanets and brown dwarfs at wide orbits. IV. Gravitational instability rarely forms wide, giant planets. A&A, 603:A3, June 2017. doi: 10.1051/0004-6361/201630133.

C. Mordasini, R. van Boekel, P. Mollière, et al. The Imprint of Exoplanet Formation History on Observable Present-day Spectra of Hot Jupiters. ApJ, 832(1):41, November 2016. doi: 10.3847/0004-637X/832/1/41.

Néstor Espinoza, Jonathan J. Fortney, Yamila Miguel, et al. Metal Enrichment Leads to Low Atmospheric C/O Ratios in Transiting Giant Exoplanets. ApJ, 838(1):L9, March 2017. doi: 10.3847/2041-8213/aa65ca.

J. D. Ilee, D. H. Forgan, M. G. Evans, et al. The chemistry of protoplanetary fragments formed via gravitational instabilities. MNRAS, 472(1):189–204, November 2017. doi: 10.1093/mnras/stx1966.

Tiziano Zingales and Ingo Peter Waldmann. ExoGAN: Retrieving Exoplanetary Atmospheres Using Deep Convolutional Generative Adversarial Networks. *ArXiv e-prints*, art. arXiv:1806.02906, June 2018.

G. Peach, S. Yurchenko, K. Chubb, et al. The resonance lines of sodium and potassium in brown dwarf spectra. *Contributions of the Astronomical Observatory Skalnaté Pleso*, 50(1):193–202, 2020. doi: 10.31577/caosp.2020.50.1.193.

G. Peach. Recent results for widths of lines important in the spectra of cool stars. *Open Astronomy*, 20(4):516–522, 2017. doi: 10.1515/astro-2017-0330.

Trent J. Dupuy, Timothy D. Brandt, Kaitlin M. Kratter, and Brendan P. Bowler. A Model-independent Mass and Moderate Eccentricity for β Pic b. ApJ, 871 (1):L4, January 2019a. doi: 10.3847/2041-8213/aafb31.

Trent J. Dupuy. The Coolest Sample of Brown Dwarf Dynamical Masses. HST Proposal, November 2018.

Trent J. Dupuy, Katelyn Allers, Brendan Bowler, et al. Resolving Mass Benchmarks for Ultracool Atmospheres. HST Proposal, May 2020a.

Michael C. Liu, Eugene A. Magnier, Niall R. Deacon, et al. The Extremely Red, Young L Dwarf PSO J318.5338-22.8603: A Free-floating Planetary-mass Analog to Directly Imaged Young Gas-giant Planets. ApJ, 777:L20, Nov 2013. doi: 10.1088/2041-8205/777/2/L20.

Brittany E. Miles, Andrew J. Skemer, Travis S. Barman, et al. Methane in Analogs of Young Directly Imaged Exoplanets. ApJ, 869:18, Dec 2018. doi: 10.3847/1538-4357/aae6cd.

Julien Lozi, Olivier Guyon, Nemanja Jovanovic, et al. SCExAO, an instrument with a dual purpose: perform cutting-edge science and develop new technologies. In *Adaptive Optics Systems VI*, volume 10703 of *Society of Photo-Optical Instrumentation Engineers (SPIE) Conference Series*, page 1070359, July 2018. doi: 10.1117/12.2314282.

Takayuki Kotani, Motohide Tamura, Jun Nishikawa, et al. The infrared Doppler (IRD) instrument for the Subaru telescope: instrument description and commissioning results. In *Ground-based and Airborne Instrumentation for Astronomy VII*, volume 10702 of *Society of Photo-Optical Instrumentation Engineers (SPIE) Conference Series*, page 1070211, July 2018. doi: 10.1117/12.2311836.

Jacklyn Pezzato, Nemanja Jovanovic, Dimitri Mawet, et al. Status of the Keck Planet Imager and Characterizer Phase II Development. *arXiv e-prints*, art. arXiv:1909.06487, September 2019.

Matteo Brogi and Michael R. Line. Retrieving Temperatures and Abundances of Exoplanet Atmospheres with High-resolution Cross-correlation Spectroscopy. AJ, 157(3):114, March 2019. doi: 10.3847/1538-3881/aaffd3.

Nikku Madhusudhan, Kanani K. M. Lee, and Olivier Mousis. A Possible Carbon-rich Interior in Super-Earth 55 Cancri e. ApJ, 759(2):L40, November 2012. doi: 10.1088/2041-8205/759/2/L40.

J. I. Moses, N. Madhusudhan, C. Visscher, and R. S. Freedman. Chemical Consequences of the C/O Ratio on Hot Jupiters: Examples from WASP-12b, CoRoT-2b, XO-1b, and HD 189733b. ApJ, 763(1):25, January 2013. doi: 10.1088/0004-637X/763/1/25.

M. S. Marley, A. S. Ackerman, J. N. Cuzzi, and D. Kitzmann. *Clouds and Hazes in Exoplanet Atmospheres*, page 367. 2013. doi: 10.2458/azu_uapress_9780816530595-ch15.

Peter Gao, Daniel P. Thorngren, Elspeth K. H. Lee, et al. Aerosol composition of hot giant exoplanets dominated by silicates and hydrocarbon hazes. *Nature Astronomy*, 4:951–956, May 2020. doi: 10.1038/s41550-020-1114-3.

Christiane Helling. Clouds in Exoplanetary Atmospheres. *arXiv e-prints*, art. arXiv:2011.03302, November 2020.

Dániel Apai, Jacqueline Radigan, Esther Buenzli, et al. HST Spectral Mapping of L/T Transition Brown Dwarfs Reveals Cloud Thickness Variations. ApJ, 768(2):121, May 2013. doi: 10.1088/0004-637X/768/2/121.

Dániel Apai, Domenico Nardiello, and Luigi R. Bedin. TESS Observations of the Luhman 16 AB Brown Dwarf System: Rotational Periods, Lightcurve Evolution, and Zonal Circulation. ApJ, 906(1):64, January 2021. doi: 10.3847/1538-4357/abcb97.

Beth A. Biller, Johanna Vos, Esther Buenzli, et al. Simultaneous Multiwavelength Variability Characterization of the Free-floating Planetary-mass Object PSO J318.5-22. AJ, 155:95, Feb 2018. doi: 10.3847/1538-3881/aaa5a6.

Johanna M. Vos, Beth A. Biller, Mariangela Bonavita, et al. A search for variability in exoplanet analogues and low-gravity brown dwarfs. MNRAS, 483(1):480–502, Feb 2019. doi: 10.1093/mnras/sty3123.

Johanna M. Vos, Beth A. Biller, Katelyn N. Allers, et al. Spitzer Variability Properties of Low-gravity L Dwarfs. AJ, 160(1):38, July 2020. doi: 10.3847/1538-3881/ab9642.

Chloe Fisher and Kevin Heng. Retrieval analysis of 38 WFC3 transmission spectra and resolution of the normalization degeneracy. MNRAS, 481(4):4698–4727, December 2018. doi: 10.1093/mnras/sty2550.

P. Tremblin, D. S. Amundsen, P. Mourier, et al. Fingering Convection and Cloudless Models for Cool Brown Dwarf Atmospheres. *The Astrophysical Journal Letters*, 804:L17, May 2015. doi: 10.1088/2041-8205/804/1/L17.

W. M. J. Best, M. C. Liu, E. A. Magnier, and T. J. Dupuy. VizieR Online Data Catalog: Hawaii IR parallax program. IV. L0-T8 BDs with UKIRT (Best+, 2020). *VizieR Online Data Catalog*, art. J/AJ/159/257, July 2020a.

Trent J. Dupuy and Michael C. Liu. The Hawaii Infrared Parallax Program. I. Ultracool Binaries and the L/T Transition. ApJS, 201(2):19, August 2012. doi: 10.1088/0067-0049/201/2/19.

Trent J. Dupuy and Adam L. Kraus. Distances, Luminosities, and Temperatures of the Coldest Known Substellar Objects. *Science*, 341(6153):1492–1495, September 2013. doi: 10.1126/science.1241917.

Michael C. Liu, Trent J. Dupuy, and Katelyn N. Allers. The Hawaii Infrared Parallax Program. II. Young Ultracool Field Dwarfs. ApJ, 833(1):96, December 2016. doi: 10.3847/1538-4357/833/1/96.

William M. J. Best, Eugene A. Magnier, Michael C. Liu, et al. Photometry and Proper Motions of M, L, and T Dwarfs from the Pan-STARRS1 3π Survey. ApJS, 234(1):1, January 2018. doi: 10.3847/1538-4365/aa9982.

William M. J. Best, Michael C. Liu, Eugene A. Magnier, and Trent J. Dupuy. The Hawaii Infrared Parallax Program. IV. A Comprehensive Parallax Survey of L0-T8 Dwarfs with UKIRT. AJ, 159(6):257, June 2020b. doi: 10.3847/1538-3881/ab84f4.

Bartosz Gauza, Victor J. S. Béjar, Antonio Pérez-Garrido, et al. Discovery of a Young Planetary Mass Companion to the Nearby M Dwarf VHS J125601.92-125723.9. ApJ, 804:96, May 2015. doi: 10.1088/0004-637X/804/2/96.

Alexandra Z. Greenbaum, Laurent Pueyo, Jean-Baptiste Ruffio, et al. GPI Spectra of HR 8799 c, d, and e from 1.5 to 2.4 μm with KLIP Forward Modeling. AJ, 155:226, Jun 2018. doi: 10.3847/1538-3881/aabcb8.

K. N. Allers, J. F. Gallimore, Michael C. Liu, and Trent J. Dupuy. The Radial and Rotational Velocities of PSO J318.5338-22.8603, a Newly Confirmed Planetary-mass Member of the β Pictoris Moving Group. ApJ, 819(2):133, Mar 2016. doi: 10.3847/0004-637X/819/2/133.

Beth A. Biller, Johanna Vos, Mariangela Bonavita, et al. Variability in a Young, L/T Transition Planetary-mass Object. ApJ, 813:L23, Nov 2015. doi: 10.1088/2041-8205/813/2/L23.

Ian S. McLean, Eric E. Becklin, Oddvar Bendiksen, et al. Design and development of NIRSPEC: a near-infrared echelle spectrograph for the Keck II telescope. In Albert M. Fowler, editor, *Infrared Astronomical Instrumentation*, volume 3354, pages 566 – 578. International Society for Optics and Photonics, SPIE, 1998. URL `https://doi.org/10.1117/12.317283`.

Trent J. Dupuy, Michael C. Liu, Eugene A. Magnier, et al. The Parallax of VHS J1256-1257 from CFHT and Pan-STARRS-1. *Research Notes of the American Astronomical Society*, 4(4):54, April 2020b. doi: 10.3847/2515-5172/ab8942.

Jordan M. Stone, Andrew J. Skemer, Kaitlin M. Kratter, et al. Adaptive Optics imaging of VHS 1256-1257: A Low Mass Companion to a Brown Dwarf Binary System. ApJ, 818(1):L12, February 2016. doi: 10.3847/2041-8205/818/1/L12.

Evan A. Rich, Thayne Currie, John P. Wisniewski, et al. Thermal Infrared Imaging and Atmospheric Modeling of VHS J125601.92-125723.9 b: Evidence for Moderately Thick Clouds and Equilibrium Carbon Chemistry in a Hierarchical Triple System. ApJ, 830(2):114, October 2016. doi: 10.3847/0004-637X/830/2/114.

Thayne Currie, Adam Burrows, Yoichi Itoh, et al. A Combined Subaru/VLT/MMT 1-5 μm Study of Planets Orbiting HR 8799: Implications for Atmospheric Properties, Masses, and Formation. ApJ, 729(2):128, March 2011. doi: 10.1088/0004-637X/729/2/128.

Andrew J. Skemer, Philip M. Hinz, Simone Esposito, et al. First Light LBT AO Images of HR 8799 bcde at 1.6 and 3.3 μm: New Discrepancies between Young Planets and Old Brown Dwarfs. ApJ, 753(1):14, Jul 2012. doi: 10.1088/0004-637X/753/1/14.

B. R. Oppenheimer, C. Baranec, C. Beichman, et al. Reconnaissance of the HR 8799 Exosolar System. I. Near-infrared Spectroscopy. ApJ, 768:24, May 2013. doi: 10.1088/0004-637X/768/1/24.

Andrew J. Skemer, Mark S. Marley, Philip M. Hinz, et al. Directly Imaged L-T Transition Exoplanets in the Mid-infrared. ApJ, 792(1):17, Sep 2014. doi: 10.1088/0004-637X/792/1/17.

Patrick Ingraham, Mark S. Marley, Didier Saumon, et al. Gemini Planet Imager Spectroscopy of the HR 8799 Planets c and d. ApJ, 794(1):L15, Oct 2014. doi: 10.1088/2041-8205/794/1/L15.

Travis S. Barman, Quinn M. Konopacky, Bruce Macintosh, and Christian Marois. Simultaneous Detection of Water, Methane, and Carbon Monoxide in the Atmosphere of Exoplanet HR8799b. ApJ, 804:61, May 2015. doi: 10.1088/0004-637X/804/1/61.

Abhijith Rajan, Travis Barman, Rémi Soummer, et al. Characterizing the Atmospheres of the HR8799 Planets with HST/WFC3. ApJ, 809(2):L33, August 2015. doi: 10.1088/2041-8205/809/2/L33.

Jason J. Wang, James R. Graham, Rebekah Dawson, et al. Dynamical Constraints on the HR 8799 Planets with GPI. AJ, 156:192, Nov 2018. doi: 10.3847/1538-3881/aae150.

D. J. M. Petit dit de la Roche, M. E. van den Ancker, M. Kissler-Patig, et al. New constraints on the HR 8799 planetary system from mid-infrared direct imaging. MNRAS, 491(2):1795–1799, January 2020. doi: 10.1093/mnras/stz3117.

Cameron P. M. Bell, Eric E. Mamajek, and Tim Naylor. A self-consistent, absolute isochronal age scale for young moving groups in the solar neighbourhood. MNRAS, 454(1):593–614, November 2015. doi: 10.1093/mnras/stv1981.

R. O. Gray, C. J. Corbally, R. F. Garrison, et al. Contributions to the Nearby Stars (NStars) Project: Spectroscopy of Stars Earlier than M0 within 40 pc-The Southern Sample. AJ, 132(1):161–170, July 2006. doi: 10.1086/504637.

B. A. Smith and R. J. Terrile. A Circumstellar Disk around β Pictoris. *Science*, 226(4681):1421–1424, December 1984. doi: 10.1126/science.226.4681.1421.

Karin I. Öberg, Ruth Murray-Clay, and Edwin A. Bergin. The Effects of Snowlines on C/O in Planetary Atmospheres. ApJ, 743(1):L16, December 2011. doi: 10.1088/2041-8205/743/1/L16.

Karin I. Öberg and Edwin A. Bergin. Astrochemistry and compositions of planetary systems. Phys. Rep., 893:1–48, January 2021. doi: 10.1016/j.physrep.2020.09.004.

A. M. Lagrange, Nadège Meunier, Pascal Rubini, et al. Evidence for an additional planet in the β Pictoris system. *Nature Astronomy*, 3:1135–1142, August 2019. doi: 10.1038/s41550-019-0857-1.

J. L. Baudino, B. Bézard, A. Boccaletti, et al. Interpreting the photometry and spectroscopy of directly imaged planets: a new atmospheric model applied to β Pictoris b and SPHERE observations. A&A, 582:A83, October 2015. doi: 10.1051/0004-6361/201526332.

Jean-Loup Baudino, Paul Mollière, Olivia Venot, et al. Toward the analysis ofJWSTExoplanet spectra: Identifying troublesome model parameters. *The Astrophysical Journal*, 850(2):150, nov 2017. doi: 10.3847/1538-4357/aa95be. URL `https://doi.org/10.3847/1538-4357/aa95be`.

Blain, D., Charnay, B., and Bézard, B. 1d atmospheric study of the temperate sub-neptune k2-18b. *A&A*, 646:A15, 2021. doi: 10.1051/0004-6361/202039072. URL `https://doi.org/10.1051/0004-6361/202039072`.

Katharina Lodders. Solar elemental abundances, 2019.

Trent J. Dupuy, Timothy D. Brandt, Kaitlin M. Kratter, and Brendan P. Bowler. A Model-independent Mass and Moderate Eccentricity for β Pic b. ApJ, 871 (1):L4, Jan 2019b. doi: 10.3847/2041-8213/aafb31.

I. A. G. Snellen and A. G. A. Brown. The mass of the young planet Beta Pictoris b through the astrometric motion of its host star. *Nature Astronomy*, 2:883–886, Aug 2018b. doi: 10.1038/s41550-018-0561-6.

Katie M. Morzinski, Jared R. Males, Andy J. Skemer, et al. Magellan Adaptive Optics First-light Observations of the Exoplanet β Pic b. II. 3-5 μm Direct Imaging with MagAO+Clio, and the Empirical Bolometric Luminosity of a Self-luminous Giant Planet. ApJ, 815(2):108, December 2015. doi: 10.1088/0004-637X/815/2/108.

Jeffrey Chilcote, Travis Barman, Michael P. Fitzgerald, et al. The First H-band Spectrum of the Giant Planet β Pictoris b. ApJ, 798(1):L3, Jan 2015. doi: 10.1088/2041-8205/798/1/L3.

M. Bonnefoy, G. D. Marleau, R. Galicher, et al. Physical and orbital properties of β Pictoris b. A&A, 567:L9, Jul 2014. doi: 10.1051/0004-6361/201424041.

M. Bonnefoy, A. Boccaletti, A. M. Lagrange, et al. The near-infrared spectral energy distribution of β Pictoris b. A&A, 555:A107, July 2013. doi: 10.1051/0004-6361/201220838.

Thayne Currie, Adam Burrows, Nikku Madhusudhan, et al. A Combined Very Large Telescope and Gemini Study of the Atmosphere of the Directly Imaged Planet, β Pictoris b. ApJ, 776(1):15, Oct 2013. doi: 10.1088/0004-637X/776/1/15.

Elena Manjavacas, Theodora Karalidi, Johanna Vos, et al. Revealing the Vertical Cloud Structure of a young low-mass Brown Dwarf, an analog to the beta-Pictoris b directly-imaged exoplanet, through Keck I/MOSFIRE spectro-photometric variability. *arXiv e-prints*, art. arXiv:2107.12368, July 2021.

C. Mordasini, Y. Alibert, C. Georgy, et al. Characterization of exoplanets from their formation. II. The planetary mass-radius relationship. A&A, 547:A112, November 2012. doi: 10.1051/0004-6361/201118464.

Clive D. Rodgers. *Inverse Methods for Atmospheric Sounding: Theory and Practice*. WORLD SCIENTIFIC, 2000. doi: 10.1142/3171.

J. M. Lee, L. N. Fletcher, and P. G. J. Irwin. Optimal estimation retrievals of the atmospheric structure and composition of HD 189733b from secondary eclipse spectroscopy. MNRAS, 420(1):170–182, February 2012. doi: 10.1111/j.1365-2966.2011.20013.x.

Travis S. Barman, Bruce Macintosh, Quinn M. Konopacky, and Christian Marois. The Young Planet-mass Object 2M1207b: A Cool, Cloudy, and Methane-poor Atmosphere. ApJ, 735(2):L39, July 2011b. doi: 10.1088/2041-8205/735/2/L39.

P. Patapis, E. Nasedkin, G. Cugno, et al. Direct emission spectroscopy of exoplanets with the medium resolution imaging spectrometer on board JWST MIRI: I. Molecular mapping and sensitivity to instrumental effects. *arXiv e-prints*, art. arXiv:2110.15756, October 2021.

G. H. Rieke, G. S. Wright, T. Böker, et al. The Mid-Infrared Instrument for the James Webb Space Telescope, I: Introduction. *Publications of the Astronomical Society of the Pacific*, 127:584, July 2015a. doi: 10.1086/682252.

G. S. Wright, David Wright, G. B. Goodson, et al. The Mid-Infrared Instrument for the James Webb Space Telescope, II: Design and Build. *Publications of the Astronomical Society of the Pacific*, 127:595, July 2015. doi: 10.1086/682253.

Patrice Bouchet, Macarena García-Marín, P. O. Lagage, et al. The Mid-Infrared Instrument for the James Webb Space Telescope, III: MIRIM, The MIRI Imager. *Publications of the Astronomical Society of the Pacific*, 127:612, July 2015. doi: 10.1086/682254.

Sarah Kendrew, Silvia Scheithauer, Patrice Bouchet, et al. The Mid-Infrared Instrument for the James Webb Space Telescope, IV: The Low-Resolution Spectrometer. *Publications of the Astronomical Society of the Pacific*, 127: 623, July 2015. doi: 10.1086/682255.

A. Boccaletti, P. O. Lagage, P. Baudoz, et al. The Mid-Infrared Instrument for the James Webb Space Telescope, V: Predicted Performance of the MIRI Coronagraphs. *Publications of the Astronomical Society of the Pacific*, 127:633, July 2015. doi: 10.1086/682256.

Martyn Wells, J.-W. Pel, Alistair Glasse, et al. The mid-infrared instrument for the james webb space telescope , vi: The medium resolution spectrometer. *Publications of the Astronomical Society of the Pacific*, 127(953):646, 2015. URL `http://stacks.iop.org/1538-3873/127/i=953/a=646`.

G. H. Rieke, M. E. Ressler, Jane E. Morrison, et al. The Mid-Infrared Instrument for the James Webb Space Telescope, VII: The MIRI Detectors. *Publications of the Astronomical Society of the Pacific*, 127:665, July 2015b. doi: 10.1086/682257.

M. E. Ressler, K. G. Sukhatme, B. R. Franklin, et al. The Mid-Infrared Instrument for the James Webb Space Telescope, VIII: The MIRI Focal Plane System. *Publications of the Astronomical Society of the Pacific*, 127:675, July 2015. doi: 10.1086/682258.

Alistair Glasse, G. H. Rieke, E. Bauwens, et al. The Mid-Infrared Instrument for the James Webb Space Telescope, IX: Predicted Sensitivity. *Publications of the Astronomical Society of the Pacific*, 127:686, July 2015. doi: 10.1086/682259.

Karl D. Gordon, C. H. Chen, Rachel E. Anderson, et al. The Mid-Infrared Instrument for the James Webb Space Telescope, X: Operations and Data Reduction. *Publications of the Astronomical Society of the Pacific*, 127:696, July 2015. doi: 10.1086/682260.

Jessica L. Luna and Caroline V. Morley. Empirically Determining Substellar Cloud Compositions in the era of JWST. *arXiv e-prints*, art. arXiv:2108.03161, August 2021.

Adam J. Burgasser, Robert A. Simcoe, John J. Bochanski, et al. Clouds in the Coldest Brown Dwarfs: Fire Spectroscopy of Ross 458C. ApJ, 725(2):1405–1420, December 2010. doi: 10.1088/0004-637X/725/2/1405.

Zhoujian Zhang, Michael C. Liu, Mark S. Marley, et al. Uniform Forward-Modeling Analysis of Ultracool Dwarfs. II. Atmospheric Properties of 55 Late-T Dwarfs. *arXiv e-prints*, art. arXiv:2105.05256, May 2021.

Alex J. Cridland, Ewine F. van Dishoeck, Matthew Alessi, and Ralph E. Pudritz. Connecting planet formation and astrochemistry. C/Os and N/Os of warm giant planets and Jupiter analogues. A&A, 642:A229, October 2020. doi: 10.1051/0004-6361/202038767.

Aaron David Schneider and Bertram Bitsch. How drifting and evaporating pebbles shape giant planets I: Heavy element content and atmospheric C/O. *arXiv e-prints*, art. arXiv:2105.13267, May 2021.

B. Goldman, S. Marsat, T. Henning, et al. A new benchmark T8-9 brown dwarf and a couple of new mid-T dwarfs from the UKIDSS DR5+ LAS. MNRAS, 405(2):1140–1152, June 2010. doi: 10.1111/j.1365-2966.2010.16524.x.

Ben Burningham, S. K. Leggett, D. Homeier, et al. The properties of the T8.5p dwarf Ross 458C. MNRAS, 414(4):3590–3598, July 2011. doi: 10.1111/j.1365-2966.2011.18664.x.

P. D. Klaassen, V. C. Geers, S. M. Beard, et al. MIRISIM: a simulator for the Mid-Infrared Instrument on JWST. MNRAS, 500(3):2813–2821, January 2021. doi: 10.1093/mnras/staa3416.

Alvaro Labiano-Ortega, Daniel Dicken, Bart Vandenbussche, et al. The MIRI Medium Resolution Spectrometer calibration pipeline. Technical report, 2016.

Klaus M. Pontoppidan, Timothy E. Pickering, Victoria G. Laidler, et al. Pandeia: a multi-mission exposure time calculator for JWST and WFIRST. In Alison B. Peck, Robert L. Seaman, and Chris R. Benn, editors, *Observatory Operations: Strategies, Processes, and Systems VI*, volume 9910 of *Society of Photo-Optical*

Instrumentation Engineers (SPIE) Conference Series, page 991016, July 2016. doi: 10.1117/12.2231768.

Marshall D. Perrin, Joseph Long, Anand Sivaramakrishnan, et al. WebbPSF: James Webb Space Telescope PSF Simulation Tool, April 2015.

JWST ETC User Documentation. JWST ETC,. `https://jwst-docs.stsci.edu/jwst-exposure-time-calculator-overview`, 2022. [Online; accessed 31-Jan-2022].

Adam Burrows, M. S. Marley, and C. M. Sharp. The Near-Infrared and Optical Spectra of Methane Dwarfs and Brown Dwarfs. ApJ, 531(1):438–446, March 2000. doi: 10.1086/308462.